Università degli Studi di Salerno

Dipartimento di Matematica

Scienze Matematiche, Fisiche ed Informatiche

XI Ciclo - Nuova Serie

Curriculum in Fisica dei sistemi complessi e dell'ambiente

Ph.D. Thesis

in

High-sensitivity strain measurements from underground interferometric stations: geodynamic phenomena at Gran Sasso and first records from Canfranc

Candidate

Verdiana Botta

Supervisor

Prof. Luca Crescentini

Coordinator

Prof. Patrizia Longobardi

Academic Year 2011-2012

The man is infinitely small compared to Nature,
but infinitely great if he agrees to be part of it.
Blaise Pascal

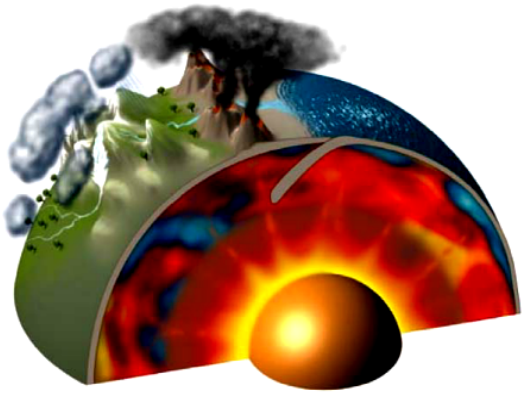

Contents

List of Figures

List of Tables

Introduction

Earth's surface and interior deform as a result of geological and geophysical processes. Earth is continually influenced by the gravitational forces, processes from within the core, and complex interactions between oceans and atmosphere.

To study these phenomena and to understand better the rheological properties of the Earth, measurements of Earth's deformation become of fundamental importance, providing a critical link between Earth's structure and dynamics, also in order to optimize the response to natural hazards and to identify potential risk areas.

The study of crustal deformation is a complex but very important research topic that encompasses several scientific disciplines, including differential geometry, theory of elasticity, geodynamics and physics in general.

The use of different kind of geodetic data to study geodynamic phenomena became increasingly important, playing a key role in the knowledge of their temporal and magnitude variations at many different spatial and time scales. These measurements provide significant constraints on the changes in Earth's lithosphere and processes that cause them, like for example movements of magma, changes in strain before, during, and after earthquakes, motion of ice sheets. Yet even today, large portions of the Earth are infrequently monitored, or not at all.

Deformation can be measured in several ways, as relative movement of points on the Earth's surface, through measurements of strain and tilt, or by GPS (Global Positioning System), VLBI (Very Long Base Interferometry) and SLR (Satellite Laser Ranging) measurements. Among the different types of instruments, the laser strainmeters (or interferometers), measuring the displacement between two points away from a few meters to over a kilometer, are characterized by very high accuracy and long-term stability, necessary to investigate processes of crustal deformation. The analysis of interferometric data allows to study both local and global geodynamic phenomena in a broad band of frequencies.

This thesis introduces results related to some analysis of data recorded by two laser interferometers installed at Gran Sasso (Italy) Underground Laboratories and describes the installation of two new laser interferometers in the Canfranc (Spain) Underground Laboratory, at the end of August 2011, with the analysis of their first sequences.

In the first chapter some general concepts about strain, crustal deformation and their measurements are introduced. The study of the deformation on the Earth's surface improved in the last fifty years, changing from mostly descriptive and qualitative to more quantitative. The state and magnitude of the stress in the Earth's lithosphere, and thus of the deformation, play an important role on various geophysical problems, such as the plate mechanisms, energy budget of the Earth, earthquake mechanism and crustal movements.

In Chapter 2 there is a description of the Earth's tidal deformation. The body tides, due to a direct effect of gravitational attraction from the Sun, Moon and other objects, can be modeled very accurately. In addition, there is a part of deformation, known as ocean loading, arising from the mass fluctuations of the oceans. These last is also rather well understood, but the modeling of its effects still needs to be improved. This phenomenon is very significant for the interferometric strain sequences because they are clearly dominated by the semidiurnal and diurnal strain tides.

Chapter 3 describes the laser interferometry and, in particular, the operating principle of the Gran Sasso (Italy) laser interferometers, which provide very high-sensitivity strain data, by comparing the optical length of a longer measurement arm (about 90 meters in length) and a shorter fixed reference arm (about 20 cm in length). Although the interferometers measure strain directly, the presence of cavities, topography, and local inhomogeneities of the crust can modify the strain measurement considerably. Also environmental and anthropic effects appear as anomalous or noise signals in a broad frequency range, which includes for example the Earth tides. It is necessary to take some or all these possible effects into account, depending on the phenomenon studied.

In Chapter 4 data produced by Gran Sasso interferometers, first alone and then together with those produced by a third laser interferometer installed in Baksan (Russia) Underground Laboratory, are used to estimate the Free Core Nutation (FCN) parameters. The analysis of the only Gran Sasso strain data provides a value for the FCN period (about 429 sidereal days) robust and comparable to those from gravity tides, obtained from the joint inversion of data from several stations. The agreement between observations and predictions looks better than in any previous work that makes use of

strain tides. The joint analysis of Gran Sasso and Baksan strain data confirms, but does not improve, these results recently obtained.

In Chapter 5 the new mode of faulting, discovered in the last decades and referred to as slow slip earthquakes, is examined. Many aspects of slow slip remain unexplained. Here an attempt to describe the characteristics of the rupture propagation through the analysis of strain records from three different slow events related to the 1978 Izu-Oshima (Japan) earthquake, the 1999 Durmid Hill (California) slow event and the 2003 Tokachi-oki (Japan) earthquake. The signals recorded during these slow events exhibit the same peculiarities observed in the strain sequences recorded at Gran Sasso during the 6 April 2009 L'Aquila earthquake, first direct measurement of the diffusive character of the rupture propagation.

In the last chapter the installation, occured in August 2011, of two new laser interferometers is described and their first records analysed. These instruments, operating since November 2011, are installed in the Canfranc (Spain) Underground Laboratory (LSC). The LSC is located at depth in one of the most seismically active areas in Western Europe, at the Pyrenean chain that marks the boundary between the European plate and the Iberian microplate. The first tests on strain data recorded by these interferometers evidence the capability of producing clear records of low-frequency signals, for example relating to seismic waves, Earth free oscillations, and possible local aseismic stress release. A preliminary tidal analysis shows a good agreement between observed and predicted tides in the diurnal tidal band, suggesting that, if any, local strain distortion effects are small. In the semidiurnal tidal band, discrepancies between observed and predicted tides are noticeable; this might be a consequence of inadequate Earth and/or ocean models.

Chapter 1

Deformation Measurements

The deformation of a body subjected to an applied stress is the ratio between the size of the body before and after the application of the stress. Depending on the body size, linear, surface or volumetric deformations are defined.

To describe the deformation in a medium, the concept of strain is introduced. The deformation, defined by the ratio of two lengths, is expressed as dimensionless quantity. Since it is often related to very small amounts, nanostrain (10^{-9} strain) or microstrain (10^{-6} strain) quantities are introduced.

The state and magnitude of the stress in the Earth's lithosphere, and thus of the deformation, play an important role for several geophysical phenomena, such as the plate mechanisms, energy budget of the Earth, earthquake mechanism and crustal movements.

The Theory of Elasticity provides mathematical relationships between stress and strain in a medium.

Measurements of crustal deformation require a very high accuracy and long-term stability. The most common techniques for continuous strain measurements are continuous GPS networks, mechanical borehole dilatometers and strainmeters, mechanical extensometers, and laser extensometers (or interferometers).

1.1 Theory of Elasticity

The Theory of Elasticity is a branch of Continuum Mechanics that describes the property of solid materials to deform under the application of an external force and return to their original shape when the force is removed.

Under the action of external forces, the particles of the body will redistribute themselves to reach a new state of equilibrium. In principle it is possible to determine this redistribution through the laws of mechanics, but the nature of the molecular forces is very complicated, so at the end it is possible to describe only the macroscopic behavior of the body.

For a quantitative analysis of the particle movements is necessary to introduce the concepts of *stress* and *strain* and establish a mathematical relationship between these two quantities, by using the approximation of small deformations and linear elastic behavior.

Within the Earth rocks are continually being subjected to forces that deform them, changing their shape or size. The forces that deform rocks are referred to as stresses. Rocks may deform in variety of ways in responses to stresses, largely imposed by plate tectonic processes. The rock deformation provides information on the tectonic history of an area. Whether rocks respond to these differential stresses by folding or faulting is determined by the pressure, temperature, composition of the rock and the rate at which the stresses are applied.

1.1.1 Stress

The deformation of a body is related to the application of a force. The forces acting can be *volume* and *surface* forces. The former act without a direct contact, uniformly distributed on the mass of body and directly proportional to it, conservative or non-conservative. The latter act on the surface of the body through a direct contact.

Stress ($\vec{\sigma}$) is defined as surface force $\mathbf{F}$ per unit area $\triangle A$, that is

$$\vec{\sigma} = \lim_{\triangle A \to 0} \frac{\mathbf{F}}{\triangle A} \tag{1.1}$$

The force, acting on a surface, can be subdivided into perpendicular and parallel components to each plane. The perpendicular and parallel components are called normal

stress (σ_n) and shear stress (σ_t), respectively. Fig. 1.1 shows the relationship between the force (**F**) and the normal and shear stress components acting on a surface point.

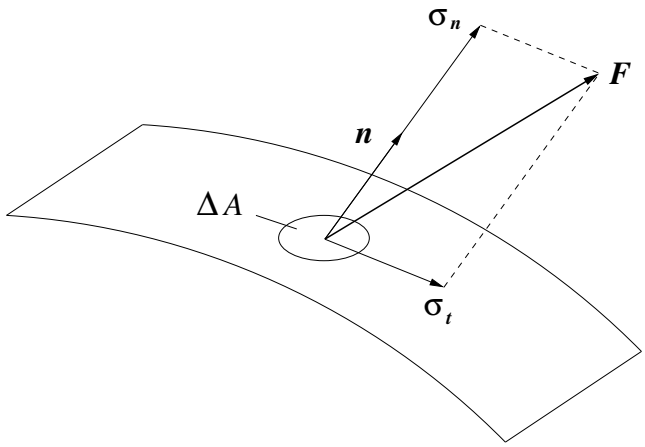

Figure 1.1: Normal and shear stress components of a force **F** acting on the unit area $\triangle A$.

In a three-dimensional space it is possible to calculate the surface forces that act in the x direction, considering a cubic element in a continuum medium (see Fig. 1.2), as

$$\begin{aligned} F_x &= \left(\sigma_{xx} + \frac{\partial \sigma_{xx}}{\partial x}\frac{dx}{2} - \sigma_{xx} + \frac{\partial \sigma_{xx}}{\partial x}\frac{dx}{2}\right) dydz + \\ &+ \left(\sigma_{yx} + \frac{\partial \sigma_{yx}}{\partial y}\frac{dy}{2} - \sigma_{yx} + \frac{\partial \sigma_{yx}}{\partial y}\frac{dy}{2}\right) dxdz + \\ &+ \left(\sigma_{zx} + \frac{\partial \sigma_{zx}}{\partial z}\frac{dz}{2} - \sigma_{zx} + \frac{\partial \sigma_{zx}}{\partial z}\frac{dz}{2}\right) dxdy \end{aligned} \tag{1.2}$$

or

$$F_x = \left(\frac{\partial \sigma_{xx}}{\partial x} + \frac{\partial \sigma_{yx}}{\partial y} + \frac{\partial \sigma_{zx}}{\partial z}\right) dxdydz = \frac{\partial \sigma_{jx}}{\partial x_j} dV \tag{1.3}$$

Similar stress terms act in the other directions, so it is possible to generalize the force acting on the surface per unit of volume as

$$f_i = \frac{\partial \sigma_{ji}}{\partial x_j} \tag{1.4}$$

$w$here the index i corresponds to the direction of the normal to the surface being acted on by the force, and j indicates the direction of the force.

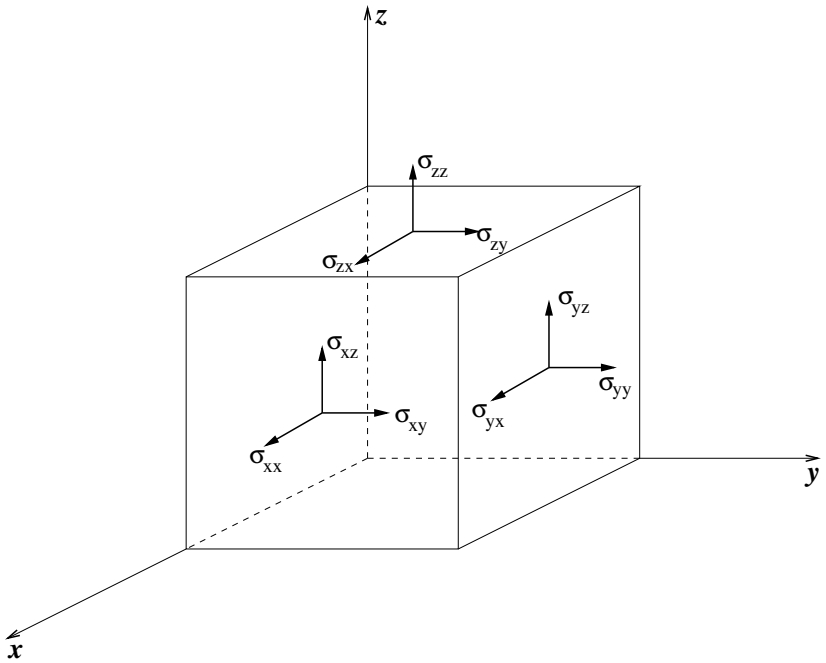

Figure 1.2: Balance of stress acting on each face of a cubic element in a continuum medium. For each stress component the first index indicates the plane that the stress acts on, and the second one the direction in which the stress acts.

So it is possible to introduce the *stress tensor* σ_{ij}

$$\sigma_{ij} = \begin{pmatrix} \sigma_{xx} & \sigma_{xy} & \sigma_{xz} \\ \sigma_{yx} & \sigma_{yy} & \sigma_{yz} \\ \sigma_{zx} & \sigma_{zy} & \sigma_{zz} \end{pmatrix} \tag{1.5}$$

This tensor is symmetric, reducing the number of independent components to six. The diagonal terms represent the normal stresses; they are also called *tensional* or *compressional* stresses if their values are positive or negative, respectively. The off-diagonal terms represent the shear stresses. At each point of the body, it is possible to show that three mutually perpendicular directions, for which no shear stress acts, exist. These directions are called *principal stress axes*. The trace of the stress tensor is invariant to choice of the referece system and related to the total stress state.

1.1.2 Deformation and Strain

Deformation within a solid body involves variation of the displacement field and represent the changes in both length and angular distortions; this deformation is expressed

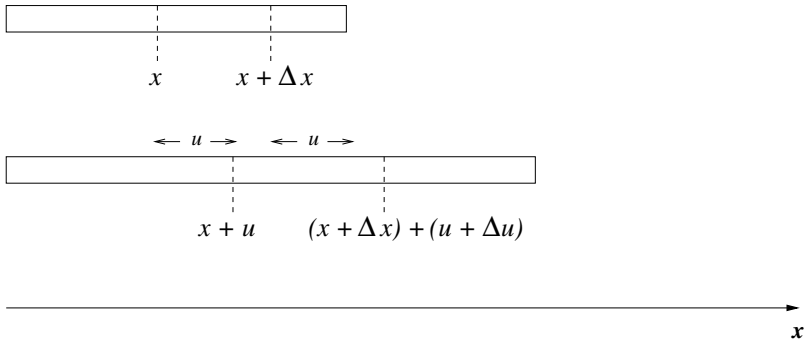

Figure 1.3: Meaning of longitudinal strain in one-dimensional space.

by spatial gradients of the displacement field, also called *strains*.

An elastic body under an applied load deforms into a new shape. In a one-dimensional space, consider two arbitrary points located close together at the positions x and $(x + \triangle x)$, respectively (see Fig. 1.3). If the point x is displaced by an infinitesimally amount u in the direction of the *x-axis*, the point $(x + \triangle x)$ will move to the position $(u + \triangle u)$, where $\triangle u = (\partial u/\partial x)\,\triangle x$. The total length increase between these points is u.

The *longitudinal strain* is defined as the fractional change in length, that is

$$\varepsilon_{xx} = \frac{\left(\triangle x + \frac{\partial u}{\partial x}\triangle x\right) - \triangle x}{\triangle x} = \frac{\partial u}{\partial x} \tag{1.6}$$

The shear components of stress produce *shear strains*, angular changes in the right angle defined between two mutually orthogonal directions of the body.

It is possible to explain simply the meaning of shear strain in a two-dimensional space. In a (x, y) plane, consider a rectangle (ABCD, see Fig. 1.4) with sides $\triangle x$ and $\triangle y$ and its distortion caused by shear stresses. If u is the displacement parallel to the *x-axis* of the point A, the point D is displaced by the amount $(\partial u/\partial y)\,\triangle y$ in the *x-axis* direction. This causes a clockwise rotation of the side AD, described through an angle ϕ_1 given by

$$\tan\phi_1 = \frac{(\partial u/\partial y)\,\triangle y}{\triangle y} = \frac{\partial u}{\partial y} \tag{1.7}$$

At the same time, if v is the displacement parallel to the *y-axis* of the point A, the point B is displaced by the amount $(\partial v/\partial x)\,\triangle x$ in the *y-axis* direction. In this case the

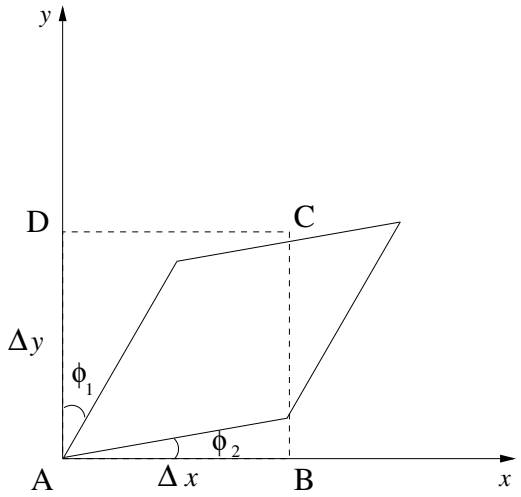

Figure 1.4: Meaning of shear strain in a two-dimensional space.

side AB rotates anticlockwise of an angle ϕ_2 given by

$$\tan \phi_2 = \frac{(\partial v/\partial x) \triangle x}{\triangle x} = \frac{\partial v}{\partial x} \tag{1.8}$$

The shear strain is defined as the half of the total angular distortion

$$\varepsilon_{xy} = \frac{1}{2} \left(\frac{\partial v}{\partial x} + \frac{\partial u}{\partial y} \right) \tag{1.9}$$

In a three-dimensional space it is possible to generalize these results and introduce the *strain tensor*

$$\varepsilon_{ij} = \frac{1}{2} \left(\frac{\partial u_i}{\partial x_j} + \frac{\partial u_j}{\partial x_i} \right) \tag{1.10}$$

For definition, the tensor is symmetric and can be represented by six independent components. As the stress, strain is split in *normal* and *shear* strains. As shown, normal strains are fractional changes in distance and measure how long the body has become, while shear strains are rotations with respect to the surrounding material.

An invariant quantity related to strain is the *dilatation*, the change in volume of material elements. Consider an undeformed volume element which sides are $\triangle x$, $\triangle y$, $\triangle z$, and the volume $V = \triangle x \triangle y \triangle z$. As result of the infinitesimal displacements, length of each side will become $\triangle x\,(1 + \varepsilon_{xx})$, $\triangle y\,(1 + \varepsilon_{yy})$, and $\triangle z\,(1 + \varepsilon_{zz})$. The fractional change

of volume to the first order is at the end

$$\frac{\triangle V}{V} = \varepsilon_{xx} + \varepsilon_{yy} + \varepsilon_{zz} \tag{1.11}$$

In the analysis of the displacement on the Earth's surface, strain tensor is often represented through spherical components (see Fig. 1.5).

Introduce the vector $u(r, \theta, \phi) = (u, v, w)$ where u, v and w are the displacement components in the r, θ, and ϕ directions respectively. In particular r is the radial distance, θ is the colatitude calculated from the pole towards equator, and ϕ the geocentric longitude. The spherical strain tensor components are expressed as

$$\varepsilon_{rr} = \frac{\partial u}{\partial r} \tag{1.12}$$

$$\varepsilon_{\theta\theta} = \frac{1}{r}\frac{\partial v}{\partial \theta} + \frac{u}{r} \tag{1.13}$$

$$\varepsilon_{\phi\phi} = \frac{1}{r\sin\theta}\frac{\partial w}{\partial \phi} + \frac{u}{r} + \frac{v}{r\tan\theta} \tag{1.14}$$

$$\varepsilon_{r\phi} = \frac{1}{2}\left(\frac{1}{r\sin\theta}\frac{\partial u}{\partial \phi} - \frac{w}{r} + \frac{\partial v}{\partial r}\right) \tag{1.15}$$

$$\varepsilon_{r\theta} = \frac{1}{2}\left(\frac{1}{r}\frac{\partial u}{\partial \theta} - \frac{v}{r} + \frac{\partial v}{\partial r}\right) \tag{1.16}$$

$$\varepsilon_{\phi\theta} = \frac{1}{2}\left(\frac{1}{r}\frac{\partial w}{\partial \theta} - \frac{w}{r\tan\theta} + \frac{1}{r\sin\theta}\frac{\partial v}{\partial \phi}\right) \tag{1.17}$$

Here ε_{rr}, $\varepsilon_{\theta\theta}$, and $\varepsilon_{\phi\phi}$ are the normal strains and adding them gives the *dilatation*; $\varepsilon_{r\phi}$, $\varepsilon_{r\theta}$, and $\varepsilon_{r\phi}$ are the shear strains.

These last relations contain additional terms that do not include derivatives of individual displacement components. Such terms are not present in the cartesian expressions given by Eq. 1.10, and their appearance is related to the curvature of the spatial coordinate system.

Clearly, the curvilinear forms appear more complicated than the corresponding cartesian relations. However, for particular problems the curvilinear relations, when combined with other field equations, allow to develop analytical solutions that could not be found using a cartesian formulation.

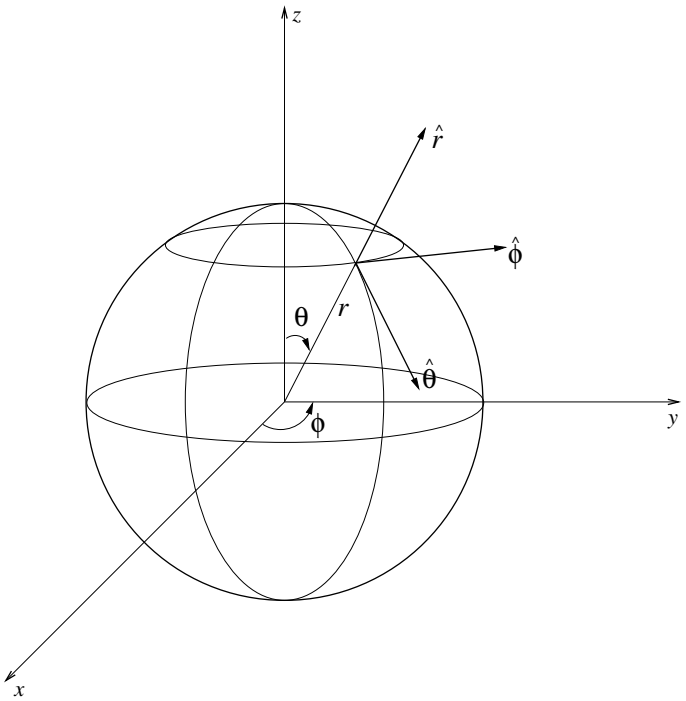

Figure 1.5: Spherical-geometry coordinate system.

1.1.3 Hooke's law

For a linear elastic material, the strain is directly proportional to stress:

$$\sigma_{ij} = C_{ijkl}\varepsilon_{kl} \tag{1.18}$$

where C_{ijkl} is a symmetric fourth-order tensor, namely *elastic tensor* and characterized by 81 components. This equation is referred to as generalized *Hooke's law*.

The symmetry of strain and stress tensors makes C_{ijkl} symmetric in k and i with respect to l and j, respectively, reducing its independent components to 21. Moreover the elastic properties of many materials in the Earth are independent from the direction and orientation of the sample. This *isotropic* characteristic makes C_{ijkl} dependent from only two elastic constants λ and μ, namely *Lamé constants*. These are related to elastic tensor by the equation

$$C_{ijkl} = \lambda\delta_{ij}\delta_{kl} + \mu\left(\delta_{ik}\delta_{jl} + \delta_{il}\delta_{jk}\right) \tag{1.19}$$

where δ is the Kroeneker delta. Substituting Eq. 1.19 into 1.18, the isotropic form of

Hooke's law is

$$\sigma_{ij} = 2\mu\varepsilon_{ij} + \lambda\varepsilon_{kk}\delta_{ij} \tag{1.20}$$

Often it is convenient to introduce other elastic constants for particular applications.

Young's modulus, E, describes the stiffness of a body, that is its resistance to elastic deformation under load. It is defined as the ratio of longitudinal stress to strain, with no lateral stress; so for example in the x direction

$$E = \frac{\sigma_{xx}}{\varepsilon_{xx}} = \frac{\mu\left(3\lambda + 2\mu\right)}{\lambda + \mu} \tag{1.21}$$

Poisson's ratio, ν, is the ratio of transverse contraction strain to longitudinal extension strain in the direction of the applied load. It is positive, so its definition contains a negative sign because the extensional and compressional deformation are considered positive and negative, respectively.

$$\nu = -\frac{\varepsilon_{yy}}{\varepsilon_{xx}} = \frac{\lambda}{2\left(\lambda + \mu\right)} \tag{1.22}$$

For most rocks of the Earth the *Poission approximation* is applied: the values of λ and μ are almost equal, so it is possible to assume $\lambda = \mu$ and $\nu = 0.25$.

Bulk modulus or *incompressibility*, K, measures the resistance of a body to uniform compression and it is defined as the ratio of hydrostatic pressure to dilatation. The pressure is defined as the average normal stress $P = \left(\sigma_{xx} + \sigma_{yy} + \sigma_{zz}\right)/3$, positive when compressive, as used in rock mechanics and interior stress in the Earth.

$$K = \lambda + \frac{\lambda}{3\mu} \tag{1.23}$$

The Eqs. 1.21 and 1.22 can be used to solve the Lamé coefficients in terms of Young's and Poisson moduli:

$$\lambda = \frac{E\nu}{\left(1 + \nu\right)\left(1 - 2\nu\right)} \qquad \mu = \frac{E}{2\left(1 + \nu\right)} \tag{1.24}$$

All these relations have been obtained assuming that it is possible to apply the hypothesis of isotropy in the medium. This condition is not fulfilled in many minerals. In this case, only the Lamé constants are not sufficient to describe the anisotropic elastic behavior but as many as 21 parameters must to be introduced, making the problem

much more complex.

Normally, a rock contains so many minerals that it is possible to assume that they are oriented at random and the rock can be considered isotropic. This assumption can be used also for large regions of the Earth's interior.

1.2 Crustal stress and faulting mechanism

The state and magnitude of the stress in the Earth's lithosphere play an important role on several geophysical phenomena such the plate mechanism, the energy budget of the Earth, earthquake mechanism and crustal movements.

All of Earth's rocks are under some kind of stress, but in many situations the stress is equal in all directions and the rocks are not deformed. In other cases the magnitude of stress is not the same in all the directions and rocks experience differential stress. As a result, the rocks yield to the unequal stress and deform by changing shape or position.

Faults are fractures in Earth's crust along which displacement has occurred.

The *faulting mechanism* is an indicator of rock deformation and reflects the state of stress acting on the region. When the stresses overcome the internal strength of the rock, resulting in a fracture, faults form. So a fault can be represented as a rock fracture where the two sides have been displaced relative to each other. They range in size from micrometers to thousands of kilometers in length and tens of kilometers in depth, but they are generally much thinner than they are long or deep. In addition to variation in size and orientation, different faults can define different types of rock deformation and regimes.

1.2.1 Faulting Geometry

The fault geometry is described through the orientation of the fault plane and the direction of slip along the plane. Faulting is a complex process and the variety of faults that exists is large. It is possible to visualize faulting as a slipping between two blocks of rocks (namely hanging wall and footwall), with slip constrained to lie in the plane connecting the two parts, namely *fault plane*. To describe the orientation of the fault plane two angular parameters are usually introduced: *dip* δ and *strike* ϕ angles (see Fig. 1.6).

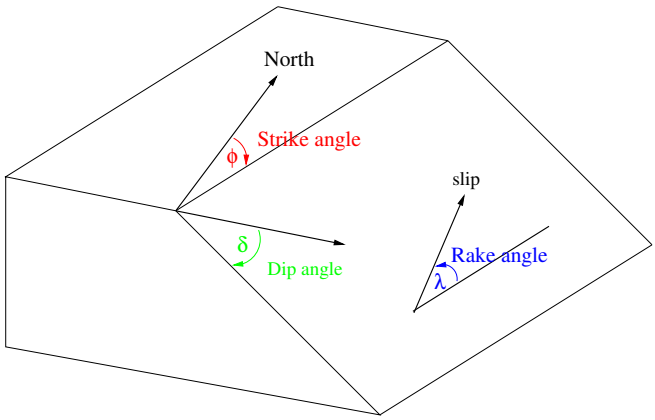

Figure 1.6: Definition of fault orientation (strike and dip angles, ϕ and δ respectively) and slip direction (rake angle, λ) parameters.

Dip angle describes the steepness of the fault surface. This angle is measured from Earth's surface, or a plane parallel to it. For example, dip of a horizontal fault is zero, and dip of a vertical fault is 90 degrees.

Strike angle specifies the azimuth of the fault. It is measured clockwise from north and specified so that the fault dips to right of an observer looking in the strike direction.

Dip and strike angles describe the orientation of the fault, but it is also necessary to introduce a quantity for describing the direction of slip motion across the fault. *Rake angle,* λ*,* (see Fig. 1.6) defines the direction of slip vector in the fault plane from the strike direction. It specifies the motion of the hanging wall (upper side) of the fault relative to the footwall.

If δ is different from 0 and 90 degrees, and λ varies in the range 0 to 180 degrees, the corresponding fault is called *reverse* or *thrust fault*; instead, if λ varies in the -180 to 0 degrees range, the fault is called a *normal* or *direct*. A *strike-slip* fault is one for which the slip vector is horizontal (λ is 0 or 180 degrees). In this last case if δ is 90 degrees the geometry is called *vertical strike-slip*. Strike-slip faults are either *right-lateral* or *left-lateral*. If λ is 0 degrees the hanging wall of the fault moves to the right, so that a point on the other side moves to the left, defining a *left-lateral slip*, if λ is 180 degrees the movement is opposite and called *right-lateral slip*.

1.2.2 Mechanism of faulting

Three kind of fault slip are usually used to characterize motions on the Earth's surface: *normal*, *strike-slip*, and *reverse* faults. This classification was deduced at first by

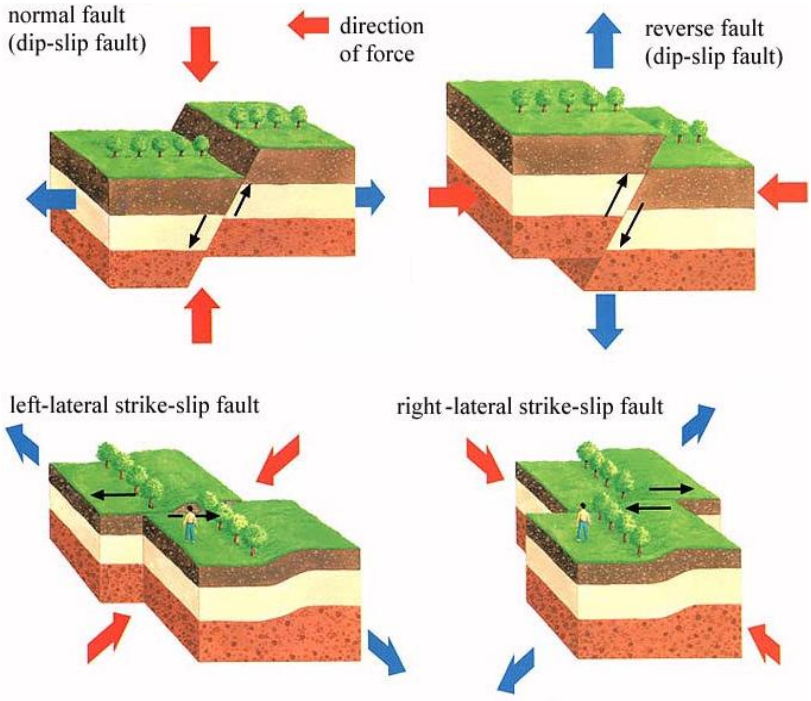

Figure 1.7: Different fault types. Extension, contraction, and lateral-slip produce different types of structures in rocks, caused by different stress orientations and magnitudes.Figure from `http://www.hp1039.jishin.go.jp/eqchreng/af1-2.htm`.

Anderson [1] using two basic criteria: there are no normal and shear stresses across a free horizontal surface, and the larger shear stress occurs across planes between the directions of maximum and minimum principal stresses.

In general the stress axes do not coincide with the spatial axes x, y and z, but at the Earth's surface one of the stress axes always coincides with the vertical axis z. This is because the Earth's surface is approximately horizontal and it is a surface of zero shear stress, neglecting the rather small shear stresses imposed by flowing water and air. Thus the direction of one principal stress is vertical and it can be the direction of maximum, σ_1, intermediate, σ_2, or minimum, σ_3, principal stresses. The other two principal stresses are horizontal. As convention, the principal stresses are positive if compressive, as done generally for the rock mechanics.

In the normal faulting, the largest (most compressive) stress σ_1 is vertical, while the intermediate σ_2 and smallest σ_3 stresses are horizontal. Consequently, the hanging wall moves down to the footwall. This fault motion is caused by tensional forces and result is an extension. Normal faults are common because rocks are weaker during extension than during compression. This type of extensional stress occurs on a global scale along

divergent plate margins. The normal faults are the dominant structures along the oceanic ridge, in continental rift systems, and along rifted continental margins.

In the reverse faulting, the smallest (less compressive) stress σ_3 is vertical. The largest σ_1 and intermediate σ_2 stresses are horizontal. In this case, the hanging wall moves up relative to the footwall and the fault block movement is toward each other, giving a compressive type of stress. In contrast to normal faults, reverse faults usually place older over younger strata and are repeated in a vertical section. Most reverse faults are at convergent plate margins; they are typically associated with folds and prominent in all of the world's major folded mountain belts.

The movement on a strike-slip fault is horizontal. There is no vertical movement and the blocks rub past each other. This is because the intermediate stress σ_2 is vertical, and both largest σ_1 and smallest σ_3 stresses are horizontal. The fault motion of a strike-slip fault is caused by shearing forces. These faults are expressed topographically by a straight valley or a series of low ridges and commonly mark discontinuities in the drainage and types of landscape.

In a compressional regime, where the maximum principal stress is horizontal, the dip angles of the fault are expected to be shallow. In an extensive regime, where the maximum principal stress is vertical, the dip angles are expected to be steep. In a strike-slip fault dip angle is closer to the direction of maximum principal stress than to the direction of minimum one.

1.3 Measurements of the Earth's deformation

Earth's surface and interior deform as a result of geological and geophysical processes. Earth is continually influenced by the gravitational forces, processes from within the core, and complex interactions with oceans and atmosphere.

In the mantle, convection phenomena convert thermal energy from radioactive decay and cooling of the Earth into continuous displacements responsible for plate tectonics.

On the surface episodic deformations arise from earthquakes and volcanic activities, whose measurements are necessary to understand these natural hazards. Also aseismic deformation before and after earthquakes can be measured; they are important to understand earthquakes themselves and the Earth's internal dynamics. Also slow large-scale deformation and fracturing have been detected; their study provides great

informations about the mechanical properties of the solid Earth. Continuous perturbations arise, moreover, from solid Earth tides and loading by variations in atmospheric pressure, oceanic circulation, and distribution of water and ice.

As a consequence of all these phenomena, measurements of Earth's deformation are essential for understanding rheology and physical processes, providing a critical link between Earth's structure and dynamics, in order to optimize responses to natural hazards and to identify potential risk areas.

1.3.1 Crustal deformation

Deformation of the Earth's surface is one of the most important phenomena associated with many geological hazards, such as tectonic movements, earthquakes, and volcano eruptions.

For example, earthquakes are related to crustal deformation of a large area. Measuring or monitoring the deformation of a seismic area might help to acquire critical information for understanding and even forecasting earthquakes.

The deformation of the Earth's surface is also an important characteristic related to volcano activities. There are a series of deformations around a volcano characterized by inflation before its eruption and deflation afterward.

Land subsidence is a worldwide phenomenon. It may result from many factors, such as tectonic movements, stretching of lithosphere, underground mining, heavy withdraw of groundwater, and so on. Monitoring such phenomena continuously is an important procedure for forecasting or preventing hazards caused by land subsidence.

Centimeter to millimeter per year accuracies are necessary to make meaningful detection of surface deformations. The study of the Earth's surface deformation has improved in the last fifty years, changing from mostly descriptive and qualitative to more quantitative. Continuum mechanics, laboratory deformation testing, the use of mathematical models, the increasing amount of geophysical data, such as seismic, gravity, magnetic data, the increased availability of satellite images, have all contributed to this change.

The goal of the surface deformation study is to measure continuous displacements of the Earth's surface on both spatial and temporal scales. Crustal deformation can be observed as relative movement of points on the Earth's surface, through ground tilt and strain measurements, or by VLBI (Very-Long Baseline Interferometry), GPS (Global Positioning System), and SLR (Satellite Laser Ranging) satellite measurements.

1.3.2 Strainmeters

Over the years strain measurements in geophysics became increasingly important.

Strainmeters measure time variation of linear strain, areal strain, shear strain, or volumetric strain. More precisely, linear strainmeters measure changes of distance between two fixed points in cavities, mines, or trenches, while volumetric strainmeters (dilatometers) measure changes of a volume which is imbedded in the ground. In Ref. [2] there is a detailed description of this kind of instruments.

The linear strainmeters are divided into three classes according to what they use to span the distance between endpoints: *rod strainmeters* (some used in boreholes), *wire strainmeters*, and *laser strainmeters*.

Benioff invented the first rod strainmeter in 1932 using an iron pipe [3, 4]. His *strain seismometer* - as this instrument was called - measured the variation in the distance between two points (one of them attached to a galvanometer), some 20 meters apart, caused by the passing of seismic waves. Because Benioff used a velocity transducer, his instrument measured strain rate, which is desirable for seismic records reducing the noise caused by environmental fluctuations and tides. His strain seismograph was the first to record Earth motions with periods up to the order of 1 hour, such as the gravest mode of the free oscillations of the Earth [5].

Significant changes were made later by the same Benioff [6]. The length was increased to 24 meters, using 3-meters sections of fused-quartz tubing cemented together and suspended by wire slings inside a concrete trough. To record low frequencies, displacements were measured with an optical lever, and later with a capacitance transducer using resonant circuits. Even if a rod strainmeter is very simple (see for example Fig. 1.8), several design details are important. One of them is how to support the rod so that it is free to move along its own axis but not sideway. In the Benioff instrument rod is suspended in wire slings every few meters. Also an accurate calibration is important. In general, for this kind of mechanical strainmeters the calibration is difficult because the associated displacements are small. One method is to apply a known force to the free end of the rod and use its known elasticity to convert this into a displacement.

The length standard of these instruments should be very stable against all kinds of environmental variables, especially temperature, air pressure and humidity. Because of these requirements, rods are mostly made of quartz, invar or superinvar.

As alternative to rod strainmeter, several designs have used a flexible wire.

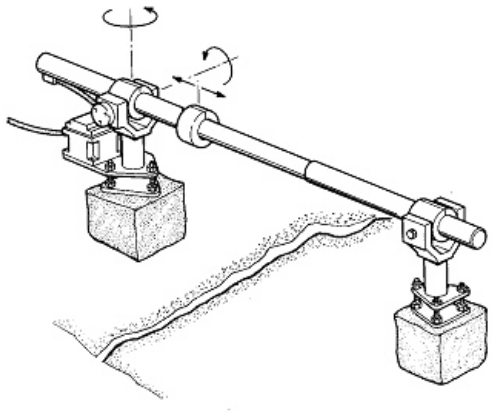

Figure 1.8: Schematic example of rod strainmeter. Figure from `http://www.afs.enea.it/protprev/www/lineeguida4/fascicolo4_4.htm#5`.

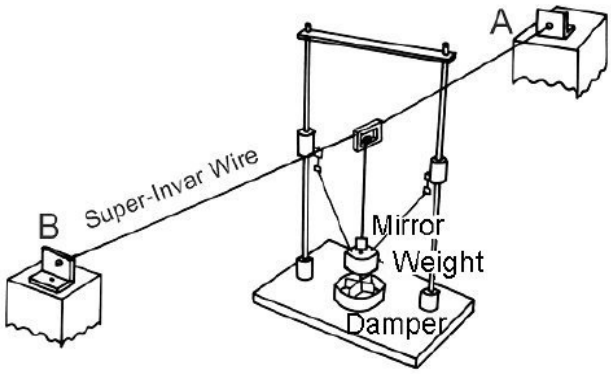

Figure 1.9: Schematic representation of a wire extensometer of the Sassa type. Figure from `http://www.eas.slu.edu/GGP/BIM_Recent_Issues/bim146-2010/takemoto_century_tides_kyoto_bim146_10.pdf`.

In 1950, Kenzo Sassa developed an extensometer using a flexible super-invar wire to measure the relative displacement between two points in a shallow catenary and fixed into the bedrock (see Fig. 1.9). Changes in distance between the ends caused an up and down catenary movement, recorded by an optical lever. In more recent instruments the wire is fixed at one end and free to move to the other where it is subjected to a constant voltage. Tension is usually applied by a weight on a lever; in a longitudinal oscillation this acts as a mass and the wire as a spring.

A widely used material for the wire is invar because it is readily available, easy to clamp, it has a low temperature coefficient and a good long-term stability. The main disadvantages of this material are related to the rust and its high density that prevents

the use for more than 10 to 20 meters. As alternative, carbon fiber is often used. It is characterized by a temperature coefficient similar to that of invar but its density is more lower than invar, so it can be used over longer spans. It is resistant to corrosion but adsorbs water; the resulting change in weight can cause purious initial drifts.

The last class of linear strainmeter includes the laser strainmeters. They measure the change in displacement between the fixed points, using the measuring principle of the Michelson optical interferometer. This kind of instruments will be discribed in detail in Chapter 3.

In his first strainmeter paper [4], Benioff suggested that the volumetric strain might be measured by burying a large container of liquid with a small opening. In the ground strains could be measured detecting the flow throught a small opening, caused by the change the volume of the container that force liquid to flow in and out.

This idea have been developed about 30 years later, when a borehole instrument based on this operating principle was constructed and widely deployed [6]. The volume changes are sensed by a liquid-filled tube, cemented into a borehole. The deformation of the volume causes the liquid to expand or contract bellows, the movement of which is transmitted to displacement transducers by a lever arm.

The Sacks-Evertson strainmeter (Fig. 1.10) consists of a stainless-steel cylinder with a sensing volume filled with silicone oil. Changes in deformation of the surrounding rock are detected by small movements of the walls of the borehole. The oil is forced in or out of the attached bellows; the top surface of the bellows (B) correspondingly moves up or down and this motion is translated into voltage by a differential transformer (DT). For a given strain, the bellows move relative to the borehole diameter. To keep the strainmeter within its operating range over indefinite time intervals, a valve is opened for a few seconds as needed so that the oil flows to or from a reservoir (R) that is decoupled from the strain field. These types of strainmeters can measure deformation for periods from a few hours to days, months, and years. This provides them to measure signals in lower frequencies that can not be detected with seismometers, recording for example the Earth's tides, and seismic waves from earthquakes. At longer time periods, they can also record accumulation of stress caused by plate tectonics, the release of this stress in earthquakes, and rapid changes of stress following earthquakes.

Greater difficulties for these instruments arise because they must to be cemented appropriately into a borehole, in order to transfer strains in the ground to the actual sensor through the borehole wall, casing and cement. In these cases a very rough cal-

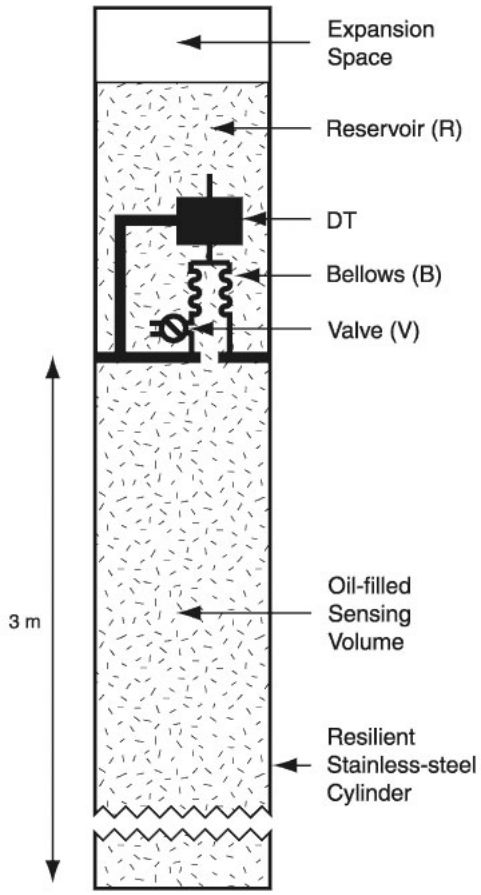

Figure 1.10: Sacks-Evertson strainmeter configuration. Figure from `http://www-odp.tamu.edu/publications/186_IR/chap_03/c3_f4.htm#31271`.

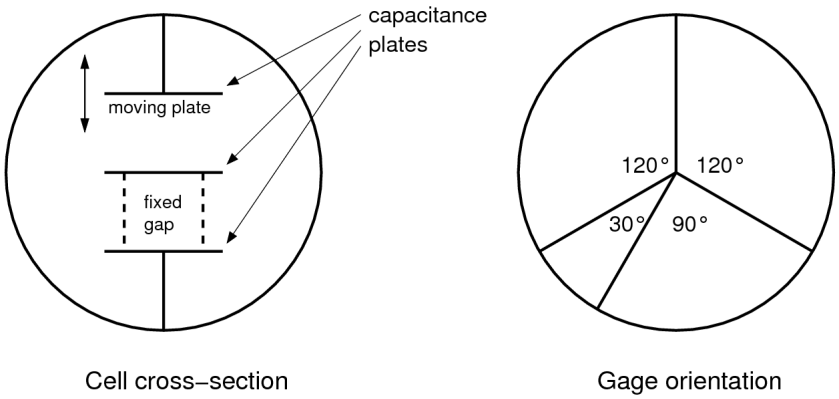

Figure 1.11: Schematic cross-section of a strain cell and gage orientation of a GTSM strainmeter.

ibration can be obtained by using the Earth's tidal strains, which are theoretically at least known to the order of magnitude.

While the Sacks-Evertson design is simple and robust, it can not provide any directional information. The Sacks-Evertson tensor strainmeter is similar in principle but the sensing volume is divided into three equal and independent segments, 120 degrees apart. The volume change of each sector is measured separately by two sets of the bellows-differential transformer-valve sensing subsystem. Changes in three diameters of the cylinder allow to record shear changes as well as areal or volume changes, so that complete horizontal strain tensor is reconstructed from these three directions.

Borehole tensor strain can be also measured through a GTSM strainmeter, built by GTSM Technologies in Queensland, Australia (`http://www.gtsmtechnologies.com`). These instruments provide direct measurements of strain in the surrounding rock in three directions, at 120 degrees from each other. These measurements are stable and accurate on very long periods.

The GTSM strainmeters were designed in the early seventies for recording stress data sampled at low frequency and used in mining applications [7]. In the eighties they were employed for the first time in studies of earthquakes, because capable of recording data to high frequency, also greater than 100 Hz.

In its current configuration this device consists of five independent modules (see Fig. 1.11), four of them measure strain at different orientations in a plane perpendicular to the borehole axis, while a further component measures the orientation of the instrument into the hole using a magneto-resistive sensor.

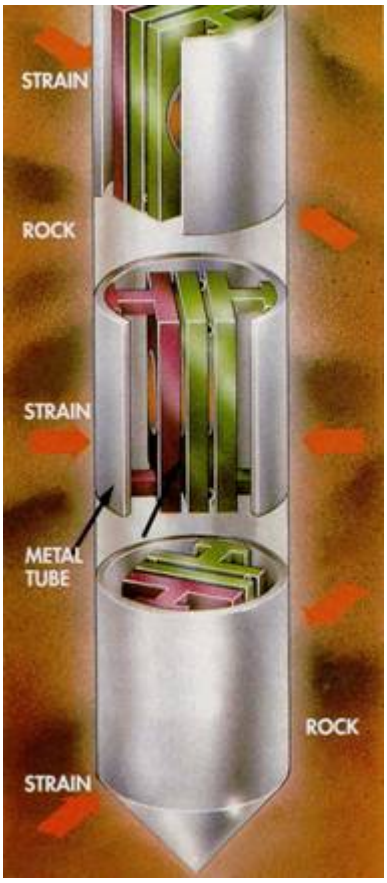

Figure 1.12: GTMS tensor strainmeter. Figure from `http://www.gtsmtechnologies.com/index_files/faqs.htm`.

These modules are isolated by rigid bulkheads and dimensioned such that strain is transmitted to the transducer without any perturbation. Within these modules four sensors, which measure the stress, are placed; three of them are at 120 degrees from each other, the fourth disposed according to a different orientation. It is a differential capacitive transducer used to measure changes in the diameter of the pipe sensitive. The sensing transducers (see Fig. 1.12) are three steel plates acting as capacitors; a moving plate (red) is mounted at the opposite side of the other two plates (green) at fixed total distance. If the diameter of the borehole changes, the red plate moves and changes in capacitance are measured; from these changes the ratio of the separation between the two plate pairs can be found. The relative position of the moving plate can be monitored to a few picometers. These measurements allow to get three strain components: change of hydrostatic strain and two shear components.

Chapter 2

Earth's tidal deformation

The gravitational attraction of bodies external to the Earth, mostly the Moon and Sun, causes cyclic variations in its gravitational potential. The main consequence is the phenomenon of ocean tide but there is also a deformation in the solid part of the Earth, namely *solid Earth tide*.

The computation of the tidal potential at a specific station and time can be carried out using different methods, obtaining a purely harmonic development with a very great number of waves. The amplitude of each wave can be expressed as a function of the latitude of the observation site.

The Earth's response to the tide generating potential can be derived analytically by the gravitational potential, combining it with the Love numbers, which are related to the rheological properties of the Earth.

The redistribution of oceanic mass produces important loading effects on the crust called *load tides*, which cause more change in the potential, plus displacements, and consequently the Earth tides are significantly perturbed. Several methods have been used to compute the ocean tidal loading, in particular the spherical harmonic expansion and the Green's function methods are usually applied.

The deformation caused by ocean loading is rather well known as the effect of the solid Earth tide, but the modeling of its effects still needs to be improved.

2.1 Tides

Tidal forces arise from the gravitational attraction of bodies external to the Earth. In particular, the luni-solar gravitational attraction and centrifugal force, due to the relative motions of the Moon around the Earth, and the Earth around the Sun, produce cyclic variations in the gravitational potential. This phenomenon causes changes in the sea level, known as *ocean tides*, but also an elastic deformation of the Earth, known as *Earth tides*.

Each point of the Earth's surface is subjected to the gravity force, produced by the attraction of the Moon (or Sun), and the centrifugal force, produced by the revolution of the Earth around its common center of gravity with the Moon. Away from the Earth's center, the forces are not in balance. Local differences in magnitude and direction exist, producing forces that vary across the Earth's surface. In particular, the centrifugal force is the same everywhere, while the attractive force varies inversely as the square of the distance from the Moon (or Sun) and always points toward the center of the Moon.

Since the Earth spins on its own axis, water is kept balanced on all sides of the planet through the centrifugal force. The gravitational forces cause a bulge of the water towards the Moon (or Sun) and the Earth's rotation causes a bulge on the opposite side of the planet.

For an observer fixed on the Earth's surface, this tidal budge moves from east to west around the Earth as it rotates each day, thus causing two lunar and two solar high Earth tides about each day. The period of the solar tide is exactly 12 hours, while the period of the lunar tide is slightly longer, 12.42 hours, due to the Moon's revolution around the Earth every 27 days. These tides are called *semidiurnal tides* since they have periods of about half a day. The inclination of the Earth's spin axis to the plane of the Moon's revolution about the Earth and the Earth's revolution about the Sun creates in addition weaker *diurnal tides* with periods of about one day.

The Moon is the dominant tidal influence because the fractional difference in its force across the Earth is greater than the fractional difference produced by Sun, but the bulges related to Moon and Sun act at times together and at other times in opposition. Thus it is necessary to combine the effects of both Sun-Earth and Moon-Earth systems (see Fig. 2.1). Twice each month, there is an approximate alignment of Sun, Moon, and Earth's positions. In this case the lunar and solar related ocean bulges also line up (and add up) to produce tides having the greatest monthly tidal range. This happens when

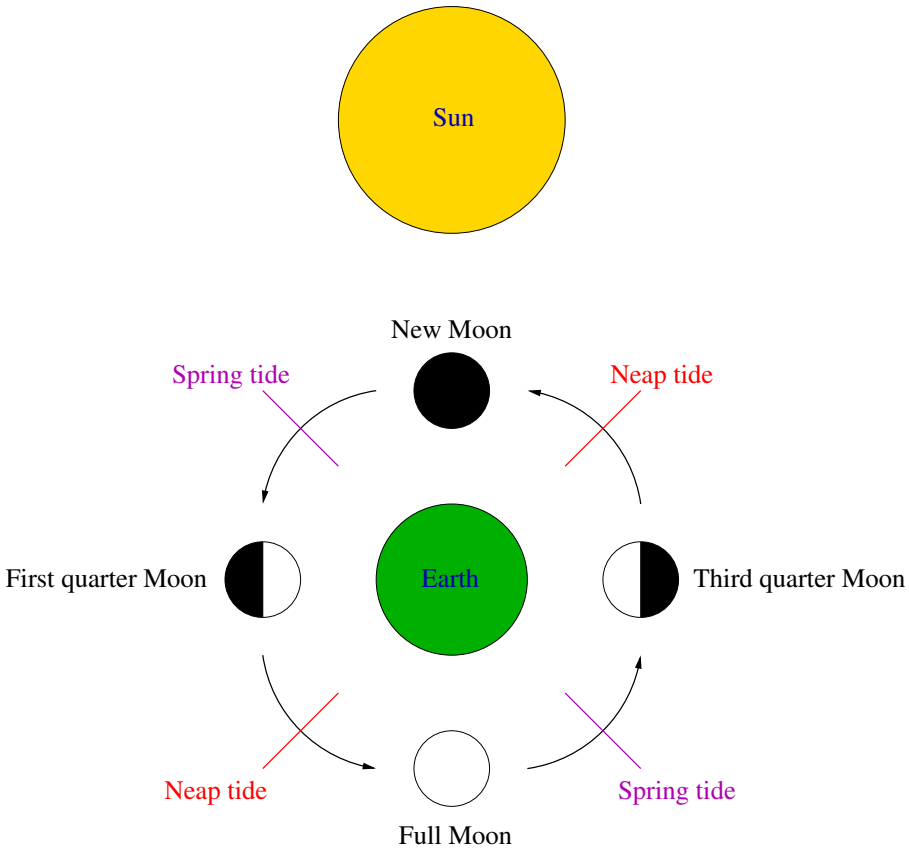

Figure 2.1: Spring and neap tides, generated when Sun, Moon and Earth are in a straight line, and when Sun and Moon are at right angles to each other, respectively. Figure from `http://www.moonfacts.co.uk/moon-affect-tides/`.

the Moon is between the Sun and the Earth (at new moon), and when the Moon is on the direct opposite side of the Sun (full moon). The high tides of the solar envelope occur at the same time as the high tides of the lunar one. This increases the height of the composite high tides. Likewise, low tides of the solar envelope occur at low tides of the Moon. This decreases the height of the composite low tides. Therefore, larger than average tidal ranges occur, namely *spring tides*.

Conversely, at the first quarter and third quarter Moon, when Sun, Earth, and Moon form right angles (approximately) to each other, tides are generally weaker. In this case, the low tides of the solar envelope occur at the times of the high tides of the Moon. This reduces the height of the composite high tides. Likewise, the high tides of the solar envelope occur at the low tides of the lunar one. This increases the height of the composite low tides. Therefore, smaller than average tidal ranges occur, called *neap tides*.

The spring and neap tide phenomena also cause changes in the time of occurrence of the high and low tide phases of the lunar tide. As the Moon goes from new to first quarter or full to third quarter, the solar envelope is behind the lunar one such that the composite envelope is retarded. Thus, as the Earth spins, the high and low tide phases of the composite envelope occur earlier than with just the lunar envelope. This is called *priming*. Similarly, as the moon goes from first quarter to full or third quarter to new, the solar envelope is ahead of the lunar one and, as consequence, the composite envelope is accelerated. In this case, because the Earth spins, the high and low tide phases of the composite envelope occur later than with just the lunar envelope. This phenomenon is called *lagging*.

The variations of the ocean surface, due to tidal forces related to Moon and Sun, are well known. First descriptions are more than two thousand years old. In contrast, the knowledge about the deformation of the solid Earth caused by the same forces is much younger. Earth tides are much easier to model than the ocean tides, both because the Earth is more rigid than water, and because the geometry of the problem is much simpler.

2.2 Earth tides

Deformations caused by gravitational attraction from the Sun, Moon and other objects can be modeled very accurately. These tidal deformations, called *body tides*, are known as direct effect. In addition, there is a part of the deformation, arising from the mass fluctuations of the oceans, known as *ocean loading*. These last are also rather well understood, but the modeling of their effects still needs to be improved.

Both effects are generated from the same sources, and have a very similar temporal character; so they are difficult to split. However, the spatial features of these two tidal effects may be very different. Body tides varies smoothly over the Earth's surface, and are more dependent on the global rheological properties of the Earth rather than the local properties. On the contrary, ocean tide loading effect has a more irregular varying structure and depends locally on the elastic properties of the lithosphere.

Using some accepted Earth's models, it is possible to know accurately the solid Earth tide effect and separate the ocean tide loading effect from the solid Earth tides, by subtracting the modeled solid Earth tides from the observations.

2.2.1 The tidal forces

For a rotating body, gravity force is the combination of gravitational attraction arising from the mass distributed in a planet, like for example the Earth or other celestial bodies, as well as the centrifugal force arising from the body's rotation about its own axis.

In 1687 Isaac Newton published the consequences of gravitation in *Principia*, including an explanation of the observed tides in terms of mechanics. Newton's universal law of gravitation governs both the orbits of celestial bodies and the tide-generating forces which occur on them. According this law, the gravitational force between two objects is directed along the line joining their centers and can be expressed as

$$F = G\frac{m_1 m_2}{r^2} \tag{2.1}$$

where m_1 and m_2 are masses of each object, r is the distance between their centers of masses, and $G = 6.67\times10^{-11} Nm^{-2}kg^{-2}$ is the gravitational constant. This law assumes that m_1 and m_2 are point masses. However, the actual dimensions of the masses must to be taken into account when computing differential gravitational forces.

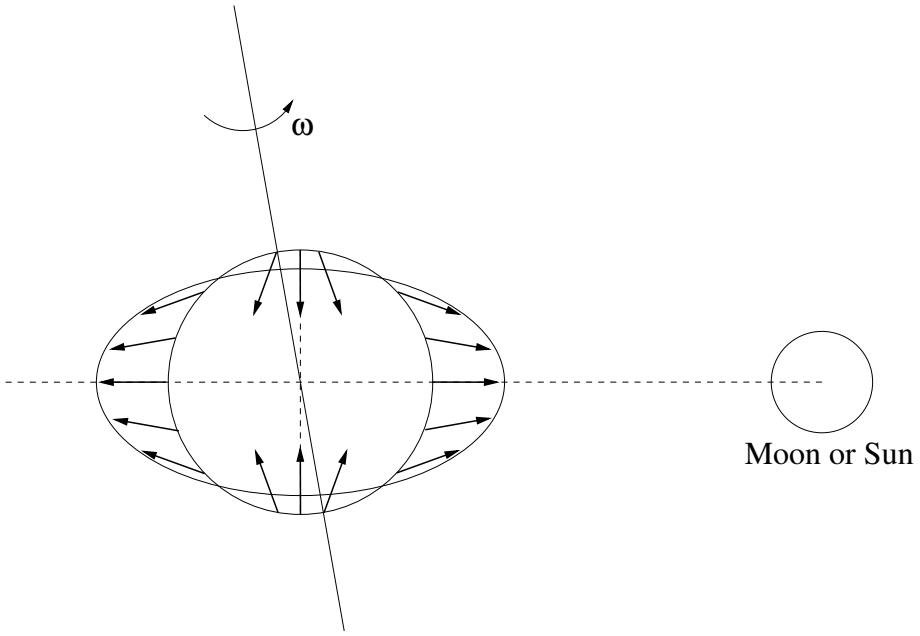

Figure 2.2: Tidal force at the surface of the Earth. The rotation of the Earth around its axis, inclined to the lunar and solar planes, introduces an asymmetry in the tides.

Considering the Earth-Moon system, both Earth and Moon describe elliptical orbits about their barycenter, assuming that both bodies are homogeneous spheres and neglecting the gravitational forces of Sun and other planets. The center of mass of Earth describes a very small ellipse around the Earth-Moon barycenter, while the center of mass of Moon describes a much larger ellipse around the same barycenter. At the same time, the Earth-Moon barycenter describes an orbit which is approximately elliptical around the barycenter of the Sun-Earth-Moon system, which lies inside the Sun.

Following Eq. 2.1, at the surface of the Earth, a spherically symmetric object of mass m is attracted to the Earth's center of mass by a force

$$F = \frac{GM_e m}{r_e^2} = mg \tag{2.2}$$

where M_e and r_e are the mass and mean radius of the Earth, and $g \equiv GM_e/r_e^2 \simeq 9.81 ms^{-2}$ is the *gravity acceleration*. At the surface of the Earth, the Earth's gravitational attraction acts in a direction inward toward its centre of mass.

As the Earth rotates around the barycentre, the centrifugal force produced at the Earth's center of mass is directed away from the barycentre. Since the centre of mass of the Earth is on the opposite side of the barycentre to the Moon, the centrifugal

force due to the Earth's center of mass is directed away from the Moon. All points on the surface of the Earth are characterized by the same magnitude and direction of this centrifugal force.

At the same time, this theory is applied to the Earth-Sun system. The centrifugal force produced by the daily rotation of the Earth on its own axis has no consequence in tidal theory, because the force at any particular location remains constant with time, so that the water surface is always in equilibrium with respect to it. Instead, the effect of gravitational force produced by another astronomical body changes from place to place. This is because the magnitude of the gravitational force exerted varies with the distance of the attracting body.

The fundamental tidal force on the Earth has two interactive but distinct components. There is a differential force, obtained combining the gravitational attraction of the bodies (Earth-Sun and Earth-Moon) at the center of mass of the Earth and the centrifugal forces on the Earth produced by the Earth's orbit around the Sun and the Moon's orbit around the Earth.

As a result of these differential forces, at any point on the Earth the tide generating forces depend on the location on the Earth's surface and are inversely proportional to the cube of the distance between the bodies. Thus

$$F = \frac{2GMM_e r_e}{r^3} \tag{2.3}$$

where M is the mass of the Moon (or Sun), and r is the distance to the Moon.

Even if the mass of the Sun is much greater than the mass of the Moon, Sun only affects the Earth half of what the Moon does, since the distance is given by the inverse cube.

At any point on the Earth's surface, the tide generating force can be split into two components: one perpendicular (vertical) and the other tangential (horizontal) to the Earth's surface respectively. The vertical component, known as *tractive* component of force, is the actual mechanism for producing tides. The tractive force is zero at the sublunar and antipodal points (the points on the side of the Earth toward and opposite the Moon, respectively) where the force is entirely vertical (see Fig. 2.2).

As the Earth rotates, in principle at the same place a high tide is followed by a low tide 6 hours later, then a second high tide after 12 hours, and so forth; but this is far from the actual situation. First, the tidal force envelope produced by the effect of the Moon interacts with the tidal force produced by the Sun. The tidal force exerted by the Sun is

a composition of the Sun's gravitational attraction and the centrifugal force created by the revolution of the Earth around the centre of mass of the Earth-Sun system, much smaller than the Moon tidal force. It is also necessary to remark the existence of some effects, as changing distances of the Moon from the Earth and the Earth from the Sun, the misalignment of the lunar and solar orbital planes, the inclination of the ecliptic (misalignment of equator and orbital plane).

2.2.2 The tidal potential

The computation of the tidal potential at a specific station and time can be performed by two different methods: using ephemerides (coordinates) of the celestial bodies, like the Moon, Sun and other planets, or through a spectral analysis of the tidal potential in spherical harmonics, producing different tidal potential catalogues (tables of amplitudes, phases and frequencies of several tidal waves).

Following Ref. [8], *tidal potential*, due to an external mass M and acting on a point of the Earth's surface (see Fig. 2.3), is expressed as

$$V = \frac{GM}{r} = \frac{GM}{R\sqrt{1 + (r_e/R)^2 - 2\,(r_e/R)\cos\alpha}} \tag{2.4}$$

Writing the square-root term as a sum of Legendre polynomials, this potential becomes

$$V = \frac{GM}{R}\sum_{n=0}^{\infty}\left(\frac{r}{R}\right)^n P_n\left(\cos\alpha\right) \tag{2.5}$$

The $n = 0$ term is constant in space, so the force, given by its gradient, is zero. The $n = 1$ term depends linearly from the coordinate directed along the line joining the centers of the two bodies and its gradient is a constant. So this term, giving a constant force along the direction to M, represents the orbital force acting on the Earth's center, which can be subtracted to get the tidal force.

Removing the two lowest terms and introducing the time dependence of the distance $R\,(t)$ and the angular distance $\alpha\,(t)$, tidal potential becomes

$$V_{tid}\,(t) = \frac{GM}{R\,(t)}\sum_{n=2}^{\infty}\left(\frac{r}{R\,(t)}\right)^n P_n\left(\cos\alpha\,(t)\right) \tag{2.6}$$

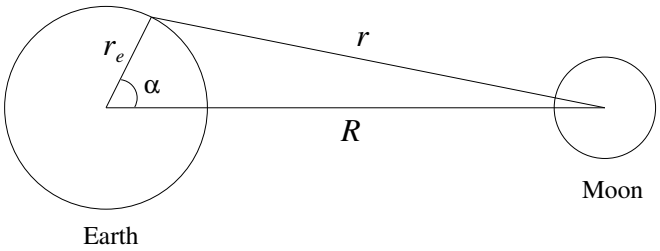

Figure 2.3: Geometry of the problem for computing the tidal force at a point of the Earth's surface, given by an external body, for example the Moon.

where the different values of n are referred to as the degree$-n$ tides.

Tidal potential is often expressed into geographical coordinates. Suppose the observation point at fixed colatitude θ and longitude ϕ and the external mass at colatitude $\theta'(t)$ and longitude $\phi'(t)$, tidal potential is

$$V_{tid}(t) = \frac{GM}{R(t)} \sum_{n=2}^{\infty} \left(\frac{r}{R(t)} \right)^n \frac{4\pi}{2n+1} \sum_{m=-n}^{n} Y_{nm}^{*}(\theta'(t), \phi'(t)) Y_{nm}(\theta, \phi) \tag{2.7}$$

The normalized complex spherical harmonics $Y_{nm}(\theta, \phi)$ are given by

$$Y_{nm}(\theta, \phi) = N_n^m P_n^m(\cos\theta) \exp(\imath m\phi) \tag{2.8}$$

where P_n^m is the associated Legendre polynomial of degree n and order m and N_n^m is the normalizing factor

$$N_n^m = (-1)^m \frac{2n+1}{4\pi} \left[\frac{(n-m)!}{(n+m)!} \right]^{1/2} \tag{2.9}$$

As conventional, tidal potential is normalized to the Earth's gravitational acceleration g, valued on the Earth's equatorial radius r_{eq}. Its new expression has the dimension of a length, and is interpreted as the change in elevation of the geoid, the surface defined by an equilibrium potential

$$\frac{V_{tid}(t)}{g} = r_{eq} \frac{M}{M_e} \sum_{n=2}^{\infty} \left(\frac{r_{eq}}{R(t)} \right)^{n+1} \frac{4\pi}{2n+1} \sum_{m=-n}^{n} Y_{nm}^{*}(\theta'(t), \phi'(t)) Y_{nm}(\theta, \phi) \tag{2.10}$$

This formulation has been obtained for a particular observation point and its time dependence comes from time variations in R, θ', and ϕ'. Considering also θ and ϕ variables, it is possible to use Eq. 2.10 for describing the geographical distribution of

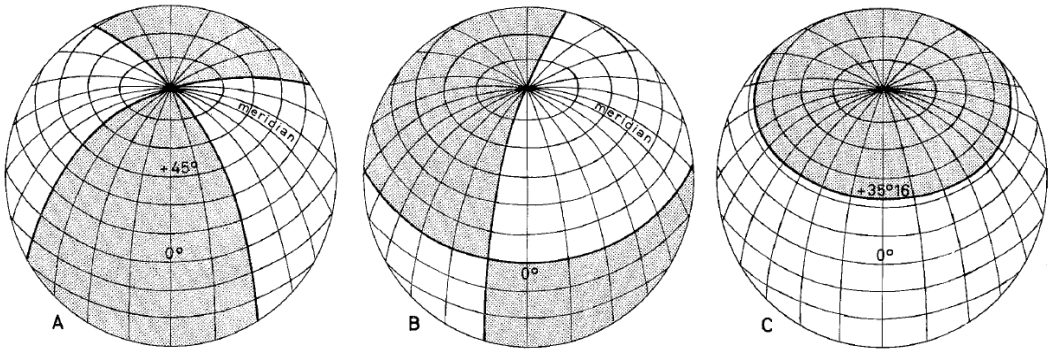

Figure 2.4: Geographical distribution of tidal potential: sectorial (A), tesseral (B), and zonal (C) functions. Figure from Ref. [8].

the normalized tidal potential. The terms in the sum over m separate the tidal potential of degree n into parts, called *tidal species*, that vary with frequencies around 0, 1, 2,..., n times per day.

The largest tides are obtained for $n = 2$ and can be divided into three such species: diurnal, semidiurnal and long-period tides. The diurnal tides vary once per day, and with colatitude as $3\sin\theta\cos\theta$, they are largest at mid-latitudes and vanishes at the equator and the poles. The semidiurnal part varies twice per day and as $3\sin^2\theta$, being largest at the equator and null at the poles. The long-period tide varies as $3\cos^2\theta - 1$, and so it is large at the pole and at the equator with opposite sign.

Diurnal, semidiurnal and long-period tides correspond to three different types of spherical harmonics, known as *sectorial, tesseral*, and *zonal* harmonics, respectively (see Fig. 2.4).

Following Ref. [8], tidal potential can be expanded to the second order in the first three terms of Laplace development. To make this mathematical expression more flexible, it is necessary to introduce both equatorial (hour-angle H and declination δ) and astronomical coordinates of the station, the latitude ϑ and the longitude ϕ, so that

$$V_2 = \frac{3}{4}\frac{GMr^2}{R^3}\left[\cos^2\vartheta\cos^2\delta\cos 2H + \sin 2\vartheta\sin 2\delta\cos H + 3\left(\sin^2\vartheta - 1/3\right)\left(\sin^2\delta - 1/3\right)\right] \tag{2.11}$$

These three terms define three types of second-order spherical harmonic functions at the surface. The first part of this expression represents the *sectorial function*. It has as nodal lines only meridians, which are situated at 45 degrees on both sides of the meridian defined by the observation point. These lines divide the sphere into four

sectors where the function is alternatively positive and negative. The regions where the potential is positive are those of high tides, the negative ones are those of low tides. The period of these tides is semidiurnal, and their amplitude is maximum at the equator when the declination of the perturbing body is zero, and zero at the poles.

The second part of Eq. 2.11 defines the *tesseral function*. It has as nodal lines a meridian at 90 degrees from the meridian of the perturbing body and the equator, forming regions that change their sign with the body's declination. The period of its tides is diurnal, and the amplitude is maximum at latitudes 45 degrees and when the body's declination is maximum.

The third function depends only on the latitude and is called *zonal function*. Its nodal lines are the parallels of $\pm 35°16'$. Because it is a function only of the sine squared of the body's declination, its period is 14 days for the Moon, and 6 months for the Sun, defining so the long-period tides. The zonal function has a constant part and as a consequence the equipotential is lowered 28 cm at the pole and raised 14 cm at the equator. This permanent tide causes an increase very slightly of the Earth's flattening.

Because the elements of the Earth's and Moon's orbits and the mass ratios of Moon and Sun to the Earth are known, it is possible to obtain a purely harmonic development with a very great number of waves. The amplitude of each of these waves can be expressed as a function of the latitude of the observation site.

The vertical components of the diurnal waves at low latitudes are maximum at 45 degrees and null at the equator. The semidiurnal waves, on the other hand, are maximum at the equator (see Fig. 2.5).

The horizontal NS components of the diurnal waves do not occur at 45 degrees latitude and at the equator, while the EW components of the semidiurnal waves are maximum at the equator. At middle latitudes, M_2 is the main wave but both types of waves are of the same order of magnitude (see Figs. 2.6 and 2.7).

For expressing the tidal potential as a function of the harmonic components, following Ref. [9], it is possible to introduce complex and time-varying coefficients

$$T_{nm}(t) = a_n^m(t) + \imath b_n^m(t) \tag{2.12}$$

such that

$$\frac{V_{tid}(t)}{g} = \Re\left[\sum_{n=2}^{\infty}\sum_{m=0}^{n} T_{nm}^*(t)\, Y_{nm}(\theta,\phi)\right] \tag{2.13}$$

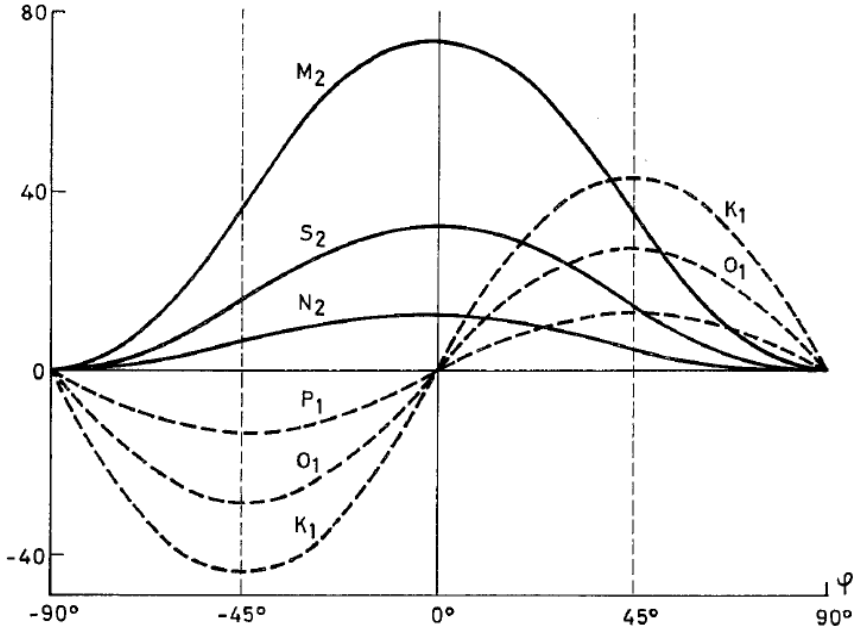

Figure 2.5: Amplitude variation (μgal) of some diurnal (K_1, O_1, and P_1) and semidiurnal (M_2, S_2, and N_2) vertical components of the tidal force as a function of latitude (degrees). Figure from Ref. [8].

This equation suggests a straightforward way to compute the tidal potential, through a description of the location of the Moon and Sun in ephemeris (celestial coordinates). This is possible by converting this celestial location to the geographical coordinates of the sub-body point (θ' and ϕ'), and the distance R, using standard transformations, and at the end combining T_{nm} to get V_{tid}/g, either for a specific location or as a distribution over the whole Earth.

Since the works of the 19th century [10, 11], it is possible to refer to an harmonic expansion of the tidal potential and express the T_{nm} terms as a sum of sinusoids

$$T_{nm}(t) = \sum_{k=1}^{K_{nm}} A_{knm} \exp\left[\imath\left(2\pi f_{knm} t + \varphi_{knm}\right)\right] \tag{2.14}$$

where for each degree n and order m there is a sum of K_{nm} sinusoids defined by specified real amplitudes A, frequencies f and phases φ. The single sinusoids are called *tidal harmonics*.

The first full expansion was by Doodson [12]. It includes 389 harmonics, of which 100 are long period, 160 are daily, 115 are twice per day, and 14 are thrice per day. Doodson needed a nomenclature for these tides, and introduced one for that the frequency of

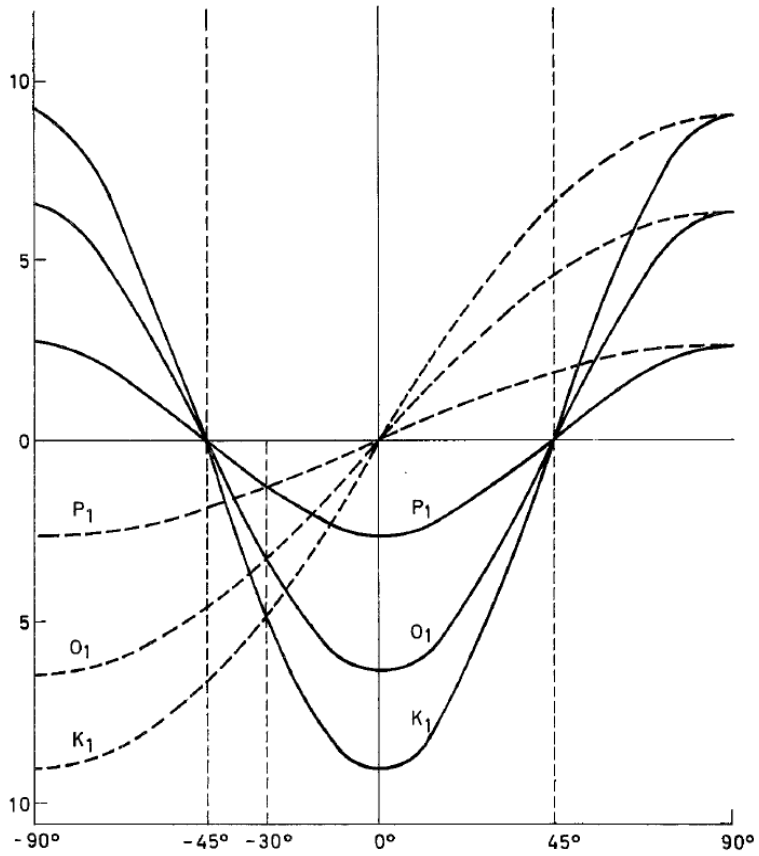

Figure 2.6: Amplitude variation ($msec$) of some diurnal (K_1, O_1, and P_1) components of the tidal force as a function of latitude (degrees). NS and EW components, solid and dashed lines, respectively. Figure from Ref. [8].

any harmonic is the sum of multiples of a few basic frequencies. For any degree n and order m, it is possible to express the argument of the exponent in the Eq. 2.14 as

$$2\pi f_k t + \varphi_k = \left(\sum_{l=1}^{6} D_{lk} 2\pi f_l \right) t + \sum_{l=1}^{6} D_{lk} \varphi_l \tag{2.15}$$

where the frequencies f_l correspond to various astronomical periods, and the phases φ_l are the phases at some suitable epoch. The same frequencies can be used for any tidal phenomenon, provided that it comes from a linear response to the driving potential.

Doodson's arguments are specified in order of decreasing frequency through six fundamental frequencies related to the local mean lunar time, the Moon's mean longitude, the Sun's mean longitude, the longitude of the Moon's mean perigee, the negative of the longitude of the Moon's mean ascending node on the ecliptic, and the longitude of

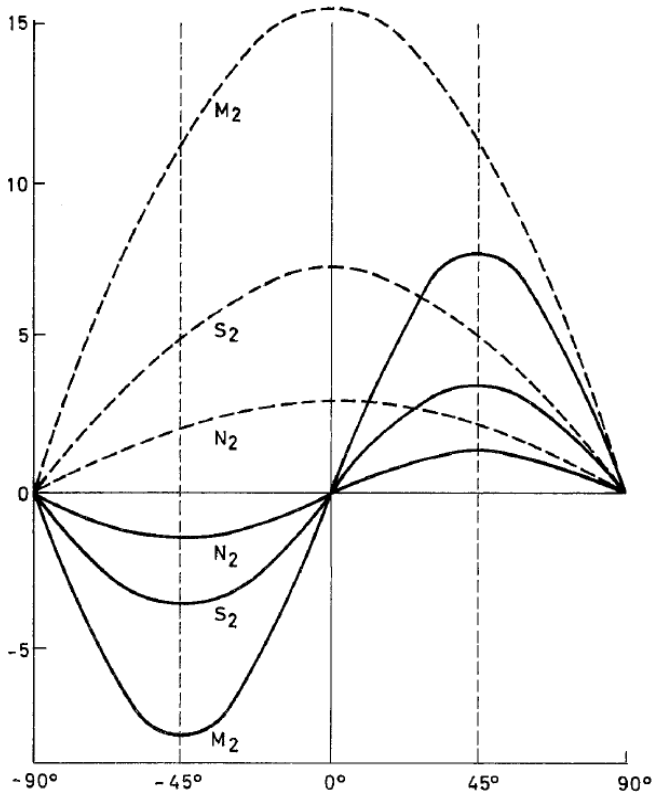

Figure 2.7: Amplitude variation (*msec*) of some semidiurnal (M_2, S_2, and N_2) components of the tidal force as a function of latitude (degrees). NS and EW components, solid and dashed lines, respectively. Figure from Ref. [8].

the Sun's mean perigee (see Table 2.1).

In the years, further expansions of the tidal potential in spherical harmonics have been computed and several tidal potential catalogues are currently available. Also the number of harmonics has continuously been increased. The catalogues differ in the number of waves and accuracy, and have either been computed by analytical or numerical spectral analysis. Analytical spectral analysis method requires analytical ephemerides of the celestial bodies, whereas numerical spectral analysis method needs numerical ephemerides only.

In particular, Cartwright catalogue contains 505 waves [10, 13]; Tamura potential catalogue contains 1200 waves [14]; in 1989 Xi introduced a planet Earth tidal model with 3070 tide waves, including the effects of the Sun, the Moon and the Earth's ellipticity [15]; in 1996 Roosbeek obtained the expansion of the tide-generating potential in 6499 terms by consecutive multiplications of the initial analytical series for the coordinates of the Moon, Sun and other planets [16].

	Frequency (°/hour)	Period	Source
f_1	14.49205211	lunar day	Local mean lunar time
f_2	0.54901653	month	Moon's mean longitude
f_3	0.04106864	year	Sun's mean longitude
f_4	>0.00464184	years	Longitude of Moon's perigee
f_5	-0.00220641	years	Longitude of Moon's ascending node
f_6	0.00000196	years	Longitude of Sun's perigee

Table 2.1: Fundamental tidal frequencies.

2.3 Tidal response of the Solid Earth

Earth's response to the tide generating potential can be derived analytically by the gravitational attraction from the Sun, Moon and other celestial objects, combined with the Love numbers, which are related to the rheological properties of the Earth.

2.3.1 Love numbers and strain tides

The deformation produced by tidal potential can be deduced using the usual approximation of a oceanless Spherical, Non-Rotating, Elastic, and Isotropic (SNREI) Earth.

It is simple to describe the response of a SNREI Earth to the tidal potential (for details see Ref. [17]); in fact because of symmetry, only the degree n is relevant.

If the potential height at a point on the Earth's surface is $V(\theta,\phi)/g$, the distortion of the Earth from tidal forces produces an additional gravitational potential V', a radial displacement u_r, and an horizontal displacement u_h, given by

$$V' = k_n V(\theta,\phi) \qquad u_r = h_n \frac{V(\theta,\phi)}{g} \qquad u_h = l_n \frac{\nabla V(\theta,\phi)}{g} \tag{2.16}$$

where k_n, h_n, and l_n are dimensionless quantities, called *Love numbers* (see Refs. [18, 19]) though the parameter l_n was actually introduced by Shida. They define the potential variation and the displacement at the Earth's surface. In particular h_n describes the height (radial) displacement attained by the solid surface relative to what would be obtained by a perfectly fluid body in response to the perturbing force, neglecting the additional potential generated by the redistribution of matter. The second

Love number, k_n, is the ratio of the potential generated by the deformed body to that of the perturbing potential. For example a rigid body has $k_n = 0$ because there is no redistribution of matter. The Shida number l_n is the ratio of the observed horizontal displacement to that which would be induced by a completely fluid surface.

By the definition of the Love numbers, displacements at the surface of the Earth in spherical coordinates will be obtained as

$$u_r = h_n \frac{V(\theta,\phi)}{g} \qquad u_\theta = \frac{l_n}{g}\frac{\partial V(\theta,\phi)}{\partial \theta} \qquad u_\phi = \frac{l_n}{g\sin\phi}\frac{\partial V(\theta,\phi)}{\partial \phi} \tag{2.17}$$

Therefore, the tensor components of the surface strain are

$$\varepsilon_{\theta\theta} = \frac{1}{gr_e}\left(h_n V + l_n \frac{\partial^2 V}{\partial^2 \theta}\right) \tag{2.18}$$

$$\varepsilon_{\phi\phi} = \frac{1}{gr_e}\left(h_n V + l_n \frac{\partial V}{\partial \theta} + \frac{l_n}{\sin\theta}\frac{\partial^2 V}{\partial^2 \theta}\right) \tag{2.19}$$

$$\varepsilon_{\theta\phi} = \frac{l_n}{gr_e \sin\theta}\left(\frac{\partial^2 V}{\partial\theta\partial\phi} - \frac{1}{\tan\theta}\frac{\partial V}{\partial\phi}\right) \tag{2.20}$$

Using Eqs. 2.13 and 2.14, it is possible to give the explicit formulas of the three components of surface strain for a particular degree n and order m

$$\begin{aligned}\varepsilon_{\theta\theta} = \frac{N_n^m}{r_e \sin^2\theta}\Big\{&\left[h_n \sin^2\theta + l_n\left(n^2\cos^2\theta - n\right)\right]P_n^m(\cos\theta) \\ &-2l_n(n-1)(n+m)\cos\theta P_{n-1}^m(\cos\theta) + l_n(n+m) \\ &(n+m-1)P_{n-2}^m(\cos\theta)\Big\}\left[a_n^m(t)\cos m\phi + b_n^m(t)\sin m\phi\right]\end{aligned} \tag{2.21}$$

$$\begin{aligned}\varepsilon_{\phi\phi} = \frac{N_n^m}{r_e \sin^2\theta}\Big\{&\left[h_n \sin^2\theta + l_n\left(n\cos^2\theta - m^2\right)\right]P_n^m(\cos\theta) \\ &-l_n(n+m)\cos\theta P_{n-1}^m(\cos\theta)\Big\}\left[a_n^m(t)\cos m\phi + b_n^m(t)\sin m\phi\right]\end{aligned} \tag{2.22}$$

$$\begin{aligned}\varepsilon_{\theta\phi} = \frac{mN_n^m l_n}{r_e \sin^2\theta}&\left\{(n-1)\cos\theta P_n^m(\cos\theta) - (n+m)P_{n-1}^m(\cos\theta)\right\} \\ &\left[a_n^m(t)\cos m\phi + b_n^m(t)\sin m\phi\right]\end{aligned} \tag{2.23}$$

To compute the total strain these components should be summed over all $n \geq 2$ and all $m = 0, 1, ..., n$ but in practice strain tides with $n > 3$ or $m = 0$ are unobservable.

2.3.2 The effects of the Earth's rotation, ellipticity and anelasticity

SNREI Earth model, so simple, has many limits and differs from the actual situation. The description of the tidal phenomenon becomes much more complicated if the effects of rotation, ellipticity, and anelasticity of the Earth are introduced [20, 21]. As a result, the Love numbers become latitude dependent and complex, and are not sufficient to describe the displacements, but some additional terms appear.

The ellipticity of core-mantle boundary combined with the rotation of the Earth produces a free oscillation mode in which the fluid core, restrained by pressure forces, and solid mantle precess around each other. This oscillation mode is known as the *Nearly Diurnal Free Wobble* or *Free Core Nutation*; it will be described in details in Chapter 4. This produces a frequency dependence in the Love numbers near 1 cycle per day, given by

$$L(f) = L_0 + \sum_{k=1}^{3} \frac{L_k}{f - f_k} \tag{2.24}$$

where f is the frequency in cycles per sidereal day, f_k (with $k = 1, ..., 3$) are the resonance frequencies associated with the Chandler Wobble (CW), the retrograde Free Core Nutation (FCN), and the Prograde Free Core Nutation, also known as Free Inner Core Nutation (FICN), and L_k are the corresponding resonance coefficients. All the parameters are complex. The values of f_k (see for example Ref. [22]) are

$$\begin{aligned} f_1 &= -0.0026010 - 0.0001361\imath \\ f_2 &= 1.0023181 + 0.000025\imath \\ f_3 &= 0.9990260 + 0.000780\imath \end{aligned} \tag{2.25}$$

At the same time, because of the Earth's ellipticity and rotation, response to forcing of degree n is coupled to spherical harmonics of other degrees, in particular spheroidal deformations of degree $n \pm 2$ and toroidal deformations of degree $n \pm 1$. For this reason, the Love numbers become slightly latitude dependent and horizontal displacement has additional terms.

The expression of the induced potential (for details see Ref. [20]) is given by Eq. 2.13

	$\Re[L_0]$	$\Im[L_0]$	$\Re[L_1]$	$\Im[L_1]$	$\Re[L_2]$	$\Im[L_2]$
$k^{(0)}$	0.29954	$-1.412{\cdot}10^{-3}$	$-7.811{\cdot}10^{-4}$	$-3.721{\cdot}10^{-5}$	$9.121\cdot10^{-5}$	$-2.971{\cdot}10^{-6}$
$h^{(0)}$	0.60671	$-2.420{\cdot}10^{-3}$	$-1.582{\cdot}10^{-3}$	$-7.651{\cdot}10^{-5}$	$1.810\cdot10^{-4}$	$-6.309{\cdot}10^{-6}$
$l^{(0)}$	0.08496	$-7.395{\cdot}10^{-4}$	$-2.217{\cdot}10^{-4}$	$-9.672{\cdot}10^{-6}$	$-5.486{\cdot}10^{-6}$	$-2.998{\cdot}10^{-7}$
k^{+}	-0.000804	$2.370\cdot10^{-6}$	$2.090\cdot10^{-6}$	$1.030\cdot10^{-7}$	$-1.820{\cdot}10^{-7}$	$6.500\cdot10^{-9}$
$h^{(2)}$	-0.000615	$-1.220{\cdot}10^{-5}$	$1.604\cdot10^{-6}$	$1.163\cdot10^{-7}$	$2.016\cdot10^{-7}$	$2.798\cdot10^{-9}$
$l^{(2)}$	0.0001933	$-3.819{\cdot}10^{-6}$	$-5.047{\cdot}10^{-7}$	$-1.643{\cdot}10^{-8}$	$-6.664{\cdot}10^{-9}$	$5.090\cdot10^{-10}$
$l^{(1)}$	0.00121	$1.360\cdot10^{-7}$	$-3.169{\cdot}10^{-6}$	$-1.665{\cdot}10^{-7}$	$2.727\cdot10^{-7}$	$-8.603{\cdot}10^{-9}$
l'	-0.000221	$-4.740{\cdot}10^{-8}$	$5.776\cdot10^{-7}$	$3.038\cdot10^{-8}$	$1.284\cdot10^{-7}$	$-3.790{\cdot}10^{-9}$

Table 2.2: Real and imaginary parts used in Eq. 2.24 to find the frequency dependence of the Love numbers, including corrections for ellipticity, in the diurnal tidal band.

where the spherical harmonics $Y_{nm}(\theta,\phi)$ are replaced by

$$k_0\left(\frac{r_e}{r}\right)^{n+1}Y_{nm}(\theta,\phi)+k_+\left(\frac{r_e}{r}\right)^{n+3}Y_{n+2,m}(\theta,\phi) \tag{2.26}$$

where the k_0 and k_+values are given in Table 2.2.

The expressions for displacements are more complicated. For example, the vertical displacement for $n=2$ is obtained replacing $Y_{nm}(\theta,\phi)$ into Eq. 2.13 with

$$h(\theta)\,Y_{2m}(\theta,\phi)+\frac{\delta_{m0}h'}{N_2^0} \tag{2.27}$$

where δ_{m0} is the Kronecker delta, N_{20} and h' are defined by Ref. [23], and

$$h(\theta)=h^{(0)}+\frac{1}{2}h^{(2)}\left(3\cos^2\theta-1\right) \tag{2.28}$$

The displacement in the $\hat{\theta}$ direction is obtained replacing $Y_{nm}(\theta,\phi)$ into Eq. 2.13 with

$$l(\theta)\frac{\partial Y_{2m}(\theta,\phi)}{\partial\theta}-\frac{ml^{(1)}\cos\theta}{\sin\theta}Y_{2m}(\theta,\phi)+\frac{\delta_{m1}l'}{N_2^1}\exp(\imath\phi) \tag{2.29}$$

where $l(\theta)$ is defined like $h(\theta)$ in the Eq. 2.28.

The displacement in the $\hat{\phi}$ direction is obtained replacing $Y_{nm}(\theta,\phi)$ into Eq. 2.13 with

$$\imath\left[\frac{ml(\theta)}{\sin\theta}Y_{2m}(\theta,\phi)+l^1\cos\theta\frac{\partial Y_{2m}(\theta,\phi)}{\partial\theta}+\frac{\delta_{m0}\sin\theta l'}{N_2^0}\right] \tag{2.30}$$

A further effect arises from the anelasticity property of mantle. The Love numbers become complex with small imaginary parts and depending on the frequency. For the semidiurnal and diurnal tides, this effect is small, especially compared to the NDFW resonance. In the long-period bands, it is significant as f approaches zero and the Love numbers become

$$L(f)=A-B\left\{\cot\frac{\alpha\pi}{2}\left[1-\left(\frac{f_m}{f}\right)^{\alpha}\right]+\left(\frac{f_m}{f}\right)^{\alpha}\right\} \tag{2.31}$$

where A and B are constants, $\alpha=0.15$ and f_m is the reference equivalent to a period of 200 sec.

2.4 Ocean loading

The redistribution of oceanic mass, mainly caused by the gravitational attraction from Sun and Moon, produces important loading effects on the crust called *load tides*. These mass fluctuations cause changes in the potential even on the solid Earth. Since the Earth is not completely rigid, it deforms under this load, causing more changes in the potential, plus displacements, and also the Earth tides are significantly perturbed.

Ocean loading effect is strongly dependent on the locally variable properties of the lithosphere [24] and, combined with variations in the ocean amplitudes, gives large loading variations especially near coastal areas.

Various methods have been developed to compute the ocean tidal loading, in particular spherical harmonic expansion and the Green's function methods are usually used.

2.4.1 Spherical harmonic expansion for the ocean loading

Using the spherical harmonic expansion, complex tidal elevation is given by

$$H(\theta',\phi')=\sum_{n=0}^{\infty}\sum_{m=-n}^{n}H_{nm}Y_{nm}(\theta',\phi') \tag{2.32}$$

where Y_{nm} are the spherical harmonics, as defined in Eq. 2.8, and the coefficients H_{nm} would be found from the integration on the surface Ω of a sphere, so that

$$\begin{aligned} H_{nm} &= \int_o^{\pi} \sin\theta' d\theta' \int_o^{2\pi} d\phi' H\left(\theta', \phi'\right) Y_{nm}^* \\ &= \int_{\Omega} H\left(\theta', \phi'\right) Y_{nm}^* d\Omega \end{aligned} \tag{2.33}$$

The mass distribution H causes a gravitational potential on the Earth's surface, given by

$$W\left(\theta, \phi\right) = G\rho_w r_e^2 \int_{\Omega} \frac{H\left(\theta', \phi'\right)}{r} d\Omega \tag{2.34}$$

where ρ_w is the density of the seawater, and r is distance from the location (θ, ϕ) to the mass (θ', ϕ'). The linear distance, as usual, can be expressed as a function of the angular distance Δ

$$\frac{1}{r} = \frac{1}{2r_e \sin\left(\Delta/2\right)} = \frac{1}{r_e} \sum_{n=0}^{\infty} P_n\left(\cos\Delta\right) \tag{2.35}$$

and using the addition theorem for spherical harmonics

$$\frac{1}{r} = \frac{1}{r_e} \sum_{n=0}^{\infty} \sum_{m=-n}^{n} \frac{4\pi}{2n+1} Y_{nm}\left(\theta', \phi'\right) Y_{nm}^*\left(\theta, \phi\right) \tag{2.36}$$

This last equation provides the potential in terms of spherical harmonics

$$W\left(\theta, \phi\right) = G\rho_w r_e \sum_{n=0}^{\infty} \sum_{m=-n}^{n} \frac{4\pi}{2n+1} H_{nm} Y_{nnm}\left(\theta, \phi\right) \tag{2.37}$$

Also in this case, following Munk and MacDonald [25], it is possible to define *load Love numbers* to describe the Earth's response to the load, differentiating them from the usual Love numbers used to describe the body tides.

For a potential of degree n, the radial displacement u_r, the horizontal displacement u_h, and the additional potential produced by the deformation of the Earth $W'\left(\theta, \phi\right)$ are defined as

$$W' = k_n' W\left(\theta, \phi\right) \qquad u_r = h_n' \tfrac{W(\theta,\phi)}{g} \qquad u_h = l_n' \frac{\nabla W\left(\theta, \phi\right)}{g} \tag{2.38}$$

where k_n', h_n', and l_n' are the *load Love numbers*. By integrating the differential equations

for the deformation of the Earth, it is possible to find the load Love numbers.

The boundary condition at the surface is obtained hypothesizing a normal stress from the load, rather than zero stress as done for the Love numbers in the case of the tidal potential. For a spherical Earth, these load numbers depend only on the degree n of the spherical harmonics. These parameters are obtained from the internal structure of the Earth and they are greatly affected by the structure of the crust and mantle, particularly in the region close to the load.

2.4.2 Green's functions for ocean loading

Green's function represents the response of the Earth to a point load. The introduction of these functions to describe the deformation of the Earth induced by a point load on the surface was first studied and approximately evaluated by Longman [26, 27]. A more accurate estimate was attained by Farrell [24], in a work still widely used.

In general Green's functions are a mathematical tool for describing the response to a unit impulse. Applying a unit point mass load $L(\mathbf{r}')$ that induces a displacement $u(\mathbf{r}')$ at point $\mathbf{r}'$ on the Earth's surface, the displacement at point $\mathbf{r}$ is defined by the Green's function $G(\mathbf{r}, \mathbf{r}')$.

Generalizing, at point $\mathbf{r}$ the effect of a real load L, covering a surface Ω instead of a point, is given by the convolution of the Green's function with the load

$$u(\mathbf{r}) = \int_{\Omega} G(\mathbf{r}, \mathbf{r}')\, L(\mathbf{r}') d\mathbf{r}' \tag{2.39}$$

To know the loads at a few places it is possible to multiply the tide model by a Green's function which gives the response to a point load, and integrate over the area that is loaded by the tides.

Following Ref. [9], in spherical coordinates at a point (θ, ϕ) the effect from a point mass at (θ', ϕ'), introduced the Green's function $G(\theta, \phi, \theta', \phi')$, is

$$\int_0^{\pi} r \sin\theta' d\theta' \int_0^{2\pi} G(\theta, \phi, \theta', \phi')\, \rho_w H(\theta', \phi') \tag{2.40}$$

Green's functions are obtained through the Love numbers. The potential from a point mass is

$$W(\theta, \phi) = G\rho_w r_e \int_{\Omega} H(\theta', \phi') \sum_{n=0}^{\infty} P_n(\cos\triangle)\, d\Omega \tag{2.41}$$

Taking

$$H\left(\theta',\phi'\right)=\rho_w r_e^2\delta_{\theta'\phi'} \tag{2.42}$$

where $\delta_{\theta'\phi'}$ is the Dirac delta, Eq. 2.41 becomes

$$W\left(\theta,\phi\right)=\frac{gr_e}{M_e}\sum_{n=0}^{\infty}P_n\left(\cos\triangle\right) \tag{2.43}$$

The surface vertical displacement at distance Δ from the point mass load can be used to define the corresponding Green's function as

$$u_r=\frac{r_e}{M_e}\sum_{n=0}^{\infty}h'_n\frac{W_n}{g}=\frac{r_e}{M_e}\sum_{n=0}^{\infty}h'_nP_n\left(\cos\triangle\right)\equiv G_r\left(\triangle\right) \tag{2.44}$$

At the same way, for the horizontal displacement the Green's function is

$$u_h=\frac{r_e}{M_e}\sum_{n=0}^{\infty}\frac{l'_n}{g}\frac{\partial W_n}{\partial\Delta}=\frac{r_e}{M_e}\sum_{n=0}^{\infty}\frac{l'_n}{g}\frac{\partial P_n\left(\cos\triangle\right)}{\partial\Delta}\equiv G_h\left(\triangle\right) \tag{2.45}$$

As the Green's function are formed by weighted infinite sum of the load Love numbers, it is necessary to truncate n at some limited value. This truncation at finite n causes problems in the loading computation in coastal regions. This problem can be solved considering that when n gets large enough h'_n, l'_n, and k'_n become constant. Farrell used and derived the asymptotic value of load Love numbers. In this case, it is possible to write for example the Green's function for the vertical displacement as

$$\begin{aligned}G_r\left(\Delta\right) &= \frac{r_e}{M_e}\left[\sum_{n=0}^{\infty}h'_\infty P_n\left(\cos\triangle\right)+\sum_{n=0}^{\infty}\left(h'_n-h'_\infty\right)P_n\left(\cos\triangle\right)\right]\\ &= \frac{r_e h'_\infty}{2M_e\sin\left(\triangle/2\right)}+\frac{r_e}{M_e}\sum_{n=0}^{\infty}\left(h'_n-h'_\infty\right)P_n\left(\cos\triangle\right)\end{aligned} \tag{2.46}$$

using the addition theorem for spherical harmonics. This sum will converge much more quickly; it is necessary to include only enough terms for h'_n to have h'_∞ with enough precision. This last equation shows also that for Δ small, the sum approaches zero, so for loads nearby, G_r varies as Δ^{-1}. This is the Boussinesq solution, that describes the vertical displacement for a point load on an elastic half-space in the limit of short distance. The sum, although terminates after finite number of terms, still converges rather slowly, because the amplitude of P_n decays only as $n^{-1/2}$. For speeding the

technique, Farrell introduced a converging disk factor into the transformed potential and the Euler's transformation on the series.

This behavior characterizes also the Green's function for the horizontal displacement; in fact

$$\begin{aligned} G_h(\Delta) &= \frac{r_e}{M_e}\left[\sum_{n=0}^{\infty}\frac{l'_\infty}{n}\frac{\partial P_n(\cos\triangle)}{\partial\Delta}+\sum_{n=0}^{\infty}(l'_n-l'_\infty)P_n(\cos\triangle)\right] \\ &= -\frac{r_e l'_\infty}{M_e}\frac{\cos(\triangle/2)\left[1+2\sin(\triangle/2)\right]}{2\sin(\triangle/2)\left[1+2\sin(\triangle/2)\right]}+\frac{r_e}{M_e}\sum_{n=0}^{\infty}(nl'_n-l'_\infty)\frac{\partial P_n(\cos\triangle)}{\partial\Delta} \end{aligned}$$

The total gravity potential due to the point load is given by the sum

$$W_n + W'_n = (1+k'_n)W_n$$

At a deformed surface of the Earth, the total change in the gravity potential would be

$$W_n + W'_n + u_r\frac{\partial V}{\partial r} = (1+k'_n)W_n + h'_n\frac{W_n}{g}\frac{\partial V}{\partial r} \tag{2.47}$$

where V is the unperturbed gravity potential of the Earth. The Green's function for the potential is given by

$$\begin{aligned} G_{pot} &= \frac{r_e}{M_e}\sum_{n=0}^{\infty}(1+k'_n-h'_n)P_n(\cos\triangle) \\ &= \frac{r_e(1-h'_\infty)}{2M_e\sin(\triangle/2)}+\sum_{n=0}^{\infty}\left[k'_n-(h'_n-h'_\infty)\right]P_n(\cos\triangle) \end{aligned} \tag{2.48}$$

and, again, there is a Δ^{-1} singularity for Δ small.

For the strain, the Green's function can be deduced considering that in the load direction

$$\varepsilon_{\Delta\Delta} = \frac{1}{r_e}\frac{\partial u_h}{\partial\Delta}+\frac{u_r}{r_e} \tag{2.49}$$

thus

$$G_{\Delta\Delta} = \frac{1}{M_e}\left[\sum_{n=0}^{\infty}h'_\infty P_n(\cos\triangle)+\sum_{n=0}^{\infty}l'_\infty\frac{\partial^2 P_n(\cos\triangle)}{\partial\Delta^2}\right] \tag{2.50}$$

Introducing the asymptotic values of h'_n and l'_n, this last equation becomes

$$\begin{aligned} G_{\Delta\Delta} &= \frac{h'_\infty}{2M_e \sin(\triangle/2)} + \frac{1}{M_e}\sum_{n=0}^{\infty}(h'_n - h'_\infty) P_n(\cos\triangle) \\ &\quad + \frac{l'_\infty}{M_e}\sum_{n=0}^{\infty}\frac{1}{n}\frac{\partial^2 P_n(\cos\triangle)}{\partial\Delta^2} + \frac{1}{M_e}\sum_{n=0}^{\infty}(l'_n - l'_\infty)\frac{\partial^2 P_n(\cos\triangle)}{\partial\Delta^2} \\ &= \frac{h'_\infty}{2M_e \sin(\triangle/2)} + \frac{l'_\infty}{M_e}\frac{1+\sin(\triangle/2)+\sin^2(\triangle/2)}{4\sin^2(\triangle/2)+[1+\sin(\triangle/2)]} \\ &\quad + \frac{1}{M_e}\sum_{n=0}^{\infty}(l'_n - l'_\infty)\frac{\partial^2 P_n(\cos\triangle)}{\partial\Delta^2} \end{aligned} \tag{2.51}$$

It shows a near-field singularity for Δ^{-2}.

In general, the Green's function for linear strain as a function of the angular distance Δ and the azimuth η of the load is given by

$$G(\Delta,\eta) = G_{\Delta\Delta}(\Delta)\cos^2\eta + \left[\frac{G_r(\Delta)}{r_e} + \cot\Delta\frac{G_h(\Delta)}{r_e}\right]\sin^2\eta \tag{2.52}$$

All of the Green's functions are computed by finding the load Love numbers for a range of n, and forming the various sums. Farrell [24] formed the sums up, computing the values of Green's functions using a grid of $n = 10000$ points, spaced logarithmically and interpolating to intermediate values. The Green's functions tabulated by Farrell are still widely used.

Several numerical methods have been developed. These Green's functions, computed for different SNREI Earth models, only show discrepancies for small angular distances between the load and the observation points. This is due to the fact that these Earth models differ essentially at the crust and upper mantle.

The classical results of Farrell have been modified to describe more realistically the response of the Earth to the tidal loading. For example, Pagiatakis [28] considered the Green's functions taking the viscoelastic behavior of the Earth into account. In this case, Green's functions become complex and frequency dependent. He found that viscoelastic Green's functions differ at a maximum of 1.5% in amplitude and 0.3 degrees in phase in comparison with a purely elastic Earth. He extended also the theory to a self-gravitating, anisotropy and rotating Earth.

Chapter 3

Gran Sasso laser interferometers

Strain measurements in geophysics became increasingly important. In order to study the processes involving the lithosphere, associated with many geological hazards, such as landslides, land subsidence, volcano eruption and earthquakes, a precise and continuous monitoring of crustal deformation is required.

The most common techniques for continuous strain measurements are possible using continuous GPS (Global Positioning System) networks, mechanical borehole dilatometers and strainmeters, mechanical extensometers, and laser extensometers (interferometers). Moreover in the last decades, high-precision measurements have gained increasing interest.

GPS networks allow monitoring large areas at relatively low cost, but their sensitivity is not high, ranging between about 10^{-6} to 10^{-7}.

Mechanical borehole dilatometers and tensor strainmeters are heavily used, mainly in United States, China and Japan. The main difficulties arise from the cementing to the surrounding rock and the calibration in situ.

Mechanical extensometers are not so used, a few of observatories are equipped with some of these instruments, for example Black Forest Observatory (`http://www-gpi.physik.uni-karlsruhe.de/pub/widmer/BFO/`) and Moxa Geodynamical Observatory (`http://www.geo.uni-jena.de/Homepage-Moxa-englisch/start.html`), in Germany.

Only a few laser interferometers, meters or hundreds of meters long, have been installed inside tunnels. Some of them are no more working instruments [29, 30] and others are still working, like for example at Baksan (Russia) and Kamioka (Japan) Underground

Observatories [31, 32]. These instruments have shown excellent behavior. Their long-term stability has proved to be better than mechanical extensometers and borehole instruments, sensitivity is higher than CGPS by orders of magnitude, and they can measure strain even in porous fluid saturated rock. Main disadvantages of these instruments are costs of tunnel excavation, prevalent use of complex electro-optical set-ups, vacuum system, and short baselines with respect to superficial installations.

Superficial long-baseline (about 1 km long) interferometers have been installed in California, their main disadvantages are due to the high cost of the vacuum system and necessity of monitoring end-monument displacements with respect to the bedrock at about 30-meter depth because of weathering effects.

Among the few high-sensitivity wide-band laser interferometers operating allover the world, since several years two geodetic laser interferometers are working at Laboratori Nazionali del Gran Sasso (LNGS), Italy. These interferometers measure the extension, along two orthogonal directions and as difference in length between two end points, by means of Michelson-type optical interferometers.

3.1 Laser interferometry, the principles

A laser interferometer system employs a highly stabilized light source and precision optics to accurately measure distances.

The laser interferometer, first introduced by Albert Michelson in 1881, has been developed into a measurement instrument with high accuracy. In the Michelson's interferometer (see Fig. 3.1) a monochromatic light is directed toward a semi-transparent beam-splitter mirror, that acts splitting the beam. The two resulting beams are coherent and travel two separate, but nearly equal, paths. Part of the light is transmitted toward a movable mirror and reflected by this mirror, along the so-called *measurement arm*. The other part of the light, that moves along the *reference arm*, is reflected at 90 degrees towards a fixed mirror, and here reflected again. The two parts are recombined at the beam splitter where their interference is observed, usually by a detector.

The electromagnetic waves, propagating along reference and measurement arms, can be expressed as

$$\mathbf{E_{ref}} = E_r \exp\left[\imath\left(\omega t + \mathbf{k}\cdot\mathbf{r_r} - \phi_r\right)\right]\hat{e}_1 \tag{3.1}$$

$$\mathbf{E_{meas}} = E_m \exp\left[\imath\left(\omega t + \mathbf{k}\cdot\mathbf{r_m} - \phi_m\right)\right]\hat{e}_2 \tag{3.2}$$

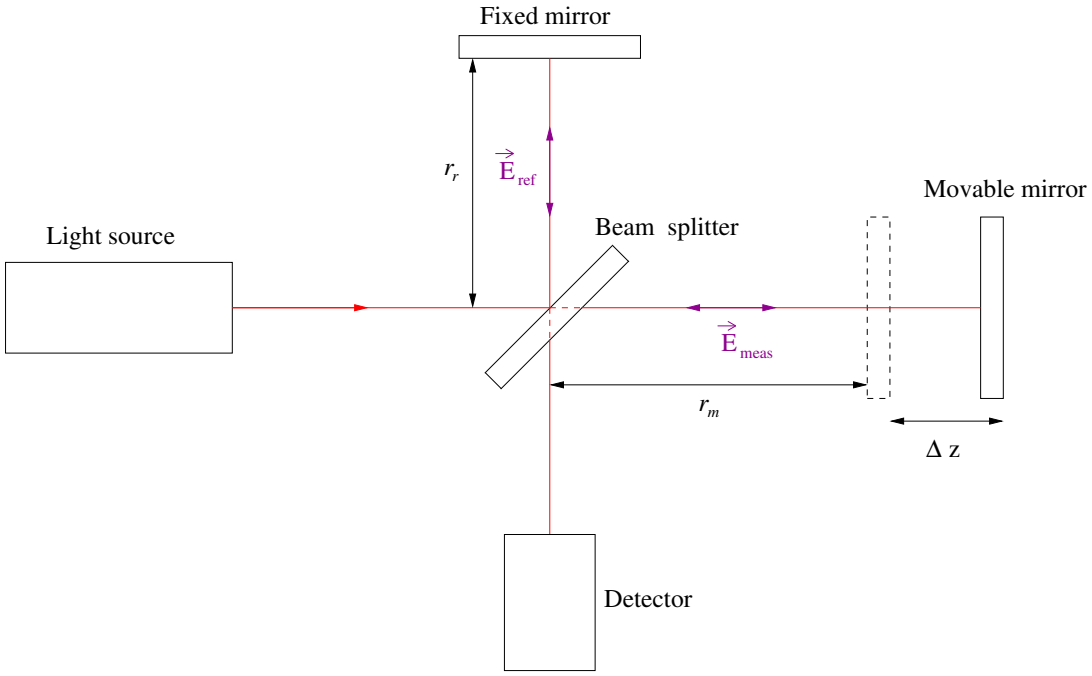

Figure 3.1: Schematic version of a Michelson's interferometer.

where E_r and E_m are the amplitude, ϕ_r and ϕ_m are the phases of the electromagnetic fields in reference and measurement arms respectively, $\mathbf{r_r}$ and $\mathbf{r_m}$ are the position vectors along the two directions, ω is the angular frequency, t the time, and $\mathbf{k}$ the propagation vector.

After the recombination in the beam splitter the electromagnetic field is the linear superposition of these waves. Assuming the propagation of the field in only one dimension, the intensity of the light at the detector becomes:

$$I = \epsilon_0 c \left\langle E^2 \right\rangle \tag{3.3}$$

that is

$$I = \epsilon_0 c \left\{ E_r^2 + E_m^2 + 2E_r E_m \cos\left[k\left(r_m - r_r\right) - \phi\right] \right\} \tag{3.4}$$

where ϵ_0 is the vacuum permittivity, c the light speed, k the propagation constant, $\phi = \phi_m - \phi_r$ is the phase difference, and r_m and r_r are the traveled optical distances in the measurement and reference arms respectively. Equation 3.4 implies that the intensity should vary sinusoidally between zero and some maximum value, visible through the interference fringes.

If the light source is monochromatic, waves are initially in phase, and $\phi_r = \phi_m$. Thus,

the cosine term depends on the difference in optical path length between reference and measurement arms, and the intensity becomes

$$\begin{aligned} I &= 2I_0 \left\{1 + \cos\left[k\left(r_m - r_r\right)\right]\right\} \\ &= 2I_0 \left\{1 + \cos\left[\frac{2\pi}{\lambda}\left(r_m - r_r\right)\right]\right\} \end{aligned} \tag{3.5}$$

Moving the measurement mirror over a distance Δz, the optical path length changes of $2n\Delta z$, where n is the refractive index of the medium through which the light travels and the factor 2 is because this distance is traveled twice by the light. In this case the measured signal will be

$$I = 2I_0 \left\{1 + \cos\left[\frac{2\pi}{\lambda}\left(2n\Delta z\right)\right]\right\} \tag{3.6}$$

If the wavelength of the light source is known, the displacement can be calculated from the change in intensity on the detector. It can also be considered as a relative measurement, and only displacement can be measured, not distance.

From Michelson's original length interferometer numerous different versions were derived, all working on the same measuring principle of displacement by using the interference. Modern interferometers use a HeNe-laser as light source, characterized by long coherence length and relatively short visible wavelength resulting in comfortable alignment and a higher resolution.

Laser interferometers can be separated in two main kinds: homodyne and heterodyne interferometers.

3.1.1 Homodyne interferometers

In a homodyne interferometer, the interference is observed through a phase difference between two beams, providing a change in the intensity of the light on a detector. The resulting light intensity is measured after the recombination of the two beams.

A homodyne laser source is typically a HeNe laser with a polarized single frequency light. The beam passes through a quarter-wave plate and becomes circularly polarized. In order to do this, the incoming beam's polarization direction needs to be at 45 degrees relative to the retarder's principal axis. The beam is then separated along the reference and measurement arms by a beam splitter. The two beams produced are reflected by

two targets and recombined at the beam splitter. For observing interference the two beams need to have the same polarization. This is accomplished using a linear polarizer oriented at 45 degrees to the beam splitter. This second polarizing beam splitter splits the output beam into two orthogonal fields, each sensed by a detector.

As a result, depending on the direction of the mirror's travel, the first detector leads or lags the second one. This phase information can be used to deduce the position of the moving mirror.

Signals I_1 and I_2 are used for phase quadrature measurements. The first one is the normal signal of a homodyne interferometer with signal $2I_0$ subtracted

$$I_1 = 2I_0 \cos \frac{4\pi n \Delta z}{\lambda} \tag{3.7}$$

The second part of the measurement signal is split off and receives a phase shift of 90 degrees, so that

$$I_2 = 2I_0 \sin \frac{4\pi n \Delta z}{\lambda} \tag{3.8}$$

Displacement is calculated as

$$\Delta z = \frac{\lambda}{4\pi n} \arctan \frac{I_2}{I_1} \tag{3.9}$$

When both signals are plotted against each other ideally a circle is described. If polarization mixing occurs periodic deviations are present in the measurement signals which result in an ellipse. Also different gains in both detector signals will give an ellipse.

3.1.2 Heterodyne interferometers

A heterodyne interferometer measures mirror displacement through a phase change caused by the Doppler effect.

The light source of a heterodyne laser interferometer (see Fig. 3.2) is a stabilized HeNe laser whose output beam contains two frequency components, located close to each other (f_1 and f_2). The two frequency components have linear polarization, orthogonal to each other. They are separated at the polarizing beam splitter.

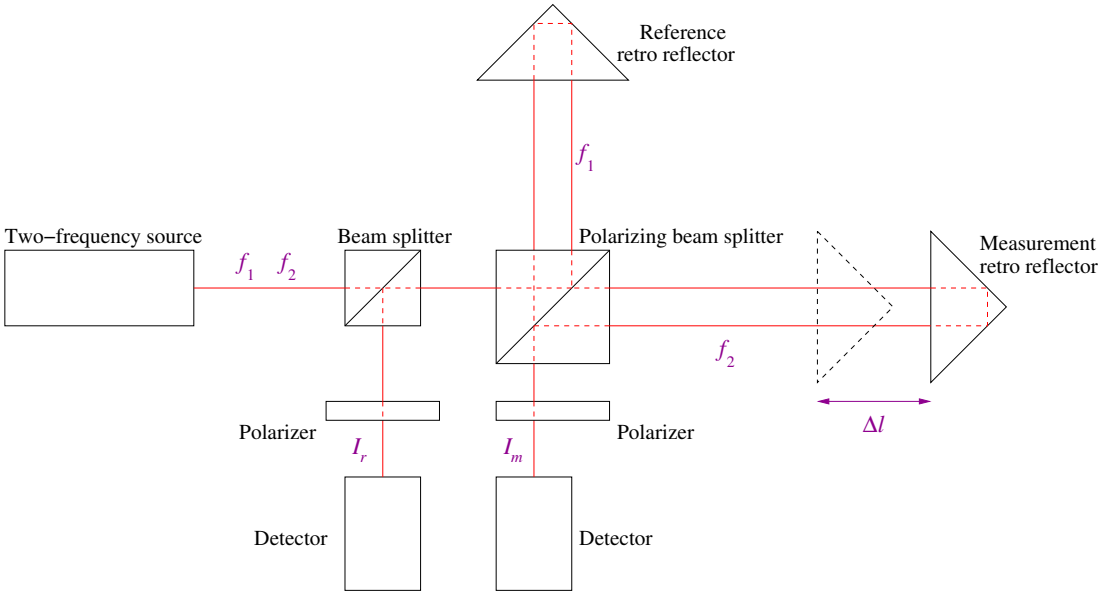

Figure 3.2: Schematic configuration of a heterodyne interferometer.

The electromagnetic fields are given by

$$\mathbf{E_1} = E_1 \exp\left[\imath\left(2\pi f_1 + \phi_1\right)\right] \hat{e}_1 \tag{3.10}$$

$$\mathbf{E_2} = E_2 \exp\left[\imath\left(2\pi f_2 + \phi_2\right)\right] \hat{e}_2 \tag{3.11}$$

where E_1 and E_2 are the amplitudes, and ϕ_1 and ϕ_2 the initial phases of the electromagnetic fields.

The envelope frequency is given by the difference of the two frequency components of the source radiation, $f_1 - f_2$. The frequency shift can be generated, for example, by a Zeeman laser, that produces two close frequencies by applying an axial magnetic field to the laser tube, or by a Bragg cell driven by a quartz oscillator.

Part of the light emitted by the laser source is split off, passes a combining polarizer and arrive at a detector characterized by a band-pass filter. The resulting signal is an alternating signal with a beat frequency equal to the split frequency in the laser head. This signal forms the reference measurement I_r, given by

$$I_r = 2E_1E_2 \cos\left[2\pi\left(f_2 - f_1\right)t + \left(\phi_2 - \phi_1\right)\right] \tag{3.12}$$

The other part of the light enters the interferometer optics, consisting of a polarizing beam splitter and two retro reflectors, one fixed and the other one movable. At the po-

larizing beam splitter the two frequencies are split. Beam with frequency f_1 is reflected and enters the reference arm, reflected by the fixed retro reflector and again reflected by the polarizing beam splitter. Beam with frequency f_2 is transmitted and travels in the measurement arm, reflected by the moving retro reflector and again transmitted by the beam splitter. Ideally, both frequencies emerge from the polarizing beam splitter in their own unique polarization orthogonal to each other. To allow interference, beams are transmitted through a polarizer under 45 degrees with their polarization axes. After the polarizer, light arrives at a second detector with band-pass filter resulting in the measurement signal

$$I_m = 2E_1E_2\cos\left[2\pi\left(f_2 - f_1\right)t + \left(\phi_2 - \phi_1\right) + \left(\phi_{meas} - \phi_{ref}\right)\right] \tag{3.13}$$

where $\phi_{meas} - \phi_{ref}$ is the difference in phase between the signals in measurement and reference arms.

In the measurement arm, retro reflector moves with velocity v. As a consequence, a Doppler shift is generated for the frequency f_2

$$\Delta f = \frac{2vnf_2}{c} \tag{3.14}$$

where n is the refractive index of the air and c is the light speed in the vacuum. From this equation, the maximum traveling speed of the retro reflector is limited because of the finite frequency shift between the two frequencies in the laser source.

Phase change in the interference pattern resulting from the Doppler shift is

$$\Delta\phi = \int_{t_1}^{t_2} 2\pi\Delta f dt = \int_{t_1}^{t_2} 2\pi\frac{2vnf_2}{c}dt = 4\pi\frac{nf_2}{c}\int_{t_1}^{t_2} vdt = 4\pi n\frac{f_2}{c}\Delta l = \frac{4\pi n}{\lambda_2}\Delta l \tag{3.15}$$

where Δl is the displacement of the retro reflector.

By measuring the phase change between measurement (Eq. 3.12) and reference (Eq. 3.13) signals, it is possible to estimate the displacement of the retro reflector through the inverse of Eq. 3.15 with vacuum wavelength λ_2

$$\Delta l = \frac{\lambda_2}{4\pi n}\Delta\phi \tag{3.16}$$

3.1.3 Error sources

The accuracy of the calculated displacement for an interferometer depends on the accuracy of the estimate of some parameters, like for example phase change, wavelength of light, and refractive index of the medium. However, there are other error sources depending on the instrument and environmental conditions.

One of the most important source of errors is the effect of the environmental parameters. Its magnitude depends on the accuracy of the compensation method, the atmosphere in which the system is operating, and the variations of atmospheric conditions during a measurement.

Deviations in temperature, as well as changes in pressure and humidity, affect the index of refraction of the medium through which the light travels, altering the optical path and at the same time the wavelength. In fact in vacuum the wavelength is constant, but in atmosphere it depends on the index of refraction of air. It is possible to control this source of error by measuring the index of refraction using a refractometer (in which the reference and measurement beams travel across the same nominal distance) or the environmental parameters.

Thermal effects cause also a linear expansion of the optical set-up and optics itself. To estimate this correction, it is necessary to monitor temperature during the measurement time and coefficient of linear thermal expansion of the system.

Changes in temperature of some optical components during the measurement can cause changes in optical path length, that appear as distance change and cause a typical thermal drift. This optical thermal drift can be reduced by either monitoring the temperature of the measurement environment, or by using interferometers that are insensitive to temperature changes. In this case, to reduce the temperature sensitivity of an interferometer, the beam components need to travel through the same type and amount of glass.

Also air turbulence and thermal gradients in the air along the beam path, influence the index of refraction, causing loss of signal strength. To minimize these effects it is possible to protect the laser beam by placing pipes along the beam path, minimizing the air flow, or operating in the vacuum.

Optical length in both the reference and measurement paths is affected by changes of index of refraction in the air. Dead path is the difference in distance in air between the reference and measurement paths in the interferometer configuration. If the measure-

ment and reference retro reflectors are at the same distance away from the polarizing beam splitter, a temperature increase changes the wavelength in both paths. Since path lengths are equal, there is no net phase change at the detector and dead path is zero in this case. But an uncompensated length between reference and movable reflectors causes dead path error. To minimize this error, reflectors should be located as close as possible to the beam splitter, and also environmental changes must to be reduced during the measurement time.

Optics itself and its alignment cause other errors. All optics has inherent inaccuracies in the form of optical non-linearity. This error can not be controlled by the user, and depends on the quality of the optics. All interferometer optics will have some amount of non-linearity, so this error can not be completely removed but it may be minimized by using high quality materials for the optical components.

A misalignment between laser beam path and mechanical axis of motion causes an error between measured distance and actual distance traveled. This error is known as cosine error, because its value depends on the cosine of the angle of misalignment. Care should be taken in aligning the laser beam and system optics to minimize the appearance of cosine error.

Other kind of error is known as Abbe error. It occurs when the measured beam does not move perfectly straight and angular movements are required, causing for example a sloping of the retro reflector. This sloping is greater if longer is the distance between the axis of measurement and the axis of movement. An Abbe error may be avoided only when no angular movements of the retro reflector are possible.

3.1.4 Laser stabilization

HeNe laser was the first continuous working laser, invented by Javan et al. in 1961 [33]. It produces an intense, monochromatic, coherent, and highly collimated light beam. This means that wavelength of laser light is extremely pure (monochromatic), photons produced have a fixed phase relationship (coherence) with respect to one another, and beam has very low divergence (collimation).

The operating principle of a laser is based on quantum theory; for an atom absorbs light, causing an electron to move from a lower energy state to a higher energy state, the energy of a single photon must to be exactly equal to the energy difference between the two states.

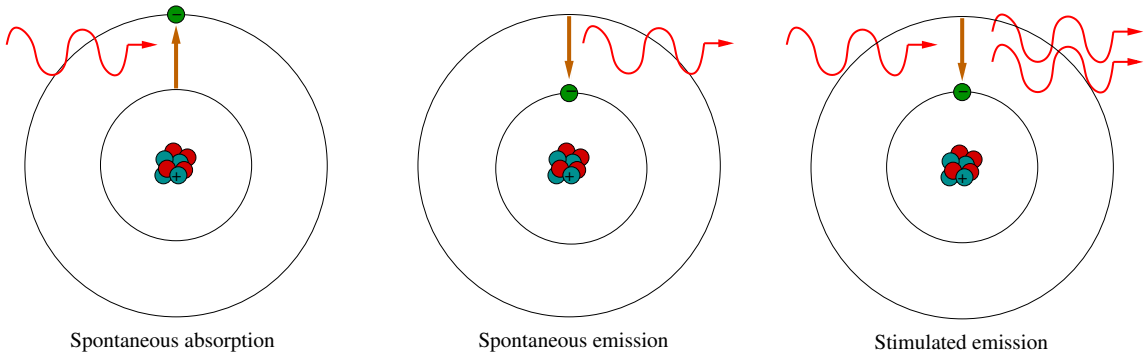

Figure 3.3: Absorption and emission processes in two level system.

Three different processes occur simultaneously within a medium (see Fig. 3.3).

When an electron is in the excited state, it may spontaneously decay to a lower energy level in a radiative transition, releasing the difference in energy between the two states as a photon with random direction and phase. This phenomenon, called *spontaneous emission*, produces fluorescent light. If the frequency of the photon is ν, its energy is

$$E_2 - E_1 = h\nu \tag{3.17}$$

where E_2 and E_1 are the energy of the higher and lower states respectively, and h is the Planck constant.

Likewise, a photon with a particular frequency could be absorbed by an electron in a lower state. This behavior is known as *spontaneous absorption.* The electron remains in this excited state for a period of time typically less than 10^{-6} second. Then it returns to the lower state spontaneously, emitting a photon.

These common processes of absorption and spontaneous emission can not give rise to the amplification of light because for every photon absorbed, another is emitted.

Alternatively, if the excited state atom is perturbed by the electric field of a photon with frequency ν, it may release a second photon with the same frequency, in phase with the first one. The atom will again decay into the lower state. This process is known as *stimulated emission.*

In a medium in thermal equilibrium, stimulated emission does not account to a significant extent because there are more electrons in the ground state than in the excited states. However stimulated emission is used to amplify light radiation.

Obviously, each time an excited atom is stimulated to emit a photon, the population

of excited atoms decreases by one. To create a laser beam, a large number of these transitions has to take place. Only when the higher energy state has a greater population than the lower energy state, the light in the system undergoes a net increase in intensity, creating a *population inversion*.

In a HeNe laser helium is the major constituent (85 percent) of the gas mixture, but the neon component is the actual lasing medium. Laser process starts with collision of electrons from the electrical discharge with the helium atoms in the gas. This excites helium from the ground state to metastable excited states. Collision of the excited helium atoms with the ground-state neon atoms results in transfer of energy to the neon atoms, exciting them. This is due to a coincidence of energy levels between helium and neon atoms. The number of neon atoms entering the excited states builds up as further collisions between helium and neon atoms occur, causing a population inversion. Spontaneous emission between states of neon results in emission of 632.8 nm wavelength light, the typical operating wavelength of a HeNe laser.

An important component of a laser is the *resonant cavity*. This is generally composed of a pair of mirrors, inside which active gas is placed, whose atoms are used for the stimulated emission process. In this way radiation generated is reflected back and forth between the mirrors and, passing through the active medium, is amplified. One of the two mirrors is fully reflective, while the other one is only partially reflective with values reflectivity ranging from 80% to 99%. This allows to extract part of the radiation that accumulates in the resonant cavity.

The resonant cavity also produces an effect of selection on the emission wavelength of the laser. For a two-mirror cavity, where mirrors are separated by optical length L, the only allowable laser wavelengths are those for which

$$L = \frac{m\lambda}{2} \tag{3.18}$$

and the frequencies

$$\nu = m\frac{c}{2L} \tag{3.19}$$

So each value of m corresponds to a different longitudinal mode.

The frequency spacing between adjacent modes is given by

$$\Delta\nu = \frac{c}{2L} \tag{3.20}$$

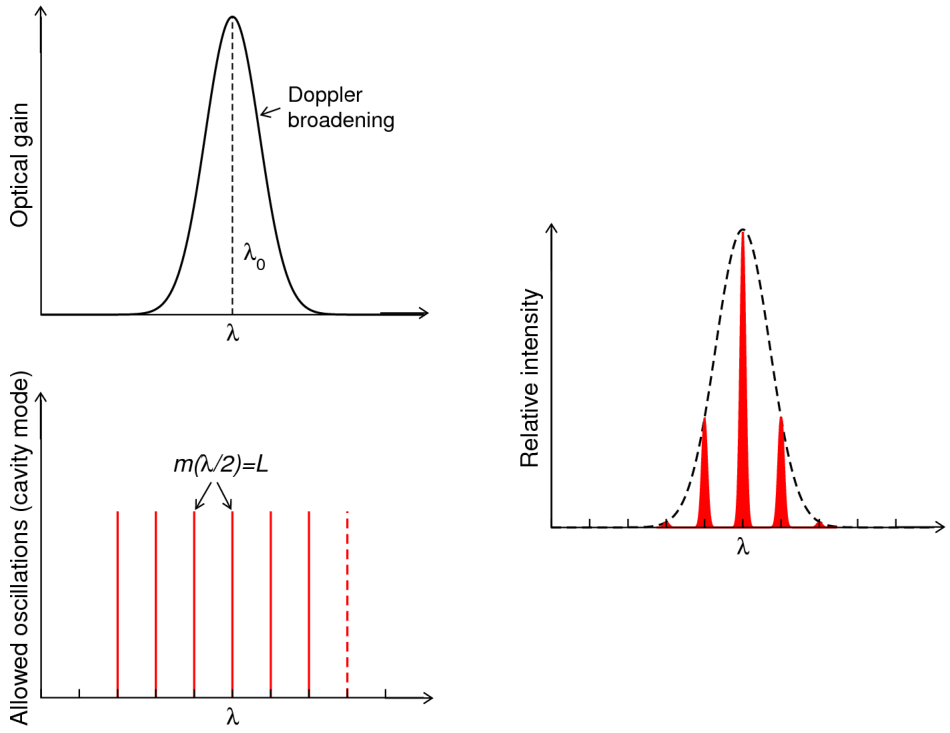

Figure 3.4: Optical gain curve of the lasing medium and allowed modes within the optical cavity. The output spectrum (relative intensity vs. wavelength) is determined by satisfying both conditions simultaneously, assuming no cavity losses.

The number of longitudinal laser modes depends primarily on two factors: the length of the laser cavity and the width of the gain envelope of the lasing medium.

Though energy is quantized in electron transitions, the output radiation is not totally monochromatic, but covers a spectrum of wavelengths with a central peak. The main cause is the phenomenon of Doppler spreading. If an observer moves away from the light source at $v \ll c$, the frequency (ν_1) of the incoming light appears to be shifted from the expected frequency (ν_0) according to the relation $\nu_1 = \nu_0 (1 - v/c)$. When the atom is moving towards the observer, the detected frequency is higher and given by $\nu_2 = \nu_0 (1 - v/c)$. Consequently, atoms at different velocities will absorb and emit photons of slightly different frequencies from the same energy line.

In a gas, atoms have a broad range of velocities, so the output peaks of a gas laser will be broadened. The emission profile is expected to be a sharp peak, but because of the Doppler broadening it is actually a Gaussian.

Considering the Maxwell velocity distribution of the gas atoms in the laser tube, the output intensity of the linewidth between the half-intensity points (full width at half

maximum, FWHM) as a function of the frequency spectrum is given by

$$\Delta\nu = 2\nu_0\sqrt{\frac{2kTln\,(2)}{mc^2}} \tag{3.21}$$

where m is the mass of the lasing atom.

Although the gas emits radiation with a Gaussian lineshape, the laser cavity does not permit a continuous spread of frequencies to resonate. Only those frequencies that achieve constructive interference in the resonator will reach the threshold gain level (see Fig. 3.4). In many lasers, there are several modes whose wavelengths fall inside the gain curve; the output of these devices is a mix of frequencies. To get a long coherence length it is necessary to work with a single frequency, exciting only one mode.

There are two ways to force a conventional two-mirror laser to operate with a single longitudinal mode.

The first one is to design the laser with an enough short cavity, so that only a single mode can be sustained. This is not a practical approach for most gas lasers because a short cavity may produce an insufficient energy to sustain any lasing action at all, and if there is lasing, the output will be very low.

The second method is to introduce a frequency-control element, typically a low-finesse Fabry-Perot etalon, into the laser cavity. The etalon free spectral range should be several time the width of the gain curve, and the reflectivity of the surface should be sufficient to provide 10% or greater loss at frequencies half a longitudinal mode spacing away from the etalon peak. The etalon is mounted at a slight angle to the optical axis of other laser to prevent oscillations between the etalon surface and the laser cavity. Once the mode is selected, it is necassary to optimize and maintain its output power. Since the laser mode moves if the cavity length changes slightly, and the etalon pass-band shifts if the etalon spacing varies slightly, it is important that both are stabilized.

3.2 Gran Sasso laser interferometers

Since several years two Michelson-type laser interferometers, operating as geodetic extensometers, are working beside the Gran Sasso Tunnel (10.4 km long), at about 5 km from the East entrance of the highway connecting Rome to Teramo (Central Italy), and in proximity of an underground laboratory for Particle Physics and Astrophysics (INFN - Laboratori Nazionali del Gran Sasso). The instruments are located in right

Figure 3.5: Location and directions of the laser strainmeters operating at Gran Sasso.

angled galleries, more than 250 m aside from the highway, and at least 1100 m under the free surface.

Until 1999 one interferometer measured difference in extension between the two baselines in an equal-arm configuration.

Since summer 2000, two independent unequal-arm interferometers, about 90 meters in length, are monitoring extension along two orthogonal directions, whose azimuths are about N66E and N24W. The former baseline, referred to as BC, is approximately perpendicular to the local direction of the Apennines Chain, and the latter, referred to as BA, is approximately parallel to it (see Fig. 3.5).

These instruments share the same stabilized HeNe laser source; they are characterized by very high nominal sensitivity (picostrain level, 10^{-12}), wide frequency band, and large dynamic range, limited only by the capability of maintaining optical alignment. Their features allow to produce records with very high signal-to-noise (S/N) ratio in the free-oscillations frequency band [34] and for aperiodic signals ranging minutes to months, for example slow earthquakes, slow fault slip propagation, afterslips [35, 36, 37].

3.2.1 Instrumental set-up

The current operating instruments were developed on the basis of a previous instrument working in the same place from 1994 to 1999, with some electronic and optical improvements. The instruments are based on the classical unequal-arm Michelson set-up and compare the optical length of a longer measurement arm, about 90 meters in length, and a shorter fixed reference arm that is about 20 cm in length [36, 38, 39]. A detailed description of instruments is in Ref. [39].

Each interferometer measures the displacements between two $1\,m^3$ concrete blocks, setting on a $8\,m^3$ underground cubic platform and linked to it by steel bars, about 8 meter long, and separated from the floor through a 20 cm wide track. The optical components are attached to the concrete blocks. A vacuum system encloses the interferometer, it is decoupled from the end monuments and optical components by bellows. The vacuum system is made of stainless steel. It consists of a main chamber (80 cm in diameter) located over the principal monument, two terminal chambers (50 cm in diameter) located over the other two monuments, and two 90 meter long pipes, each one 3 meters long, that connect the terminal chambers. Vacuum is obtained with a pumping group, a roots pump and a rotary pump. A pressure level of about 10^{-2} Pa is reached and dynamically maintained.

A temperature controlled hut has been built around the monument where the laser and the electronics are kept. Temperature is maintained at $291 \pm 0.1\,K$. A continuous monitoring of air temperature and pressure inside the hut and in the tunnels is carried out by different sensors.

Fig. 3.6 shows a schematic view of optical set-up in the older configuration.

A collimated light beam, vertically polarized, from HeNe laser is deviated by an alignment mirror and arrives at a beam splitter, where it is separated equally moving toward two retroreflectors, along the reference and measurement arms, respectively. Each retroreflector consists of a combination of lens and mirror, namely *cat's eye*, which minimizes beam distortion and alignment problems, but overlaps the reflected and incident beams. The light beam, moving along the reference arm, reaches the cat's eye and is reflected back, passing twice through a transverse-field electro-optical phase modulator, while the transmitted part, moving along the measurement arm, is reflected back by the latter cat's eye.

The returned beams interfere again at the beam splitter and thenreach the detectors,

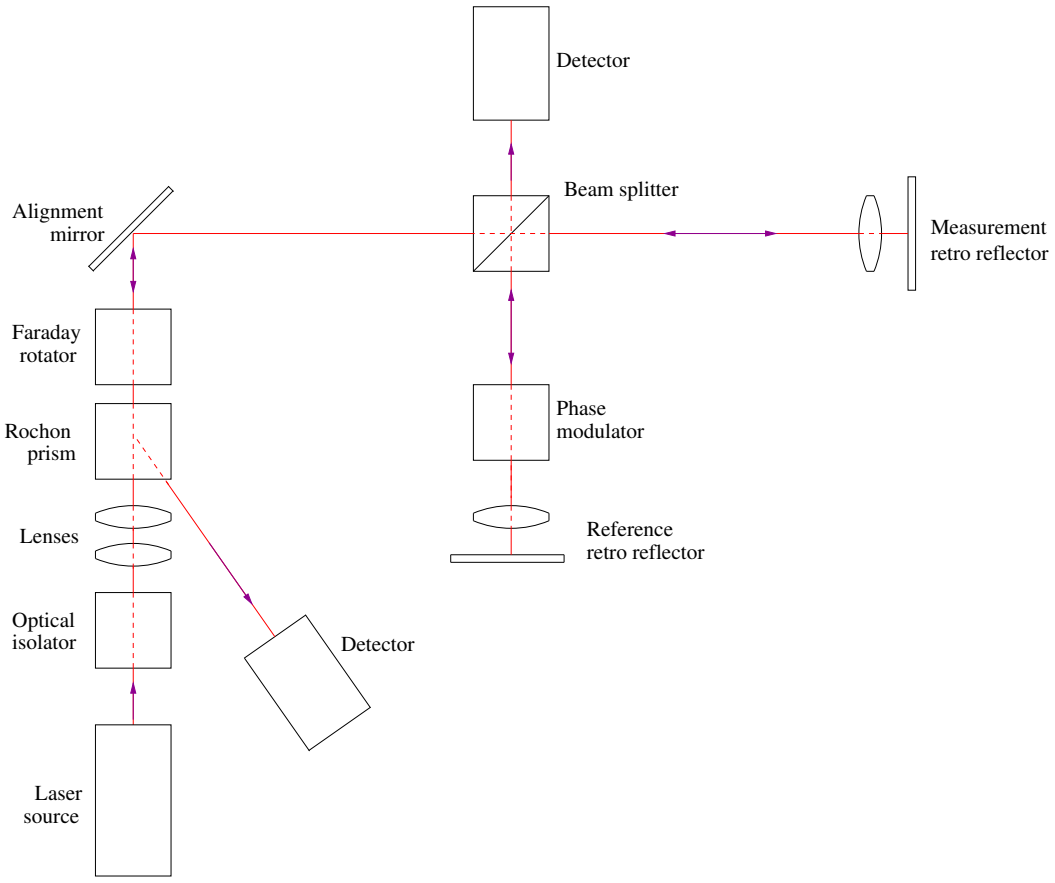

Figure 3.6: Optical set-up of each Gran Sasso interferometer.

giving two complementary outputs depending on the difference in length between the reference and measurements arms, ΔL. The output intensities are

$$I_1 = \frac{1}{2} I \left[1 + \cos\left(k\Delta L + \phi\right)\right] \tag{3.22}$$

$$I_2 = \frac{1}{2} I \left[1 - \cos\left(k\Delta L + \phi\right)\right] \tag{3.23}$$

where I is the total intensity of the laser beam, k is the wave number, and ϕ is a phase shift introduced by the optical components.

Since the incident and reflected beams are overlapped, it is necessary to separate again the two beams between the beam splitter and the laser. This is possible using an optical isolator, consisting of a Faraday rotator and two polarizers. In this way the light can be transmitted in the forward direction and its polarization plane is rotated by 45 degrees. The beam is then collimated through two lenses and arrives at a Rochon prism polarizer without deflections. A further Faraday rotator rotates the plane of polarization back by 45 degrees, making it vertical again.

One of the beam outputs is directly measured by a photodetector. The other one comes back through the Faraday rotator, with a total 90 degrees phase lag with respect the inizial polarization, and it is deviated by the Rochon prism polarizer by 10 degrees toward a second photodetector. The difference in light intensity between the output beams becomes the input signal for a control system acting on the optical length of the phase modulator in order to maintain a fixed phase delay around 45 degrees between the reference and measurement arms.

The reference arm includes an electro-optical phase modulator, consisting of an optically active crystal whose optical length depends on the electric field embedded in. The electric field is dynamically modulated by a feedback loop to stabilize the interference pattern between the laser beams propagating through the reference and measurement arms. The dynamic range of the instrument is limited by the maximum voltage acting on the phase modulator. To extend it, a reset circuit is included. It permits a change of the phase modulator optical length by $\pm\lambda$ each time that the path length difference ΔL reaches $\mp\lambda/2$.

Voltage applied to the phase modulator is sampled at 800 samples per second by a 12-bit analog-to-digital converter (ADC). Each datum consists of two numbers, the former related to the voltage applied to the phase modulator, and the latter related to the number of jumps since the acquisition started. Both sequences of numbers are

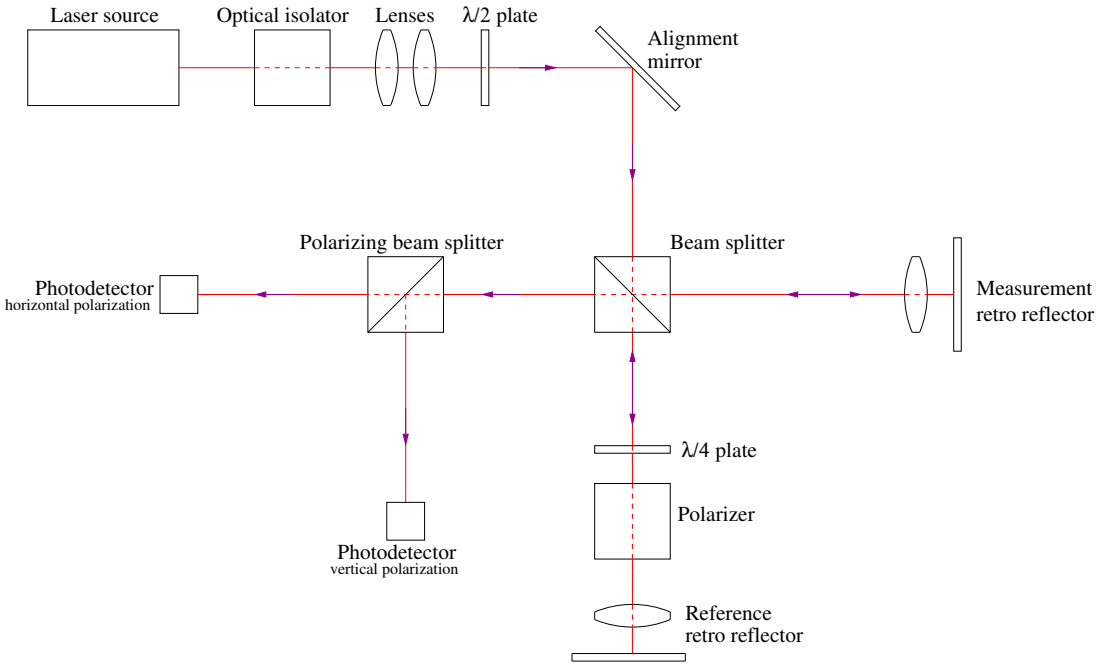

Figure 3.7: Current optical set-up of Gran Sasso interferometers.

digitally filtered using a linear non-recursive filter, decimated at 5 samples per second, and recorded.

This configuration was particularly useful in the past, when the storage of data was a difficult task, but it required expensive electro-optical components, a very accurate optical alignment and electronic adjustments, and an occasional careful data pre-analysis to correct for wrong jump counting.

Since February 2005 the electro-optical system has been simplified (see Fig. 3.7, Ref. [36] for details). The reference arm includes only a polarizer and a quarter-wave retarder plate; the Faraday rotators have been removed in the external optics. The new configuration gets two quadrature signals at one output for each interferometer, while the other output is no more used. Also electronics is now more simple, consisting only in what necessary to measure light intensity at the photodiodes.

As disadvantage, the phase is no more a linear function of the ADC output, which can not be simply low-passed and decimated before storage. The real time conversion from light intensity to phase is not possible, because instabilities of DC level and amplitude of the interference signal. Moreover the phase lag fluctuations between the quadrature signals require for non-linear fitting of the Lissajous figure given by few hours of quadrature data. The related Lissajous figure (see Fig. 3.8) can be inverted for changes

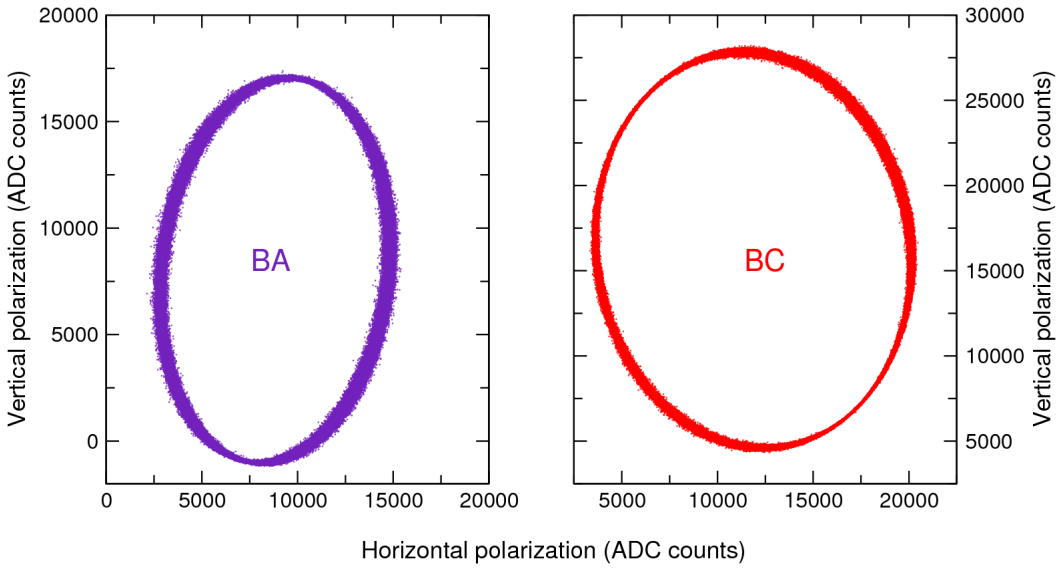

Figure 3.8: Scatter plot of 12 M samples recorded by the two interferometers.

in length of the 90-m long baseline and thus for strain. A baseline length change of $\lambda/2$ of the laser light (about 3.5×10^{-9} in strain) corresponds to a complete round along the ellipse, whose axis lengths and orientations slightly change with time. Photodiode's signals are sampled and stored at 600 samples per second, to avoid artificial mixing of frequencies due to the non-linear dependence of the light intensity on phase mismatch. Intensity-to-phase conversion is accomplished on stored signals when needed.

In this typical unequal-arm Michelson interferometer, measurement arm is much longer than the reference arm, so deformation related to the measurement arm and fractional changes in wavelength, or equivalently frequency, of the laser light are numerically equivalent.

Thus a change in the laser light wavenumber can not be distinguished from a change in the length of the measurement arm. If $\Delta l/l$ is the apparent difference in optical length between the measurement and reference arms, and f is the laser light frequency, then $\Delta l/l = \Delta f/f$. Laser frequency fluctuations can give spurious strain signals whose amplitude depends on the difference in length between the measurement and reference arms. These spurious wavelength fluctuations can be eliminated considering the difference between the two measured strains, since the two interferometers share the same laser source. This noise cancellation behavior implies that S/N ratio should be higher for measured deviatoric strain than for uniform horizontal expansion or contraction.

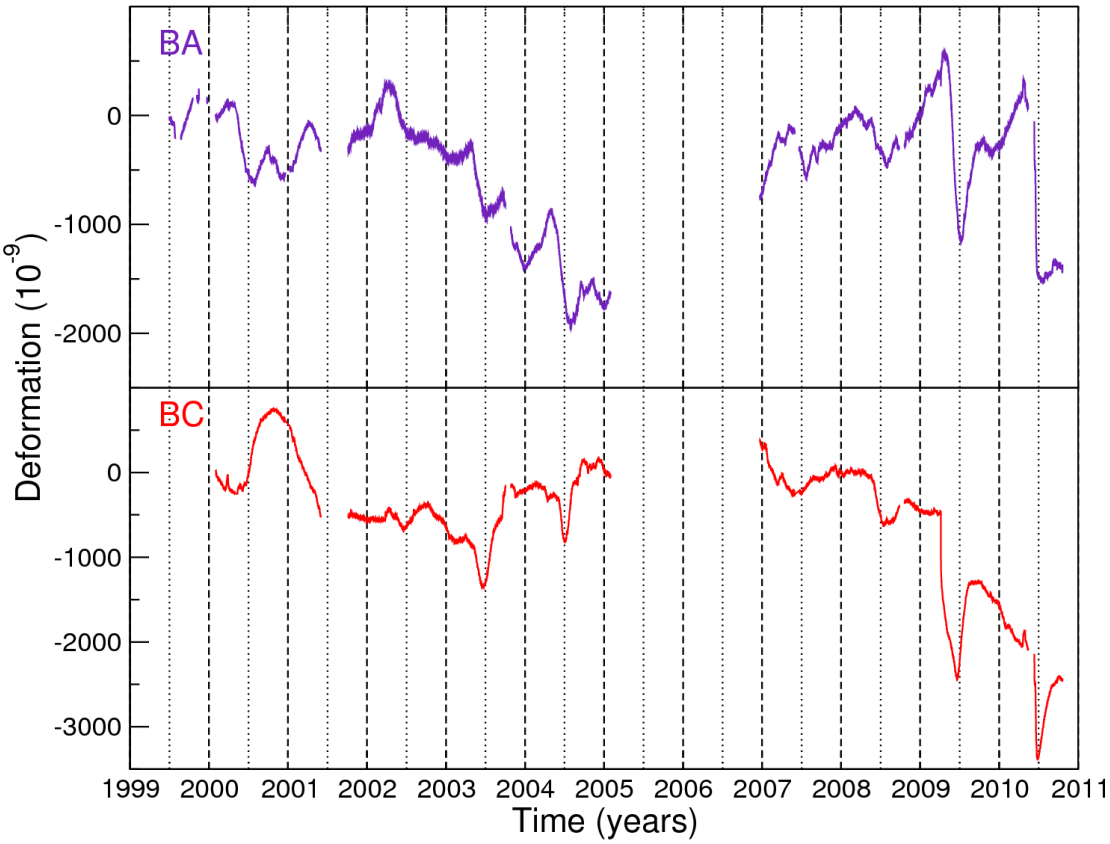

Figure 3.9: Strain data, decimated at 2 cycles per hour, recorded from 1999 to the second half of 2010 (upper plot, BA; lower plot, BC).

3.2.2 Available data

Available records at Gran Sasso from 1999 to the second half of 2010 are depicted in Fig. 3.9. A long break in data acquisition occurred since the beginning of 2005 for about two years, because of a major modification of the electro-optical set-up described above. Other shorter gaps are present in the records.

The instruments are still acquiring. Fig. 3.10 shows a typical set of raw data, recorded at the end of 2011. Earth tides are clearly visible in the records. As explained before, the difference between BA and BC signals deletes the spurious fluctuations due to laser.

A strain sequence, about 45 days in length, has been analysed to estimate the S/N level of the interferometers (see Fig. 3.11). For eliminating the contamination related to Earth tides, these ones have been removed by least-squares fitting a sum of sine and cosine functions of variable amplitude at different fixed frequency.

A segment of the detided sequence whose length is 7 days, characterized by the absence

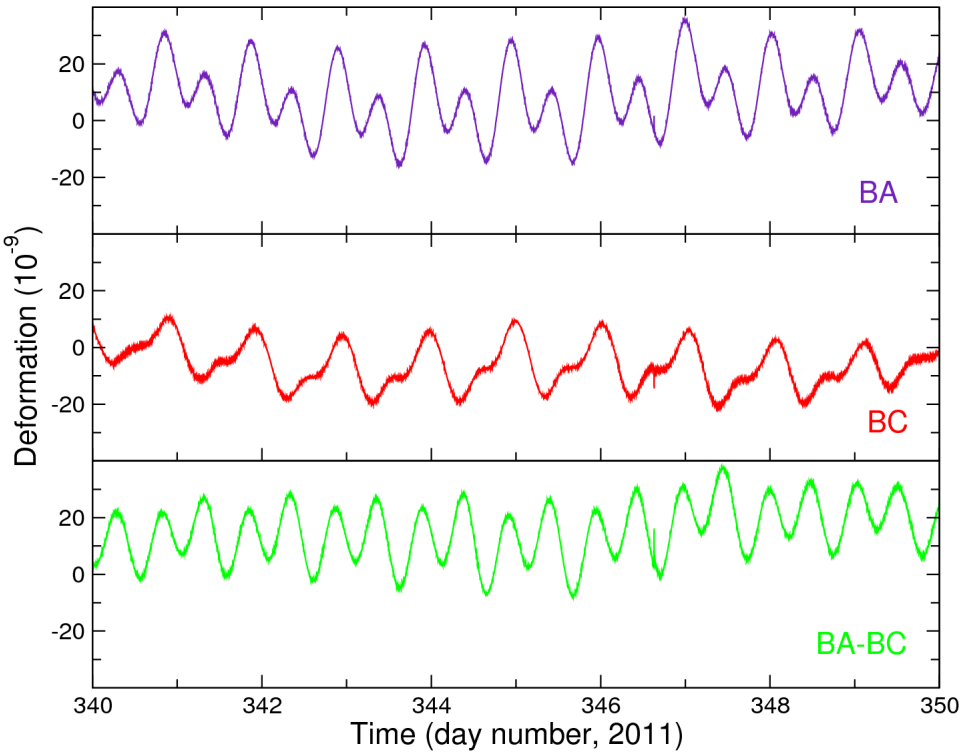

Figure 3.10: Ten-day-long strain signals recorded by the interferometers during 2009 (upper plot, BA; middle plot, BC) and difference between them (lower plot, BA-BC).

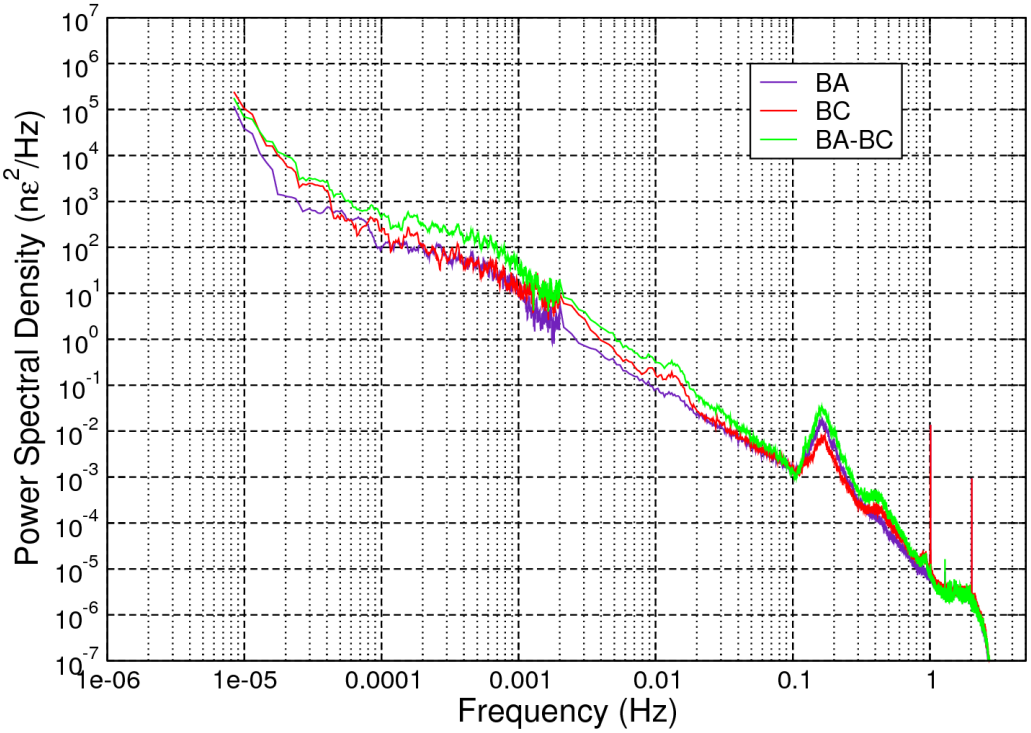

Figure 3.11: Power Spectral Density of Gran Sasso strain data (violet and red lines, BA and BC respectively) and their difference (green line, BA-BC).

of signals attributable to telesisms, anomalies, periodic or aperiodic phenomena, has been extracted and analysed to obtain the spectrum. The higher ($f > 0.002$ Hz) part of the spectrum has been obtained filtering data with a low-pass filter and decimating them at 10 samples per second. To compute the Power Spectral Density (PSD), BA and BC records have been broken into about 3300-sec-long 50%-overlapped windows, each window has been tapered with a cosine-bell taper, and finally an average of Fast Fourier Transforms (FFTs) on all the windows has been calculated. The lower part of spectrum has been obtained filtering data with a low-pass filter and decimating filtered data at 3 samples per minute, and calculating the FFT on an only one window, again 3300 sec in length, tapering with a cosine-bell taper.

In order to understand the effects of the laser wavelength fluctuations, also the spectrum of the difference between BA and BC has been calculated, showing that the noise level does not change substantially.

Comparing the noise level recorded at Gran Sasso with that obtained at Pinon Flat Observatory [40] in United States, Queensbury Tunnel [41] in United Kingdom and Kamioka [32] in Japan, it is possible to observe that at frequiencies lower than 10^{-4}

Hz spectra are comparable. At frequencies higher than 10^{-4} Hz the noise level at Gran Sasso is comparable with that shown in Ref. [41] but it is about two orders of magnitude larger than that shown in spectra in Ref. [40] and some orders of magnitude largerv than that in spectra in Ref. [32] between 10^{-3} and 10^{-1} Hz.

3.3 Strain data corrections, application to Gran Sasso records

Although the interferometer measures strain directly, local distortions, such as cavity effects due to tunnel installation, surface topography, and rock inhomogeneities, can bias strain measurements significantly. Siting effects can also produce coupling among the different strain components, so that locally measured strain is not equal to the large-scale Earth strain. Strain distortions can be estimated under the assumption that the scale of these effects is much smaller than the scale of the measured stress and strain perturbations.

3.3.1 Cavity and topographic effects and strain-cross coupling

Following the numerical modeling results in Ref. [42], cavity effects are expected to be small for the two interferometers, since they measure extension along the axis of tunnels and the distance between the end monuments and the tunnel end faces are more than one tunnel diameter. Though topographic effects (see Fig. 3.12) are expected to be small on BA (which is oriented parallel to the Apennines Chain) and decrease the measured strain from 20% to 40% on BC (which is oriented perpendicular to the Apennines).

Accurate estimations of local strain distortion can be obtained using known reference strains, such as those due to Earth tides, and a matrix representation of the relationship between instrument and remote strains (along x-axis, y-axis, and shear strain; for details see Ref. [43]). Given a (x, y) coordinate system, with the x-axis directed along the interfetometer and the y-axis directed perpendicular to it, local effects on the extension ε can be described by three coupling coefficients α, β, γ

$$\varepsilon = \alpha\varepsilon_{xx} + \beta\varepsilon_{yy} + \gamma\varepsilon_{xy} \tag{3.24}$$

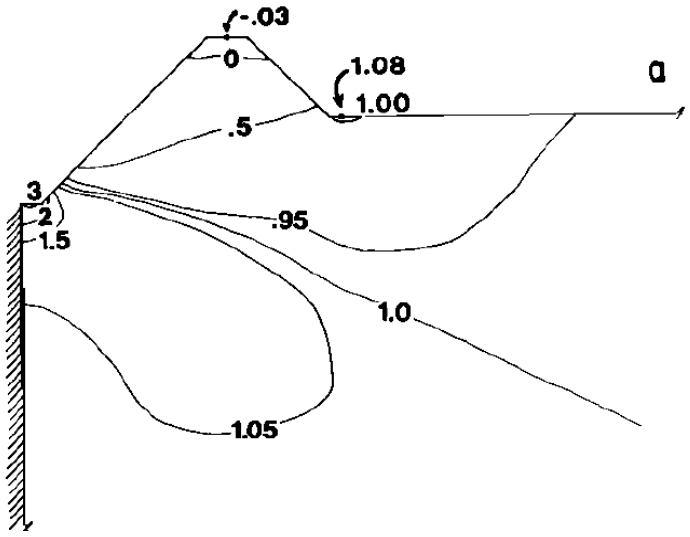

Figure 3.12: Effect of topography with 45 degrees slopes on the strain factor (ratio of the strain ε_{xx} and the strain produced in a uniform plate) measured near the Earth's surface. Figure from Ref. [42].

The three coupling coefficients assume different values for the extension along BA ($\varepsilon_{\mathrm{BA}}$) and BC ($\varepsilon_{BC}$).

Introducing a second coordinate system (x',y'), rotated by 45 degrees from (x,y), the shear strain ε_{xy} can be expressed as a function of normal strain components in the new coordinate system, that is

$$\varepsilon_{xy} = \frac{1}{2}\left(\varepsilon_{x'x'} - \varepsilon_{y'y'}\right) \tag{3.25}$$

and thus

$$\varepsilon = \alpha\varepsilon(\eta) + \beta\varepsilon(\eta) - \frac{1}{2}\gamma\left[\varepsilon\left(\eta - 45^{\circ}\right) - \varepsilon\left(\eta - 135^{\circ}\right)\right] \tag{3.26}$$

In particular for BA and BC interferometers

$$\varepsilon_{BA} = \alpha_{BA}\varepsilon(\eta_{BC}) + \beta_{BA}\varepsilon(\eta_{BA}) - \frac{1}{2}\gamma_{BA}\left[\varepsilon\left(\eta_{BC} + 45^{\circ}\right) - \varepsilon\left(\eta_{BA} + 45^{\circ}\right)\right] \tag{3.27}$$

$$\varepsilon_{BC} = \alpha_{BC}\varepsilon(\eta_{BC}) + \beta_{BC}\varepsilon(\eta_{BA}) - \frac{1}{2}\gamma_{BC}\left[\varepsilon\left(\eta_{BC} + 45^{\circ}\right) - \varepsilon\left(\eta_{BA} + 45^{\circ}\right)\right] \tag{3.28}$$

where $\eta_{BC} = 66^{\circ}$ and $\eta_{BA} = -24^{\circ}$ are the azimuthal directions of BC and BA.

Following [34], to estimate the coupling coefficients for BA and BC, a least-square fitting technique has been used, by comparing predicted and observed amplitudes and phases of the larger tides out of the Free Core Resonance range (see Chapter 4 for details), namely Q_1, O_1, N_2, M_2, and K_2, without including S_2 because of possible contamination

	α	β	γ
BA	0.92601	-0.00508	0.18771
BC	0.70067	-0.01437	0.04676

Table 3.1: Coupling coefficients for BA and BC obtained using continental Gutenberg-Bullen Earth model and global TPXO7.2 ocean model, integrated by local Mediterranean Sea model.

from air pressure effects. The fit thus involves ten equations (five cosine and five sine amplitudes) and three unknown coupling coefficients for each interferometer.

Following this procedure, cross coupling of shear strain (γ in Eq. 3.24) is about 20% for BA and 5% for BC, and cross coupling of the direction perpendicular to the baseline (β in Eq. 3.24) about 1% for both Gran Sasso interferometers. Because of local effects, extension decreases by about 7% for BA and 30% for BC. These results are consistent with what expected on the basis of the numerical modeling results from Ref. [42]. Retrieved values of coupling coefficients (see Table 3.1) differ by a few percent when considering different Earth and Ocean model combinations, mainly due to a small ocean loading contribution to strain Earth tides at Gran Sasso, as will be shown later.

3.3.2 Environmental effects

Strain data are affected by the ground deformation induced by environmental effects, like temperature and pressure fluctuations. This problem can be particularly remarkable when looking for signals periodic around 24 hours.

The unusual depth of the Gran Sasso station largely reduces contamination caused by atmospheric effects. Some sensors of temperature and barometric pressure, placed at different points of the interferometers, are available at Gran Sasso. Actually only air temperature inside the tunnel (T_{gal}, see Fig. 3.13) appears to affect strain around 1 cycle per day. Air temperature records span little more than one year, and fluctuate by about 1 °C and few 10^{-2} °C on monthly and daily time scales respectively. Even if the rock temperature is not monitored, its fluctuations can be expected much lower than air temperature ones.

Pressure (see Fig. 3.14) records span about six years.

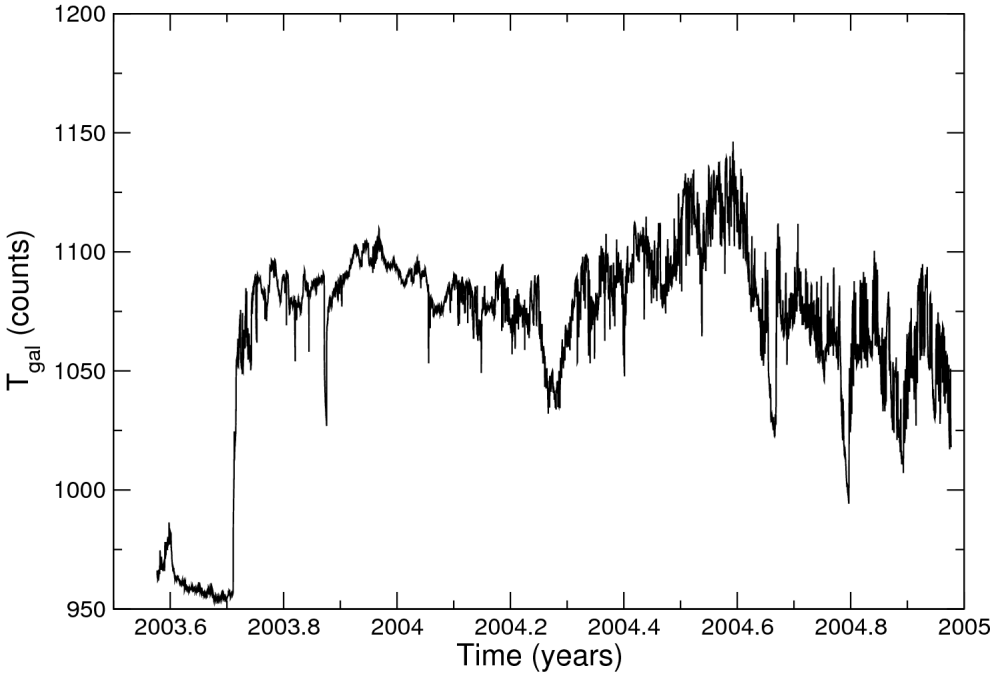

Figure 3.13: Air temperature (counts), decimated at 2 cycles per hour, recorded inside the tunnel.

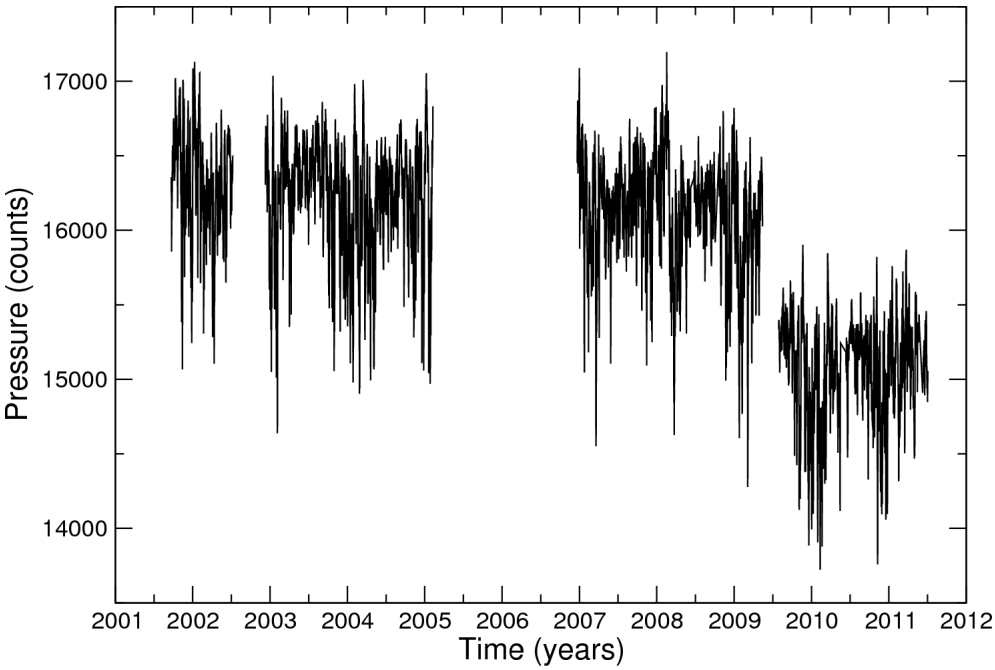

Figure 3.14: Pressure (counts), decimated at 2 cycles per hour, recorded inside the tunnel at node C.

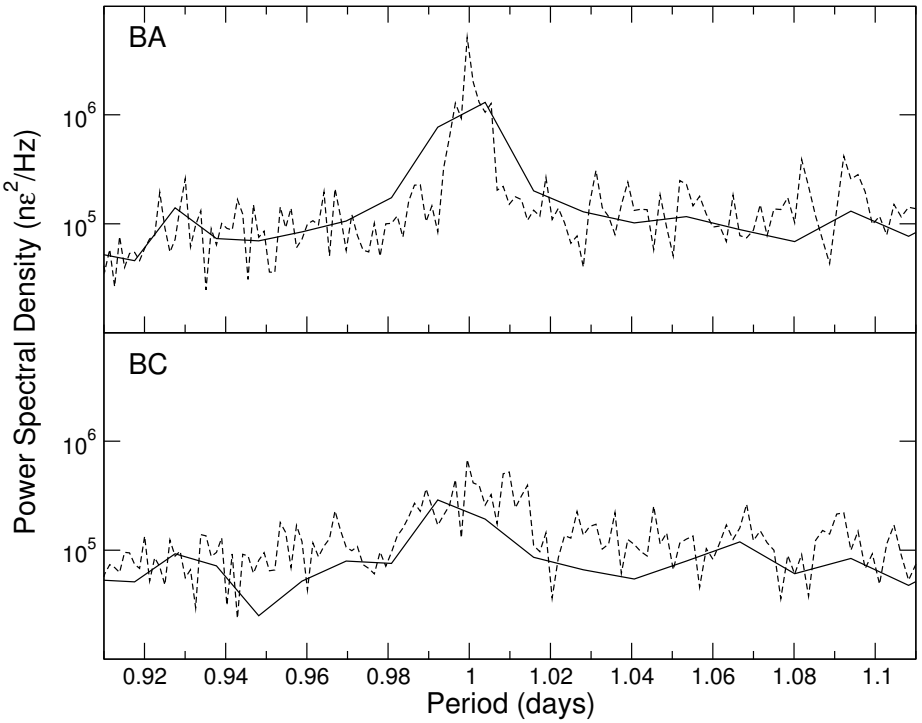

Figure 3.15: PSD of recorded data in the diurnal tidal band (upper plot, BA; lower plot, BC). Solid lines, PSDs obtained with an about 85-day-long moving window; dashed lines, PSDs obtained with an about 680-day-long moving window.

Several attempts to correct strain data for environmental effects have been carried out, according to what has already been published in Ref. [45].

PSD of recorded data in the diurnal tidal band (see Fig. 3.15) shows a broad peak around 1 cycle per day, mainly evident for BA. Its presence is probably attributable to a combination of environmental effects (temperature and barometric pressure) and anthropic activities. Although environmental effects are expected to be very similar for both BA and BC, anthropic activities are particularly considerable near one of the BA end monuments, because of the presence of other experiments. This asymmetry suggests that only the low peak visible in the BC spectrum might be actually related to environmental effects.

Because of the presence of the gaps, FFT is not appropriate for estimating the noise level at any frequency. Since deformation noise is red (i.e. its power spectral density increases as frequency decreases) while most fitting techniques assume a gaussian residual distribution, characterized by a white spectrum, in the following always pre-whitened sequences (see Ref. [44] for details) are used. They are obtained by first-differencing

ungapped data segments, that is

$$y'_i = y_{i+1} - y_i \qquad t'_i = \frac{t_{i+1} + t_i}{2} \tag{3.29}$$

where y_i and t_i refer to raw data and y'_i and t'_i to pre-whitened data.

Spectra have been obtained using the following procedure, as done in Ref. [45]:

- ✓ filtering of the ungapped pre-whitened segments using a low-pass filter;
- ✓ decimation of the filtered ungapped pre-whitened segments at 2 cycles per hour (i. e. sampling interval is 1800 s);
- ✓ analysis of the decimated records using VAV03 code [46] (see Appendix A) and generation of the residuals removing the tidal harmonics;
- ✓ removal of the largest spikes from the residuals;
- ✓ computation of the power spectral density breaking each ungapped residual segment into about 85-day-long 50%-overlapped windows, tapering each window with a cosine-bell taper, and finally averaging FFTs of all the windows.

Several attempts to correct strain for temperature and pressure effects have been performed. First VAV03 results from a joint analysis of strain and one environmental sequence and those obtained analysing strain only have been compared. The same strain data are used with or without the environmental sequence. Also the residual spectra obtained following the previously outlined procedure, but using an about 170-day-long moving window are compared. Fig. 3.16 shows PSD in the diurnal tidal band, with and without temperature corrections. The strain series are as long as the temperature sequence (about 500 and 480 days, for BA and BC respectively). The noise level in the diurnal band does not lower; indeed for BC it increases around 1 cycle per day.

Also taking pressure into account, the strain noise level does not lower for both BA and BC interferometers (see Fig. 3.17).

Other attempts to correct strain have been performed using Baytap08 [47] (see Appendix B). Tables 3.2 to 3.5 show the results obtained through a joint analysis of pre-whitened strain and one environmental sequence with those obtained analysing strain only. Also in this case, the same strain data are used with or without the environmental sequence. The measured-to-theoretical S1 amplitude ratio decreases from 4.6 to 3.6 for

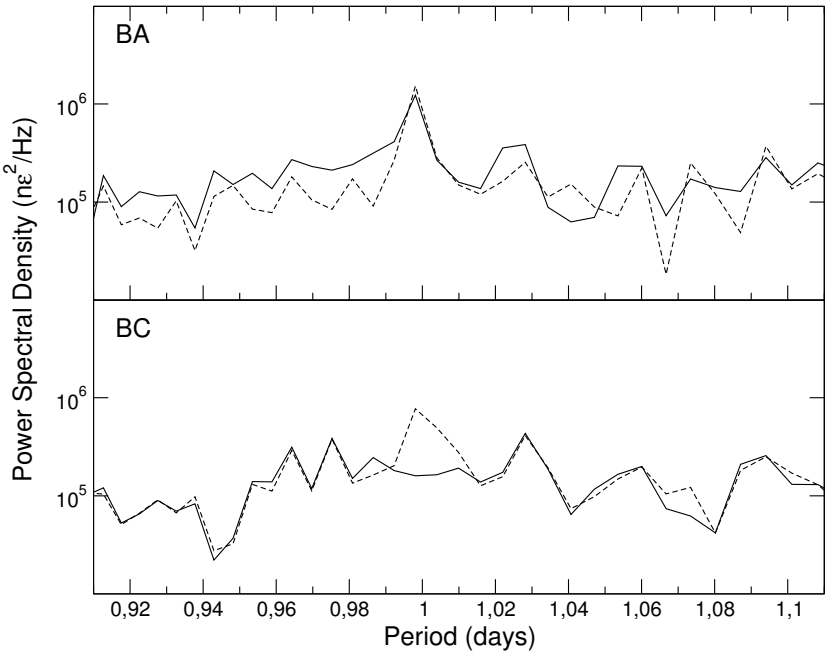

Figure 3.16: PSD in the diurnal tidal band, with and without temperature corrections (upper plot, BA; lower plot, BC). Solid and dashed lines, VAV03 residuals of strain series without and with temperature corrections respectively.

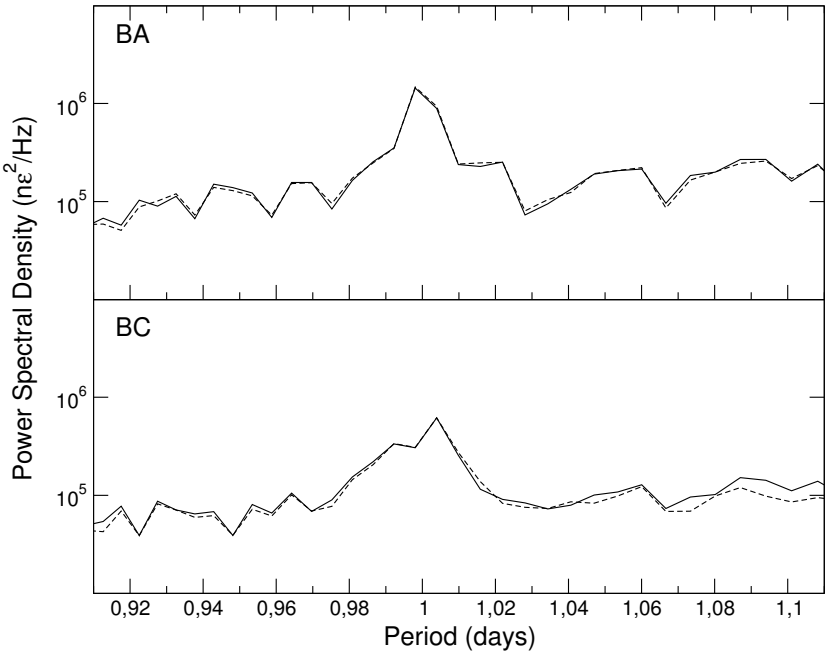

Figure 3.17: PSD in the diurnal tidal band, with and without pressure corrections (upper plot, BA; lower plot, BC). Solid and dashed lines, VAV03 residuals of strain series without and with pressure corrections respectively.

BA and increases from 1.2 to 1.4 for BC when taking temperature into account. It does not change for BA and increases from 0.8 to 1.0 when taking pressure into account. Moreover in general the noise level in the diurnal band does not lower.

	grp		symbol	factor	rmse	phase (local, lags negative)	rmse	amplitude	rmse
>	1	1-143:	Q1	0.12163	0.00960	97.188	4.522	0.112	0.009
>	2	144-201:	O1	0.11517	0.00176	89.992	0.875	0.556	0.008
>	3	202-249:	M1	0.09014	0.02437	100.573	15.489	0.034	0.009
>	4	250-266:	P1	0.10990	0.00407	92.618	2.125	0.247	0.009
>	5	267-270:	S1	4.57602	0.25260	110.315	3.174	0.243	0.013
>	6	271-305:	K1	0.08754	0.00122	84.888	0.801	0.595	0.008
>	7	306-345:	J1	0.13137	0.02003	87.666	8.723	0.050	0.008
>	8	346-450:	OO1	0.18528	0.02487	96.780	7.690	0.038	0.005
>	9	451-549:	2N2	0.22781	0.01420	105.744	3.569	0.063	0.004
>	10	550-599:	N2	0.23343	0.00289	97.346	0.710	0.488	0.006
>	11	600-655:	M2	0.24577	0.00054	98.677	0.126	2.685	0.006
>	12	656-681:	L2	0.28269	0.01357	99.936	2.750	0.087	0.004
>	13	682-710:	S2	0.25004	0.00112	97.868	0.257	1.271	0.006
>	14	711-827:	K2	0.25518	0.00333	100.751	0.747	0.353	0.005
>	15	828-909:	M3	0.28853	0.09100	131.054	18.070	0.017	0.005

---

	grp		symbol	factor	rmse	phase (local, lags negative)	rmse	amplitude	rmse
>	1	1-143:	Q1	0.12467	0.00487	96.736	2.237	0.115	0.004
>	2	144-201:	O1	0.11608	0.00094	89.809	0.466	0.561	0.005
>	3	202-249:	M1	0.10703	0.01377	102.571	7.375	0.041	0.005
>	4	250-266:	P1	0.11226	0.00240	88.528	1.224	0.252	0.005
>	5	267-270:	S1	3.62466	0.14946	94.104	2.378	0.192	0.008
>	6	271-305:	K1	0.09086	0.00073	86.114	0.457	0.617	0.005
>	7	306-345:	J1	0.13818	0.01236	86.685	5.122	0.052	0.005
>	8	346-450:	OO1	0.20210	0.01598	88.764	4.530	0.042	0.003
>	9	451-549:	2N2	0.21038	0.01275	107.131	3.475	0.058	0.004
>	10	550-599:	N2	0.22938	0.00261	98.051	0.652	0.480	0.005
>	11	600-655:	M2	0.24551	0.00049	98.594	0.115	2.682	0.005
>	12	656-681:	L2	0.27081	0.01235	102.024	2.612	0.084	0.004
>	13	682-710:	S2	0.25311	0.00102	97.565	0.232	1.286	0.005
>	14	711-827:	K2	0.25704	0.00304	100.201	0.677	0.355	0.004
>	15	828-909:	M3	0.31983	0.08636	138.376	15.471	0.019	0.005

Table 3.2: Tidal factors, amplitudes, phases, and corresponding errors obtained analysing pre-whitened BA strain data without (upper plot) and with (lower plot) temperature corrections by Baytap08.

	grp		symbol	factor	rmse	phase (local, lags negative)	rmse	amplitude	rmse
>	1	1-143:	Q1	0.07231	0.00370	87.169	2.943	0.091	0.005
>	2	144-201:	O1	0.08639	0.00072	89.130	0.475	0.566	0.005
>	3	202-249:	M1	0.09185	0.01079	98.736	6.729	0.047	0.006
>	4	250-266:	P1	0.09446	0.00179	90.758	1.086	0.288	0.005
>	5	267-270:	S1	1.24731	0.11110	11.969	5.085	0.090	0.008
>	6	271-305:	K1	0.07593	0.00054	92.639	0.408	0.700	0.005
>	7	306-345:	J1	0.11464	0.00925	89.128	4.620	0.059	0.005
>	8	346-450:	OO1	0.13989	0.01208	79.560	4.943	0.039	0.003
>	9	451-549:	2N2	0.17412	0.02675	73.932	8.801	0.023	0.004
>	10	550-599:	N2	0.16249	0.00546	88.412	1.925	0.163	0.005
>	11	600-655:	M2	0.17032	0.00102	86.850	0.344	0.895	0.005
>	12	656-681:	L2	0.22924	0.02335	76.017	5.838	0.034	0.003
>	13	682-710:	S2	0.19695	0.00213	71.963	0.619	0.481	0.005
>	14	711-827:	K2	0.19052	0.00631	81.327	1.897	0.127	0.004
>	15	828-909:	M3	0.21351	0.17208	131.552	46.179	0.006	0.005

---

	grp		symbol	factor	rmse	phase (local, lags negative)	rmse	amplitude	rmse
>	1	1-143:	Q1	0.07273	0.00364	87.043	2.878	0.091	0.005
>	2	144-201:	O1	0.08652	0.00070	89.038	0.466	0.567	0.005
>	3	202-249:	M1	0.09521	0.01061	98.369	6.385	0.049	0.005
>	4	250-266:	P1	0.09382	0.00176	89.842	1.076	0.286	0.005
>	5	267-270:	S1	1.38461	0.10946	0.499	4.522	0.100	0.008
>	6	271-305:	K1	0.07673	0.00053	92.525	0.397	0.708	0.005
>	7	306-345:	J1	0.11550	0.00909	88.875	4.511	0.060	0.005
>	8	346-450:	OO1	0.14143	0.01188	77.196	4.810	0.040	0.003
>	9	451-549:	2N2	0.17190	0.02631	70.598	8.769	0.023	0.004
>	10	550-599:	N2	0.16028	0.00537	87.932	1.919	0.161	0.005
>	11	600-655:	M2	0.17050	0.00101	86.784	0.338	0.896	0.005
>	12	656-681:	L2	0.22284	0.02297	75.149	5.906	0.033	0.003
>	13	682-710:	S2	0.19789	0.00209	72.462	0.606	0.484	0.005
>	14	711-827:	K2	0.19242	0.00620	81.637	1.847	0.128	0.004
>	15	828-909:	M3	0.19785	0.16926	139.359	49.015	0.006	0.005

Table 3.3: Tidal factors, amplitudes, phases, and corresponding errors obtained analysing pre-whitened BC strain data without (upper plot) and with (lower plot) temperature corrections by Baytap08.

	grp		symbol	factor	rmse	phase (local, lags negative)	rmse	amplitude	rmse
>	1	1-143:	Q1	0.11812	0.00567	88.429	2.751	0.109	0.005
>	2	144-201:	O1	0.11658	0.00104	89.286	0.513	0.563	0.005
>	3	202-249:	M1	0.11708	0.01225	90.770	5.986	0.044	0.005
>	4	250-256:	Pi1	0.19245	0.03897	123.556	11.603	0.025	0.005
>	5	257-266:	P1	0.11196	0.00230	83.797	1.179	0.252	0.005
>	6	267-270:	S1	3.22754	0.13960	111.041	2.483	0.171	0.007
>	7	271-288:	K1	0.09020	0.00069	85.021	0.441	0.613	0.005
>	8	289-292:	Psi1	0.18926	0.09325	85.788	28.212	0.010	0.005
>	9	293-305:	Phi1	0.18908	0.05350	82.784	16.218	0.018	0.005
>	10	306-345:	J1	0.13440	0.01084	87.017	4.620	0.051	0.004
>	11	346-450:	OO1	0.14096	0.01351	89.283	5.490	0.029	0.003
>	12	451-549:	2N2	0.22225	0.00531	104.045	1.368	0.061	0.001
>	13	550-599:	N2	0.23662	0.00108	98.906	0.262	0.495	0.002
>	14	600-655:	M2	0.24501	0.00021	98.708	0.048	2.677	0.002
>	15	656-663:	Lambda2	0.25174	0.02776	88.835	6.318	0.020	0.002
>	16	664-681:	L2	0.26374	0.00652	99.655	1.416	0.081	0.002
>	17	682-701:	T2	0.22498	0.00729	85.830	1.857	0.067	0.002
>	18	702-710:	S2	0.25067	0.00043	97.587	0.098	1.274	0.002
>	19	711-827:	K2	0.25681	0.00128	99.475	0.286	0.355	0.002
>	20	828-909:	M3	0.20008	0.03131	138.936	8.968	0.012	0.002

---

	grp		symbol	factor	rmse	phase (local, lags negative)	rmse	amplitude	rmse
>	1	1-143:	Q1	0.11833	0.00566	88.301	2.742	0.109	0.005
>	2	144-201:	O1	0.11657	0.00104	89.288	0.512	0.563	0.005
>	3	202-249:	M1	0.11657	0.01223	90.838	6.002	0.044	0.005
>	4	250-256:	Pi1	0.19269	0.03891	122.668	11.569	0.025	0.005
>	5	257-266:	P1	0.11195	0.00230	83.914	1.177	0.252	0.005
>	6	267-270:	S1	3.28755	0.13946	109.745	2.434	0.174	0.007
>	7	271-288:	K1	0.09022	0.00069	85.022	0.440	0.613	0.005
>	8	289-292:	Psi1	0.18020	0.09310	84.362	29.584	0.010	0.005
>	9	293-305:	Phi1	0.18820	0.05342	80.569	16.267	0.018	0.005
>	10	306-345:	J1	0.13399	0.01082	87.137	4.626	0.051	0.004
>	11	346-450:	OO1	0.14084	0.01349	89.300	5.486	0.029	0.003
>	12	451-549:	2N2	0.22211	0.00530	103.956	1.366	0.061	0.001
>	13	550-599:	N2	0.23660	0.00108	98.925	0.262	0.495	0.002
>	14	600-655:	M2	0.24505	0.00021	98.700	0.048	2.677	0.002
>	15	656-663:	Lambda2	0.25308	0.02771	88.713	6.273	0.020	0.002
>	16	664-681:	L2	0.26378	0.00651	99.568	1.414	0.081	0.002
>	17	682-701:	T2	0.22287	0.00728	86.662	1.872	0.066	0.002
>	18	702-710:	S2	0.25275	0.00044	97.788	0.099	1.285	0.002
>	19	711-827:	K2	0.25745	0.00128	99.470	0.285	0.356	0.002
>	20	828-909:	M3	0.20190	0.03126	138.844	8.872	0.012	0.002

Table 3.4: Tidal factors, amplitudes, phases, and corresponding errors obtained analysing pre-whitened BA strain data without (upper plot) and with (lower plot) pressure corrections by Baytap08.

	grp	symbol	factor	rmse	phase (local, lags negative)	rmse	amplitude	rmse
>	1	1-143: Q1	0.07465	0.00228	87.605	1.751	0.094	0.003
>	2	144-201: O1	0.08532	0.00043	88.849	0.286	0.559	0.003
>	3	202-249: M1	0.09199	0.00510	94.264	3.175	0.047	0.003
>	4	250-256: Pi1	0.10926	0.01641	97.976	8.607	0.019	0.003
>	5	257-266: P1	0.08334	0.00097	88.169	0.668	0.254	0.003
>	6	267-270: S1	0.83021	0.05915	26.159	4.077	0.060	0.004
>	7	271-288: K1	0.07553	0.00029	92.180	0.223	0.697	0.003
>	8	289-292: Psi1	0.16308	0.03953	92.770	13.878	0.012	0.003
>	9	293-305: Phi1	0.06914	0.02267	103.976	18.801	0.009	0.003
>	10	306-345: J1	0.10180	0.00467	85.906	2.627	0.052	0.002
>	11	346-450: OO1	0.10348	0.00594	80.002	3.285	0.029	0.002
>	12	451-549: 2N2	0.13559	0.00912	86.174	3.853	0.018	0.001
>	13	550-599: N2	0.15565	0.00187	89.059	0.688	0.157	0.002
>	14	600-655: M2	0.16913	0.00036	87.703	0.123	0.888	0.002
>	15	656-663: Lambda2	0.15218	0.04886	86.645	18.396	0.006	0.002
>	16	664-681: L2	0.20944	0.01102	81.939	3.014	0.031	0.002
>	17	682-701: T2	0.20202	0.01296	77.337	3.676	0.029	0.002
>	18	702-710: S2	0.19812	0.00076	71.791	0.220	0.484	0.002
>	19	711-827: K2	0.18919	0.00228	78.626	0.691	0.126	0.002
>	20	828-909: M3	0.48701	0.05838	99.175	6.868	0.014	0.002

---

	grp	symbol	factor	rmse	phase (local, lags negative)	rmse	amplitude	rmse
>	1	1-143: Q1	0.07503	0.00225	87.243	1.719	0.094	0.003
>	2	144-201: O1	0.08530	0.00042	88.855	0.282	0.559	0.003
>	3	202-249: M1	0.09075	0.00503	94.634	3.175	0.047	0.003
>	4	250-256: Pi1	0.10840	0.01619	95.755	8.560	0.019	0.003
>	5	257-266: P1	0.08347	0.00096	88.349	0.658	0.255	0.003
>	6	267-270: S1	1.03679	0.05847	27.089	3.224	0.075	0.004
>	7	271-288: K1	0.07562	0.00029	92.199	0.220	0.697	0.003
>	8	289-292: Psi1	0.13588	0.03900	95.321	16.433	0.010	0.003
>	9	293-305: Phi1	0.05688	0.02237	98.706	22.550	0.007	0.003
>	10	306-345: J1	0.10154	0.00460	86.195	2.599	0.052	0.002
>	11	346-450: OO1	0.10308	0.00586	80.524	3.253	0.029	0.002
>	12	451-549: 2N2	0.13739	0.00899	85.708	3.751	0.018	0.001
>	13	550-599: N2	0.15526	0.00184	89.106	0.680	0.156	0.002
>	14	600-655: M2	0.16941	0.00036	87.765	0.121	0.890	0.002
>	15	656-663: Lambda2	0.15644	0.04819	87.921	17.653	0.006	0.002
>	16	664-681: L2	0.21097	0.01087	81.602	2.952	0.031	0.002
>	17	682-701: T2	0.18023	0.01279	77.457	4.065	0.026	0.002
>	18	702-710: S2	0.19405	0.00076	75.419	0.235	0.474	0.002
>	19	711-827: K2	0.18946	0.00225	79.967	0.682	0.126	0.001
>	20	828-909: M3	0.48901	0.05759	100.481	6.747	0.015	0.002

Table 3.5: Tidal factors, amplitudes, phases, and corresponding errors obtained analysing pre-whitened BC strain data without (upper plot) and with (lower plot) pressure corrections by Baytap08.

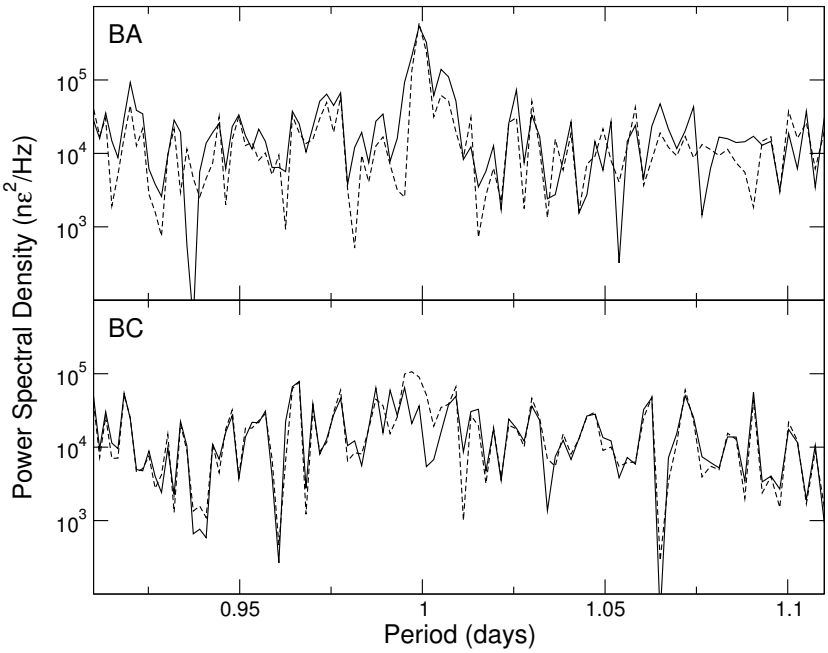

Figure 3.18: PSD in the diurnal tidal band obtained using LSSA, with and without temperature corrections (upper plot, BA; lower plot, BC). Solid and dashed lines, VAV03 residuals of strain series without and with temperature corrections respectively.

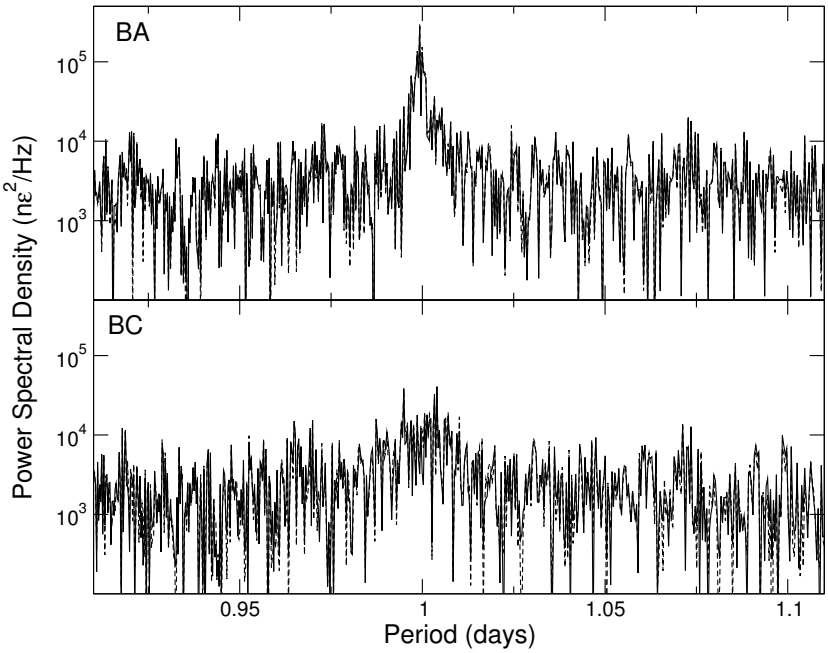

Figure 3.19: PSD in the diurnal tidal band obtained using LSSA, with and without pressure corrections (upper plot, BA; lower plot, BC). Solid and dashed lines, VAV03 residuals of strain series without and with pressure corrections respectively.

Also the analyses of residuals with LSSA [48] (see Appendix C) show that taking or not environmental sequences into account the average noise level does not lower (see Figs. 3.18 and 3.19).

At last it is not necessary to correct strain records for temperature and pressure fluctuations, at least when performing analysis of Gran Sasso strain data within the diurnal tidal band.

3.4 Conclusions

Since their installation, the laser interferometers at Gran Sasso produced very interesting results as regards for example the slow earthquakes, detecting the diffusive character of the rupture propagation; the free oscillations of the Earth, producing clear records of the long-period toroidal free oscillations excited by the 2004 December 26 Sumatra-Andaman earthquake; the constraints on earthquake nucleation processes analysing the strain recorded before and after the 2009 L'Aquila earthquake; and more recently the estimate of Free Core Nutation parameters.

Even if these instruments give high-sensitivity strain data, the analyses of strain records can be performed after correcting measured strain for local distortion of the regional strain field, such as cavity effects due to tunnel installation, surface topography, and inhomogeneities in the medium.

Tidal strain processing includes correction for local strain distortions, such as cavity effects, surface topography, and rock inhomogeneities.

Cavity effects are expected to be small on both Gran Sasso interferometers, since they measure extension along the axis of two tunnels and the distance between the end-monuments and the tunnel end faces are more than one tunnel diameter.

Topographic effects are expected to be small on BA, parallel to the local trend of the Apennines mountain chain, but as large as 20-40% on BC, perpendicular to it. The siting effects produce coupling among the different strain components, so that measured strain is not equal to the large-scale Earth strain.

Local distortion of strain field is estimated using reference tidal strains and a matrix representation of the relationship between instrument and remote strains, and in particular through three coupling coefficient, different for each interferometer and obtained by best-fitting between observed and predicted tides.

Retrieved values of coupling coefficients differ by a few percent when considering different Earth and Ocean model combinations, mainly due to a small ocean loading contribution to strain Earth tides at Gran Sasso, as will be shown later.

It is also important to introduce, if necessary, corrections for possible environmental (temperature and barometric pressure) effects and anomalous signals, for example of anthropic nature.

Analysing the Gran Sasso strain data by using different codes, it seems does not necessary to correct strain records for temperature and pressure fluctuations, since any attempt to correct data does not lower the S/N ratio in the diurnal tidal band, which is interesting for the following investigation of the Free Core Nutation.

Chapter 4

Free Core Resonance parameters from Gran Sasso strain data

The Free Core Nutation (FCN) is a rotational eigenmode arising from the dynamic influence of the rotating fluid outer core and the rotating, elastic and elliptical mantle. It induces a resonance (namely Free Core Resonance, FCR) in the diurnal tidal band which appears in addition to the well-known Chandler Wobble.

Most of the experimental studies to observe the existence of this mode are based on the analysis of two different techniques: the first one is from the analysis of tidal gravimetry, the other one using the Very Long Baseline Interferometry (VLBI) technique.

Gravity data allow to estimate the amplitude and phase of some diurnal tides, perturbed by the resonance process because their frequency is in the vicinity of the eigenfrequency. VLBI allows to measure changes in the Earth orientation. From orientation parameters of the Earth, the nutations can be determined, and from the nutation coefficients it is possible to investigate the FCN.

Few studies rely on tidal strain data. One of these, here detailed, is carried out at first using strain records from the laser interferometers operating at the Gran Sasso [45, 49] and then from a joint analysis of these data with about six years of strain recorded discontinuously by an extensometer installed in the Baksan Underground Observatory (Russia) [50].

The values for the period of the FCN, obtained analysing Gran Sasso strain data only or combined with Baksan ones, are robust and comparable to those from gravity tides,

obtained from the joint inversion of data from several stations. The quality factor is not well constrained because of the large uncertainty on the Ψ_1 phase; however its values are consistent with recently published values (≈ 20000). The agreement between observations and predictions looks better than in any previous work that makes use of strain tides.

4.1 Free Core Nutation

The luni-solar tidal potential produces changes of gravity associated with Earth deformations. In this context, the study of the Free Core Nutation (FCN, for a general introduction on tidal phenomena see Ref. [51]), detectable in addition to the Chandler Wobble (due to slightly misalignment of the rotation axes of the mantle and core) is very interesting.

The harmonics of the luni-solar gravitational forcing induce forced nutation terms. The frequencies of some of them (mainly the annual and semi-annual retrograde nutations) are close to the FCN frequency and this modifies their amplitude and phase.

In the Earth-fixed reference frame, the frequency of FCN is inside the diurnal tidal band. As a consequence, some diurnal tidal waves with frequencies close to the FCN one (mainly P_1, K_1, Ψ_1 and Φ_1) are modified, hence the acronymous Free Core Resonance (FCR). The resonant modifications of these diurnal tidal waves and forced nutations can be employed to investigate the Earth's FCN and calculate the related resonance parameters.

The comparison between theoretical modeling and experimental measurements of these parameters using Earth tides and nutations is very important for studying the Earth's deep interior dynamics and structure and in particular the dynamical processes at Core Mantle Boundary (CMB) of the Earth.

For example, in a space-fixed reference frame FCN period is inversely proportional to the dynamical flattening of CMB. The coupling changes the figure of the fluid core or the topography of CMB, and strongly depends on the mechanisms acting at the CMB, such as flattening, both elliptical and non-elliptical boundary topography, electro-magnetic coupling. If the liquid core is assumed to be viscous and electrically conducting, visco-magnetic friction may also act at the CMB, leading to a coupling which is partly dissipative [52, 53, 54]. The imaginary part of the FCR frequency arises primarily from the dissipative part of the electromagnetic torque.

4.1.1 Theoretical modeling

The nutation has two modes, the forced and free modes. The forced nutation is due to the luni-solar and planetary tidal forces, while the free mode appears because pressure coupling between the liquid core and the solid mantle acts as a restoring force. For these reasons, this mode was called Free Core Nutation (FCN) by Toomre [55].

The Earth rotation axis changes continuously its orientation with respect to both a space-fixed and an Earth-fixed reference system, and the angular velocity of the rotation fluctuates with time.

This rotary motion is comparable to that of a physical gyroscope. Therefore it is possible to describe the variations of Earth's rotation by a motion of precession of its instantaneous rotation axis around the geometric axis and a nutation of the rotation axis around the axis of the total angular momentum.

Following Ref. [56], in an Earth-fixed, rotating, reference system, the balance between the Earth's angular momentum $\mathbf{H}$ and external torques $\mathbf{L}$, due to luni-solar and planetary gravitational forces, is described by the dynamic Euler equation [57]:

$$\frac{d\mathbf{H}}{dt} + \omega \times \mathbf{H} = \mathbf{L} \tag{4.1}$$

where ω is the angular velocity of the Earth with respect to inertial space and, defined the inertia tensor of the rigid body $\mathbf{I}$, the angular momentum can be expressed as

$$\mathbf{H} = \mathbf{I} \cdot \omega \tag{4.2}$$

In the case of a rotating deformable body, it is possible to introduce the angular momentum relative to the deformation $\mathbf{h}$. Its definition follows from the motion of mass elements that occurs with velocity $\mathbf{v}_r$ relative to the rotating reference system, in which the rotation is described

$$\mathbf{h} = \int\int\int \rho\,(x, y, z)\, \mathbf{r} \times \mathbf{v}_r dV \tag{4.3}$$

where $\rho\,(x, y, z)$ is the density at the position $\mathbf{r}$.

Thus, the angular momentum of a rotating deformable body is

$$\mathbf{H} = \mathbf{I} \cdot \omega + \mathbf{h} \tag{4.4}$$

where the first part is also referred to as *mass term*, the second one as *motion term*. Inserting Eq. 4.4 into Eq. 4.1, the *Euler-Liouville* equation, also known in short as *Liouville equation* [25], is obtained

$$\frac{d}{dt}\left(\mathbf{I}\cdot\omega+\mathbf{h}\right)+\omega\times\left(\mathbf{I}\cdot\omega+\mathbf{h}\right)=\mathbf{L} \tag{4.5}$$

In theoretical studies on Earth's rotation, the quantities in the Liouville equation are often related to a rotating reference system, according to which the mass elements of a rotating rigid body are invariant with respect to their position at all times.

The external torques, acting on the Earth because of the luni-solar gravitational attraction, cause the Earth to nutate and precess.

Changes in the Earth's rotation are studied by applying the principle of conservation of angular momentum to the Earth system. The rotation of the solid Earth varies as a result of applied external torques, internal mass redistribution, and transfer of angular momentum between the solid Earth and the fluid regions with which it is in contact; other torques are due to hydrodynamic or magneto-hydrodynamic stresses acting at the CMB. The Earth's rotation deviates only slightly from a state of uniform rotation. This deviation is a few parts in 10^8 in speed, corresponding to changes of a few milliseconds in the length of the day, and about a part in 10^6 in the position of the rotation axis with respect to the crust of the Earth, and corresponding to a variation of several hundred milliarcseconds in polar motion.

For a simple model of the Earth in which mantle and fluid core are separated through a spheroidal CMB, it is possible to separate the Liouville equation for these two parts, adding a coupling torque $\mathbf{N}$ that mantle and core exert on each other and null when considering the whole Earth

$$\frac{d\mathbf{H}^c}{dt}+\omega\times\mathbf{H}^c = \mathbf{L}^c+\mathbf{N} \tag{4.6}$$

$$\frac{d\mathbf{H}^m}{dt}+\omega\times\mathbf{H}^m = \mathbf{L}^m-\mathbf{N} \tag{4.7}$$

where $\mathbf{L}=\mathbf{L}^c+\mathbf{L}^m$ is the external torque, and $\mathbf{N}$ is the total coupling torque acting between mantle and core, including topographic, electromagnetic, viscous and gravitational coupling terms.

Among the coupling torques acting between mantle and core, the most important is due to pressure on the CMB caused by the fluid of the core. It arises when the core

rotates around an axis not aligned with the axis of symmetry of the ellipsoid CMB.

Following Ref. [58], this problem can be dealt by introducing the elasticity of the mantle and the visco-magnetic coupling. The differential equations are linearized and only small deviations from rigid rotation with angular velocity Ω around the axis of symmetry of the Earth are allowed. The differential equations for the equatorial components of the angular velocity of the whole Earth and core are expressed using the complex representation for the components of the rotation vector lying in the equatorial plane

$$\begin{aligned}
\dot{\omega}\left(1+\alpha\frac{k}{k_s}\right)-\imath\Omega\omega\left(1-\frac{k}{k_s}\right)+\left(\dot{\omega}^c+\imath\Omega\omega^c\right)\left(\frac{A^c}{A}-\frac{\alpha k_1}{k_s}\right) &= \frac{3\alpha k}{k_s r_e^2}\left(\frac{\dot{W}}{\Omega}+\imath W\right)-\frac{3\imath\alpha W}{r_e^2} \\
\dot{\omega}\left(1+\frac{q_0 h^c}{2}\right)-\dot{\omega}^c\left(1-\frac{q_0 h_1^c}{2}\right)+\imath\Omega\omega^c\left(1+\alpha^c+K'-\imath K\right) &= \frac{3q_0 h^c}{2r_e^2}\frac{\dot{W}}{\Omega} \qquad (4.8)
\end{aligned}$$

where the frequencies ω and ω^c are complex, W is the tesseral part of tidal potential of degree 2 and order 1, k and l are the Love numbers which take into account of the changes with time of inertia tensor and ellipticity of the CMB caused by the tidal deformation, K and K' are the dimensionless viscomagnetic coupling constants, $q_0 = \Omega^2 r_e/g$ is the ratio between centrifugal force and gravity at equator, A, C and $\alpha = (C-A)/A$ (and similarly A^c, C^c, and α^c for the core) are the Earth's mean equatorial and polar moment of inertia and dynamic ellipticity respectively.

Assuming no external torques acting on Earth, that is $W = 0$, it is possible to find the eigenfrequencies of the model

$$\sigma_{CW} = \frac{A}{A^m}\left(1-\frac{k}{k_s}\right)\Omega \qquad (4.9)$$

$$\sigma_{NDFW} = -\Omega\left[1+\frac{A}{A^m}\left(\alpha^c-q_0\frac{h_1^c}{2}+K'-\imath K\right)\right] \qquad (4.10)$$

The first of these two solutions (Eq. 4.9), called *Chandler Wobble*, represents the free oscillation frequency of the pole which occurs with a period of about 435 days (the actual observed value deviates from the predicted one because of mantle anelasticity and ocean effects). The existence of this oscillation is due to the irregular shape of the Earth and in its rotation around an axis not aligned with the inertia axis of the Earth. This misalignment causes an oscillation of the Earth together with the rotation.

The second solution (Eq. 4.10), called *Nearly Diurnal Free Wobble* (NDFW), defines the free oscillation in the diurnal tidal band. It has a negative sign because of the

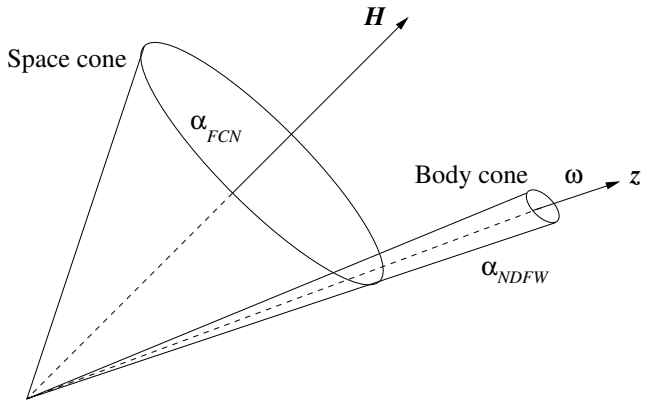

Figure 4.1: Poinsot representation of the NWDF and FCN rotational free mode of the Earth.

retrograde motion of the instantaneous rotation axis and the axis around each other. The deviation from the diurnal frequency is controlled by the dynamic ellipticity of the core α^c. The term including the Love number h_1^c describes the distortion in the dynamic ellipticity caused by the instantaneous elastic deformation of CMB due to the wobble. The values of K and K' and other effects not included in the above equations have large uncertainties because of the lack of knowledge.

The period of the associated retrograde nutation of the instantaneous rotation axis in space can be obtained from the relation

$$\frac{\sigma_{NDFW}}{2\pi} = \frac{1}{T_{FCN}} - \frac{\Omega}{2\pi} \tag{4.11}$$

The motion can be represented by the Poinsot representation [55, 59, 60] as a fixed body cone which rolls without slipping in a fixed space cone, having axes of rotation coinciding with the axis of the Earth and angular momentum vector, respectively (see Fig. 4.1). These two directions and the instantaneous rotation vector lie in the same plane of the space that slowly revolves around the angular momentum vector, which would result fixed in the inertial space if the external torque is zero.

These geometrical conditions are equivalent to the relationship between the amplitudes of the wobble and nutation, given by

$$\frac{\alpha_{NDFW}}{\alpha_{FCN}} = \frac{A\alpha^c}{A^m} \tag{4.12}$$

Using these equations, it is also possible to obtain the rotational response of the Earth's

mantle and core subjected to the tesseral tidal potential $W = W_0 \exp(\imath\sigma t)$. The equatorial components of the rotation for Earth and core become $\omega = \omega_0 \exp(\imath\sigma t)$ and $\omega^c = \omega_0^c \exp(\imath\sigma t)$, where

$$\omega_0 = \frac{A\left[(\sigma+\Omega)\left(1 - A^c q_0 h^c/(2\alpha A)\right) + \Omega\left(\alpha^c - q_0 h_1^c/2\right)\right] 3\alpha W_0}{A^m\left(\sigma - \sigma_{NDFW}\right)\Omega r_e^2} \tag{4.13}$$

$$\omega_0^c = \frac{A\left[1 - q_0 h^c/(2\alpha)\right] 3\alpha W_0}{A^m\left(\sigma - \sigma_{NDFW}\right) r_e^2} \tag{4.14}$$

Because of the existence of this eigenmode, the response of the Earth becomes resonant in the diurnal tidal band.

4.1.2 Observations

The FCN was predicted and explained theoretically already at the end of 19th century [61]. Many attempts were made in the past to detect the FCN oscillation.

Theoretical works include the initial computations for hydrostatic seismologically constrained Earth's models, that take account of the instantaneous deformation of the CMB, the anelasticity of the mantle [52, 62, 64, 63, 66, 65, 67], the non-hydrostatic CMB-topography [69, 70] and the effects of ocean tides [64, 68]. A more complete model of precession–nutation phenomena, recommended by the International Astronomical Union (IAU2000A) [22], takes all these features into account by adding a non-rigid Earth nutation model.

Using these models, different values of the FCR parameters (mainly T_{FCN} and quality factor Q) are predicted: from $T_{FCN} \approx 470$ sidereal days and $Q \approx 40000$ in Wahr's early papers to $T_{FCN} = 429.93 - 430.48$ sidereal days and $Q \approx 20000$ obtained in Ref. [22].

Investigation of the FCR and determination of its parameters are important in order not only to improve theoretical modeling of the nutations but also to understand nature of the Earth's interior. For this purpose, comparison between theoretical modeling and experimental measures using Earth tides and nutations is very important. Retrieved values of T_{FCN} from the literature span about 410 to 432 sidereal days; the estimated quality factor changes by orders of magnitude (see Tables 4.1 and 4.2). Several works suggest temporal variation of FCR parameters as a global phenomenon [54], but the analyses of VLBI data [88] conclude that the resonant period is stable in time within less than half a day.

Historically, most of the experimental studies of the FCR are based on the analysis of

Reference	T_{FCN}	Q
Neuberg et al., 1987 [76]	431 ± 6	2800 ± 500
Sato et al., 1994 [77]	437 ± 15	$3200 - \infty$
Florsch et al., 1994 [78]	431 ± 1	$1700 - 2500$
Merriam, 1994 [79]	430 ± 4	$5500 - 10000$
Hinderer et al., 1995 [80]	429 ± 8	$7700 - \infty$
Florsch et al., 2000 [81]	428	> 20000
Sato et al., 2004 [82]	429.7 ± 1.4	$9350 - 10835$
Rosat and Lambert, 2009 [83]	426.9 ± 1.2	16630 ± 3562
Rosat et al., 2009 [84]	428 ± 3	$7762 - 31989$

Table 4.1: Retrieved values of T_{FCN} (sidereal days) and Q analysing superconducting gravimeter data.

tidal gravity data [71, 72, 73, 74, 75]. In fact, as shown above, the amplitude and phase of some diurnal tides of luni-solar origin are perturbed by the resonance process in the diurnal tidal band because their frequency is located near the eigenfrequency. Some important results have been obtained from analysis on superconducting gravimeter data (see Table 4.1).

The FCN can also be detected by the estimation of its indirect effect (using the resonance effects on the forced terms of nutation) on the Earth's rotation, using the VLBI network analyses.

VLBI is a technique for an high-resolution imaging which allows to measure accurately changes in the Earth's orientation, by comparing differences in the arrival time of a radio signal at two or more radio telescopes that are simultaneously observing the same distant extragalactic radio source. Analysing these data the retrieved values of the FCR parameters are very accurate and stable in time (see Table 4.2).

Only few studies rely on tidal strain data: from a first attempt using quartz tube extensometers at the Esashi station in Japan [77], to the analyses of 2-year strain recorded by the laser extensometer at the Rokko-Takao station [91], later the expanded analysis of the Rokko-Takao data to 7.1-year [92], and at the end the estimation of the FCR parameters using 17 years of records from three extensometers at the Esashi station [93].

Reference	T_{FCN}	Q
Herring et al., 1986 [85]	435 ± 1	$22000 - 10^5$
Defraigne et al., 1994 [72]	432 ± 4	> 15000
Roosbeek et al., 1999 [86]	$431 - 434$	——
Vondràk and Ron, 2006 [87]	430.32 ± 0.07	20600 ± 340
Lambert and Dehant, 2007 [88]	430 ± 0.4	17000 ± 3000
Koot et al., 2008 [89]	430	13750 ± 514
Rosat and Lambert, 2009 [83]	429.6 ± 0.6	16683 ± 884
Ducarme et al., 2009 [75]	430 ± 2	≈ 15000

Table 4.2: Retrieved values of T_{FCN} (sidereal days) and Q analysing VLBI data.

4.2 FCR in the diurnal strain tides

FCR parameters can be estimated through the analysis of main diurnal strain tides. Obviously it is necessary to model the effect of the FCR on each diurnal strain tidal harmonic. Although S/N ratio for strain is usually lower than for gravity, the relative perturbations in strain tides are about 10 times larger than in gravity tides. For this reason the analysis of strain data is promising.

For the first time, a comparison between the resolving power of gravity and strain tides as regards the FCR parameters was performed [45]. It is possible to show that both resolving powers are comparable if tidal parameters are inverted minimizing the $\mathcal{L}^2$ misfit, as usually done for gravity data.

In case of linear problems, the $\mathcal{L}^2$ misfit exhibits a single minimum, which can be computed by matrix inversion. Because of this feature, $\mathcal{L}^2$ minimization is usually adopted even if not robust with respect to the presence of outliers.

FCR parameter estimate is non-linear and there is no advantage in minimizing the $\mathcal{L}^2$ misfit instead of the $\mathcal{L}^1$ one, which is more robust. To confirm this, the inversions of realistic synthetic tidal parameters show that both resolving powers improve if tidal parameters are inverted minimizing the $\mathcal{L}^1$ misfit, and this improvement is particularly noticeable for gravity tides.

4.2.1 Modeling

Following Ref. [9], using Eq. 2.13 introduced in Chapter 2, tidal potential can be espressed as

$$\frac{V_{tid}}{g} = \sum_{n=2}^{\infty}\sum_{m=0}^{n} N_n^m P_n^m (\cos\theta) \left[a_n^m (t)\cos(m\phi) + b_n^m (t)\sin(m\phi)\right] \tag{4.15}$$

where g is the Earth's gravitational acceleration, ϕ and θ are the east longitude and colatitude respectively, P_n^m is the associated Legendre polynomial of degree n and order m, and N_n^m is the normalizing factor defined into Eq. 2.9.

Using also Eq. 2.14, it is possible to write

$$a_n^m (t) + \imath b_n^m (t) = \sum_{k=1}^{K_{nm}} A_{knm} \left[\cos(2\pi f_{knm} t + \varphi_{knm}) + \imath \sin(2\pi f_{knm} t + \varphi_{knm})\right] \tag{4.16}$$

where for each degree and order K_{nm} harmonics with specified real amplitudes, frequencies, and phases A, f, and φ, are summed.

In particular, considering diurnal degree-2 tides ($n = 2$, $m = 1$), tidal potential becomes

$$\frac{V_{tid}}{g} = N_2^1 P_2^1 (\cos\theta) \left[a_2^1 (t)\cos\phi + b_2^1 (t)\sin\phi\right] \tag{4.17}$$

where $P_2^1 (\cos\theta) = -3\sin\theta\cos\theta$.

From Eqs. 4.16 and 4.17, for each k

$$\frac{V_{tid}}{g} = \frac{3}{2}\sqrt{\frac{5}{6\pi}} A_{k21} \sin\theta\cos\theta\cos(2\pi f_{k21} t + \varphi_{k21} - \phi) \tag{4.18}$$

The three horizontal strain components ($\varepsilon_{\theta\theta}$, $\varepsilon_{\phi\phi}$, $\varepsilon_{\theta\phi}$) are related to the tidal potential through Eqs. 2.18 to 2.20 and their specific expressions are given by Eqs. 2.21 to 2.23. Substituting 4.18 into Eqs. 2.21 to 2.23

$$\varepsilon_{\theta\theta} = \frac{3}{2a}\sqrt{\frac{5}{6\pi}} A_{k21} (h_2 - 4l_2) \sin\theta\cos\theta\cos(2\pi f_{k21} t + \varphi_{k21} - \phi) \tag{4.19}$$

$$\varepsilon_{\phi\phi} = \frac{3}{2a}\sqrt{\frac{5}{6\pi}} A_{k21} (2l_2 - h_2) \sin\theta\cos\theta\cos(2\pi f_{k21} t + \varphi_{k21} - \phi) \tag{4.20}$$

$$\varepsilon_{\theta\phi} = -\frac{3}{2a}\sqrt{\frac{5}{6\pi}} A_{k21} l_2 \sin\theta\cos\theta\sin(2\pi f_{k21} t + \varphi_{k21} - \phi) \tag{4.21}$$

Each diurnal strain tidal harmonic in a given azimuthal direction η can be expressed as

$$\varepsilon(\eta) = \alpha^2 \varepsilon_{\theta\theta} + \beta^2 \varepsilon_{\phi\phi} + 2\alpha\beta\varepsilon_{\theta\phi} \tag{4.22}$$

where α and β are the direction cosines. Substituting the explicit expressions of the three components of the horizontal strain, it becomes

$$\begin{aligned} \varepsilon(\eta) &= \frac{3}{2a}\sqrt{\frac{5}{6\pi}} A_{k21} \sin\theta\cos\theta \left\{ \left[h_2 - 2l_2 \left(1 + \cos^2\eta\right) \right] \cos\left(2\pi f_{k21} t + \varphi_{k21} - \phi\right) \right. \\ &\quad \left. - l_2 \frac{\sin 2\eta}{\cos\theta} \sin\left(2\pi f_{k21} t + \varphi_{k21} - \phi\right) \right\} \end{aligned} \tag{4.23}$$

For the sake of brevity, it is possible to introduce a function $F(\theta)$ depending on the location of the station and proportional to the amplitude of the tidal potential harmonic

$$F(\theta) = \frac{3}{2r_e}\sqrt{\frac{5}{6\pi}} A_{k21} \sin\theta\cos\theta \tag{4.24}$$

and express each diurnal strain tidal harmonic as

$$\begin{aligned} \varepsilon(\eta) &= F(\theta) \left\{ \left[h_2 - 2l_2 \left(1 + \cos^2\eta\right) \right] \cos\left(2\pi f_{k21} t + \varphi_{k21} - \phi\right) \right. \\ &\quad \left. - l_2 \frac{\sin 2\eta}{\cos\theta} \sin\left(2\pi f_{k21} t + \varphi_{k21} - \phi\right) \right\} \end{aligned} \tag{4.25}$$

Because the solid Earth tides are affected by the FCR, h and l depend on f through the expressions

$$h = h_0 + h_1 \frac{f - f_0}{f_{FCR} - f} \qquad l = l_0 + l_1 \frac{f - f_0}{f_{FCR} - f} \tag{4.26}$$

where f_0 is the frequency of O_1 harmonic and f_{FCR} is the FCR frequency.

Because of the anelasticity of the Earth, h_0, h_1, l_0, l_1, and f_{FCR} are complex. In particular, f_{FCR} becomes

$$f_{FCR} = f_1 \left(1 + \imath \frac{1}{2Q}\right) \tag{4.27}$$

It is possible to re-write the diurnal strain tidal harmonic in Eq. 4.25 as

$$\varepsilon(\eta) = \left\{ C(f) \cos\left(2\pi f t + \varphi - \phi\right) + D(f) \sin\left(2\pi f t + \varphi - \phi\right) \right\} F(\theta) \tag{4.28}$$

where

$$C(f) \equiv a_0 + f_2 \left\{ a_1 (f_1 - f) + b_1 \frac{f_1}{2Q} \right\} \tag{4.29}$$

$$D(f) \equiv b_0 + f_2 \left\{ b_1 (f_1 - f) - a_1 \frac{f_1}{2Q} \right\} \tag{4.30}$$

with

$$f_2 \equiv \frac{(f - f_0)}{(f_1 - f)^2 + (f_1/2Q)^2} \tag{4.31}$$

The coefficients a_0, a_1, b_0, and b_1 can be expressed in a compact form as

$$a_k \equiv \Re \left\{ h_k - 2l_k \left(1 + \cos^2 \eta\right) \right\} + \Im \left\{ l_k \sin 2\eta / \cos\theta \right\} \tag{4.32}$$

$$b_k \equiv \Im \left\{ h_k - 2l_k \left(1 + \cos^2 \eta\right) \right\} - \Re \left\{ l_k \sin 2\eta / \cos\theta \right\} \tag{4.33}$$

where k is 0 or 1.

Because of the local effects, substituting Eqs. 4.25 to 4.33 into Eq. 3.26, for each interferometer the coefficients a_k and b_k are

$$\begin{aligned} a_k = {} & \Re \left\{ (\alpha + \beta)(h_k - 3l_k) - l_k \left[(\alpha - \beta)\cos(2\eta) + \gamma \sin(2\eta) \right] \right\} \\ & + \Im \left\{ l_k \left[(\alpha - \beta)\sin(2\eta) - \gamma \cos(2\eta) \right] / \cos\theta \right\} \end{aligned} \tag{4.34}$$

$$\begin{aligned} b_k = {} & \Im \left\{ (\alpha + \beta)(h_k - 3l_k) - l_k \left[(\alpha - \beta)\cos(2\eta) + \gamma \sin(2\eta) \right] \right\} \\ & - \Re \left\{ l_k \left[(\alpha - \beta)\sin(2\eta) - \gamma \cos(2\eta) \right] / \cos\theta \right\} \end{aligned} \tag{4.35}$$

where h_k and l_k ($k = 0, 1$) are frequency independent and α, β and γ are the three coupling coefficients, different for each interferometer.

4.2.2 Resolving power

Fig. 4.2 shows the expected amplitudes of $C(f)$ and $D(f)$ around the FCR frequency for the two interferometers BA and BC, striking -24 and 66 degrees respectively, obtained using $T_{FCN} = 430$ sidereal days and $Q = 20000$ [22]. Complex Love and Shida numbers and FCR parameters are from IERS Convention 2003 [94].

To compute the sensitivity of strain tides to different parameters, some tests have been

performed calculating the expected amplitudes when one of them is null. The different sensitivities reflect their different numerical weights.

For example, $D(f)$ can be expressed explicitly as

$$\begin{aligned} D(f) &= h_0^I - 2l_0^I\left[1+\cos^2(\delta)\right] - l_0^R \sin 2\delta/\cos\theta \\ &\quad + f_2\left\{\left[h_1^I - 2l_1^I\left[1+\cos^2(\delta)\right] - l_1^R\sin 2\delta/\cos\theta\right](f_1 - f)\right\} \\ &\quad - f_2\left\{\left[h_1^R - 2l_1^R\left[1+\cos^2(\delta)\right] - l_1^I\sin 2\delta/\cos\theta\right] f_1/2Q\right\} \end{aligned} \tag{4.36}$$

where the apices R and I refer to the real and imaginary parts respectively, and in particular $h_0^R = 0.60264$, $h_0^I = -2.409\times10^{-3}$, $h_1^R = -2.491\times10^{-3}$, $h_1^I = 8.68296\times10^{-5}$, $l_0^R = 8.4817\times10^{-2}$, $l_0^I = -7.4502\times10^{-4}$, $l_1^R = 7.549\times10^{-5}$, $l_1^I = 4.1262\times10^{-6}$.

Substituting the numerical values of complex Love and Shida numbers, for BA and BC

$$\begin{aligned} D_{BA}(f) &= -2.409\times10^{-3} + 2.734\times10^{-3} + 9.3369\times10^{-2} \\ &\quad + f_2\left\{\left[8.68\times10^{-5} - 1.51\times10^{-5} + 8.31\times10^{-5}\right](f_1 - f)\right\} \\ &\quad - f_2\left\{\left[-2.491\times10^{-3} - 2.77\times10^{-4} + 4.54\times10^{-6}\right] f_1/2Q\right\} \end{aligned}$$

and

$$\begin{aligned} D_{BC}(f) &= -2.409\times10^{-3} + 1.735\times10^{-3} - 9.3369\times10^{-2} \\ &\quad + f_2\left\{\left[8.68\times10^{-5} - 9.618\times10^{-6} - 8.31\times10^{-5}\right](f_1 - f)\right\} \\ &\quad - f_2\left\{\left[-2.491\times10^{-3} - 1.76\times10^{-4} - 4.54\times10^{-6}\right] f_1/2Q\right\} \end{aligned}$$

Some terms prevail on the others. It is evident, for example, that $\Im(l_1)$ does not affect predictions appreciably, and the effects of $\Im(l_0)$, $\Re(l_1)$, $\Im(h_0)$, $\Im(h_1)$ and Q are generally smaller than or comparable ($D(K_1)$ only) to the uncertainties.

As a comparison, Fig. 4.3 shows the amplitudes of the real and imaginary part of the complex gravimetric factor δ, here expressed as

$$\Re\{\delta\} = 1 + \Re\{a_0\} + f_2\left[\Re\{a_1\}(f_1 - f) + \Im\{a_1\}\frac{f_1}{2Q}\right] \tag{4.37}$$

$$\Im\{\delta\} = \Im\{a_0\} + f_2\left[\Im\{a_1\}(f_1 - f) - \Re\{a_1\}\frac{f_1}{2Q}\right] \tag{4.38}$$

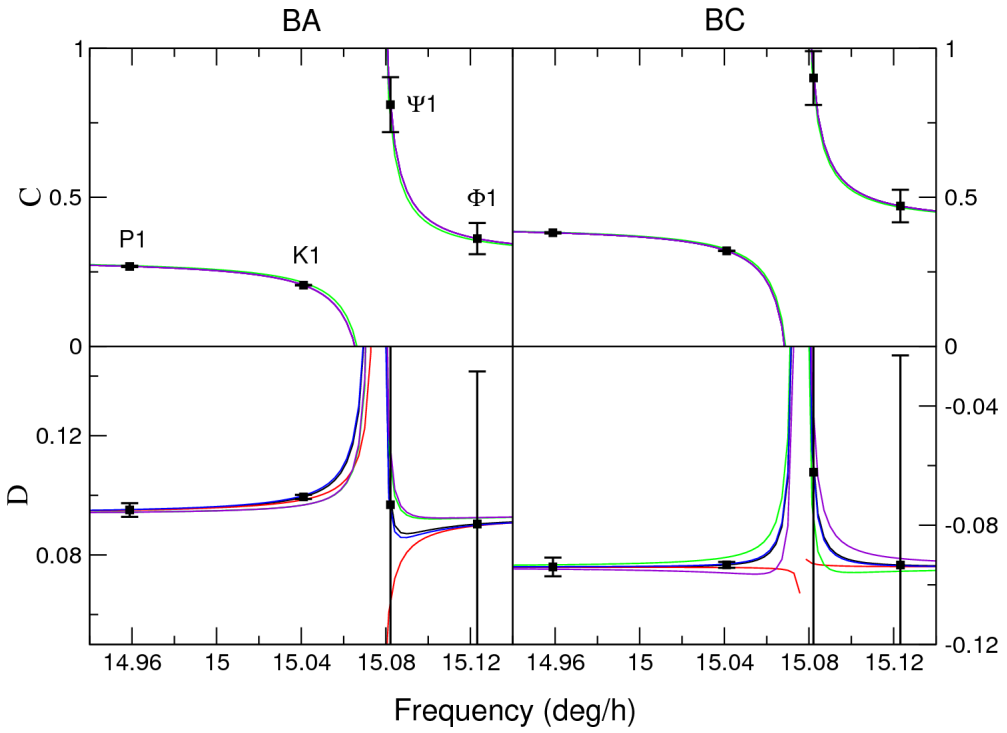

Figure 4.2: Black lines: theoretical values of $C(f)$ and $D(f)$ around f_{FCR} for $T_{FCN} = 430$ sidereal days and $Q = 20000$ [22]; complex Love and Shida numbers from Ref. [94]. Red lines, $1/Q = 0$; green lines, $\Re(l_1) = 0$; blue lines, $\Im(l_1) = 0$; violet lines, $\Im(h_1) = 0$. Squares, theoretical values for P_1, K_1, Ψ_1, and Φ_1; error bars (1σ) from the Gran Sasso strain analysis by VAV03. Left plots refer to the BA azimuthal direction (N24W); right plots to the BC one (N66E).

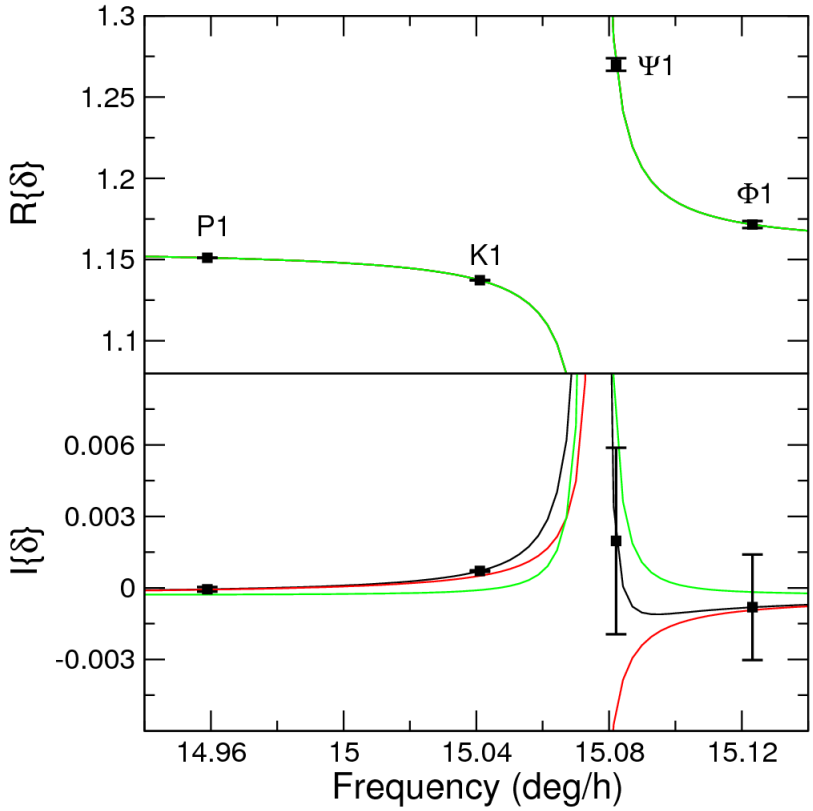

Figure 4.3: Black lines: theoretical values of $\Re\{\delta\}$ and $\Im\{\delta\}$ around f_{FCR} for $T_{FCN} =$ 430 sidereal days and $Q = 20000$ [22]; complex Love and Shida numbers from Ref. [94]. Red lines, $1/Q = 0$; green lines, $\Im(a_1) = 0$. Squares, theoretical values for P_1, K_1, Ψ_1, and Φ_1; error bars (1σ) from the tidal analysis of the Strasbourg 1997-2008 gravity data (S. Rosat, personal communication).

where

$$a_k \equiv h_k - \frac{3}{2}k_k$$

and in particular $a_0^R = 0.156381$, $a_0^I = -2.9667 \times 10^{-4}$, $a_1^R = -6.0805 \times 10^{-4}$, $a_1^I = 2.54961 \times 10^{-5}$.

Also in this case to test the sensitivity of gravity tides to some different parameters, the expected amplitudes are estimated when one of these parameters is null. In this case the real part of the gravimetric factor is not appreciably affected by any parameter.

For testing the capability of strain tides to estimate the FCR parameters, the amplitudes and phases of Q_1, O_1, P_1, K_1, Ψ_1, Φ_1, J_1 and OO_1 at Gran Sasso are calculated by using the complex Love and Shida numbers in Ref. [94] and fixing T_{FCN} and $\log Q$ on a regular grid. In particular T_{FCN} ranges between 420 and 460 sidereal days, increasing

its value of 1 day and $\log Q$ spans between 4 and 7, increasing its value of 0.5.

For each (T_{FCN}, $\log Q$) point, 10000 synthetic tidal parameter sets are generated by adding to each tidal parameter a null-mean random noise (both double-exponential, also called Laplace, DEN, and gaussian, GN), whose scale parameter is the standard deviation given by the tidal analysis of data.

Each synthetic set is inverted using a fast downhill simplex algorithm [95] starting from the relevant a-priori model, at first leaving all the 10 parameters ($1/T$, $\log Q$, $\Re(h_0)$, $\Im(h_0)$, $\Re(h_1)$, $\Im(h_1)$, $\Re(l_0)$, $\Im(l_0)$, $\Re(l_1)$, and $\Im(l_1)$) free and then fixing some of them ($\Im(h_0)$, $\Im(h_1)$, $\Im(l_0)$, $\Re(l_1)$, and $\Im(l_1)$) to their a-priori values.

Inversions are carried out by minimizing two different misfit functions, namely the mean squared deviation of residuals (chi-square fitting, $\mathcal{L}^2$, formally appropriate for normally distributed errors) and the mean absolute deviation of residuals ($\mathcal{L}^1$, formally appropriate for two-sided-exponentially distributed errors and commonly used for robust fitting):

$$\mathcal{L}^1 = \sum_{j=1}^{2}\sum_{i=1}^{16}\left|\frac{x_i^{(j)} - f_i^{(j)}(\mathbf{a})}{\sigma_i^{(j)}}\right| \qquad \mathcal{L}^2 = \sum_{j=1}^{2}\sum_{i=1}^{16}\left(\frac{x_i^{(j)} - f_i^{(j)}(\mathbf{a})}{\sigma_i^{(j)}}\right)^2 \tag{4.39}$$

where $j = 1, 2$ indicates the two interferometers, $i = 1, ..., 16$ indicates data (x_i) in each data set, i. e. the amplitudes of the sine and cosine terms of the eight tides, $f_i(\mathbf{a})$ is model prediction of x_i given a set of model parameters $\mathbf{a}$, and σ_i is uncertainty of x_i.

For each (T_{FCN}, $\log Q$) point the frequentist probability (i. e. the event occurrence frequency) of obtaining $428 < T_{FCN} < 430$ sidereal days (representative range of the results in Ref. [83]) is calculated. The same procedure is followed for getting the probability of obtaining $4 < \log Q < 5$.

Fig. 4.4 shows the results obtained minimizing the $\mathcal{L}^1$ misfit for the DEN-randomized synthetics (upper panels) and the $\mathcal{L}^2$ misfit for the GN-randomized synthetics (lower panels).

Similar plots are obtained fixing $\Im(h_0)$, $\Im(h_1)$, $\Im(l_0)$, $\Re(l_1)$, and $\Im(l_1)$ parameters (see Fig. 4.5) and using different combinations of the misfit and random noise (that means inverting GN-randomized synthetics with $\mathcal{L}^1$ misfit and DEN-randomized synthetics with $\mathcal{L}^2$ misfit, see Fig. 4.6).

The distributions lack in any dependence (trade-offs) between parameters, thus the marginal probability of obtaining $428 < T_{FCN} < 430$ sidereal days given a 'real' value

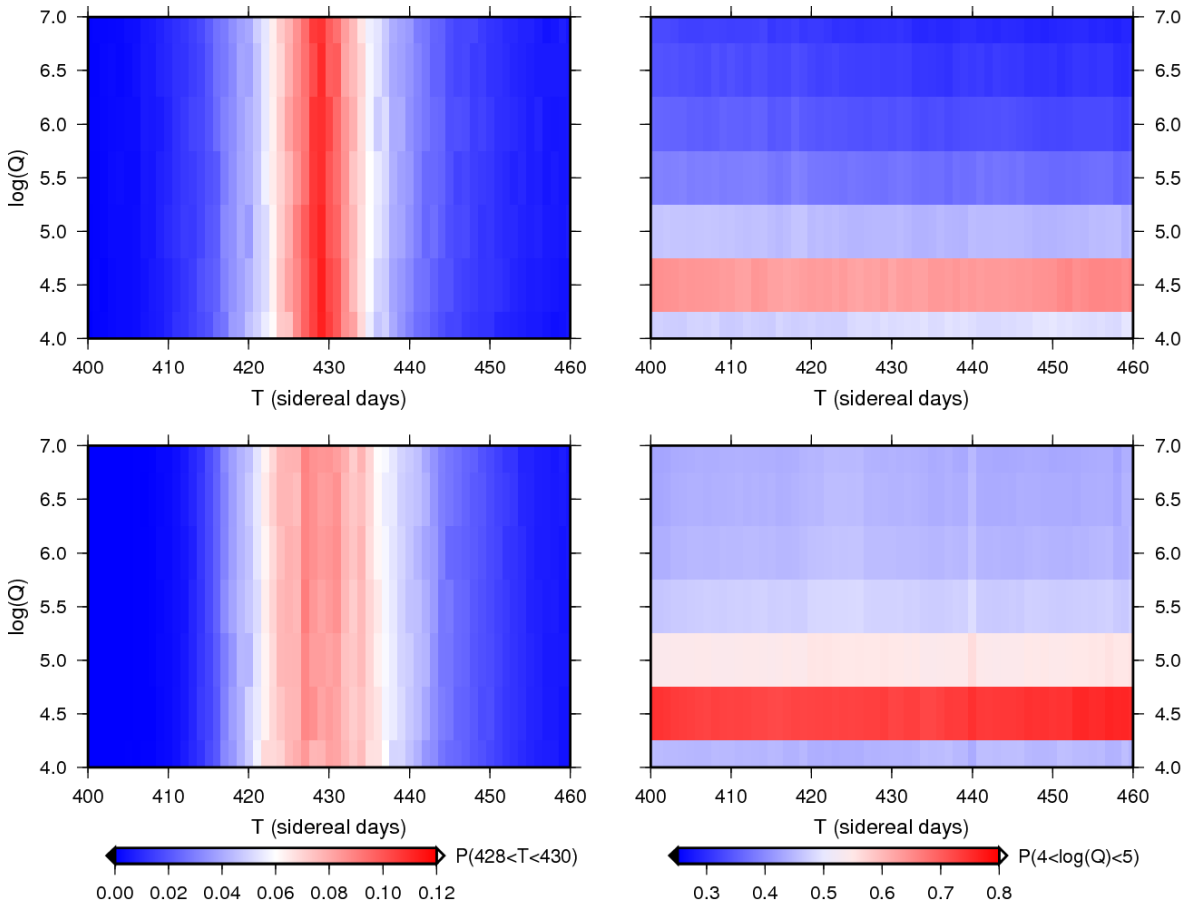

Figure 4.4: Frequentist probability of obtaining $428 < T_{FCN} < 430$ sidereal days (left plots) and $4 < \log Q < 5$ (right plots) for different 'real' $(T_{FCN}, \log Q)$ values, as obtained from the inversions of synthetic strain tidal parameter sets, leaving all the 10 parameters free. Upper plots, $\mathcal{L}^1$ minimization; lower plots, $\mathcal{L}^2$ minimization.

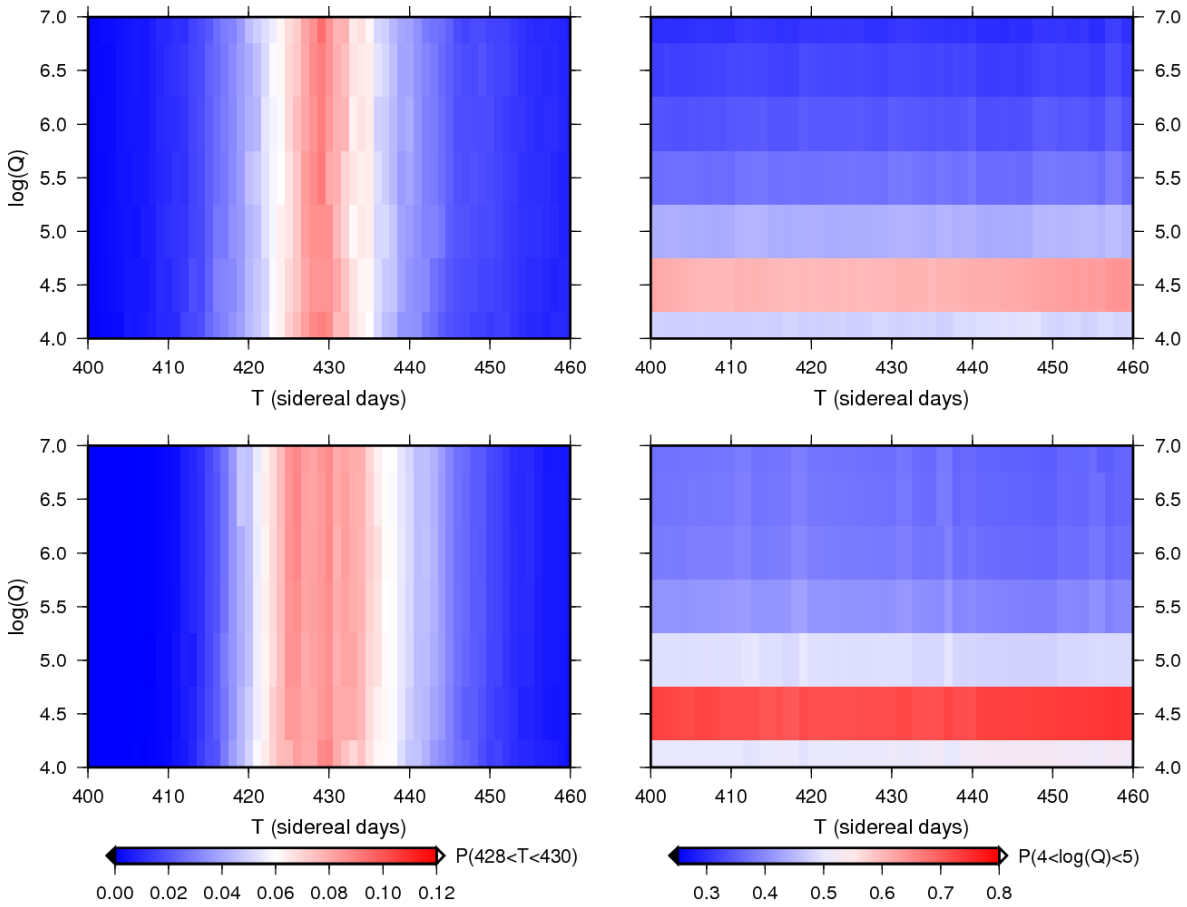

Figure 4.5: Frequentist probability of obtaining $428 < T_{FCN} < 430$ sidereal days (left plots) and $4 < \log Q < 5$ (right plots) for different 'real' $(T_{FCN}, \log Q)$ values, as obtained from the inversions of synthetic strain tidal parameter sets fixing $\Im(h_0)$, $\Im(h_1)$, $\Im(l_0)$, $\Re(l_1)$, and $\Im(l_1)$. Upper plots, $\mathcal{L}^1$ minimization; lower plots, $\mathcal{L}^2$ minimization.

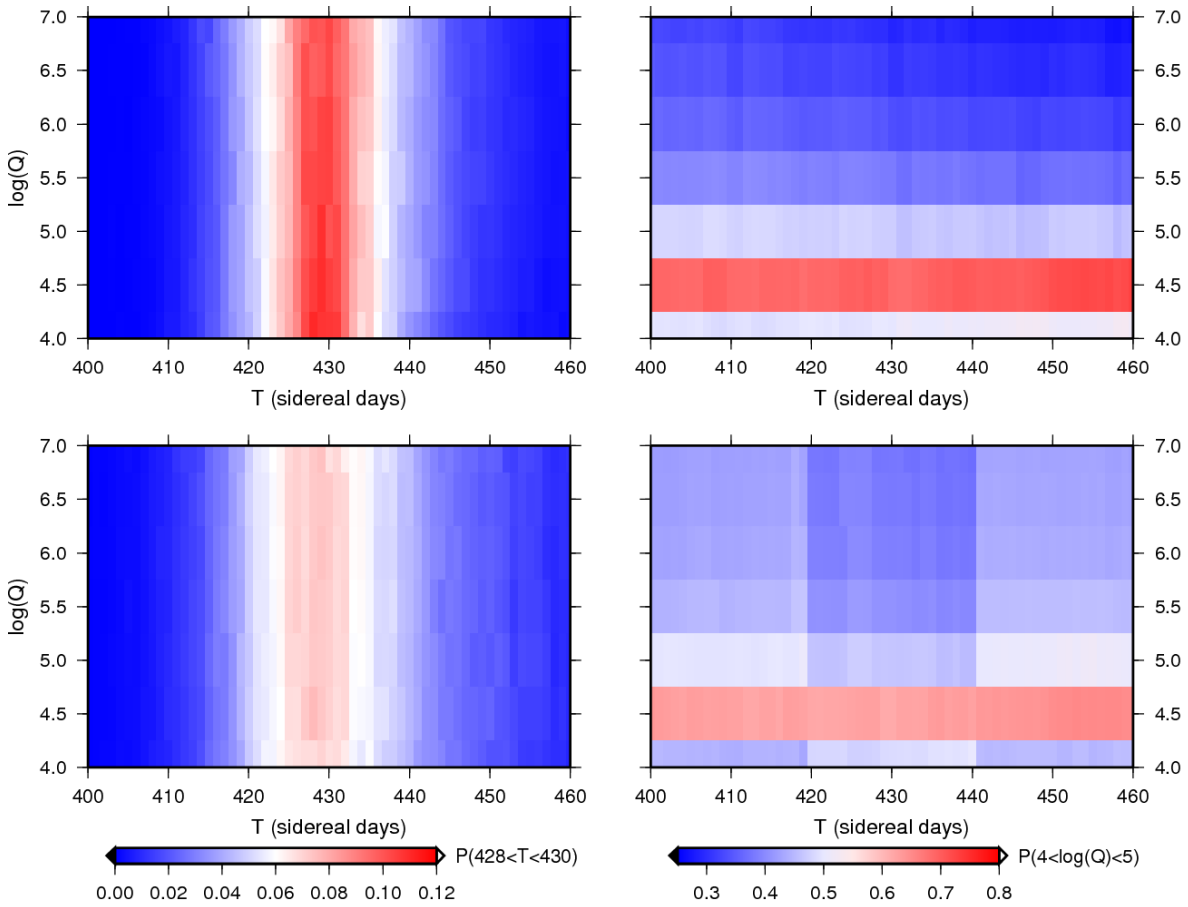

Figure 4.6: Frequentist probability of obtaining $428 < T_{FCN} < 430$ sidereal days (left plots) and $4 < \log Q < 5$ (right plots) for different 'real' (T_{FCN}, $\log Q$) values, as obtained from the inversions of synthetic strain tidal parameter sets, leaving all the 10 parameters free. Upper plots, $\mathcal{L}^1$ minimization for GN-randomized synthetics; lower plots, $\mathcal{L}^2$ minimization for DEN-randomized synthetics.

of T_{FCN} is estimated by summing the T_{FCN} frequentist probability for all the $\log Q$ values, without loss of information. The resulting distributions are shown in Fig. 4.7 (left plots) for different combinations of the misfit and random noise, and numbers (10 or 5, see above) of free parameters. All the curves are approximately symmetric around $T_{FCN} \simeq 429$ sidereal days, but the right tails are larger than the left ones.

If all ten parameters are left free, the cumulative distributions show that a 'real' T_{FCN} value is between 418 (424) and 443 (435) sidereal days at the 80% (50%) confidence level for the DEN-randomized synthetics inverted using the $\mathcal{L}^1$ misfit and between 420 (425) and 443 (436) sidereal days at the 80% (50%) confidence level for the GN-randomized synthetics. When using the $\mathcal{L}^2$ misfit, the 'real' T_{FCN} value is between 418 (424) and 448 (439) sidereal days at the 80% (50%) confidence level for the DEN-randomized synthetics and between 420 (425) and 445 (438) sidereal days at the 80% (50%) confidence level for the GN-randomized synthetics.

Thus, $\mathcal{L}^1$ minimization performs better than $\mathcal{L}^2$ minimization.

To verify if this may be a consequence of the large uncertainty on Ψ_1 and Φ_1 phases, these last are diminished down to 2 degrees, obtaining the same probability distribution shape, as evident from Fig. 4.8.

The same procedure is used for testing the capability of gravity tides to estimate the FCR parameters (see Figs. 4.9 to 4.11 and Fig. 4.7, right plots), using the standard deviation given by the tidal analysis of the Strasbourg 1997-2008 gravity data (S. Rosat, personal communication).

Even if in this case a slight trade-off between parameters appears, nevertheless it is so feeble that once again it is possible to generate the marginal probabilities without loss of information. At first, synthetics are inverted leaving all the 6 relevant parameters T_{FCN}, $\log Q$, $\Re\{a_0\}$, $\Im\{a_0\}$, $\Re\{a_1\}$, and $\Im\{a_1\}$ free, as shown in Fig. 4.9.

Then $\Im\{a_1\}$ has been fixed to its a-priori value (see Fig. 4.10) and at the end different combinations of the misfit and random noise (that means inverting GN-randomized synthetics with $\mathcal{L}^1$ misfit and DEN-randomized synthetics with $\mathcal{L}^2$ misfit, see Fig. 4.11) are used. Similar plots are obtained in all the three cases.

Again, all the marginal probabilities are approximately symmetric around $T_{FCN} \simeq 429$ sidereal days, but now the cumulative distributions show that the 'real' T_{FCN} value is between 424 (428) and 434 (431) sidereal days at the 80% (50%) confidence level for the DEN-randomized synthetics inverted using the $\mathcal{L}^1$ misfit and between 422 (428) and 434 (431) sidereal days at the 80% (50%) confidence level for the GN-randomized synthetics.

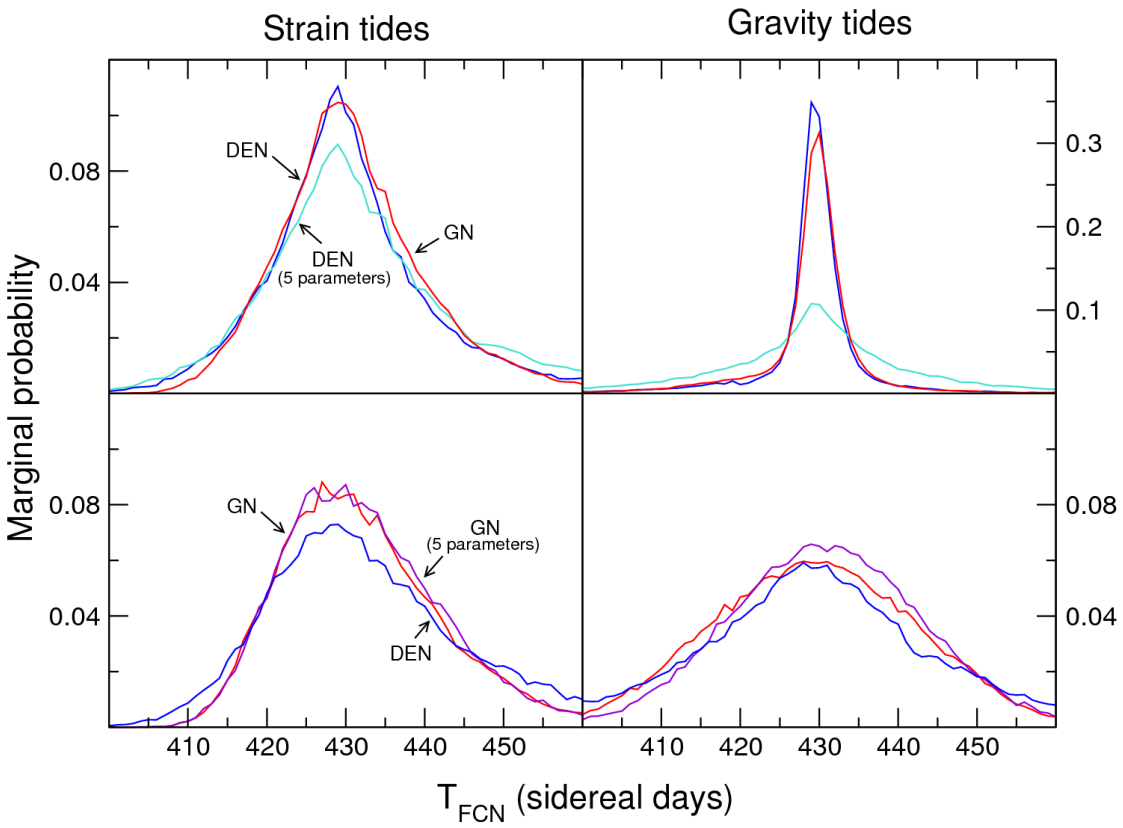

Figure 4.7: Marginal probability of obtaining $428 < T_{FCN} < 430$ sidereal days, given a 'real' T_{FCN} value, as obtained from the inversions of synthetic data sets. Upper plots, $\mathcal{L}^1$ minimization; lower plots, $\mathcal{L}^2$ minimization. Left plots, strain tides: blue lines, DEN-randomized synthetics, 10 free parameters; red lines, GN-randomized synthetics, 10 free parameters; turquoise lines, DEN-randomized synthetics, 5 free parameters; violet lines, GN-randomized synthetics, 5 free parameters. Right plots, gravity tides: blue lines, DEN-randomized synthetics, 6 free parameters; red lines, GN-randomized synthetics, 6 free parameters; turquoise lines, DEN-randomized synthetics, 5 free parameters; violet lines, GN-randomized synthetics, 5 free parameters.

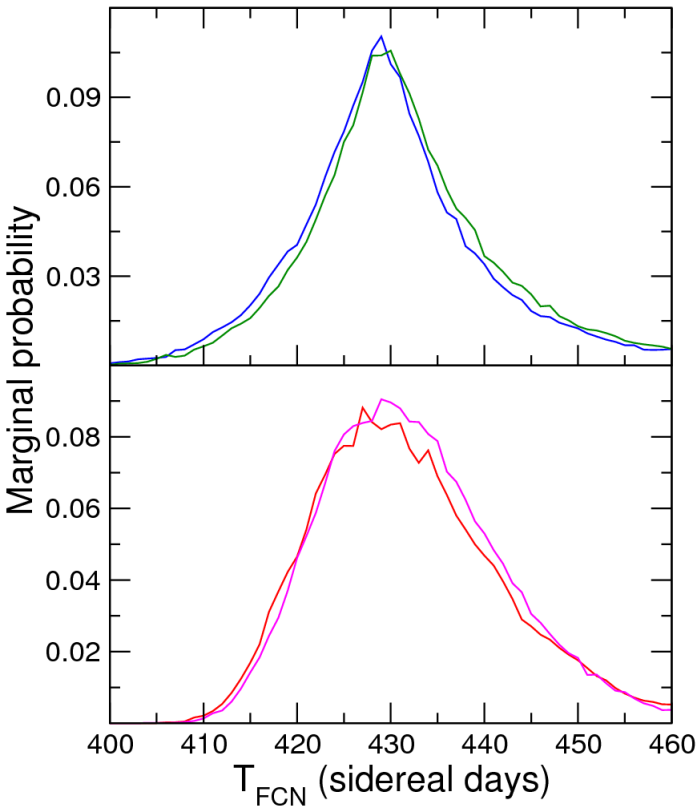

Figure 4.8: Marginal probability of obtaining $428 < T_{FCN} < 430$ sidereal days, given a 'real' T_{FCN} value, as obtained from the inversions of synthetic strain data sets. Upper plots, $\mathcal{L}^1$ minimization for DEN-randomized synthetics, 10 free parameters: blue line, error from the tidal analysis for all tides; green line, Ψ_1 and Φ_1 phase error fixed to 2 degrees; lower plots, $\mathcal{L}^2$ minimization for GN-randomized synthetics, 10 free parameters: red line, error from the tidal analysis for all tides; magenta line, Ψ_1 and Φ_1 phase error fixed to 2 degrees; lower plots, $\mathcal{L}^2$ minimization

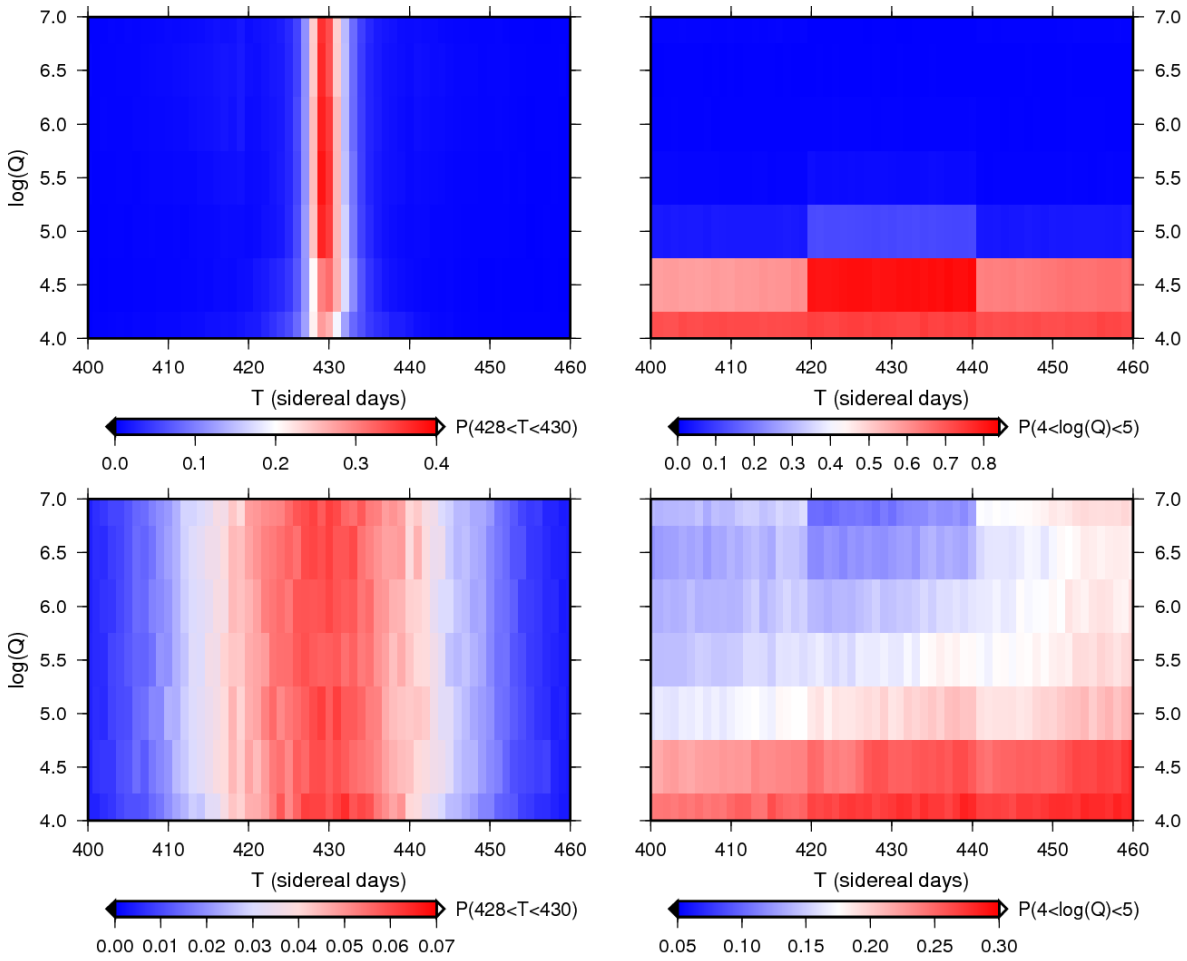

Figure 4.9: Frequentist probability of obtaining $428 < T_{FCN} < 430$ sidereal days (left plots) and $4 < \log Q < 5$ (right plots) for different 'real' $(T_{FCN}, \log Q)$ values, as obtained from the inversions of synthetic gravity tidal parameter sets, leaving all the 6 parameters free. Upper plots, $\mathcal{L}^1$ minimization; lower plots, $\mathcal{L}^2$ minimization.

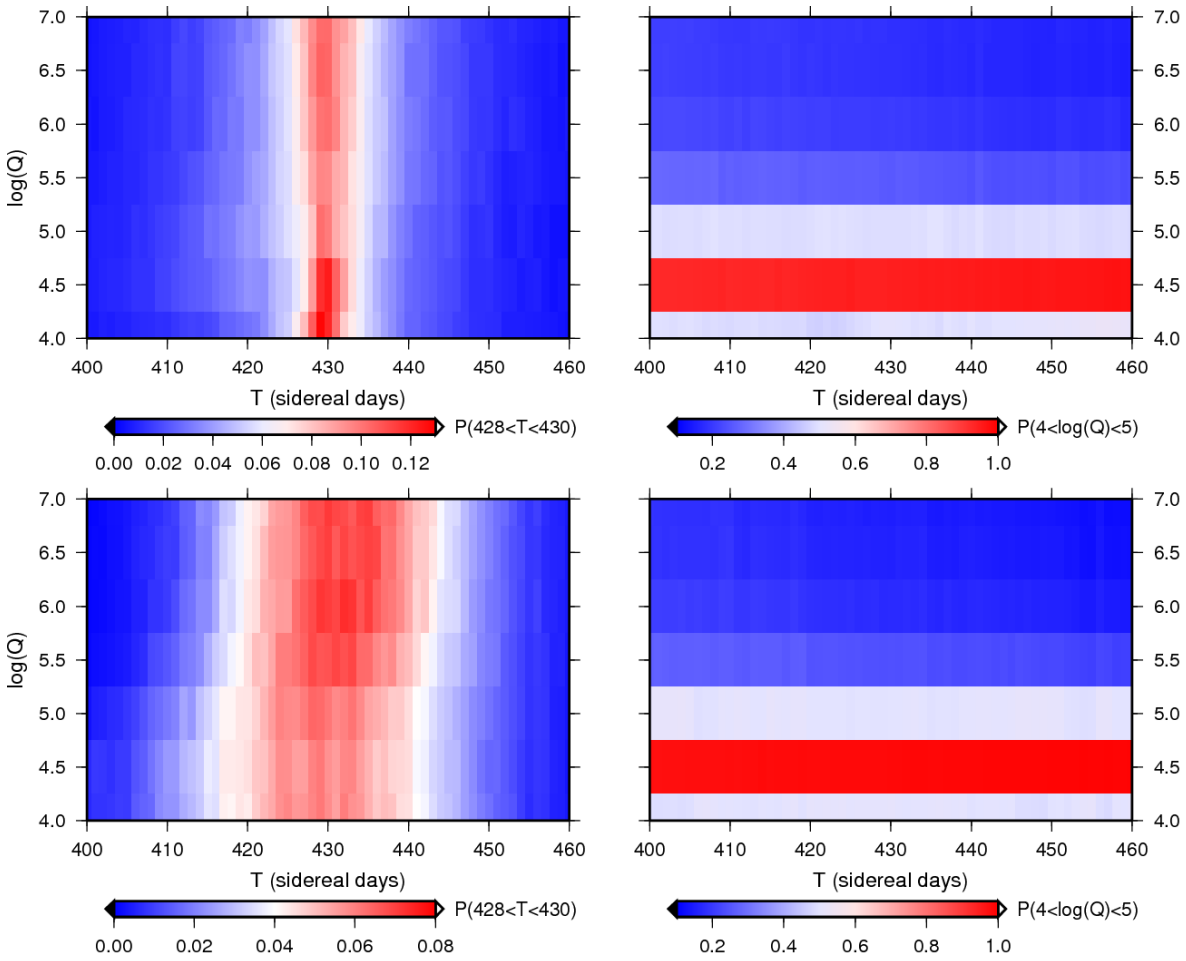

Figure 4.10: Frequentist probability of obtaining $428 < T_{FCN} < 430$ sidereal days (left plots) and $4 < \log Q < 5$ (right plots) for different 'real' $(T_{FCN}, \log Q)$ values, as obtained from the inversions of synthetic gravity tidal parameter sets fixing $\Im\{a_1\} = 0$. Upper plots, $\mathcal{L}^1$ minimization; lower plots, $\mathcal{L}^2$ minimization.

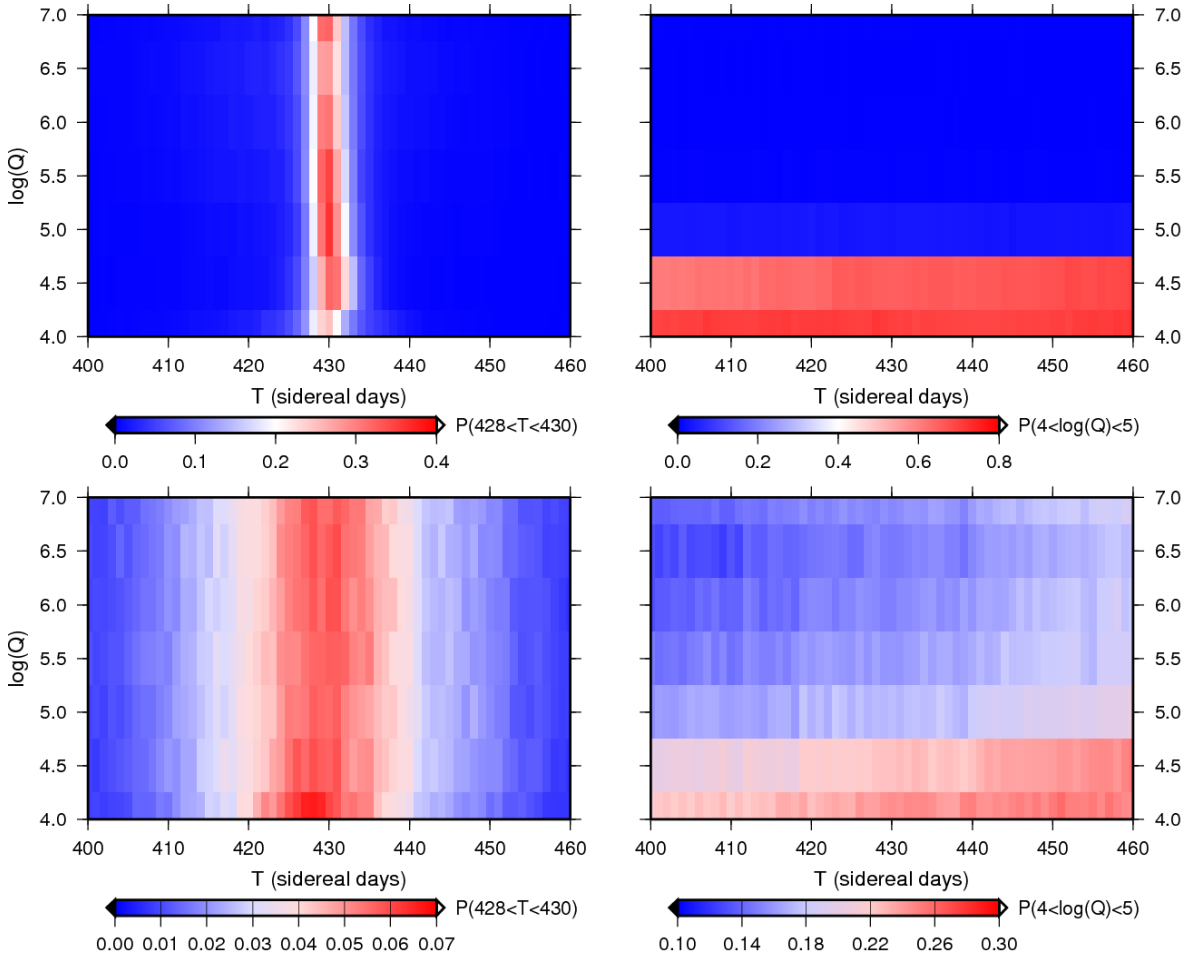

Figure 4.11: Frequentist probability of obtaining $428 < T_{FCN} < 430$ sidereal days (left plots) and $4 < \log Q < 5$ (right plots) for different 'real' $(T_{FCN}, \log Q)$ values, as obtained from the inversions of synthetic gravity tidal parameter, leaving all the 6 parameters free. Upper plots, $\mathcal{L}^1$ minimization for GN-randomized synthetics; lower plots, $\mathcal{L}^2$ minimization for DEN-randomized synthetics.

When using the $\mathcal{L}^2$ misfit, the 'real' T_{FCN} value is between 412 (421) and 447 (438) sidereal days at the 80% (50%) confidence level for the DEN-randomized synthetics and between 413 (421) and 446 (438) sidereal days at the 80% (50%) confidence level for the GN-randomized synthetics.

All these inversions of synthetics suggest some important conclusions.

First, the resolving power of gravity and strain tides seem comparable if tidal parameters are inverted minimizing the $\mathcal{L}^2$ misfit, as usually done for gravity data.

If tidal parameters are inverted minimizing the $\mathcal{L}^1$ misfit the resolving power of both gravity and strain tides improve, and this improvement is particularly noticeable for gravity tides.

It is also interesting to note that in case of strain tides, fixing five parameters to their a-priori values causes a small worsening of the $\mathcal{L}^1$ misfit resolving power. A much larger effect occurs in case of gravity tides when $\Im\{a_1\}$ is fixed to its a-priori value (see the upper right panel in Fig. 4.7, turquoise line).

4.3 FCR parameter estimation from Gran Sasso strain data

Eight years of discontinuous strain records from the two crossed 90-m long laser interferometers operating at Gran Sasso Underground Observatory have been analysed to investigate the FCN parameters [45]. The analyses of strain records have been performed after correcting measured strain for local distortion of the regional strain field and ocean loading. Data are inverted minimizing the $\mathcal{L}^1$ misfit, following the results of the previous section.

4.3.1 Pre-analysis

Fig. 4.12 shows the power spectral density for both interferometers in the diurnal tidal band and the apparent power spectral density $A^2T/2$, where A is the VAV03 amplitude and T is the actual record length (3020 days for BA and 2870 days for BC) of the main tidal harmonics, Q_1, O_1, P_1, K_1, Ψ_1, Φ_1, J_1 and OO_1. All the apparent PSDs (squares) are above the noise level when analysing the whole Gran Sasso records.

Reliable use of strain data requires correction for local distortions. These in turn can

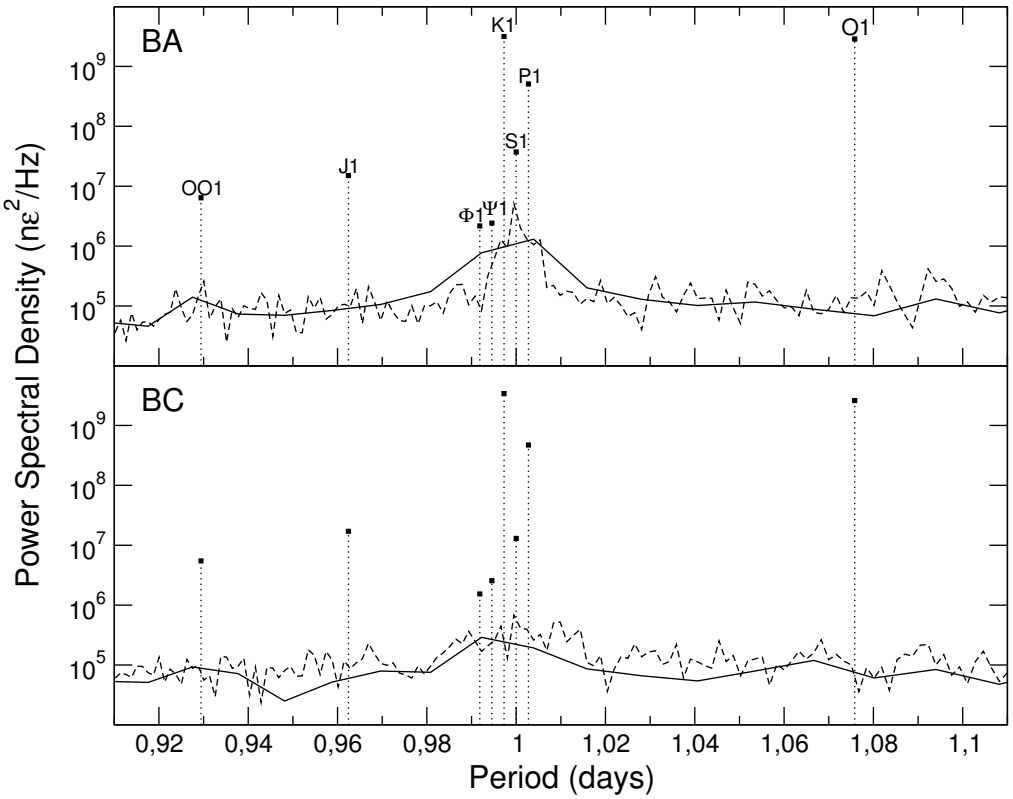

Figure 4.12: PSD of recorded data in the diurnal tidal band. Upper plot: BA interferometer; lower plot: BC interferometer. Solid lines, PSDs obtained with an about 85-day-long moving window; dashed lines, PSDs obtained with an about 680-day-long moving window; vertical lines, apparent PSDs from VAV03 analysis.

be estimated from tidal records, to which both solid and ocean loading tides contribute. After ocean loading and local distortion corrections, comparison of predicted and retrieved total strain tides can be used to estimate the Free Core Resonance parameters.

Tidal strain includes two contributions: the response of the solid Earth to the forcing tidal potential and the deformation of the crust induced by the water load due to ocean tides.

The deformation induced by luni-solar tidal forcing on a spherical non-rotating layered Earth (SNRE) can be predicted introducing the Love numbers, which are integral elastic properties of the Earth. In principle, an accurate estimate of Love numbers from experimental data could put tight constraints on Earth models.

Ocean tides contribute to deformation of the Earth's surface by the related pressure changes on the ocean floor. Observed ocean loading contribution depends on values of the elastic parameters between the observation and loading points, thus an accurate estimate of this effect could in principle be used to improve knowledge of regional rheology.

Accurate estimate of the Love numbers and ocean loading have been a major goal of strain measurements in the past, but very soon it became clear that tidal strain measurements are too affected by local distortions and knowledge of ocean tides is too poor to allow reaching this goal (for a discussion, see Ref. [96]).

Ocean loading effects are estimated using SPOTL [97] (see Appendix D). Mass-loading Green's functions are computed for the Gutenberg-Bullen Earth model A ([24], hereinafter referred to as *gbavap*) and two its variants, obtained after replacing top 1000 km by the continental shield crust and mantle structure of Ref. [98] and the oceanic crust and mantle structure of Ref. [98], hereinafter referred to as *contap* and *ocenap*. Gbavap, contap and ocenap models are representative of an average Earth, a thick continental crust and a thin oceanic crust respectively. Details about Green's functions and the Earth models are in Ref. [97].

The ocean loading is usually calculated using global ocean models (e.g. TPXO7.2 [99]; GOT00.2 [100]; CSR4.0 [101]) but these models give very different and inaccurate representations of the Mediterranean Sea, and thus very different values of ocean loading strain at Gran Sasso. For this reason, global ocean models have been integrated by a local Mediterranean Sea model at 1/30° resolution (`http://volkov.oce.orst.edu/tides/med.html`), including four diurnal (Q_1, O_1, P_1, K_1) and four semidiurnal (N_2, M_2, S_2, K_2) constituents.

BA interferometer

Earth Model	Q_1		O_1		P_1		K_1	
	A	ϕ	A	ϕ	A	ϕ	A	ϕ
contap	0.951	-17.886	4.796	-17.004	2.237	-14.201	6.810	-13.802
gbavap	0.952	-17.915	4.780	-17.094	2.236	-14.398	6.808	-13.998
ocenap	0.952	-17.932	4.805	-17.106	2.241	-14.435	6.816	-14.063

Table 4.3: Amplitude A ($n\varepsilon$) and phase ϕ (degrees) of diurnal tidal components for BA interferometer using different Earth models. Ocean model: TPXO7.2 and local Mediterranean Sea model; Love numbers: IERS 2003.

BC interferometer

Earth model	Q_1		O_1		P_1		K_1	
	A	ϕ	A	ϕ	A	ϕ	A	ϕ
contap	1.234	12.748	6.601	12.737	3.089	11.256	9.335	10.988
gbavap	1.233	12.629	6.612	12.527	3.089	10.669	9.341	10.314
ocenap	1.233	12.847	6.608	12.851	3.094	11.235	9.355	10.940

Table 4.4: Amplitude A ($n\varepsilon$) and phase ϕ (degrees) of diurnal tidal components for BA interferometer using different Earth models. Ocean model: TPXO7.2 and local Mediterranean Sea model; Love numbers: IERS 2003.

Tides in the Mediterranean Sea have small amplitude with respect to those in principal oceans, but contribute about half the total ocean loading strain at Gran Sasso, because of the dependence of ocean loading strain on distance (see Figs. 4.13 to 4.16).

A first prediction of tidal harmonics was conducted using a single global ocean model (TPXO7.2) combined to local Mediterranean Sea model and varying Earth models. All tested Earth models give very similar results as regards total computed tides (see Tables 4.3 and 4.4).

Global ocean models give very different and inaccurate representations of the Mediterranean Sea, and thus very different values of ocean loading strain at Gran Sasso. If the local Mediterranean Sea model is introduced, all tested global models give very similar results as regards total computed tides (see Tables 4.5 and 4.6).

The maximum discrepancy being less than 10^{-3} in amplitude ratio and 0.1 degrees in phase; the only exception relates to Q_1 as predicted using CSR4.0, whose phase differs

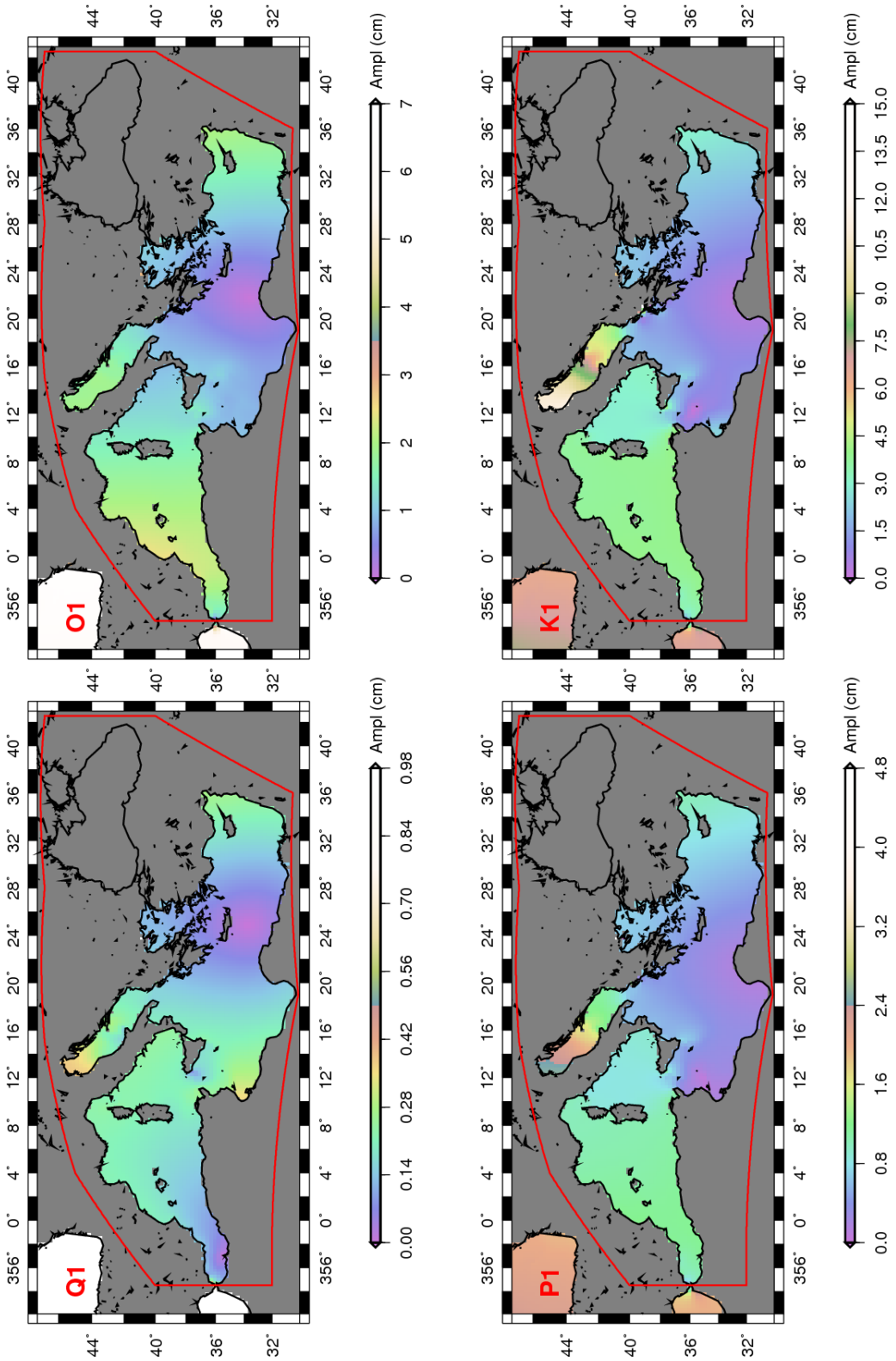

Figure 4.13: Amplitude (cm) of the diurnal tidal components (Q_1, O_1, P_1, K_1) in the Mediterranean region using TPXO7.2 ocean global model.

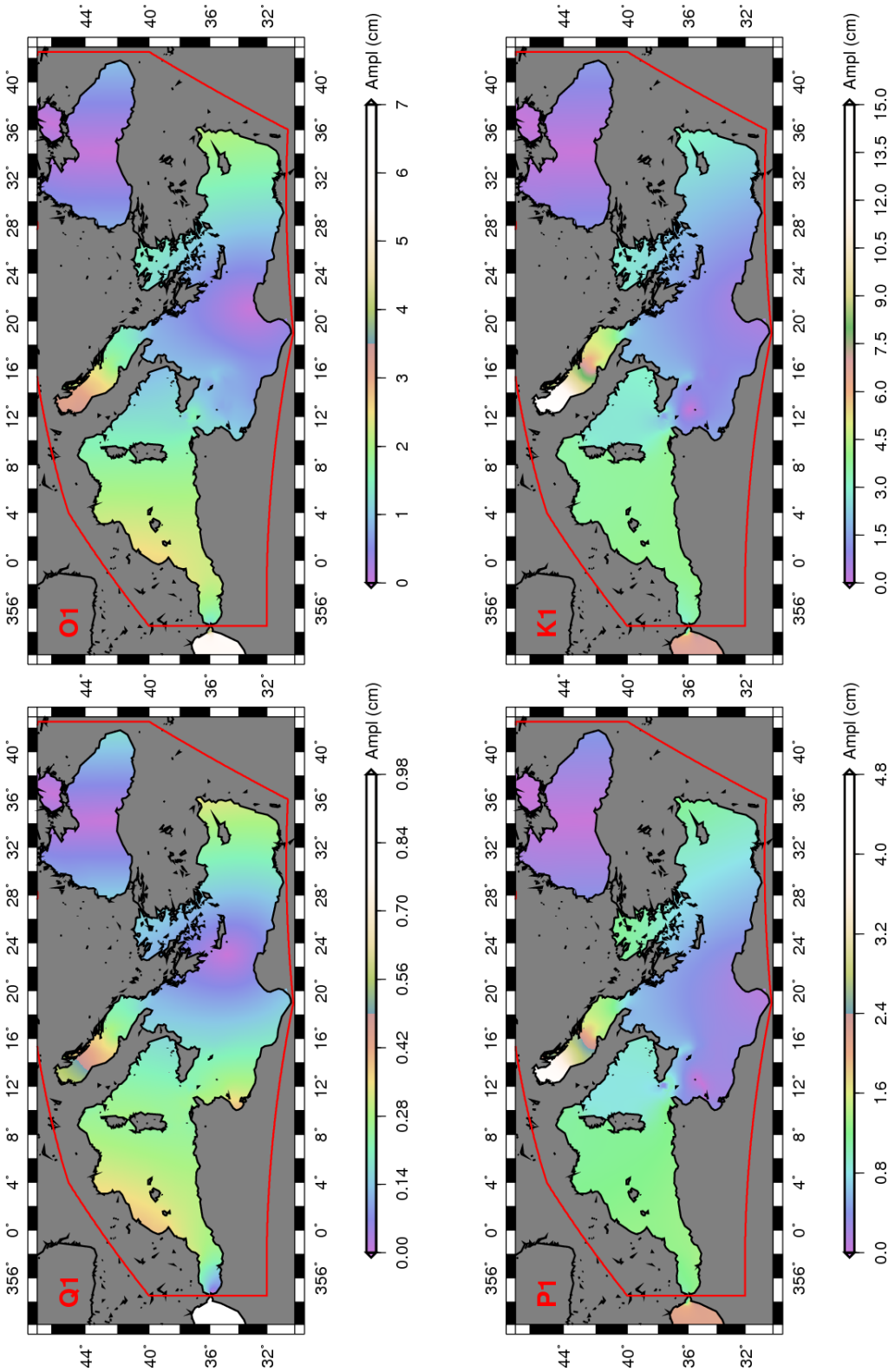

Figure 4.14: Amplitude (cm) of the diurnal tidal components (Q_1, O_1, P_1, K_1) in the Mediterranean region using the local Mediterranean Sea model.

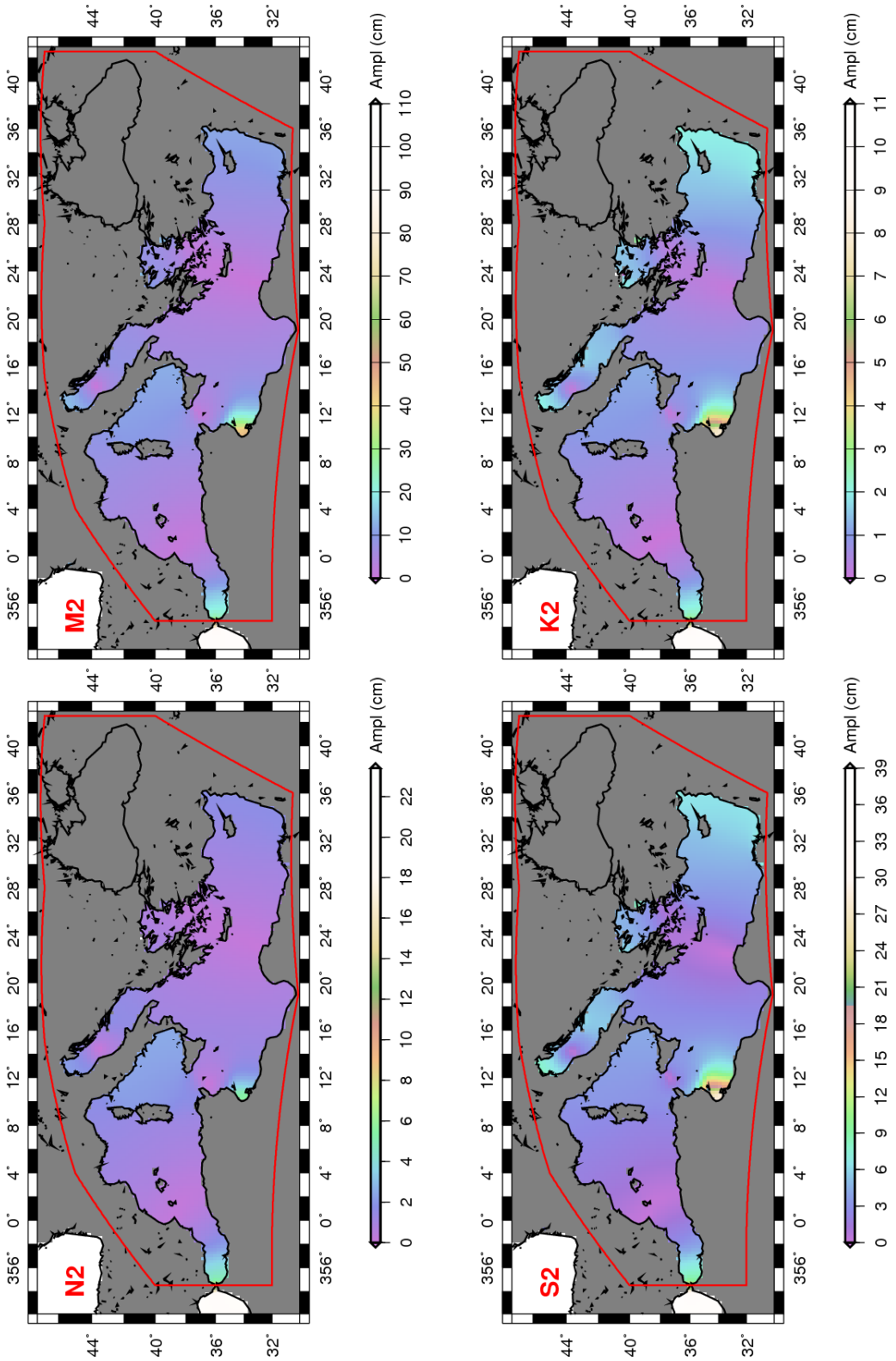

Figure 4.15: Amplitude (cm) of the semidiurnal tidal components (N_2, M_2, S_2, K_2) in the Mediterranean region using TPXO7.2 ocean global model.

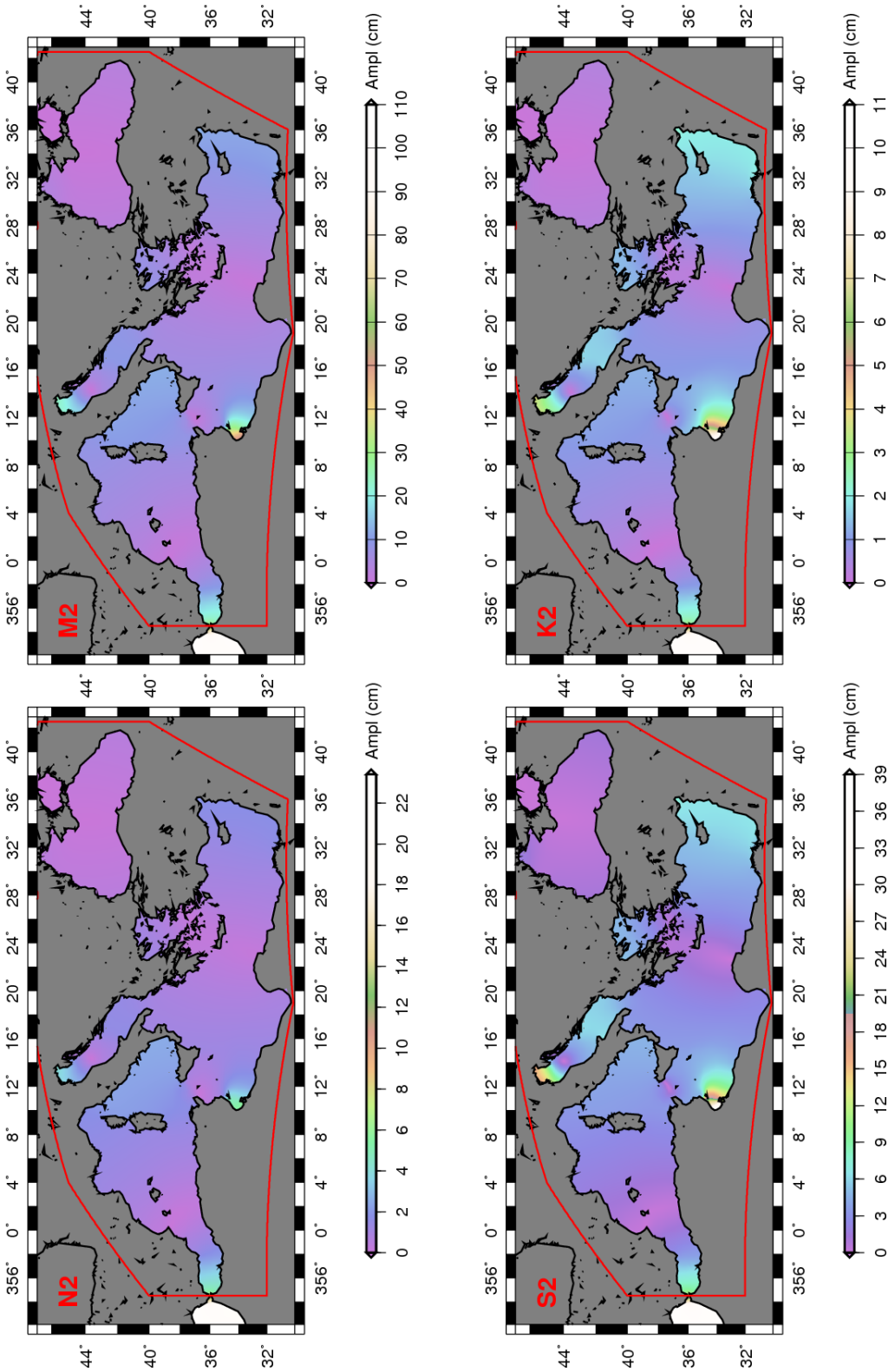

Figure 4.16: Amplitude (cm) of the semidiurnal tidal components (N_2, M_2, S_2, K_2) in the Mediterranean region using the local Mediterranean Sea model.

BA interferometer

Ocean model	Q_1		O_1		P_1		K_1	
	A	ϕ	A	ϕ	A	ϕ	A	ϕ
TPXO7.2	0.951	-17.886	4.796	-17.004	2.237	-14.201	6.810	-13.802
CSR4.0	0.951	-18.115	4.792	16.990	2.235	-14.222	6.802	-13.791
GOT00.2	0.953	-17.813	4.792	-16.996	2.240	-14.252	6.803	-13.781

Table 4.5: Amplitude A ($n\varepsilon$) and phase ϕ (degrees) of diurnal tidal components for BA interferometer using different global ocean models integrated by the local Mediterranean Sea model. Earth model for mass-loading Green functions: contap; Love numbers: IERS 2003.

BC interferometer

Ocean model	Q_1		O_1		P_1		K_1	
	A	ϕ	A	ϕ	A	ϕ	A	ϕ
TPXO7.2	1.234	12.748	6.601	12.737	3.089	11.256	9.335	10.988
CSR4.0	1.237	12.958	6.592	12.803	3.089	11.329	9.314	11.008
GOT00.2	1.235	12.845	6.595	12.836	3.092	11.248	9.331	11.017

Table 4.6: Amplitude A ($n\varepsilon$) and phase ϕ (degrees) of diurnal tidal components for BC interferometer using different global ocean models integrated by the local Mediterranean Sea model. Earth model for mass-loading Green functions: contap; Love numbers: IERS 2003.

BA interferometer

	SNRE		Ocean loading		Expected total		Observed	
	A	ϕ	A	ϕ	A	ϕ	A	ϕ
Q_1	0.925	-17.827	0.027	19.961	0.929	-19.718	0.872	-18.658
O_1	4.831	-17.830	0.077	99.000	4.690	-19.120	4.692	-18.833
P_1	2.248	-17.827	0.142	78.319	2.179	-16.320	1.977	-18.400
K_1	6.794	-17.827	0.478	72.311	6.614	-15.931	4.918	-22.298
N_2	2.112	17.053	0.297	80.334	1.988	26.325	2.007	26.803
M_2	11.030	17.053	1.607	68.349	10.595	25.765	10.590	25.740
K_2	1.390	17.053	0.180	59.538	1.336	24.849	1.355	25.760

Table 4.7: Amplitudes ($n\varepsilon$) and phases (degrees) of solid SNRE, ocean loading, expected total (sum of solid SNRE and ocean loading tidal strain corrected for local effects) and observed tidal strain for BA. Ocean model: TPXO7.2 and local Mediterranean Sea model; Earth model for mass-loading Green's functions: contap; Love numbers: IERS 2003.

by about 0.3 degrees from the values computed using the other models.

In what follows global ocean model TPXO7.2 is integrated by the local Mediterranean Sea model. Ocean loading affects amplitude of diurnal tides for less than 5% and phase for less than 5 degrees (see Tables 4.7 and 4.8, and Fig. 4.17). The ocean loading correction essentially consists in a small rotation of phasors, whose amount and sign depend on the tidal component and interferometer.

The discrepancies between tidal predictions and observations out of the Free Core Resonance spectral region can be substantially recovered taking local distortion effects into account.

As regards ocean loading effects on Ψ_1 and Φ_1, since their frequencies are close to the K_1 one and J_1 and OO_1 are not included in the local Mediterranean Sea model, it is possible to apply a linear extrapolation from P_1 and K_1 to estimate them. For doing that, following Ref. [64], tidal admittance is separated into two factors, one of which takes account of the FCR effects on the ocean loading. Both the expressions of tidal admittance in IERS 2003 [94] and in Ref. [102] provide analogous results.

The distance of J_1 and OO_1 from K_1 makes it unreliable to estimate their loading by extrapolation; for this reason two completely different approaches are tested. In the

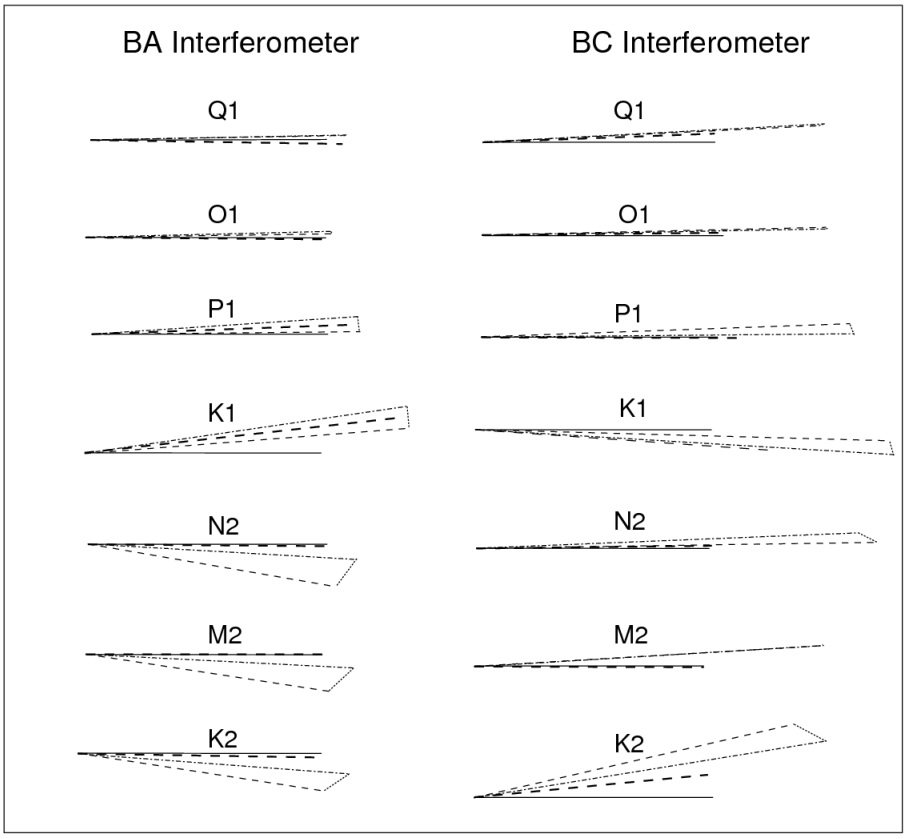

Figure 4.17: Phasor plot of solid SNRE (dashed lines), ocean loading (dotted lines), total (dashed dotted lines), expected total (sum of solid SNRE and ocean loading tidal strain corrected for local effects, long dashed lines) and observed (solid lines) tidal strain. Ocean model: TPXO7.2 and local Mediterranean Sea model; Earth model for mass-loading Green's functions: contap; Love numbers: IERS 2003. Amplitudes are normalized to the amplitude of the observed tidal strain and phases given with respect to the phase of the observed tidal strain.

BC interferometer

	SNRE		Ocean loading		Expected total		Observed	
	A	ϕ	A	ϕ	A	ϕ	A	ϕ
Q_1	1.256	13.031	0.023	-151.487	0.861	12.389	0.863	10.257
O_1	6.559	13.030	0.055	-25.470	4.600	12.320	4.588	11.747
P_1	3.052	13.031	0.102	-56.781	2.154	10.841	1.954	10.987
K_1	9.224	13.031	0.349	-59.555	6.507	10.581	5.252	14.558
N_2	1.023	-37.236	0.066	113.613	0.630	-38.935	0.623	-39.555
M_2	5.345	-37.236	0.034	-24.513	3.509	-40.782	3.512	-40.615
K_2	0.674	-37.236	0.079	-78.153	0.481	-44.715	0.490	-50.203

Table 4.8: Amplitudes ($n\varepsilon$) and phases (degrees) of solid SNRE, ocean loading, expected total (sum of solid SNRE and ocean loading tidal strain corrected for local effects) and observed tidal strain for BC. Ocean model: TPXO7.2 and local Mediterranean Sea model; Earth model for mass-loading Green's functions: contap; Love numbers: IERS 2003.

former approach a mere rotation is applied to the tidal phasors, like those observed for Q_1, O_1, P_1, and K_1 (4 degrees anticlockwise for BA, 2 degrees clockwise for BC). In the latter one all the discrepancies between observations and predictions (spherical non-rotating Earth, SNRE, corrected for local distortions) are ascribed to ocean loading. It will show that the retrieved FCR parameters are quite the same for both cases, although the estimated loadings are different. This result is not surprising, since J_1 and OO_1 do not influence the determination of the FCR parameters significantly.

After applying the ocean loading corrections, predicted and observed tides still show differences, whose most plausible explanation involves siting effects (e.g. cavity effects, surface topography and rock inhomogeneities) that can affect strain measurements significantly, so that locally measured strain is not equal to the large-scale Earth strain.

4.3.2 FCR parameter estimation

For the FCR parameter estimation a comparison between measurements and model predictions of 8 diurnal tidal constituents (namely Q_1, O_1, P_1, K_1, Ψ_1, Φ_1, J_1 and OO_1) is performed, through a joint fit on BA and BC tidal parameters, using the $\mathcal{L}^1$ misfit function.

VAV03 results

	BA		BC	
harmonic	A	ϕ	A	ϕ
Q_1	0.872	-18.658	0.863	10.257
O_1	4.692	-18.833	4.588	11.747
P_1	1.977	-18.400	1.954	10.987
K_1	0.534	-3.902	0.324	-58.430
Ψ_1	4.918	-22.298	5.252	14.558
Φ_1	0.136	0.155	0.144	18.301
J_1	0.129	-41.156	0.112	-2.205
OO_1	0.222	-15.555	0.210	5.842

Table 4.9: Amplitudes A ($n\varepsilon$) and phases ϕ (degrees) of observed tidal strain for BA and BC interferometers, obtained using VAV03 code and corrected for effects of pre-whitening.

As measurements the amplitudes of the sine and cosine terms of the observed tides are used, obtained from the output amplitudes and phases of the VAV03 code (see Appendix A) applied on the pre-whitened strain series. Retrieved tidal parameters are corrected for the effects of pre-whitening (Table 4.9) and ocean loading. As regards pre-whitening

$$A = \frac{A_{PW}}{2\sin(2\pi f \Delta t/2)} \qquad \varphi = \varphi_{PW} - 90^\circ \tag{4.40}$$

where A_{PW} (φ_{PW}) and A (φ) are the amplitude (phase) for the pre-whitened and real series respectively, f is frequency and Δt is sampling time (1800 s).

The tidal analysis results have been checked against those obtained using Baytap08 [47] (see Appendix B), LSSA [48] (see Appendix C), and GSLAB code [44]. These codes give amplitudes and phases which differ from one another less than the VAV03 standard deviations (std). As a consequence, the VAV03 stds are used to estimate the measurement sine and cosine uncertainties. The only exceptions are Ψ_1 and Φ_1, whose phases differ more than the VAV03 stds (6 to 8 degrees) when using different codes. A 20 degrees uncertainty is attributed to both phases and measurement sine and cosine uncertainties are estimated accordingly. This value is arbitrary, but using other phase uncertainties (e. g. 40 degrees) the results do not change. Predictions are calculated

after applying the appropriate strain cross-coupling corrections.

In all the inversions $1/T_{FCN}$, $\log Q$ and the complex Love and Shida numbers, $\Re(h_0 - 3l_0)$, $\Re(h_1 - 3l_1)$ and $\Re(l_0)$ are free, while $\Re(l_1)$, $\Im(l_1)$, $\Im(l_0)$, $\Im(h_0 - 3l_0)$ and $\Im(h_1 - 3l_1)$ can be free or fixed to their IERS 2003 values [94].

Ocean loading (corrected for site effects) is subtracted from the retrieved Q_1, O_1, P_1 and K_1 amplitudes and phases, by using contap or gbavap mass-loading Green functions; Ψ_1 and Φ_1 ocean loadings are obtained by extrapolation from P_1 and K_1; J_1 and OO_1 ocean loadings are estimated using a mere phasor rotation or a full correction of discrepancies between observations and predictions.

In what follows, to indicate each of the eight different cases a three-letter abbreviation is used. The first letter is C for contap or G for gbavap; the second letter is R for J_1 and OO_1 phasor rotation or D for full discrepancy correction; the third letter indicates if all the complex Love and Shida numbers are free (A) or some of them are fixed (B).

Misfit minimization is performed using Adaptive Simulated Annealing (ASA, see Ref. [103] for details) which proposes to find the best global fit of a non-linear non-convex misfit function over a D-dimensional space, self-optimizing its own cooling parameters recursively. Parameter uncertainty assessment is performed inverting synthetic tidal parameter sets, obtained from the real one by adding a DEN random noise whose amplitude for each measurement datum is given by its uncertainty.

To invert synthetics a fast downhill simplex algorithm [95] is used, starting from the relevant best-fit model obtained running ASA. For the sake of comparison, the marginal probability of model parameters are estimated also by using NA (Neighbourhood Algorithm) and NAB (NA-Bayes). NA [104] generates ensembles of models which preferentially sample the good data fitting regions of the parameter space; NAB [105] uses the entire ensemble of models produced by NA and derives information from them, in the form of bayesian measures of resolution, covariance, and marginal Probability Density Function (PDF).

For each case ASA is used for determining the best-fit FCR parameters; then 400000 synthetic tidal parameter sets are generated, adding a DEN random noise, and inverted by simplex. The retrieved distributions of T_{FCN} (Fig. 4.18) give its PDF. The eight different PDFs can be divided into two groups. The former group includes all the inversions with 10 free parameters (CRA, CDA, GRA, and GDA; dashed lines); its distributions are peaked around 430 sidereal days (as obtained in Ref. [83] from VLBI data). The latter group includes all the inversions with 5 free parameters (CRB, CDB,

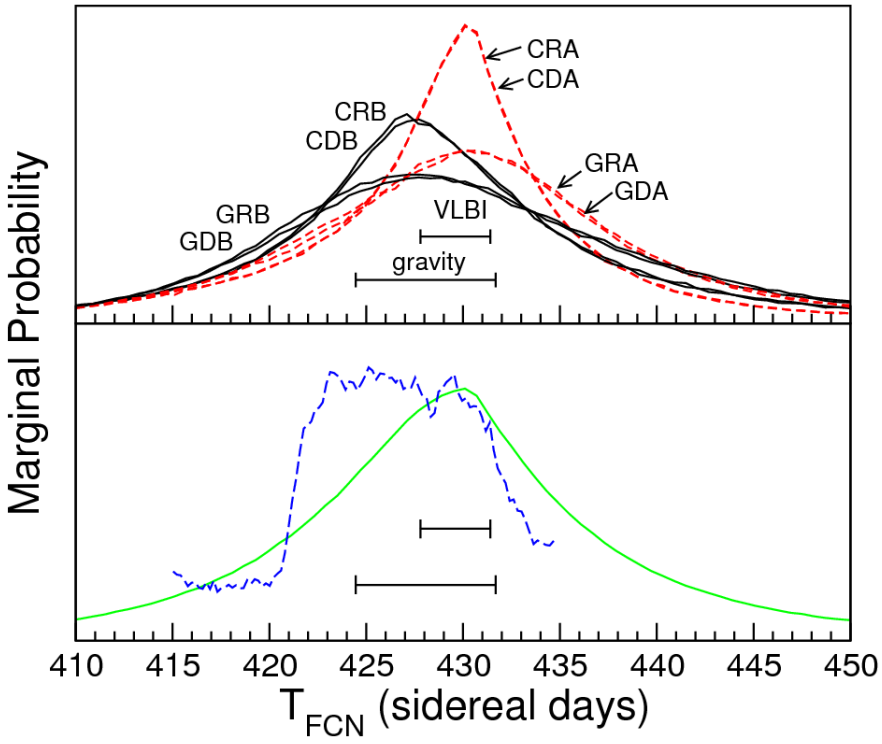

Figure 4.18: T_{FCN} PDFs obtained analysing pre-whitened (top panel) strain series and inverting synthetic tidal parameters obtained by adding a null-mean random noise to real data. The red dashed line distributions (CRA, CDA, GRA and GDA) are peaked around 430 sidereal days, all the others (black solid lines) around 427 sidereal days. The bottom panel shows the mean PDF (green solid line) and an example of T_{FCN} PDFs generated by NAB (blue dashed line, CDB inversion). All the results are consistent with those obtained from the analysis of gravity and VLBI data in Ref. [83] (horizontal bars).

GRB, and GDB; solid lines); its distributions are peaked around 427 sidereal days (as obtained in Ref. [83] from gravity data). The mean PDF (bottom panel of Fig. 4.18, green solid line) gives a conservative picture of all results.

Cumulative distributions (Fig. 4.19) show that at the 80% (50%) confidence level the T_{FCN} value is between 417.1 (425.5) and 439.3 (433.3) sidereal days for CRA and CDA, 418.3 (424.6) and 444.6 (436.4) sidereal days for GRA and GDA, 418.2 (423.9) and 444.7 (434.6) sidereal days for CRB and CDB, and 417.4 (423.3) and 447.3 (437.2) sidereal days for GRB and GDB. PDFs do not depend on the estimation of J_1 and OO_1 ocean loading. PDF widths are somewhat larger for B cases than for A cases, consistently with the results shown in Subsection 4.2.2, and much larger for G mass-loading Green's functions than C ones, maybe indicating a worse ocean loading estimate.

The cumulative distribution of mean PDF (bottom panel of Fig. 4.18, green solid line) indicates that the T_{FCN} value is between 418.2 (428.3) and 444.1 (435.2) sidereal days at the 80% (50%) confidence level, taking different Earth models, ocean loading estimates, and number of free parameters into account.

The blue dashed curve in Fig. 4.18 gives one example (CDB) of the T_{FCN} PDFs generated by NAB. It is characterized by a broad maximum from about 431 down to 422 sidereal days. The existence of the broad maximum is linked to the weak dependence of misfit on T_{FCN} inside the same range, as evident from Fig. 4.20. Similar curves are obtained in the other cases.

Q is poorly constrained. The Q values returned by the inversion code (ASA) are usually large ($> 10^6$), but the only appreciable effect of decreasing Q down to 20000 [22] is a change of the Ψ_1 phase by less than 2 degrees, i. e. much less than the estimated uncertainties. As a consequence, Q PDFs obtained using NAB are neither flat or peaked at large Q values, but show a case-to-case pronounced maximum in the 10000 to 50000 range (see Fig. 4.21). Fixing Q to values spanning several orders of magnitude has no consequence on the retrieved best-fit values of T_{FCN}.

The resonance strength is dominated by $\Re\left(h_1 - 3l_1\right)$, (Eqs. 4.29 and 4.32, $k = 1$) which is left free in the inversions. The curves in the uper plot of Fig. 4.22 show its marginal probability distribution obtained after inverting synthetics or using NAB and give an independent estimate of $\Re\left(h_1 - 3l_1\right)$ with respect to other works. All the PDFs are consistent with one another and in agreement with results in Ref. [94] (vertical line). The NAB CRA PDF appears much larger than the others, maybe because of some difficulty of NA in sampling the parameter space efficiently when the cost function

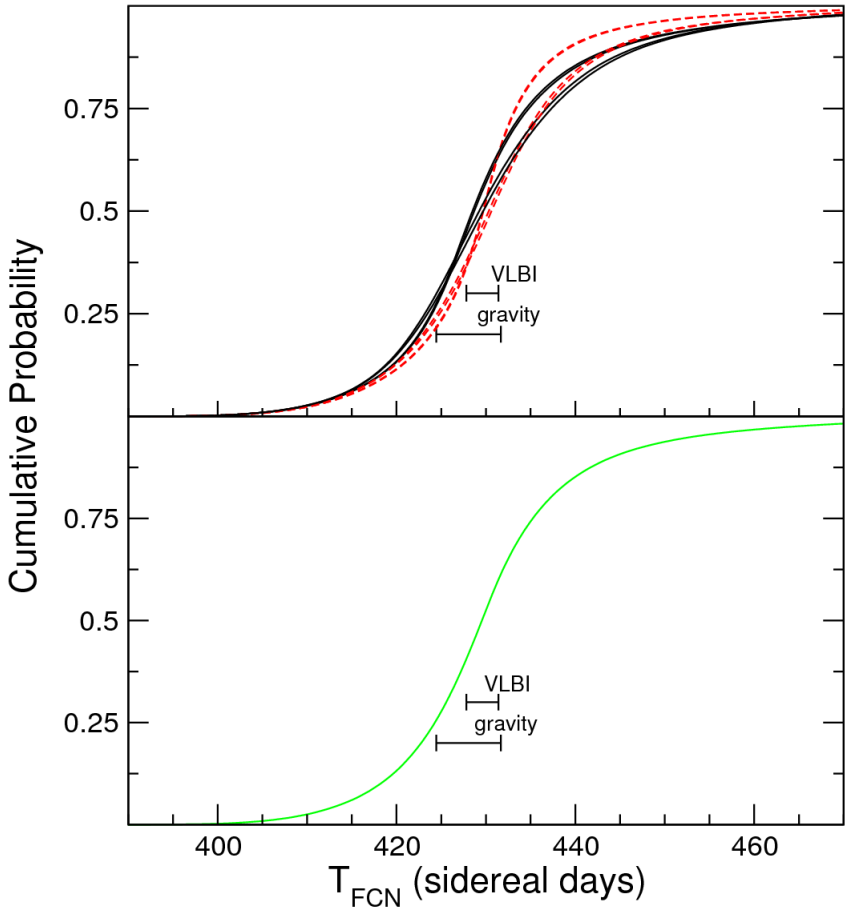

Figure 4.19: Cumulative distributions of T_{FCN} obtained analysing pre-whitened (top panel) strain series and inverting synthetic tidal parameters. Red dashed lines: CRA, CDA, GRA and GDA (whose distributions are peaked around 430 sidereal days), black solid lines: CRB, CDB, GRB and GDB (peaked around 427 sidereal days). The bottom panel shows the mean PDF (green solid line). Horizontal bars: results from the analysis of gravity and VLBI data in Ref. [83].

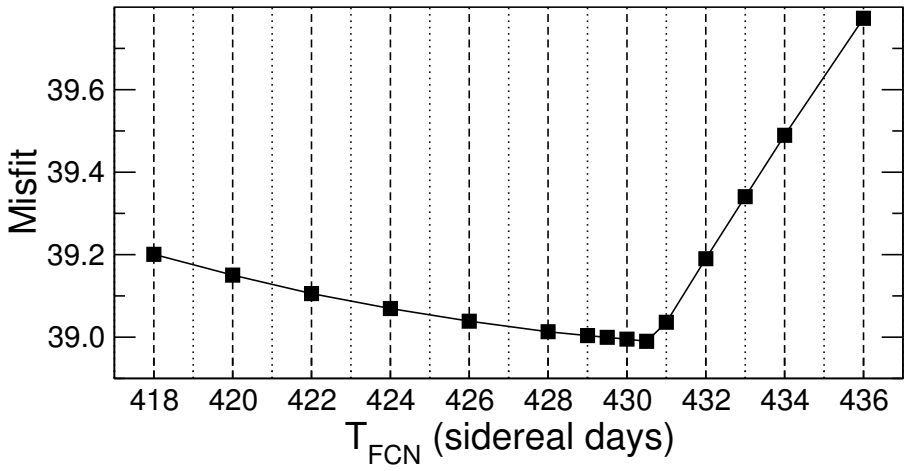

Figure 4.20: Misfit variation as a function of T_{FCN} for pre-whitened records. The other nine model parameters are left free in the inversions. The misfit curve is strongly asymmetric, increasing more rapidly at the right side of the minimum (431.5 sidereal days).

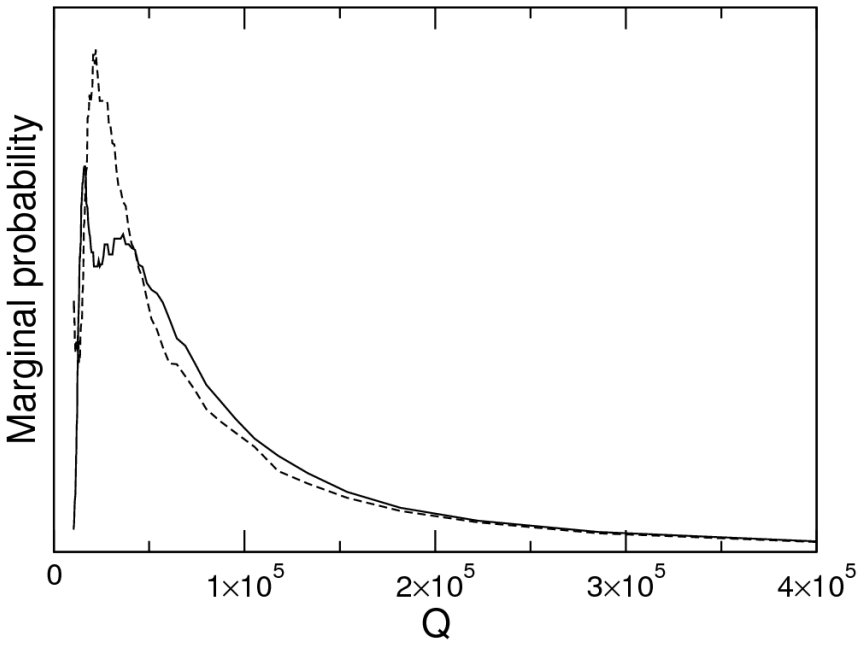

Figure 4.21: Marginal probability of the quality factor Q obtained for CRA and CDA (solid and dashed lines respectively) by NAB.

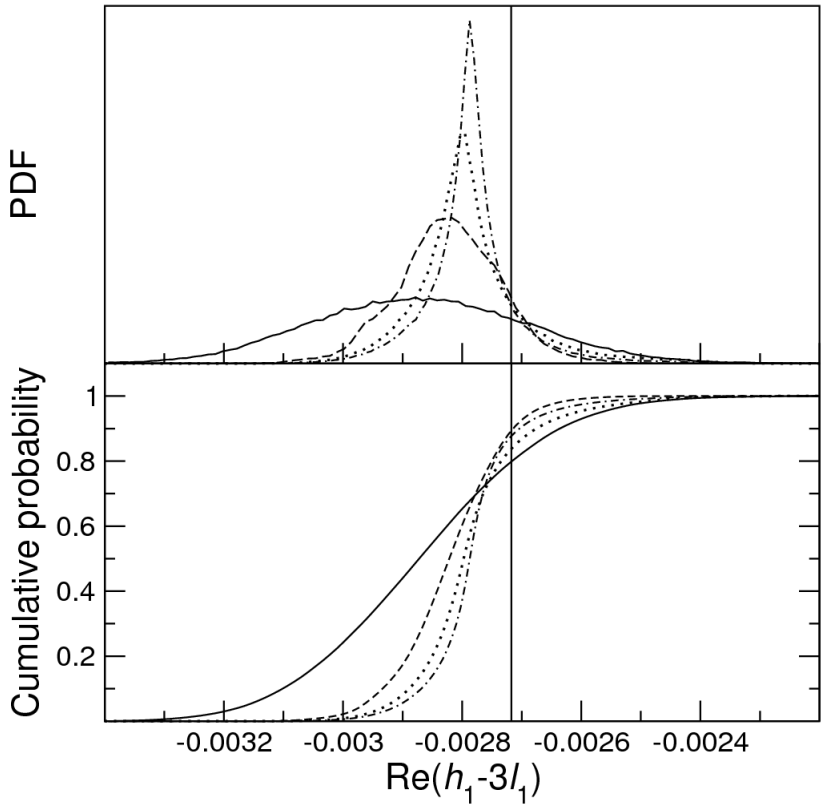

Figure 4.22: PDFs and cumulative probability of the resonance strength obtained for CRA and CRB cases by NAB (solid and dashed lines respectively) and after inverting synthetic tidal parameters (dashed-dotted and dotted lines respectively). All the PDFs are consistent with one another and with IERS 2003 value [94] (vertical line).

is slightly sensitive to some parameters. The existence of this difficulty is supported by the fact that the minimum obtained by NA is slightly worse (higher misfit) than that obtained by ASA. Since $\Re\left(h_1 - 3l_1\right)$ enters in Eq. 4.32 through multiplication of $(\alpha + \beta)$, Fig. 4.22 is an a-posteriori validation of the goodness of coupling modeling, being the results in agreement with Ref. [94].

The good agreement in the diurnal band between measured tidal parameters, corrected for ocean loading effects, and predicted curves for both BA and BC interferometers is shown in Fig. 4.23.

To make it easier comparing these results with those published for gravity tides, the amplitudes of the in-phase and out-of-phase (with respect to SNRE tides) terms, normalized to the SNRE tidal amplitudes are plotted. In all cases but out-of-phase Φ_1 for BA the discrepancies are inside the uncertainties and the fit goodness seems comparable to that from gravity data (see for example Fig. 4.24 from Ref. [83]). The agreement be-

tween observations and predictions looks better than in any previous work that makes use of strain tides (see for example Fig. 4.25 from Ref. [92]).

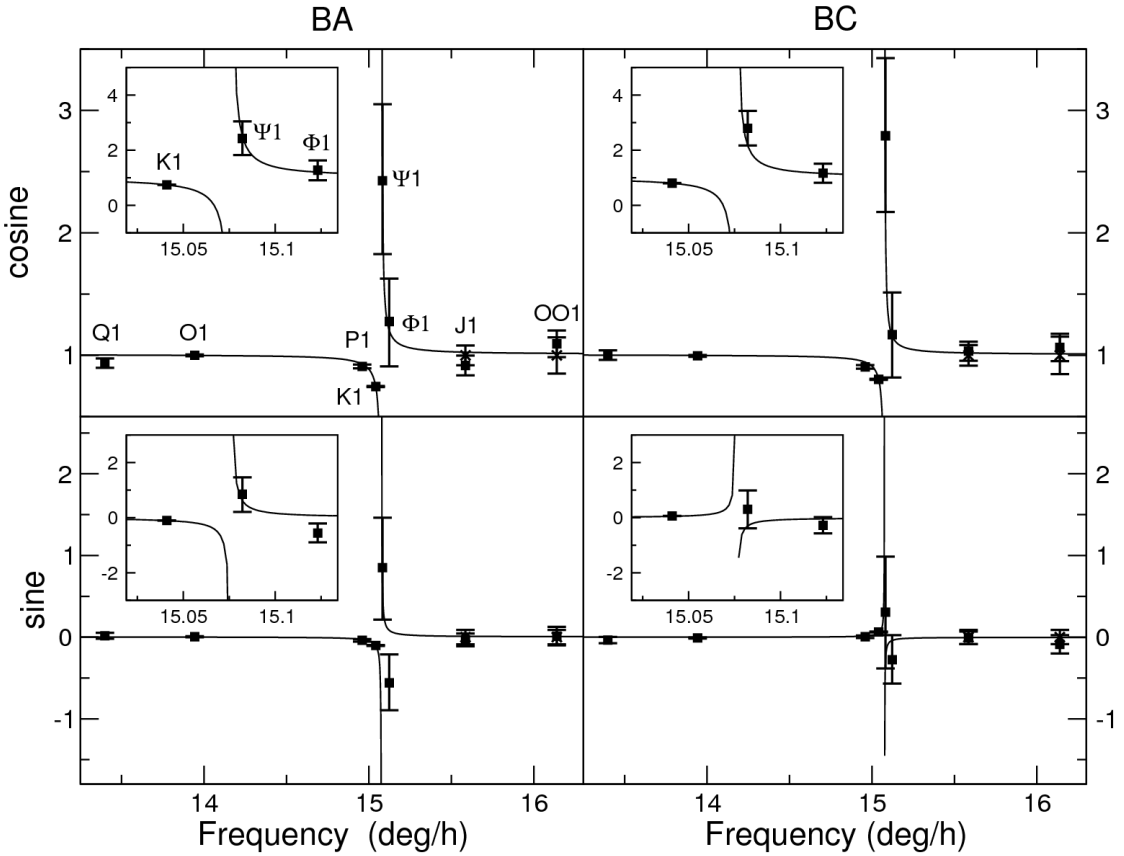

Figure 4.23: Amplitudes of the in-phase and out-of-phase (with respect to SNRE tides) terms, normalized to the SNRE tidal amplitudes, for BA and BC obtained by analysing pre-whitened records (squares, CRA; crosses, CDA). Error bars give twice the uncertainties from VAV03 tidal analysis. Insets represent an enlargement around the resonance.

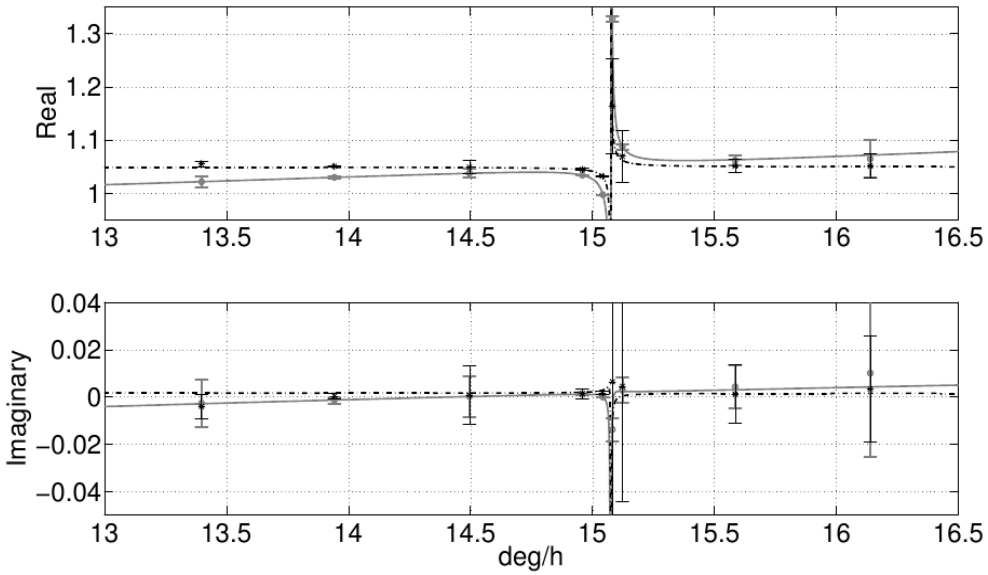

Figure 4.24: Observed transfer functions for nutation (dots) and gravity (stars) obtained from VLBI and SG measurements respectively. Solid and dashed lines, theoretical transfer function for nutation and gravity respectively. Figure 3 in Ref. [83].

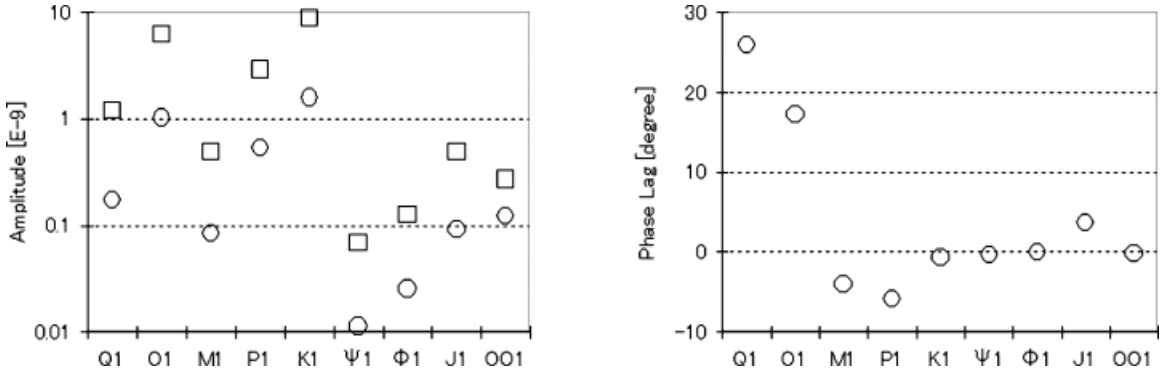

Figure 4.25: Left plot: comparison between amplitude (circle) of the oceanic loading tides and amplitude of the solid Earth tides (square); right plot: phases of the oceanic loading tides (positive phase indicates lag). Figure 8 in Ref. [92].

4.4 FCR parameters from Gran Sasso and Baksan strain data

After the analysis of Gran Sasso strain data to investigate the FCN parameters, a joint analysis of these data and those from a third laser interferometer installed in the SSAI (Sternberg State Astronomical Institute) Baksan (Russia) station is performed. The same procedure previously outlined, is followed.

4.4.1 Baksan available data and environmental effects

The SSAI (Sternberg State Astronomical Institute) Baksan station is located in the Elbrus area (Baksan gorge) of the Kabardino-Balkaria region 30 km southwest of the town of Tyrnyauz; the distance of the station from Elbrus Volcano is 20 km.

The interferometer is mounted at a mark of 650 m along the main tunnel of the Baksan neutrino observatory, Institute of Nuclear Research (INR), Russian Academy of Sciences (RAS) and located 400 m below the Earth's surface.

The Baksan laser interferometer (whose azimuth is about -29 degrees) is a Michelson two-beam unequal-arm interferometer operating in the regime of separated beams [106, 107]. The lengths of its measuring and reference arms are about 75 and 0.3 meters respectively. The optical elements of the interferometer are mounted in two cylindrical vacuum chambers whose lower parts are built onto pedestals. The supporting pedestals of the interferometer are concrete pillars 1.5 meters depth, rigidly connected to the rock, and prominent beyond the lower level of the tunnel for 30 cm. The chambers are connected with each other by three bellows and vacuum pipes (30 cm in diameter). In a stationary regime, the pressure in the system is 1.33×10^{-2} Pa. An electronic recording system allows to operate in a wide frequency range, from ultralow (limited only by the time interval of continuous observations) to thousands of hertz. The instrumental resolution of the strain measurements is 2.3×10^{-13}.

About six years of strain recorded at Baksan (Fig. 4.26) are used together with about eight years of data from Gran Sasso to estimate the FCR parameters.

Fig. 4.27 shows the power spectral density for BAKSAN data in the diurnal tidal band, the apparent power spectral density (where the actual record length is 2270 days) of the main tidal harmonics (Q_1, O_1, P_1, K_1, Ψ_1, Φ_1, J_1 and OO_1) and also the PSD obtained using about 85- and 680-day-long windows (dashed lines). Increasing window length

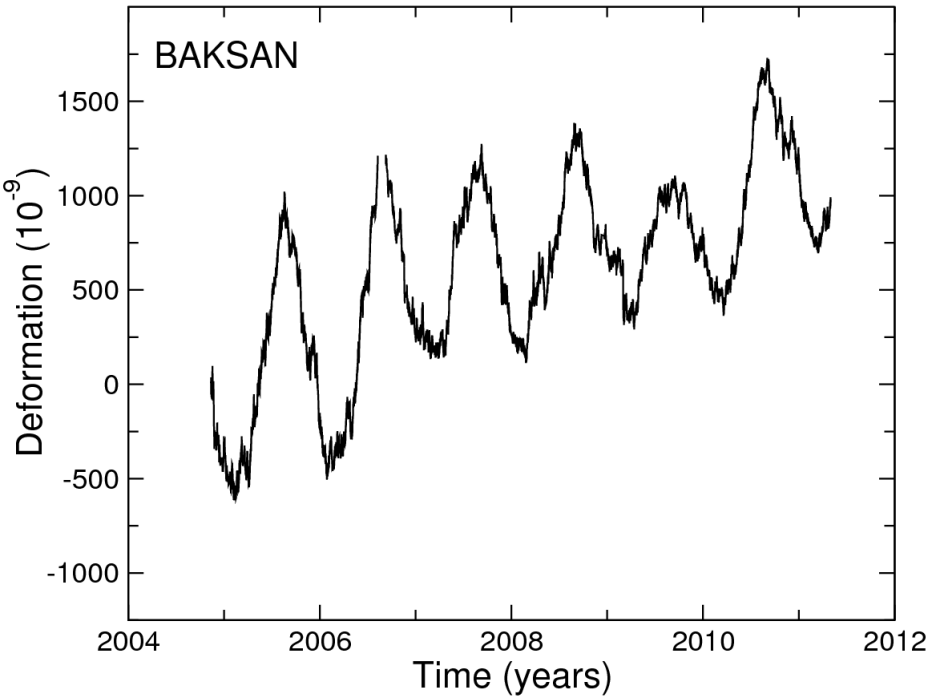

Figure 4.26: Strain recorded at BAKSAN, decimated at 2 cycles per hour, and used to estimate the FCR parameters.

decreases spectrum stability, but the increased frequency resolution makes it easier to detect possible anomalous periodic signals, e. g. of anthropic origin. Spectra suggest the presence of contaminations attributable to typical environmental parameters like atmospheric temperature and barometric pressure, and anthropogenic activity.

Three records of temperature and one of barometric pressure are available for Baksan; they are as long as the strain record but characterized by several additional breaks. The three temperature sensors are installed in the lower part of the vacuum chamber in the laser box (T_{box}), on the surface of the vacuum pipe (T_{gal}), and on the concrete basement below the tunnel floor level (T_{rock}). Air temperature fluctuates by about 6°C and 1°C on monthly and daily time scales respectively.

Also in this case, several attempts to correct strain for temperature and pressure effects are performed, by comparing VAV03 results obtained through a joint analysis of strain and one environmental sequence with those obtained analysing strain only. The same strain data are used with or without the environmental sequence. Also a comparison between residual spectra (obtained following the previously outlined procedure) is performed, but using an about 170-day-long moving window (see Fig. 4.28 as regards the diurnal band).

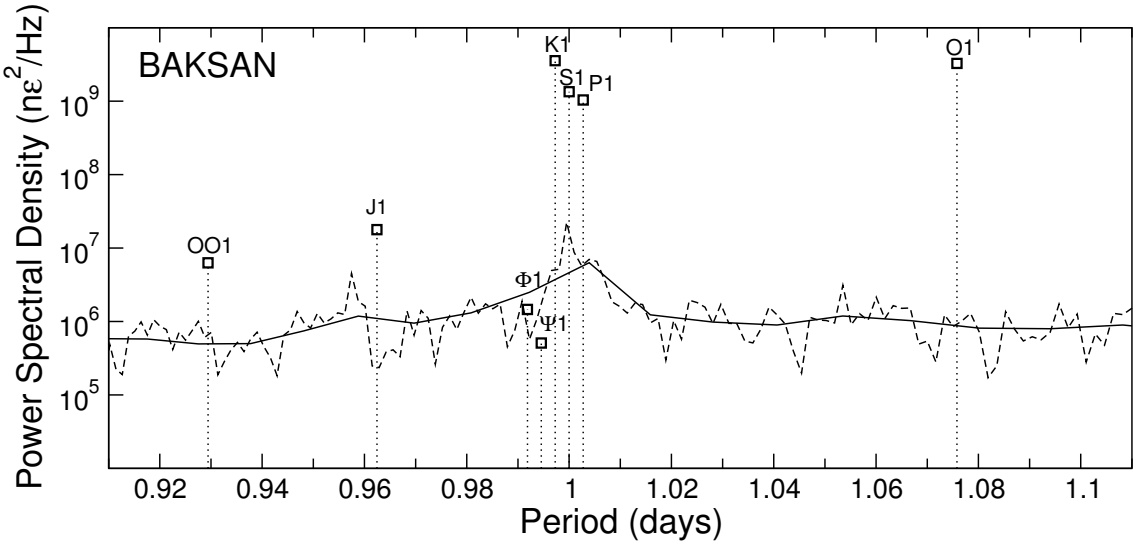

Figure 4.27: PSD of data recorded at Baksan in the diurnal tidal band. Solid lines, PSDs obtained with an about 85-day-long moving window; dashed lines, PSDs obtained with an about 680-day-long moving window; vertical lines, apparent PSDs from VAV03 analysis.

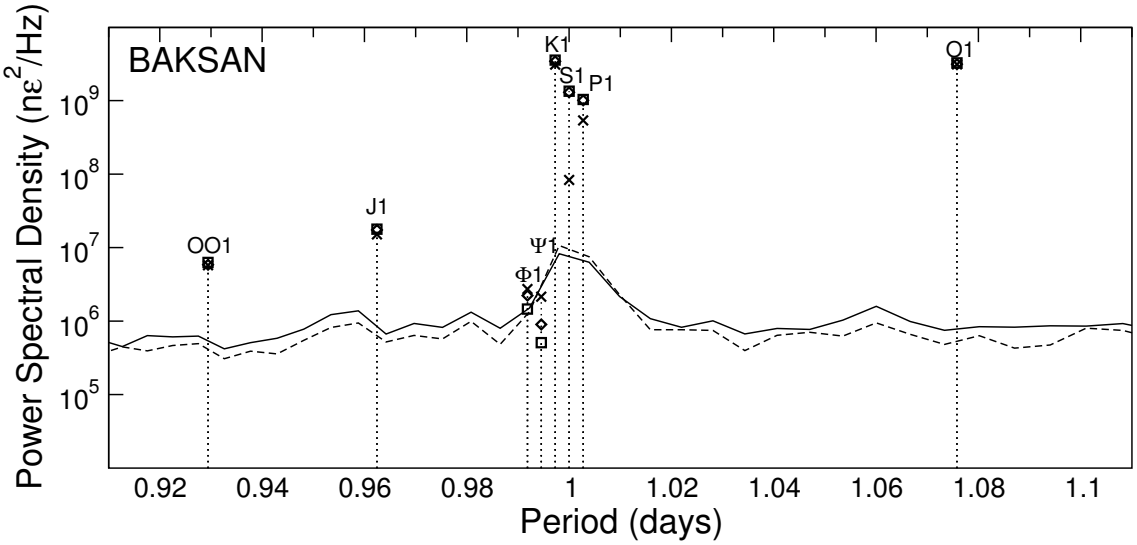

Figure 4.28: PSD in the diurnal band, with and without T_{gal} corrections. The strain series is as long as the related temperature sequence (about 2130 days). Solid lines, residuals of strain series obtained using VAV03 without correcting for temperature; dashed lines, VAV03 residuals of strain series correcting for temperature; squares, apparent PSDs from VAV03 analysis on the whole strain data records; diamonds and crosses, apparent PSDs from VAV03 analysis on strain records as long as T_{gal} ones, with or without T_{gal} corrections respectively.

VAV03 analyses indicate that it is necessary to correct BAKSAN data for the effect of T_{gal}. Measured-to-theoretical amplitude ratio at 1 cycle-per-day decreases from 8.8 to 2.2 when taking T_{gal} into account. However, even after correcting BAKSAN strain data for T_{gal} effects, the Ψ_1 apparent PSD remains below the noise level, thus it is impossible to give reliable estimates of its tidal parameters. Moreover, when using different tidal analysis codes, P_1 tidal parameters differ by more than the uncertainties attributed by the codes.

4.4.2 Ocean loading and strain cross-coupling

Ocean loading effects are estimated using SPOTL [97] (see Appendix D). Mass-loading Green functions are computed for gbavap, contap and ocenap, representative of an average Earth, a thick continental crust and a thin oceanic crust respectively. Three recent high resolution global ocean models are used, i. e. TPXO7-atlas2011 (`http://volkov.oce.orst.edu/tides/`) developed at Oregon State University [101, 99], FES2004 [108], the most recent version of the Grenoble tide models, and HAMTIDE (`http://icdc.zmaw.de/hamtide.html`), developed at Institut für Meereskunde of the Hamburg University.

TPXO7-atlas2011 is an updated version of TPXO7.2; it best-fits, in a least-square sense, the Laplace Tidal Equations and averaged data from TOPEX/Poseidon and Jason, two consecutive satellite missions mapping ocean surface topography (`http://sealevel.jpl.nasa.gov/`). The tides are provided as complex amplitudes of earth-relative sea-surface elevation for eight primary (Q_1, O_1, P_1, K_1, N_2, M_2, S_2, K_2), two long period (M_f, M_m) and three non-linear (M_4, MS_4, MN_4) harmonic constituents, on a 1440×721, $1/4°$ resolution full global grid. TPXO7-atlas2011 incorporates existing higher resolution local solutions, which are interpolated onto the coarser grid of the global model in coastal areas. It fits coastal tide gauges significantly better than TPXO7.2.

FES2004 is a fully revised version of the global finite-element hydrodynamic tide solutions [109], which uses a refined mesh and assimilates tide gauge and altimetry data from TOPEX/Poseidon and Earth-observing satellites (ERS) data. It contains the same eight primary diurnal and semidiurnal tides (Q_1, O_1, P_1, K_1, N_2, M_2, S_2, K_2) as TPXO7-atlas2011, on a $1/8°$ resolution full global grid.

HAMTIDE solution is obtained by a direct minimization in a least-square sense of cross-calibrated altimeter data from TOPEX/Poseidon, Jason-1, ERS-1, ERS-2, ENVISAT

	solid SNRE		ocean loading		Black Sea effect	
harmonic	A	ϕ	A	ϕ	A	ϕ
Q_1	0.976	-19.264	0.044	-45.660	0.004	-131.059
O_1	5.097	-19.264	0.202	-55.829	0.036	-98.203
P_1	2.372	-19.264	0.085	-53.602	0.016	-99.886
K_1	7.168	-19.264	0.286	-55.441	0.056	-99.038
N_2	1.991	21.292	0.036	-58.220	0.019	-113.982
M_2	10.396	21.292	0.187	-74.877	0.119	-117.275
S_2	4.837	21.292	0.106	-88.314	0.051	-117.078
K_2	1.311	21.292	0.026	-87.043	0.011	-114.152

Table 4.10: Amplitudes A ($n\varepsilon$) and phases ϕ (degrees) of solid SNRE, total ocean loading using contap Earth model and global TPXO7-atlas2011 ocean model, integrated by the local Mediterranean Sea and Indian Ocean models, and Black Sea ocean loading estimated using local Mediterranean Sea model.

and GFO satellite missions. This model provides Q_1, O_1, P_1, K_1, N_2, M_2, S_2, K_2 and M_4 constituents on a 1/8° resolution full global grid.

To improve loading predictions at the two strain stations two local models are used. The local model of the Mediterranean Sea at 1/30° resolution (`http://volkov.oce.orst.edu/tides/med.html`) is used for both Gran Sasso and Baksan stations, and in addition the local model of Indian Ocean at 1/12° resolution (`http://volkov.oce.orst.edu/tides/atlas.html`) is used for Baksan. The two local models include four diurnal (Q_1, O_1, P_1, K_1) and four semidiurnal (N_2, M_2, S_2, K_2) constituents.

Baksan is located between the Black Sea and the Caspian Sea, but no tidal model or tidal gauge data are available for the Caspian Sea. The Caspian Sea is a closed sea, whose dimensions are comparable to those of the Black Sea and whose distance from Baksan is about four times that of the Black Sea. It seems reasonable to expect the Caspian ocean loading to be much smaller than or at most comparable to the Black Sea one. This, in turn, results in about 1% of the solid tide (see Table 4.10). It seems reasonable to neglect possible Caspian Sea contributions to the ocean loading.

Fig. 4.29 compares ocean loading tidal strain estimated using global TPXO7-atlas2011 ocean model and three different Earth models (gbavap, contap, ocenap; see Tables 4.11 to 4.13).

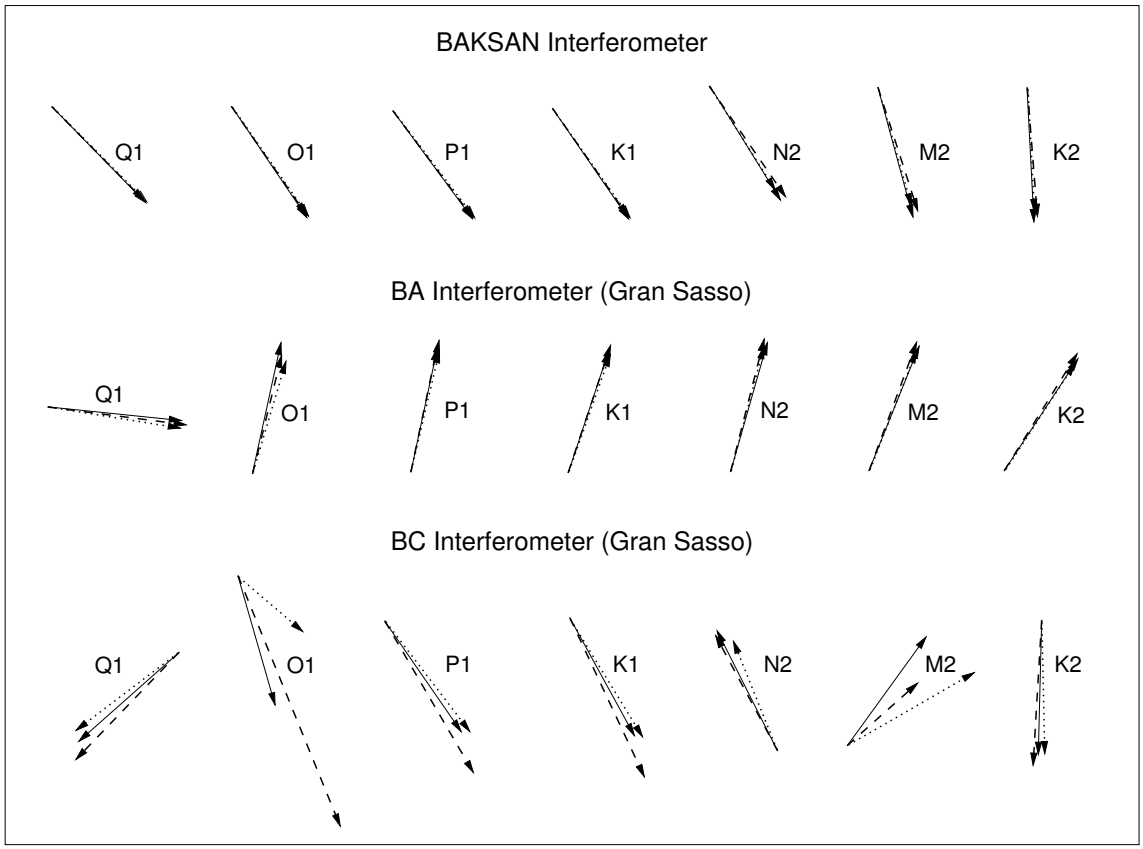

Figure 4.29: Phasor plot of ocean loading tidal strain using gbavap (dashed lines), contap (solid lines), and ocenap (dotted lines) Earth models. Ocean model: TPXO7-atlas2011, integrated by the local Mediterranean Sea and Indian Ocean models. Amplitudes are normalized to the amplitude obtained for contap (see Tables 4.11 to 4.13).

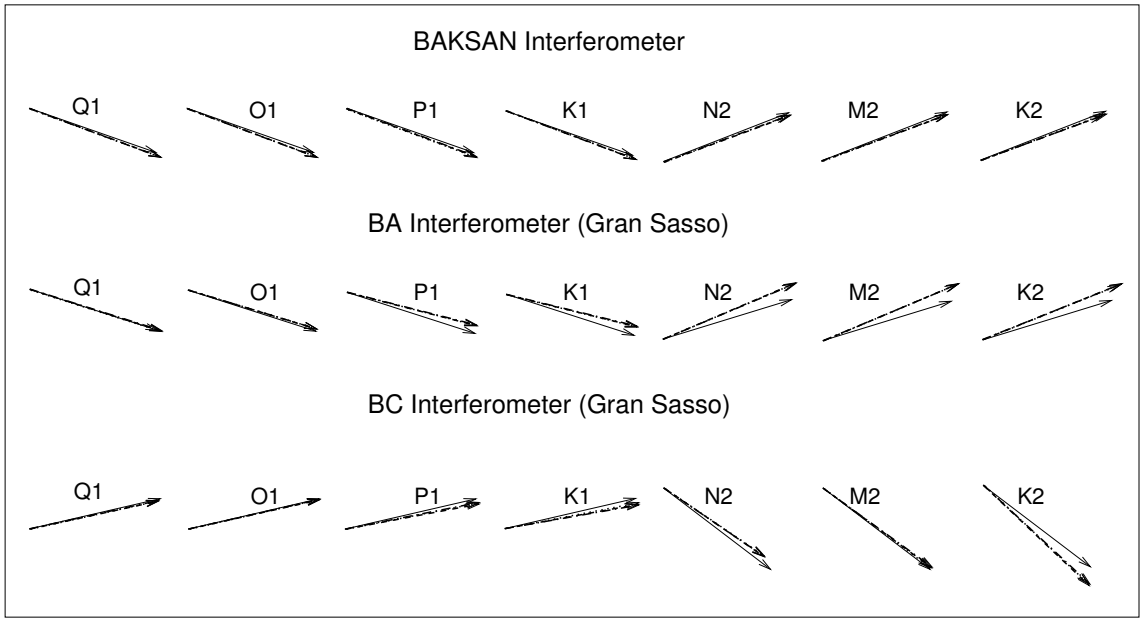

Figure 4.30: Phasor plot of solid SNRE tidal strain (solid lines) and expected total tidal strain using gbavap (dashed lines), contap (dashed-dotted lines), and ocenap (dotted lines) Earth models. Global TPXO7-atlas2011, integrated by local Mediterranean Sea and Indian Ocean models. Amplitudes are normalized to the amplitude obtained of solid SNRE tidal strain (see Tables 4.11 to 4.13).

The results differ by less than 13% in amplitude and 3 degrees in phase for both BAKSAN and BA interferometers. The discrepancies are much higher for BC interferometer, up to about a factor two in amplitude and 34 degrees in phase. In any case, ocean loading tides are much smaller than solid SNRE ones and so the expected total tidal strain does not change substantially by more than 1% in amplitude and 1 degree in phase (see Fig. 4.30 and Tables 4.11 to 4.13) using the three different Earth models. As the plot detail, even if results from the three Earth model are very different, predictions are indistinguishable in all cases.

Fig. 4.31 compares ocean loading tidal strain estimated using contap as Earth model and three global ocean models at Baksan and Gran Sasso stations (TPXO7-atlas2011, FES2004, and HAMTIDE, see Tables 4.14 to 4.16).

The results differ by less than 12% in amplitude and 8 degrees in phase for BAKSAN, 11% in amplitude and 6 degrees in phase for BA, and 15% in amplitude and 14 degrees in phase for BC. Since ocean loading tides are much smaller than solid SNRE ones, expected total tidal strain does not change by more than 1% in amplitude and 1 degree in phase (see Fig. 4.32 and Tables 4.14 to 4.16) using TPXO7-atlas2011, FES2004,

Baksan interferometer

	solid SNRE		ocean loading		expected total	
harmonic	A	ϕ	A	ϕ	A	ϕ
			Gbavap Earth model			
Q_1	0.976	-19.264	0.043	-45.450	1.014	-20.332
O_1	5.097	-19.264	0.198	-55.353	5.258	-20.532
P_1	2.372	-19.264	0.084	-53.235	2.442	-20.360
K_1	7.168	-19.264	0.280	-55.013	7.398	-20.533
N_2	1.991	21.292	0.036	-55.379	1.999	20.302
M_2	10.396	21.292	0.181	-72.150	10.387	20.293
K_2	1.311	21.292	0.025	-85.522	1.304	20.247
			Contap Earth model			
Q_1	0.976	-19.264	0.044	-45.660	1.015	-20.357
O_1	5.097	-19.264	0.202	-55.829	5.261	-20.576
P_1	2.372	-19.264	0.085	-53.602	2.443	-20.395
K_1	7.168	-19.264	0.286	-55.441	7.401	-20.573
N_2	1.991	21.292	0.036	-58.220	1.997	20.267
M_2	10.396	21.292	0.187	-74.877	10.378	20.264
K_2	1.311	21.292	0.026	-87.043	1.303	20.229
			Ocenap Earth model			
Q_1	0.976	-19.264	0.044	-45.243	1.016	-20.351
O_1	5.097	-19.264	0.201	-55.133	5.261	-20.548
P_1	2.372	-19.264	0.085	-52.765	2.443	-20.364
K_1	7.168	-19.264	0.285	-54.571	7.403	-20.539
N_2	1.991	21.292	0.033	-57.622	1.978	20.589
M_2	10.396	21.292	0.171	-74.212	10.281	20.593
K_2	1.311	21.292	0.024	-87.025	1.291	20.550

Table 4.11: Amplitudes A ($n\varepsilon$) and phases ϕ (degrees) of solid SNRE, ocean loading and expected total tidal strain for BAKSAN using gbavap, contap and ocenap Earth models, and global TPXO7-atlas2011 integrated by the local Mediterranean Sea and Indian Ocean models.

BA interferometer

	solid SNRE		ocean loading		expected total	
harmonic	A	ϕ	A	ϕ	A	ϕ
			Gbavap Earth model			
Q_1	0.925	-17.827	0.028	-7.350	0.952	-17.525
O_1	4.831	-17.827	0.079	76.232	4.826	-16.892
P_1	2.248	-17.827	0.134	78.171	2.238	-14.407
K_1	6.794	-17.827	0.474	71.528	6.816	-13.843
N_2	2.112	17.053	0.275	75.797	2.267	23.008
M_2	11.030	17.053	1.560	69.689	12.041	22.964
K_2	1.390	17.053	0.205	58.103	1.550	22.022
			Contap Earth model			
Q_1	0.925	-17.827	0.027	-5.858	0.951	-17.489
O_1	4.831	-17.827	0.087	77.683	4.823	-16.803
P_1	2.248	-17.827	0.142	77.920	2.238	-14.219
K_1	6.794	-17.827	0.496	71.585	6.817	-13.653
N_2	2.112	17.053	0.270	74.081	2.270	22.769
M_2	11.030	17.053	1.528	68.048	12.050	22.707
K_2	1.390	17.053	0.200	56.622	1.550	21.777
			Ocenap Earth model			
Q_1	0.925	-17.827	0.027	-9.130	0.952	-17.579
O_1	4.831	-17.827	0.076	73.529	4.829	-16.928
P_1	2.248	-17.827	0.132	76.745	2.242	-14.456
K_1	6.794	-17.827	0.463	70.609	6.822	-13.934
N_2	2.112	17.053	0.262	75.251	2.241	22.930
M_2	11.030	17.053	1.469	68.664	11.897	22.786
K_2	1.390	17.053	0.190	56.908	1.528	21.799

Table 4.12: Amplitudes A ($n\varepsilon$) and phases ϕ (degrees) of solid SNRE, ocean loading and expected total tidal strain for BA using gbavap, contap and ocenap Earth models, and global TPXO7-atlas2011 integrated by the local Mediterranean Sea model.

BC interferometer

	solid SNRE		ocean loading		expected total	
harmonic	A	ϕ	A	ϕ	A	ϕ
			Gbavap Earth model			
Q_1	1.256	13.031	0.031	-133.924	1.230	12.249
O_1	6.559	13.031	0.050	-67.802	6.567	12.599
P_1	3.052	13.031	0.133	-59.701	3.094	10.678
K_1	9.224	13.031	0.446	-64.854	9.328	10.351
N_2	1.023	-37.236	0.107	118.291	0.927	-34.503
M_2	5.345	-37.236	0.088	41.639	5.363	-36.311
K_2	0.674	-37.236	0.096	-93.358	0.731	-43.460
			Contap Earth model			
Q_1	1.256	13.031	0.028	-138.435	1.231	12.415
O_1	6.559	13.031	0.025	-73.999	6.560	12.811
P_1	3.052	13.031	0.102	-55.318	3.092	11.267
K_1	9.224	13.031	0.343	-61.268	9.323	10.003
N_2	1.023	-37.236	0.110	116.708	0.926	-34.233
M_2	5.345	-37.236	0.125	54.113	5.344	-35.896
K_2	0.674	-37.236	0.089	-91.455	0.729	-42.884
			Ocenap Earth model			
Q_1	1.256	13.031	0.027	-142.820	1.231	12.518
O_1	6.559	13.031	0.016	-40.406	6.568	12.918
P_1	3.052	13.031	0.106	-52.604	3.098	11.247
K_1	9.224	13.031	0.355	-58.505	9.343	10.964
N_2	1.023	-37.236	0.097	111.937	0.924	-35.070
M_2	5.345	-37.236	0.136	29.881	5.306	-36.701
K_2	0.674	-37.236	0.088	-88.743	0.721	-43.470

Table 4.13: Amplitudes A ($n\varepsilon$) and phases ϕ (degrees) of solid SNRE, ocean loading and expected total tidal strain for BC using gbavap, contap and ocenap Earth models, and global TPXO7-atlas2011 integrated by the local Mediterranean Sea model.

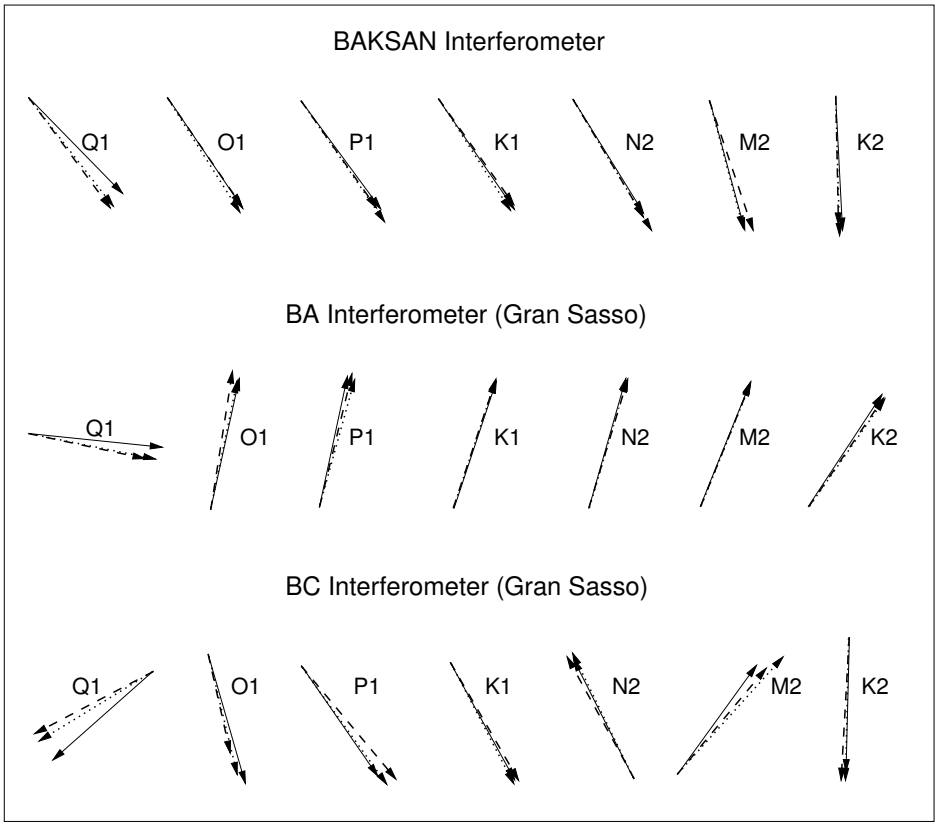

Figure 4.31: Phasor plot of ocean loading tidal strain using contap as Earth model and TPXO7-atlas2011 (solid lines), FES2004 (dashed lines) and HAMTIDE (dotted lines) as ocean model, integrated by the local Mediterranean Sea and Indian Ocean models. Amplitudes are normalized to the amplitude obtained for TPXO7-atlas2011 (see Tables 4.14 to 4.16).

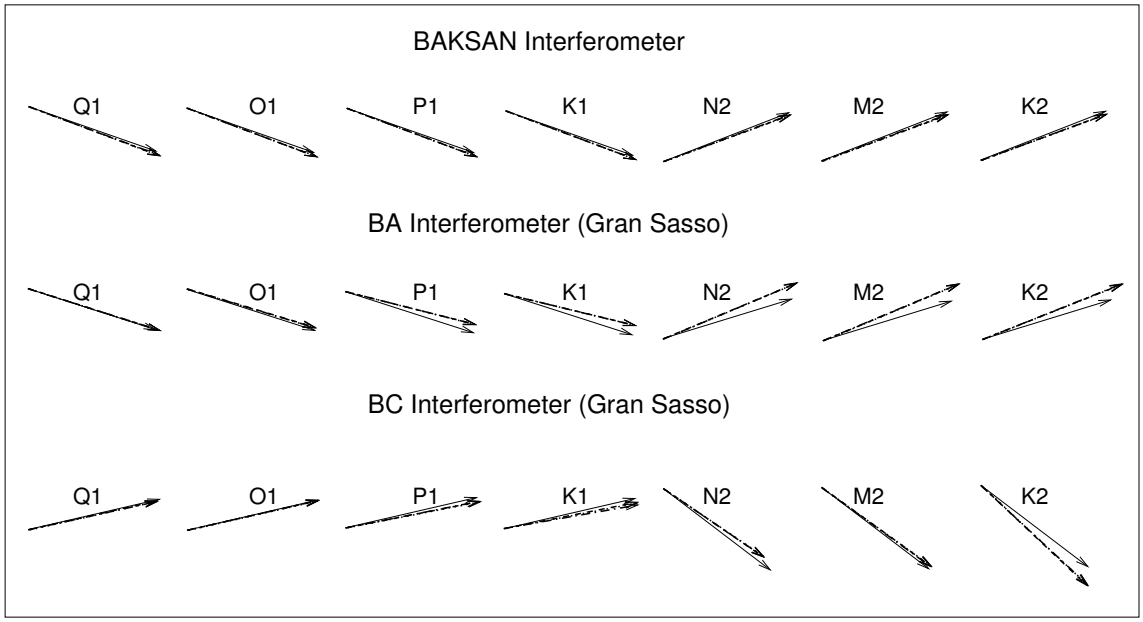

Figure 4.32: Phasor plot of solid SNRE tidal strain (solid lines) and expected total tidal strain using contap as Earth model and TPXO7-atlas2011 (dashed-dotted lines), FES2004 (dashed lines), and HAMTIDE (dotted lines) as ocean model, integrated by the local Mediterranean Sea and Indian Ocean models. Amplitudes are normalized to the amplitude of solid SNRE tidal strain (see Tables 4.14 to 4.16).

and HAMTIDE. Also in this case, although changing the ocean model, predictions are indistinguishable.

In general, ocean loading affects amplitude of diurnal tides by less than 10% at Baksan and 5% at Gran Sasso and phase by less than 5 degrees in all the three cases. Ocean loading is much more important in the semidiurnal band; its effects are about 20% in amplitude and 1 degree in phase at Baksan, 4% in amplitude and 8 degrees in phase for BA, and 40% in amplitude and 8 degrees in phase for BC at Gran Sasso (see Fig. 4.33 and Table 4.17).

After applying the ocean loading corrections, predicted and observed tides still show differences. These discrepancies out of the FCR spectral region can be substantially recovered taking strain local distortion into account. Following the same procedure outlined in Subsection 3.3.1, it is possible to estimate the coupling coefficients for each interferometer, by using a least-square fitting technique (Eqs. 3.24 to 3.26) and comparing predicted and observed amplitudes and phases of the larger tides out of the FCR range (Q_1, O_1, N_2, M_2, K_2). Results confirm that discrepancies are substantially recovered by using the coupling coefficients (see Table 4.18).

Baksan interferometer

	solid SNRE		ocean loading		expected total	
harmonic	A	ϕ	A	ϕ	A	ϕ
TPXO7-atlas2011 ocean model						
Q_1	0.976	-19.264	0.044	-45.660	1.015	-20.357
O_1	5.097	-19.264	0.202	-55.829	5.261	-20.576
P_1	2.372	-19.264	0.085	-53.602	2.443	-20.395
K_1	7.168	-19.264	0.286	-55.441	7.401	-20.573
N_2	1.991	21.292	0.036	-58.220	1.997	20.267
M_2	10.396	21.292	0.187	-74.877	10.378	20.264
K_2	1.311	21.292	0.026	-87.043	1.303	20.229
FES2004 ocean model						
Q_1	0.976	-19.264	0.045	-53.556	1.014	-20.706
O_1	5.097	-19.264	0.198	-55.516	5.258	-20.542
P_1	2.372	-19.264	0.083	-54.856	2.440	-20.401
K_1	7.168	-19.264	0.277	-54.538	7.396	-20.502
N_2	1.991	21.292	0.041	-59.135	1.998	20.144
M_2	10.396	21.292	0.191	-71.342	10.389	20.240
K_2	1.311	21.292	0.025	-88.799	1.302	20.264
HAMTIDE ocean model						
Q_1	0.976	-19.264	0.045	-51.993	1.014	-20.652
O_1	5.097	-19.264	0.204	-57.579	5.258	-20.641
P_1	2.372	-19.264	0.093	-55.448	2.448	-20.551
K_1	7.168	-19.264	0.283	-57.257	7.393	-20.613
N_2	1.991	21.292	0.037	-59.238	1.997	20.237
M_2	10.396	21.292	0.184	-75.191	10.377	20.280
K_2	1.311	21.292	0.027	-88.429	1.302	20.192

Table 4.14: Amplitudes A ($n\varepsilon$) and phases ϕ (degrees) of solid SNRE, ocean loading and expected total tidal strain for BAKSAN using contap Earth model and global TPXO7-atlas2011, FES2004, and HAMTIDE ocean models, integrated by the local Mediterranean Sea and Indian Ocean models.

BA interferometer

	solid SNRE		ocean loading		expected total	
harmonic	A	ϕ	A	ϕ	A	ϕ
TPXO7-atlas2011 ocean model						
Q_1	0.925	-17.827	0.027	-5.858	0.951	-17.489
O_1	4.831	-17.827	0.087	77.683	4.823	-16.803
P_1	2.248	-17.827	0.142	77.920	2.238	-14.219
K_1	6.794	-17.827	0.496	71.585	6.817	-13.653
N_2	2.112	17.053	0.270	74.081	2.270	22.769
M_2	11.030	17.053	1.528	68.048	12.050	22.707
K_2	1.390	17.053	0.200	56.622	1.550	21.777
FES2004 ocean model						
Q_1	0.925	-17.827	0.024	-12.124	0.949	-17.681
O_1	4.831	-17.827	0.091	81.097	4.817	-16.755
P_1	2.248	-17.827	0.145	76.350	2.242	-14.127
K_1	6.794	-17.827	0.502	71.713	6.816	-13.603
N_2	2.112	17.053	0.272	73.149	2.275	22.754
M_2	11.030	17.053	1.531	68.041	12.052	22.717
K_2	1.390	17.053	0.197	55.444	1.550	21.585
HAMTIDE ocean model						
Q_1	0.925	-17.827	0.026	-11.408	0.951	-17.653
O_1	4.831	-17.827	0.085	78.348	4.822	-16.840
P_1	2.248	-17.827	0.139	74.477	2.247	-14.291
K_1	6.794	-17.827	0.494	71.707	6.816	-13.672
N_2	2.112	17.053	0.268	73.642	2.270	22.709
M_2	11.030	17.053	1.515	68.022	12.042	22.663
K_2	1.390	17.053	0.197	54.976	1.551	21.533

Table 4.15: Amplitudes A ($n\varepsilon$) and phases ϕ (degrees) of solid SNRE, ocean loading and expected total tidal strain for BA using contap Earth model and global TPXO7-atlas2011, FES2004, and HAMTIDE ocean models, integrated by the local Mediterranean Sea and Indian Ocean models.

BC interferometer

	solid SNRE		ocean loading		expected total	
harmonic	A	ϕ	A	ϕ	A	ϕ
TPXO7-atlas2011 ocean model						
Q_1	1.256	13.031	0.028	-138.435	1.231	12.415
O_1	6.559	13.031	0.025	-73.999	6.560	12.811
P_1	3.052	13.031	0.102	-55.318	3.092	11.267
K_1	9.224	13.031	0.343	-61.268	9.323	10.003
N_2	1.023	-37.236	0.110	116.708	0.926	-34.233
M_2	5.345	-37.236	0.125	54.113	5.344	-35.896
K_2	0.674	-37.236	0.089	-91.455	0.729	-42.884
FES2004 ocean model						
Q_1	1.256	13.031	0.028	-152.339	1.229	12.702
O_1	6.559	13.031	0.019	-77.393	6.559	12.864
P_1	3.052	13.031	0.112	-50.110	3.104	11.191
K_1	9.224	13.031	0.348	-60.011	9.332	10.987
N_2	1.023	-37.236	0.114	118.838	0.920	-34.350
M_2	5.345	-37.236	0.129	50.069	5.353	-35.857
K_2	0.674	-37.236	0.095	-93.223	0.731	-43.411
HAMTIDE ocean model						
Q_1	1.256	13.031	0.028	-148.637	1.229	12.618
O_1	6.559	13.031	0.023	-76.465	6.559	12.829
P_1	3.052	13.031	0.111	-54.058	3.097	11.147
K_1	9.224	13.031	0.350	-62.475	9.318	10.949
N_2	1.023	-37.236	0.115	116.001	0.922	-34.022
M_2	5.345	-37.236	0.147	47.947	5.360	-35.665
K_2	0.674	-37.236	0.095	-91.247	0.734	-43.249

Table 4.16: Amplitudes A ($n\varepsilon$) and phases ϕ (degrees) of solid SNRE, ocean loading and expected total tidal strain for BC using contap Earth model and global TPXO7-atlas2011, FES2004, and HAMTIDE ocean models, integrated by the local Mediterranean Sea and Indian Ocean models.

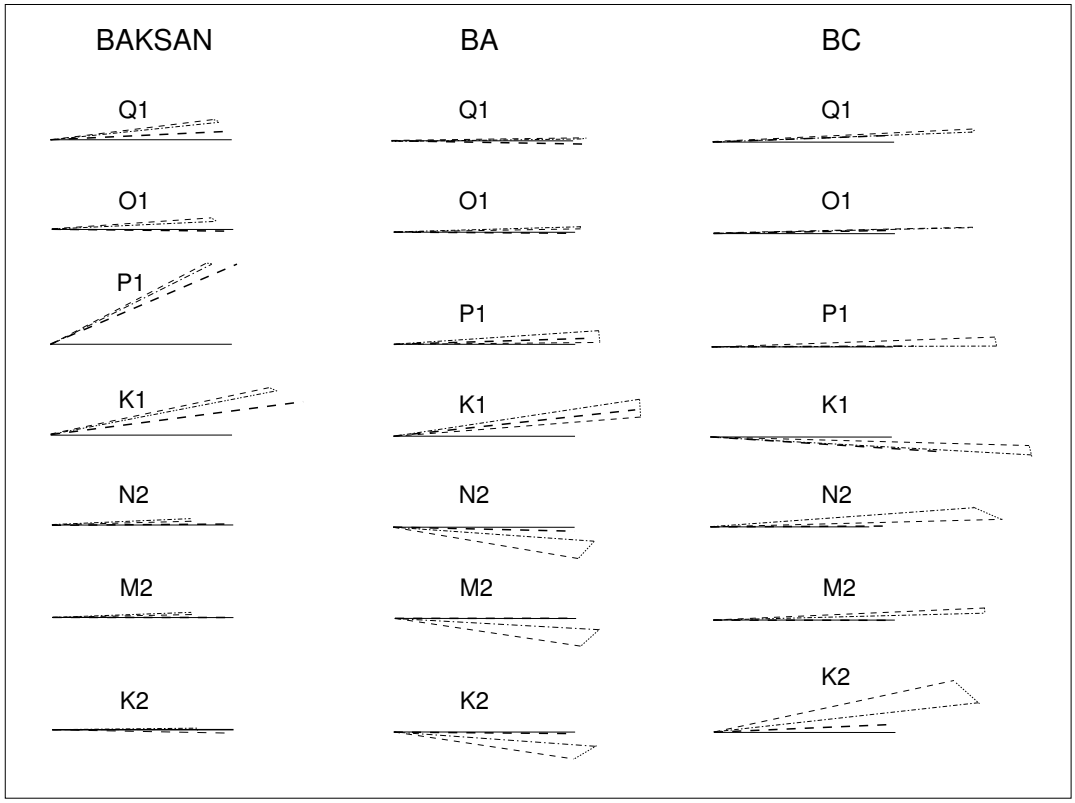

Figure 4.33: Phasor plot of solid SNRE (dashed lines), ocean loading (dotted lines), total (dashed dotted lines), expected total (sum of solid SNRE and ocean loading tidal strain corrected for local effects, long dashed lines) and observed (solid lines) tidal strain. Ocean model: TPXO7-atlas2011 and local Mediterranean Sea and Indian Ocean models for BAKSAN, TPXO7-atlas2011 and local Mediterranean Sea model for BA and BC; Earth model for mass-loading Green functions: contap; Love numbers: IERS 2003. Amplitudes are normalized to the amplitude of the observed tidal strain and phases given with respect to the phase of the observed tidal strain (see Table 4.17).

	solid SNRE		ocean loading		expected total		observed	
harmonic	A	ϕ	A	ϕ	A	ϕ	A	ϕ
BAKSAN interferometer								
Q_1	0.976	-19.264	0.044	-45.660	1.125	-23.589	1.075	-26.346
O_1	5.097	-19.264	0.202	-55.829	5.822	-23.876	5.807	-23.260
P_1	2.372	-19.264	0.085	-53.602	2.703	-23.606	2.416	-46.823
K_1	7.168	-19.264	0.286	-55.441	8.197	-23.810	5.795	-31.245
N_2	1.991	21.292	0.036	-58.220	2.541	20.205	2.541	19.805
M_2	10.396	21.292	0.187	-74.887	13.188	20.144	13.198	20.149
K_2	1.311	21.292	0.026	-86.043	1.654	20.140	1.618	21.176
BA interferometer								
Q_1	0.925	-17.827	0.027	-5.858	0.924	-19.594	0.872	-18.658
O_1	4.831	-17.827	0.087	77.683	4.691	-19.194	4.692	-18.833
P_1	2.248	-17.827	0.142	77.920	2.164	-16.581	1.977	-18.400
K_1	6.794	-17.827	0.496	71.585	6.583	-16.044	4.918	-22.298
N_2	2.092	17.246	0.270	74.081	2.002	25.535	2.007	26.803
M_2	10.925	17.246	1.528	68.048	10.588	25.768	10.590	25.740
K_2	1.377	17.246	0.200	56.622	1.362	25.339	1.355	25.760
BC interferometer								
Q_1	1.256	13.031	0.028	-138.435	0.866	12.453	0.863	10.257
O_1	6.559	13.030	0.025	-73.999	4.618	12.792	4.588	11.747
P_1	3.052	13.031	0.102	-55.318	2.175	11.222	1.954	10.987
K_1	9.224	13.031	0.343	-61.268	6.557	10.945	5.252	14.558
N_2	1.006	-38.064	0.110	116.708	0.604	-39.241	0.623	-39.555
M_2	5.253	-38.064	0.125	54.113	3.509	-40.629	3.512	-40.615
K_2	0.662	-38.064	0.089	-91.455	0.484	-47.709	0.490	-50.203

Table 4.17: Amplitudes A ($n\varepsilon$) and phases ϕ (degrees) of solid SNRE, ocean loading, expected total (sum of solid SNRE and ocean loading tidal strain corrected for local effects) and observed tidal strain for BAKSAN, BA and BC interferometers. Global TPXO7-atlas2011, integrated by the local Mediterranean Sea and Indian Ocean models; Earth model for mass-loading Green functions: contap; Love numbers: IERS 2003.

Coupling coefficients			
interferometer	α	β	γ
BAKSAN	1.25368	-0.10680	-0.16540
BA	0.93614	-0.01470	0.17473
BC	0.71184	-0.01871	0.17621

Table 4.18: Coupling coefficients for BAKSAN (corrected for T_{gal} effects), BA, and BC obtained using contap as Earth model and TPXO7-atlas2011 as ocean model, integrated by the local Mediterranean Sea and Indian Ocean models.

Cross coupling of shear strain (γ in Eq.3.24) is about 20% in all cases, while cross coupling of the direction perpendicular to the baseline (β in Eq. 3.24) is about 10% for Baksan and as low as 2% for both Gran Sasso interferometers. Because of local effects, extension increases by about 25% at Baksan, decreases by about 6% for BA and 30% for BC at Gran Sasso.

What found is consistent with what expected on the basis of the numerical modeling results in Ref. [42]. Cavity effects are expected to be small for all the three interferometers; topographic effects are expected to be small on BA, decrease the measured strain from 20% to 40% on BC, and increase the measured strain by about 25% on BAKSAN interferometer. This last amount is also consistent with estimations in Ref. [110], obtained using the perturbation method of Ref. [111].

Goodness of the fit gives an indication of the assumption reliability. Results confirm that discrepancies are substantially recovered by using the coupling coefficients. The residual discrepancies in P_1 and K_1 might be ascribable to the FCR.

4.4.3 FCR parameter estimation

The FCR parameter estimation is performed by comparing measurements and model predictions of the 8 diurnal tidal constituents (Q_1, O_1, P_1, K_1, Ψ_1, Φ_1, J_1 and OO_1) through a joint fit on BAKSAN, BA, and BC tidal parameters.

As previously mentioned, tidal parameters obtained from the VAV03 analysis (see Appendix A) of pre-whitened strain series are inverted (see Tables 4.19 and 4.9, for BAKSAN, BA and BC, respectively), both leaving all the complex Love and Shida numbers free or fixing some of them. BAKSAN record is corrected for T_{gal} effects.

Ocean loading (corrected for site effects) is subtracted from the retrieved Q_1, O_1, P_1, and

BAKSAN VAV03 results

harmonic	A	ϕ
Q_1	1.075	-26.346
O_1	5.807	-23.260
P_1	2.416	-46.823
K_1	0.951	90.349
Ψ_1	5.795	-31.245
Φ_1	0.153	103.542
J_1	0.172	-49.873
OO_1	0.250	-23.552

Table 4.19: Amplitude A ($n\varepsilon$) and phase ϕ (degrees) of observed tidal strain for BAKSAN interferometer, obtained using VAV03 code and corrected for effects of pre-whitening and temperature inside the tunnel.

K_1 amplitudes and phases, by using contap mass-loading Green's functions; Ψ_1 and Φ_1 ocean loadings are obtained by extrapolation from P_1, and K_1, except for BAKSAN Ψ_1, unused in the inversions; J_1 and OO_1 ocean loadings are estimated using a mere phasor rotation (1 degree anticlockwise, 4 degrees anticlockwise, and 2 degrees clockwise, for BAKSAN, BA, and BC, respectively).

P_1 tidal parameters for BAKSAN are not used because they differ more than the uncertainties attributed by using different tidal analysis codes.

The same procedure, previously described, is used. For each case as first step the best-fit FCR parameters are estimated by ASA; then 400000 synthetic tidal parameter sets are generated. The retrieved distributions of T_{FCN} (Fig. 4.34) give its PDF. The PDF distributions, leaving all or 5 parameters free, are peaked around 428.5 and 426.5 sidereal days respectively. In the first case the result is consistent with those obtained from the analysis of VLBI and gravity data in Ref. [83].

Cumulative distributions show that at the 80% (50%) confidence level the T_{FCN} value is between 413.5 (421.2) and 436.8 (431.0) sidereal days leaving free all the parameters, and 409.3 (417.1) and 440.2 (430.8) sidereal days fixing $\Re(l_1)$, $\Im(l_1)$, $\Im(l_0)$, $\Im(h_0 - 3l_0)$ and $\Im(h_1 - 3l_1)$.

Also in this case, Q is badly constrained and its values returned by the inversion code (ASA) are usually large ($> 10^6$). Q PDF obtained using NAB decreases starting from

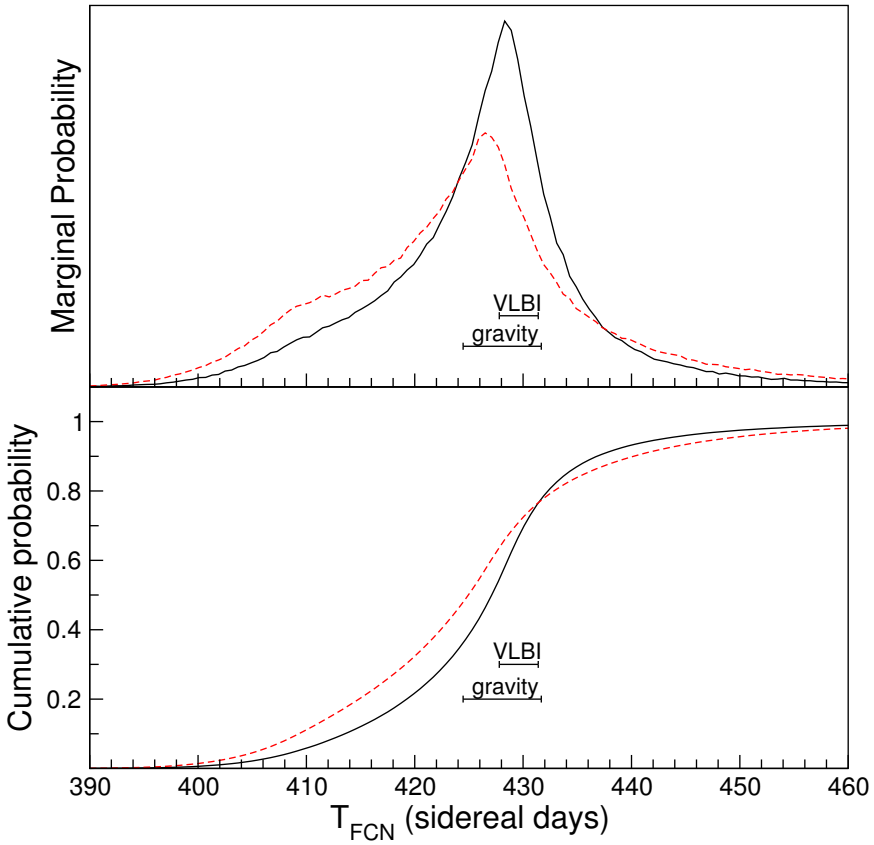

Figure 4.34: T_{FCN} PDFs and cumulative probability obtained analysing pre-whitened strain series and inverting synthetic tidal parameters by adding a null-mean random noise to real data. Black solid line, free parameters; red dashed line, fixed parameters; horizontal bars, results obtained from the analysis of gravity and VLBI data in [83].

about 300 when all parameters are left free, and shows a peak around 18000 when $\Re(l_1)$, $\Im(l_1)$, $\Im(l_0)$, $\Im(h_0 - 3l_0)$ and $\Im(h_1 - 3l_1)$ are fixed to their IERS 2003 values (see Fig. 4.35).

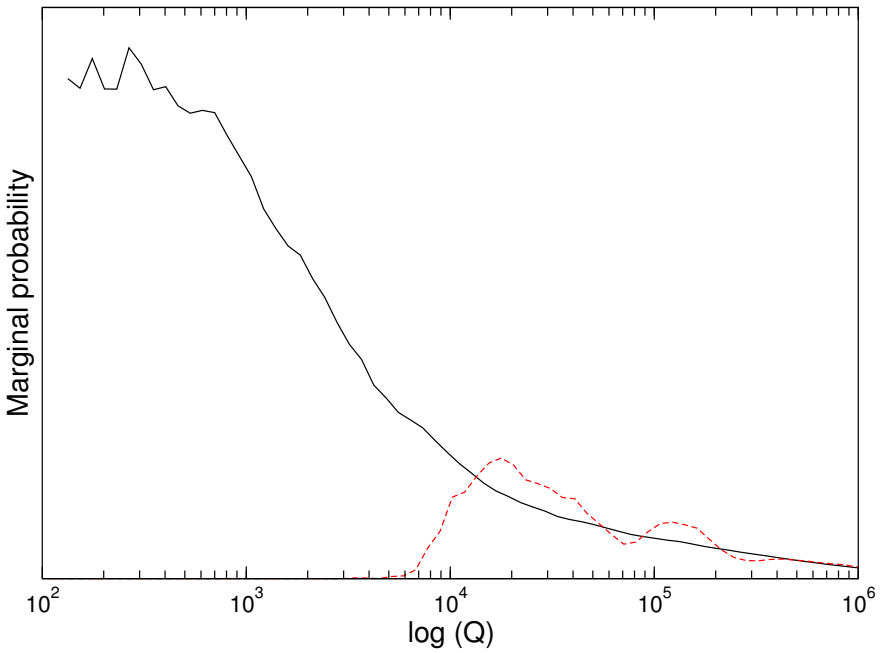

Figure 4.35: Marginal probability of the quality factor Q obtained leaving all or 5 parameters free (black solid and red dashed lines respectively) by NAB.

The curves in Fig. 4.36 show the marginal probability distribution of $\Re(h_1 - 3l_1)$, which dominates the resonance strength. All the PDFs are consistent with one another and in agreement with Ref. [94] (vertical line).

Comparison between measured tidal parameters for the three interferometers in the diurnal band, corrected for ocean loading effects, with predicted curves is shown in Fig. 4.37. Also in this case, to make it easier comparing results here obtained with those published for gravity tides, the amplitudes of the in-phase and out-of-phase (with respect to SNRE tides) terms, normalized to the SNRE tidal amplitude, are plotted. The out-of-phase Φ_1 discrepancies are outside the uncertainties from VAV03 for BAKSAN, BA and BC, but inside the uncertainties used for the inversion procedure for BA and BC. Also the BAKSAN out-of-phase J_1 discrepancy is outside the uncertainty.

The joint analysis confirms, but does not improve, the results recently obtained from the analysis of the Gran Sasso strain tides only and from gravity tides.

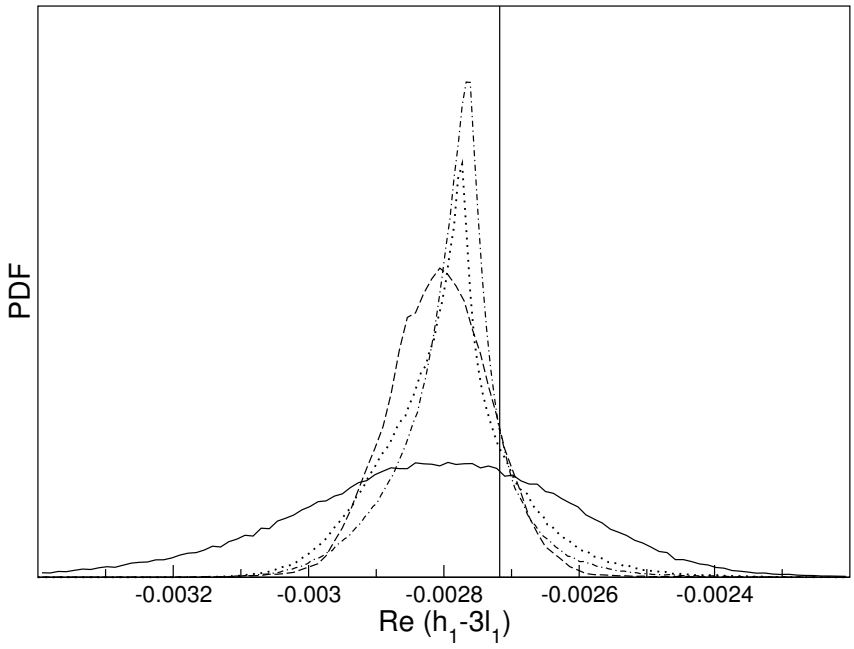

Figure 4.36: PDFs of the resonance strength obtained leaving all or 5 free parameters by NAB (solid and dashed lines respectively) and after inverting synthetic tidal parameters (dashed-dotted and dotted lines respectively). IERS 2003 value [94] (vertical line).

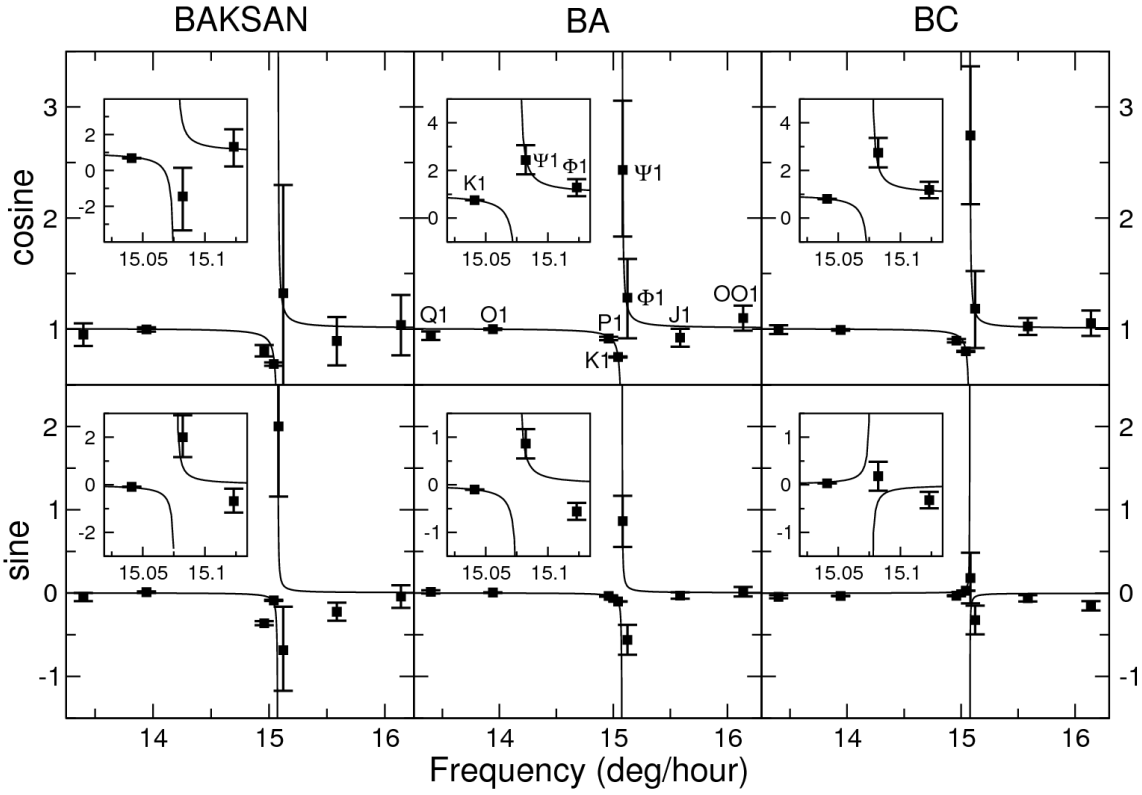

Figure 4.37: Amplitudes of the in-phase and out-of-phase (with respect to SNRE tides) terms, normalized to the SNRE tidal amplitudes, for BAKSAN (corrected for T_{gal} effects), BA and BC obtained by analysing pre-whitened records (squares). Error bars give twice the uncertainties from VAV03 tidal analysis; predicted values (solid line). Insets represent an enlargement around the resonance.

4.5 Conclusions

Most of the experimental studies related to the FCR are based on the analysis of tidal gravity and VLBI data. Even if tidal S/N ratio for strain is usually lower than for gravity, the analysis of strain data is promising, because relative perturbations in strain tides are about 10 times larger than in gravity tides.

First about eight years of discontinuous strain records from two crossed 90-m long laser interferometers (extensometers) operating in the Gran Sasso Underground Observatory (Italy), and then these data in a joint analysis with about six years of strain recorded discontinuously by an extensometer installed in the Baksan Underground Observatory (Russia), have been used to investigate the FCN parameters.

The inversion of realistic synthetic tidal parameters (obtained from observed amplitude and phase of eight diurnal tidal components) shows that the resolving power of strain tides is comparable to that of gravity tides if tidal parameters are inverted minimizing the $\mathcal{L}^2$ misfit (as usually done). Both resolving powers improve if data are inverted minimizing the $\mathcal{L}^1$ misfit, and this improvement is particularly notable for gravity tides.

The analyses of strain records have been performed after correcting measured strain for local distortion of the regional strain field and ocean loading.

Ocean loading effects are somewhat short-range and decay rapidly while increasing the distance of the station from the coast. In several cases they can be very small, so that uncertainties on local rheology and ocean tides have little influence on the expected total strain tides. In this case, at both Baksan and Gran Sasso stations the ocean loading contribution may differ from case to case even substantially, but the expected total strain tides (sum of solid spherical non-rotating layered Earth and ocean loading tides) are always very similar to one another. The effect of ocean loading tidal strain can be interpreted essentially as a small rotation of phasors whose amount and sign depend on the tidal component and the interferometer.

After correcting tidal amplitudes and phases for ocean loading, the residual discrepancies between experimental and predicted values far from the FCR frequency are attributable to the local distortion of the strain field. Comparison of predicted and observed (corrected for ocean loading effects) tides of the larger tides out of the FCR can give informations on local distortions, which in turn can be used to correct strain data. For both stations the cross-coupling coefficients, estimated using a least-square fitting technique, provide a reliable estimate of the matrix describing local effects. The

results are consistent with what expected on the basis of numerical simulations in Ref. [42] and indicate, at least in the two tested cases, the preminent role of topography in causing local effects with respect to heterogeneities.

The small ocean loading contributions and the reliable estimate of local distortions at Gran Sasso and Baksan make it possible to highlight the effects of the Free Core Resonance in the diurnal tidal band.

For estimating the FCR parameters, eight diurnal tidal constituents (Q_1, O_1, P_1, K_1, Ψ_1, Φ_1, J_1 and OO_1) have been used, by comparing measurements (corrected for ocean loading) and model predictions (corrected for the local strain distortion), minimizing the $\mathcal{L}^1$ misfit function.

The agreement between observations and predictions looks better than in any previous work that makes use of strain tides.

The analysis of the only Gran Sasso strain data provides value of the FCN period (about 429 sidereal days) robust and comparable to those from gravity tides, obtained from the joint inversion of data from several stations.

The joint analysis of Gran Sasso and Baksan strain data confirms, but does not improve, the results recently obtained analysing the Gran Sasso strain tides only and from gravity tides.

In both cases the quality factor is not well constrained because of the large uncertainty on the Ψ_1 phase; however the results are consistent with recently published values (≈ 20000).

The inversions provide also an independent estimate of $\Re\left(h_1 - 3l_1\right)$, which is the dominating term in the resonance strength expression, in agreement with IERS Conventions (2003).

Chapter 5

Slow Slip diffusion

After more than one century of observations, earthquakes have given a detailed knowledge of the Earth's structure but the physical processes, that explain their occurrence, remain quite unknown.

Elasticity theory explains how strain and stress build until the rock fractures, sliding along a fault surface, with the fracture propagation moderated by elastic waves. Currently it is not possible to explain exhaustively the mechanisms that generate the earthquakes.

Earthquakes occur when rock inside the lithosphere moves abruptly, as a consequence of a gradual stress accumulation in a region that eventually exceeds some threshold value, greater than that the rock can withstand, generating a rupture. Usually, this movement is along large cracks in Earth's crust called *faults*. Most earthquakes happen at or near the boundaries between Earth's tectonic plates, marking their large or small relative motion.

Every year, more than one million earthquakes occurs all over the world. Most of these are so small that people do not feel them; but some are large enough that people feel them, and a few are large enough to cause significant damage.

In the last decades, the discovery of a new mode of faulting, referred to as *slow slip events*, very different from regular earthquakes, has been detected. Slow slip events, preceding, following or without ordinary earthquakes, have duration of tens of seconds to several days and have been observed at transcurrent margins, extensional areas and almost all subduction zones.

This kind of events might play an important role in the stress redistribution process and seismic hazard assessment.

5.1 Slow earthquakes

Most of the world's seismicity, including the largest earthquakes, is associated with interplate slip along convergent plate boundaries [112]. Continuous geodetic measurements from convergent margins have shown the existence of deep transient events that can release large amounts accumulated stress too slowly to produce seismic waves that can be felt or just recordable by seismometers. These events are known as *slow earthquakes*.

Slow earthquakes were firstly observed at the Earth's surface above subduction zones by geodetic high-sensitivity strainmeters [113, 114, 116, 115, 35] with duration ranges from tens of seconds to days, and for sources fairly shallow. These continuous measurements revealed a range of transient deformation consistent with creep along the deeper plate interface.

Slow events have also been observed by continuous Global Positioning System (GPS) networks worldwide along some subduction plate boundaries in Japan, Cascadia, Canada and Mexico. The analysis of data indicates that transient aseismic slip occurs over large areas of the deeper subduction interface and is often associated with episodic seismic tremor [117].

Many aspects of slow slip remain unexplained. For example, the mechanism by which slow slip occurs remains uncertain, as well as the reason for which it occurs in the absence of detectable seismicity or simultaneous with seismicity.

Like regular earthquakes, slow slip events can be small or large and their duration ranges vary widely. But they differ from regular earthquakes in several features; for example the stress released is orders of magnitude smaller, the speed and direction of propagation follow their own distinct pattern.

Also the relationship between duration (τ) and moment (M) is strongly different for the two types of events.

For a regular earthquake the fault length is proportional to the event duration, the ruptured area is proportional to the square of fault length, and the amount of slip is proportional to length. Therefore, the duration is proportional to the cube root of the moment.

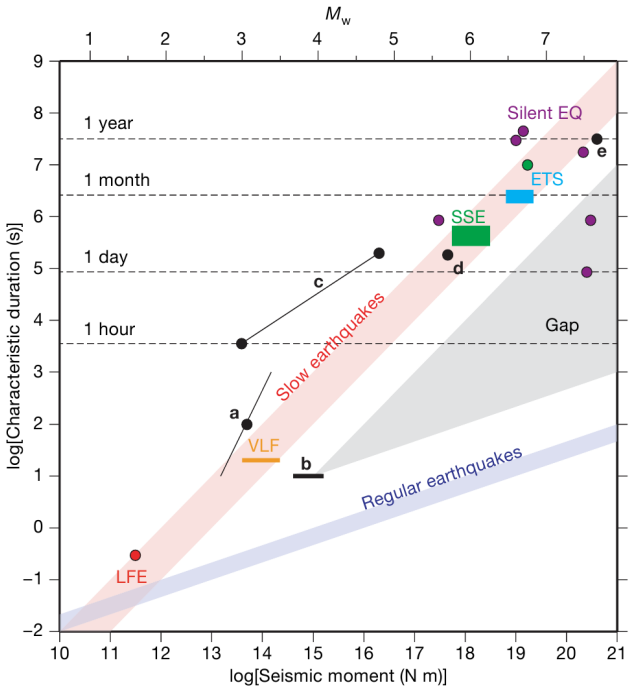

Figure 5.1: Comparison between seismic moment and the characteristic duration of various slow earthquakes in Ref. [118]. LFE (low-frequency earthquakes, red), VLF (very-low-frequency earthquakes, orange), and SSE (slow-slip events, green) occured in the Nankai trough while ETS (episodic tremor and slip, light blue) occured in the Cascadia subduction zone.

For a slow event, in 1999 Crescentini et al. suggested a diffusive slow slip propagation along the fault, observing that $M \propto \sqrt{\tau}$ for a one-dimensional (1D) model [35].

More recently, in 2007 Ide at al. proposed a model in which the duration is directly proportional to the moment [118] (Fig. 5.1). In their study, they showed that duration and seismic moment of regular and slow earthquakes follow two completely different scaling laws, defining two different manifestations of the same phenomenon. A gap between them exists because they represent different modes of slip propagation, and the only events able to fill this gap would be a compound of two rupture modes.

Assuming that the proportionality between seismic moment and characteristic time holds at all times during an earthquake, the seismic moment rate function would be constant until the event's termination.

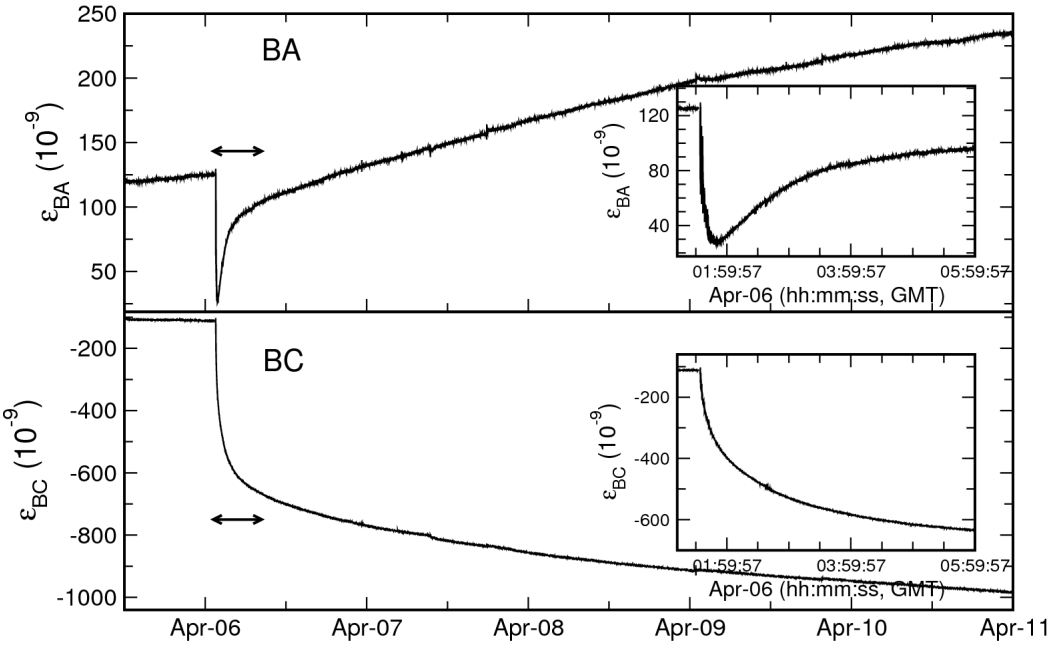

Figure 5.2: Post-seismic transient recorded at the two interferometers BA and BC after removal of Earth tides and environmental effects. Insets represent an enlargement during the first 4 hours from the beginning of signals.

5.1.1 Slow diffusive fault slip propagation following L'Aquila (6 April 2009) earthquake: first direct observation

The diffusive character of the rupture propagation was mainly deduced indirectly from the observed relationship between seismic moment and characteristic time. The first direct observation of the diffusive nature of these processes occurred after the 6 April 2009 L'Aquila (Italy) earthquake [37].

Tens of slow earthquakes have been observed in the L'Aquila area, one of the most active seismogenic region of Italy, during 1997 and the following years using the two laser interferometers of Gran Sasso [35, 119].

During the 6 April 2009 L'Aquila earthquake the interferometers produced unusually clean recordings of post-seismic strain and very clear signals due to a slow earthquake (Fig. 5.2).

For several hours the transient of the two interferometers is quite different; BA signal shows a non-monotonic behavior with a compression after a fast initial compression long about 15 minutes, while BC decreases monotonically. This indicates that the first hours of this transient are dominated by a different phenomenon or a different phase of the

same phenomenon with respect to longer term deformation. After about 1.5 days post-seismic strain is monotonic and quite similar for both interferometers ($\varepsilon_{BC} \sim -1.8\varepsilon_{BA}$). Such features suggest that fracture propagation crosses a nodal line on the fault plane, which separates areas able to produce deformation of opposite sign at the observation point.

5.1.2 Modeling

The slip propagation has been modeled in a 1D space for two propagation mechanisms: a constant rupture velocity and a diffusive processes, as explained in detail in Ref. [37].

The propagation occurs along straight paths from $x = 0$ to $x = L$, where L is the total path length, starting at time $t = 0$. In fact dimensionless coordinates are used, so the along-path distance x becomes x/L, varying between 0 and 1. At the time $t_0(x)$, the point x starts to move along the path, following different behaviors depending on the type of propagation.

For a constant rupture velocity model characterized by velocity v, the temporal dimensionless coordinate tv/L is used and $t_0 = x$.

For a diffusive model, introducing the similarity variable $\eta = x^2/t$, slip is expected to depend on the similarity variable far from the path end. Even if the diffusion equation does not allow to define exactly the velocity of slip propagation, the diffusive process can be approximated by a propagation velocity c/x, where c is the diffusion coefficient. In this case, the temporal dimensionless coordinate becomes tc/L^2 and $t_0 = x^2$. Close to the path end, the process tends towards an asymptotic configuration, and a propagation velocity proportional to $1/x - 1/L$ has been used for taking properties of slip propagation far from and close to the path end into account at the same time. In this case $t_0 = -x - log(1 - x)$.

Once propagation started, the linear density of seismic moment reaches its maximum value $s(x)$ with a history $u(t_s(x), t - t_0(x))/s(x)$, where $t_s(x)$ is the rise time of the signal which may in turn depend on x. The expected signal is modeled as

$$e(t) = L \int_0^1 dx \left[m(x)\, u(t_s(x), t - t_0(x))\, k(x) \right] \tag{5.1}$$

where x is the dimensionless distance on each path; $m(x)$ the linear density of the seismic moment released along the path; $u(t_s(x), t - t_0(x))$ is the time history of the

seismic moment released at each point of the path that may have different slope (step function, linear ramp, exponential function); the fault kernel $k(x)$ defines the strain generated at the station by small rectangular sources located in different positions on the fault plane by using the same focal mechanism as the main shock and seismic moment fixed.

Discretizing Eq. 5.1, the expected signal becomes

$$e_{ij} = \sum_{l=1}^{n_s} w_{jl} m_l \tag{5.2}$$

with

$$w_{jl} = \frac{L}{n_x} \sum_{h=1}^{n_h} u_{ji} k_i \qquad i = (l-1)\, n_h + h \tag{5.3}$$

where m_l is piecewise constant and defines the linear density of the seismic moment released along the path; j and i are the temporal and spatial indices respectively; u_{ji} is the time history of the seismic moment released at each point of the path, expressed through different functions (step function, linear ramp, exponential function); k_i is the fault kernel along the path; n_x and n_t are the number of spatial and temporal intervals; n_s and $n_h = n_x/n_s$ are the number of ranges with constant slip and the number of detailed intervals on each range.

Along each path generated changing the starting point, length and direction, the linear density of the seismic moment is optimized with respect to the observed signals at station, using the different propagation mechanisms.

In the misfit function a roughness penalty (proportional to the second derivative of the moment linear density) is added for reduce irregular seismic moment distributions.

The consistency of different paths against observations is tested by using a gridding technique, instead of searching for the optimal solution in terms of the misfit.

5.1.3 L'Aquila slow slip propagation: results

Slip propagation has been modeled using the fault geometry and slip distribution from Ref. [120]. The fault plane is characterized by strike and dip angles of 144 degrees and 51 degrees, and the dimensions along the strike and dip directions are 20 and 16 km in length, respectively (see Fig. 5.3). These results have been shown in Ref. [37].

Fig. 5.4 shows the expected deformation generated by very small sub-faults located in

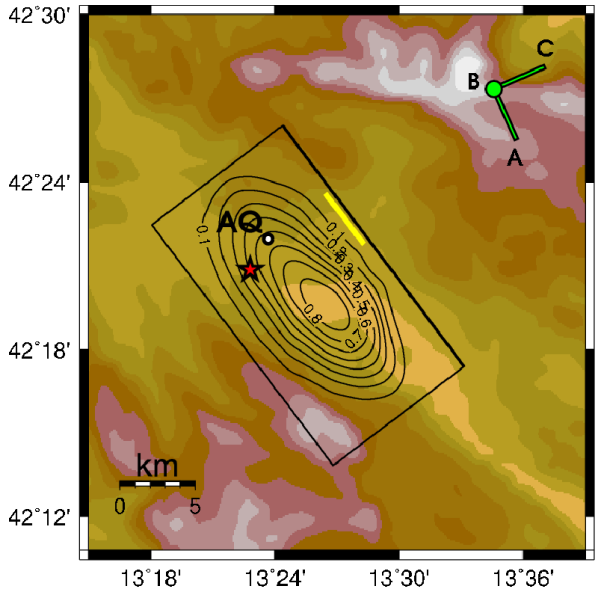

Figure 5.3: Map of the epicentral region of the 6 April 2009 L'Aquila earthquake and location of the two interferometers. The fault geometry and slip distribution are from Ref. [120]. Figure from Ref. [37].

different positions on the fault plane at both interferometers, using a seismic moment fixed ($M = 2.5 \times 10^{16}$Nm) and for a simple homogeneous half-space approximation (Poisson ratio 0.29; rigidity 2×10^{10}N/m^2).

The fault kernels highlight the areas of the fault rupture with significant slip, that cause a contraction at BC, and at the same time are crossed by a nodal line, which separates areas capable of producing deformation of opposite sign at BA interferometer.

Fig. 5.5 shows the optimum propagations in the early 35000 sec obtained using both constant rupture velocity and diffusive models. Strain history at both interferometers is fully consistent with diffusive slip propagation, but inconsistent with constant velocity propagation, unable to fit the shape of minimum that characterizes BA signal.

The diffusive character of the rupture propagation is supported also from the observed relationship between linear density of the seismic moment and distance along the path. The linear density of the seismic moment decreases about linearly with distance like the steady-state solution of 1D diffusive processes (Fig. 5.6).

In conclusion, the analysis of L'Aquila slow event suggests that a detailed direct study of the slip propagation is only possible when a nodal line crosses the strain field on the fault plane, thus reversing the recorded strain direction. Constraints given by monotonic signals are much fainter.

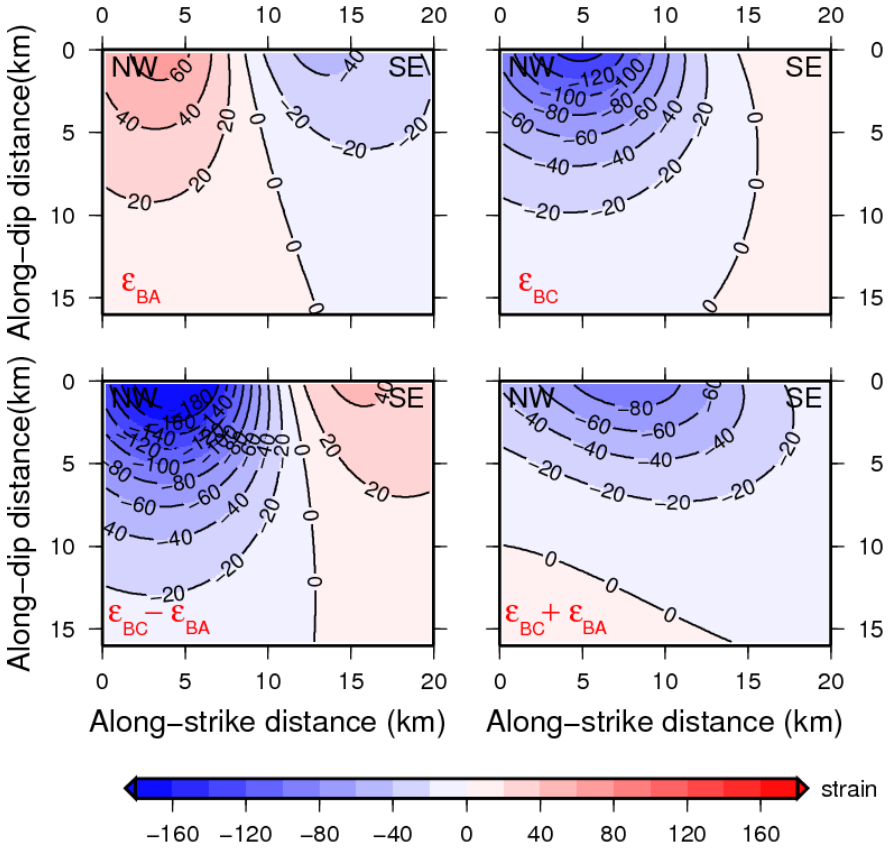

Figure 5.4: Strain ($n\varepsilon$) generated by a small rectangular source ($M = 2.5 \times 10^{16}$Nm, same focal mechanism as the main shock) located in different positions on the fault plane at BA and BC interferometers.

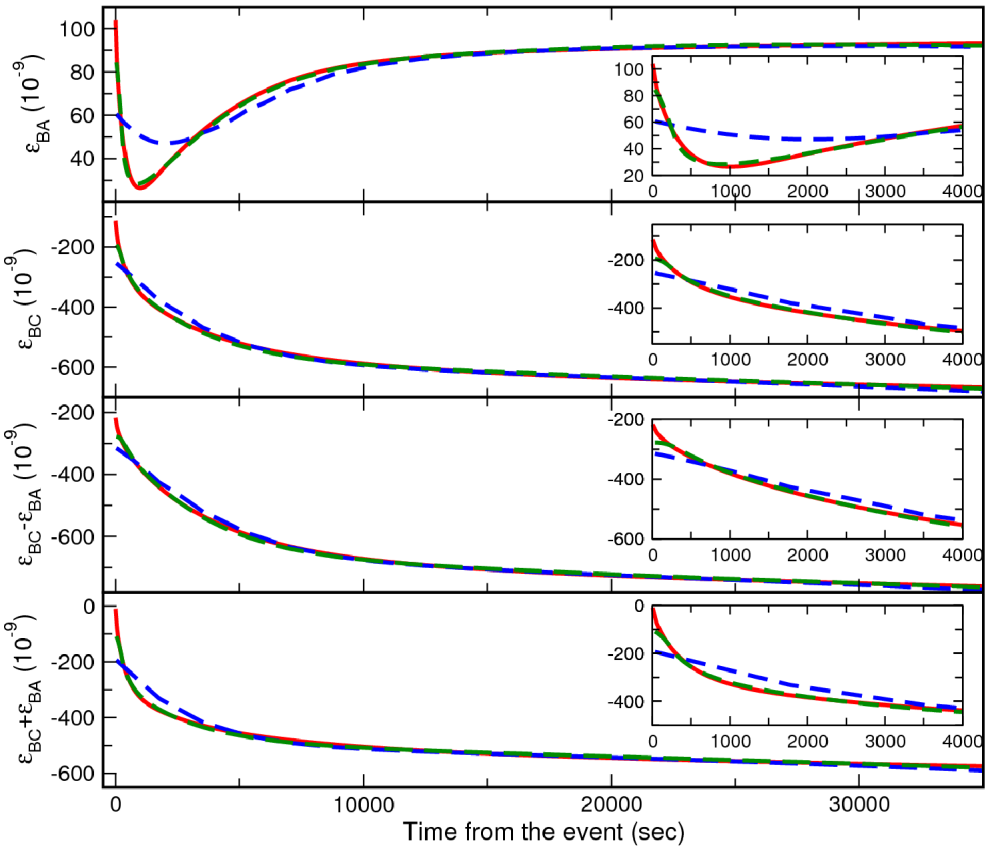

Figure 5.5: Initial smoothed detrended postseismic transient recorded at BA and BC interferometers (red lines) after removal of Earth tides and environmental effects. Blue dashed lines, predicted strain history for the best constant propagation velocity model ($L \sim 10000\,\mathrm{m}$, velocity $v \sim 0.3\,\mathrm{m/s}$). Green dashed lines, predicted strain history for the best diffusive model ($L \sim 11000\,\mathrm{m}$, diffusion velocity $c \sim 120\,\mathrm{ms}^{-1/2}$).

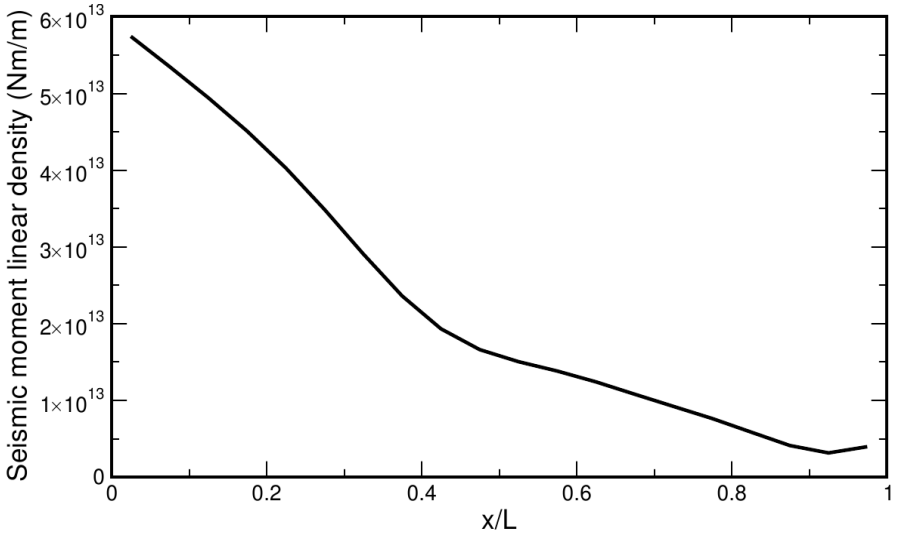

Figure 5.6: Linear density of the seismic moment as a function of the distance along the path for the best diffusive model.

5.2 Analysis of three slow earthquakes

Searching for other direct evidences of the diffusive rupture propagation, looking at strain records similar to those recorded after L'Aquila earthquake, three additional strain records sharing these features have been found and analysed [121, 122]. These events are related to the 1978 Izu-Oshima (Japan) earthquake [123]; the 1999 Durmid Hill (California) slow event [124] and the 2003 Tokachi-oki (Japan) earthquake [125].

5.2.1 The 1978 Izu-Oshima (Japan) slow earthquake

Along the Pacific coast of Honshu, at south of Tokyo, one of the most seismically active region in Japan, a network of three Sacks-Evertson borehole strainmeters recorded a slow event following the 14 January 1978 Izu-Oshima earthquake. These instruments, called AJI, SHI and IRO (see Fig. 5.7), are characterized by a wide dynamic range and high-sensitivity frequency in a range between zero and several hertz.

They recorded a sequence of two slow earthquakes whose temporal duration is about one hour.

According Ref. [123], the propagation started with a precursor earthquake F1, followed after 6 seconds by the main event (F2) characterized by magnitude 7.0. After about 20 seconds the slow propagation occurred on two quasi-orthogonal faults (F3 and F4, see

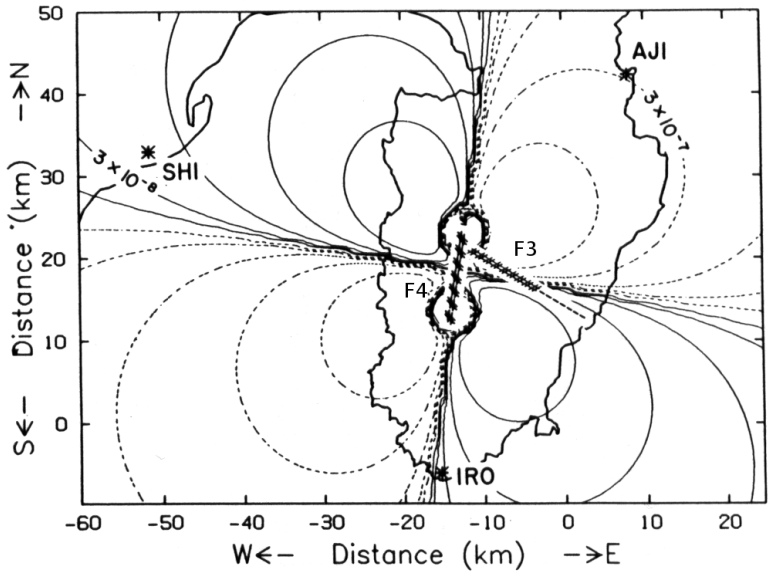

Figure 5.7: Location of IRO, SHI and AJI borehole strainmeters and faults F3 and F4 (EW and NS directions, respectively). Figure from Ref. [123].

Fig. 5.7), starting along the F3 fault for about 1000 seconds in the east-west direction. This fault extends for about 8 km in the strike direction (N302E) at a depth of about 5 km and is characterized by a dip angle of about 80 degrees and rake of 172 degrees and it is well-constrained from the aftershock activity. At the end of this first process a second fault is activated. It is a vertical left-lateral strike-slip fault, 10 km long and 7.5 km wide, placed at a depth of 5 km and characterized by a strike angle of 189 degrees, where the rupture has propagated in the north-south direction for about one hour.

Slow events are generated on faults F3 and F4, whose geometries and dimensions are constrained by the aftershock activity, although F4 is not well constrained. Two of the recorded strain signals are monotonic, while the other one, related to SHI strainmeter, shows a minimum (see Fig. 5.8).

These signals have been digitized and analysed by using the two propagation mechanisms (constant propagation velocity and diffusive processes) along straight paths on F3 and F4. The geometry of the two faults is modeled through the fault kernel (see Fig. 5.9).

Fig. 5.10 shows the results obtained using both constant velocity and diffusive propagation models. Observations for F3 fault are only consistent with diffusive slip propagation, while the constant velocity model is unable to fit the shape of minimum observed on SHI signal. Both constant velocity and diffusive slip propagation are consistent

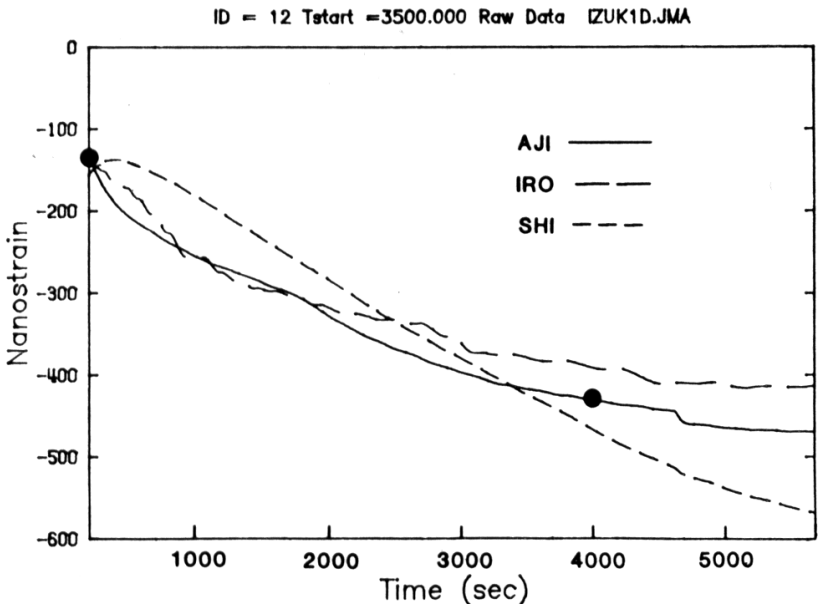

Figure 5.8: Post-seismic transient recorded at the three borehole strainmeters AJI, SHI and IRO. Figure from Ref. [123].

with observations on F4 fault, where it is not possible to distinguish the actual type of propagation.

For both mechanisms the linear density of seismic moment along the paths is optimized with respect to the observed signals at the borehole strainmeters (see Fig. 5.11).

The seismic moment released along the path on F3 fault decreases about linearly with distance using a diffusive model, as observed for the Gran Sasso slow slip propagation and like the steady-state solution of a 1D diffusive process.

Along the path on F4, the shape of seismic moment seems somewhat unrealistic, being a bell-shaped distribution, peaked on the nodal line. This behavior claims for a deeper insight on the characteristics of source (F3 is not well constrained). The assumption of very thin 1D path could be a major source of problems.

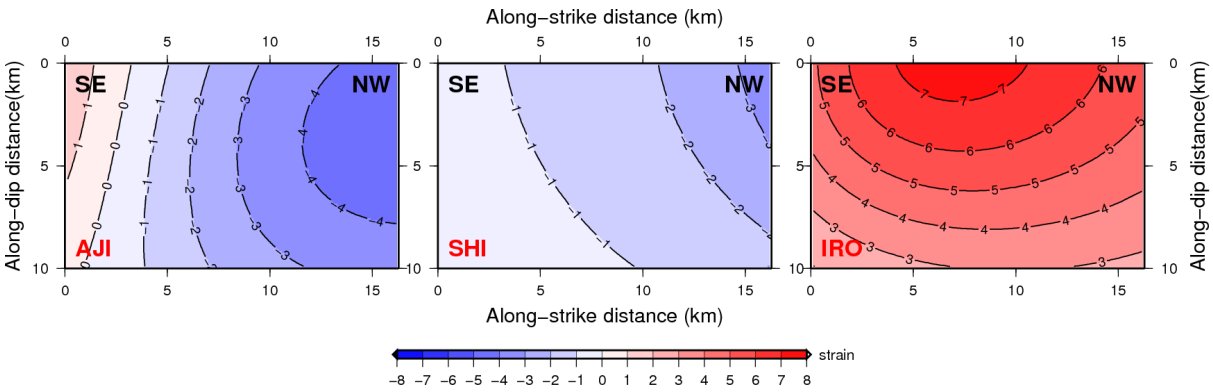

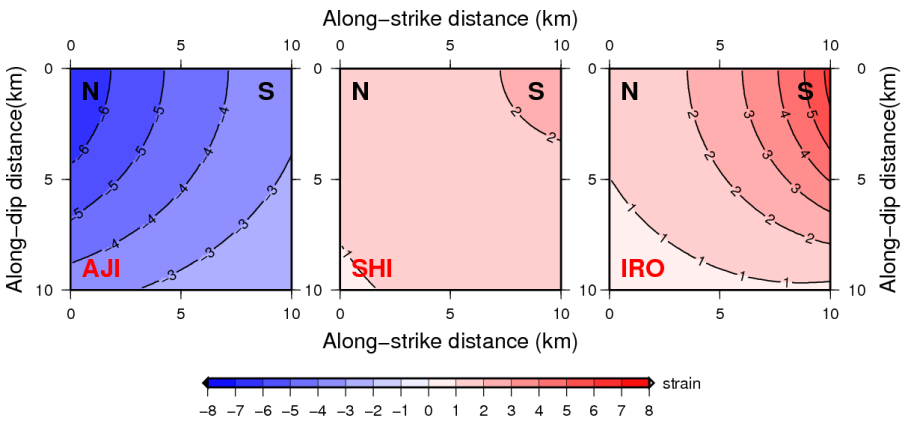

Figure 5.9: Strain ($n\varepsilon$) generated by a small rectangular source ($M = 2.5 \times 10^{16}$Nm, strike slipping faults) located in different positions on the F3 (upper plots) and F4 (lower plots) fault planes at AJI, SHI and IRO borehole strainmeters.

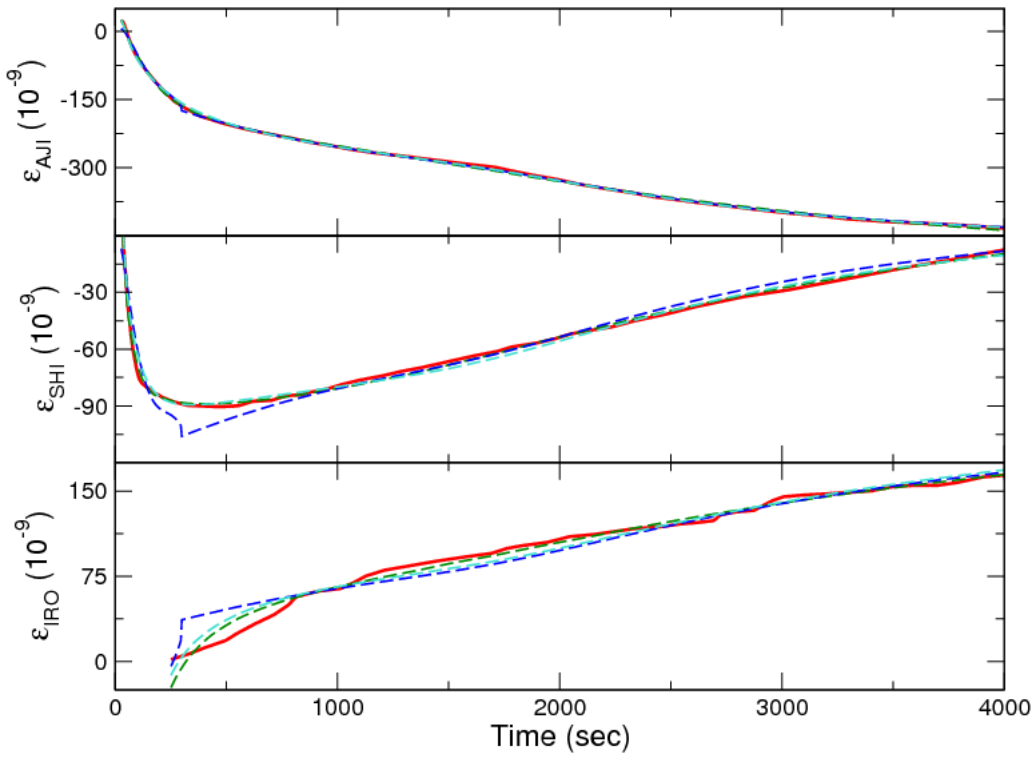

Figure 5.10: Smoothed post-seismic transient recorded at AJI, SHI and IRO borehole strainmeters (red lines). Blue dashed lines, predicted strain history for the best constant propagation velocity model for both F3 and F4 faults ($L_3 \sim 11000\,\mathrm{m}$ and $v_3 \sim 37\,\mathrm{m/s}$, $L_4 \sim 5000\,\mathrm{m}$ and $v_4 \sim 1.3\,\mathrm{m/s}$). Green dashed lines, predicted strain history for the best diffusive model for both F3 and F4 faults ($L_3 \sim 9000\,\mathrm{m}$ and $c_3 \sim 460\,\mathrm{ms}^{-1/2}$, $L_4 \sim 5000\,\mathrm{m}$ and $c_4 \sim 63\,\mathrm{ms}^{-1/2}$). Turquoise dashed lines, predicted strain history for the best diffusive and constant propagation velocity models for F3 and F4 faults respectively ($L_3 \sim 10000\,\mathrm{m}$ and $c_3 \sim 500\,\mathrm{ms}^{-1/2}$, $L_4 \sim 6000\,\mathrm{m}$ and $v_4 \sim 1.5\,\mathrm{m/s}$).

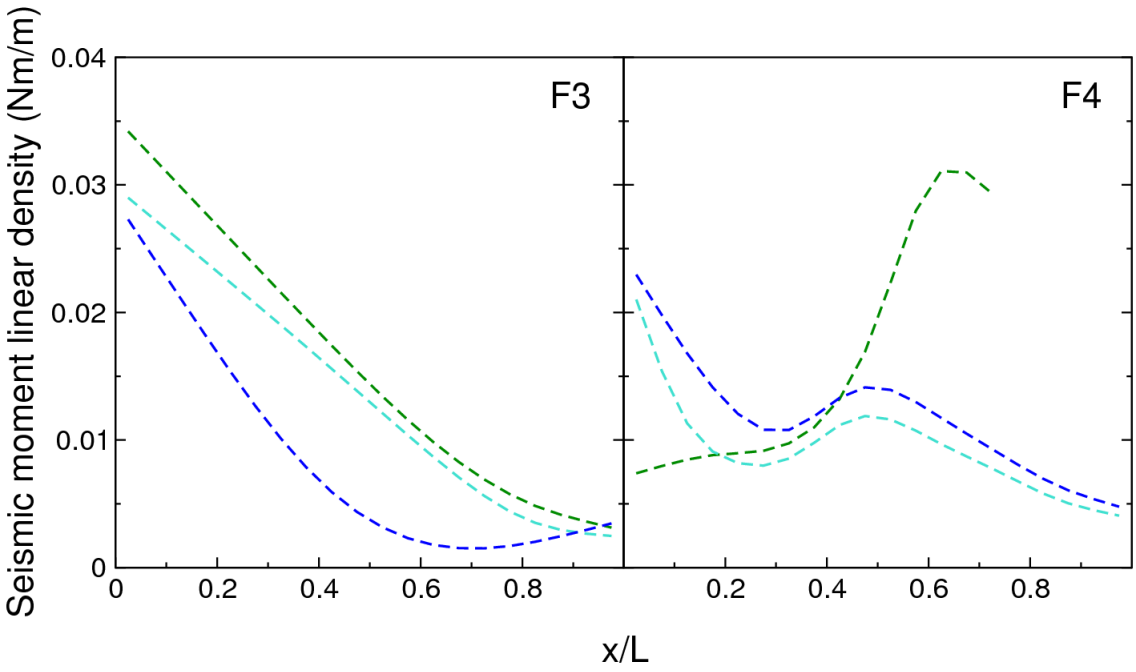

Figure 5.11: Seismic moment linear density as a function of the distance along the path for the best constant velocity slip propagation on both faults (blue dashed line), the best diffusive slip propagation on both faults (green dashed line), and the best diffusive and constant propagation velocity models on F3 and F4 respectively (turquoise dashed line).

5.2.2 The 1999 Durmid Hill (California) slow earthquake

Durmid Hill is located near the intersection between the southern section of the San Andreas Fault (extending from San Gorgonio Pass to the Salton Sea near Bombay Beach) and the northern extension of the Brawley Seismic Zone. This area is in the region of strike-slip faults, next to the San Andreas one, the most active of these faults (see Fig. 5.12).

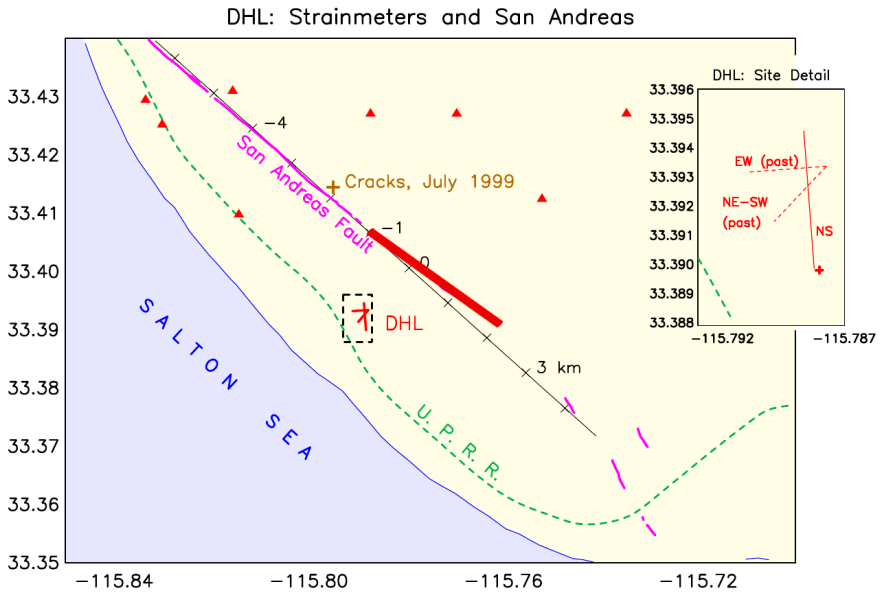

Figure 5.12: DHL region in which San Andreas fault (magenta line) and segment fault source of the slow event (red line) are located. The inset shows the location of the three surface long-baseline strainmeters, NS, NESW and EW. Figure from Ref. [124].

Three surface long-baseline strainmeters were installed in 1997 in this area. One of these instruments, namely NS (with azimuth -4.3 degrees) is permanent; the other two were "portable" long-base strainmeters operating in the EW (-94.3 degrees) and NE-SW (-139.3 degrees) azimuths for 23.1 and 15.9 months respectively (see inset in Fig. 5.12). The NS permanent DHL instrument, characterized by a very low noise level, is entirely buried; its terminal ends and the vacuum pipe are to a depth of few meters and 0.5 meters respectively. Some interesting signals have been recorded by these instruments. They correspond to rapid aseismic changes in deformation due to a slow slip propagation on the fault plane. There are some examples of this kind of signals recorded during the years since 1997.

One of the most significant, here analysed, was observed in October 1999 (see Fig. 5.13). This short signal (about one minute in time length) evidences a different behavior at

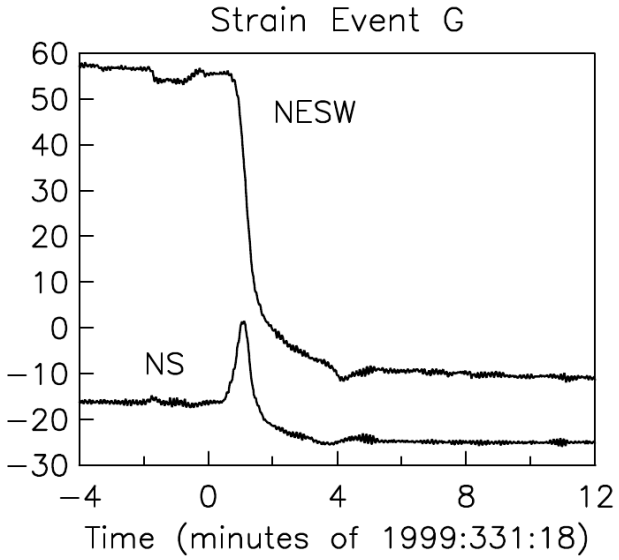

Figure 5.13: Strain($n\varepsilon$) history recorded by two NS and NESW long-base laser strainmeters. One of the strain signals is monotonic, while the other one shows a marked maximum. Figure 26 in Ref. [124].

NS and NESW strainmeters. It appears monotonously negative on NESW, while on NS it is characterized by a reversed deformation: the initial phase of the process is dominated by a dilation followed, after about 40 seconds, by a compression.

The San Andreas fault is a right-lateral strike-slip fault, therefore, characterized by a dip angle $\delta = 90$ degrees and rake angle $\lambda = 180$ degrees. In particular, the fault segment source of the slow event (red line in Fig. 5.12) has a length of about 6 and 3 km along the strike and directions, respectively. These features are taken into account in the inversions through the fault kernel (see Fig. 5.14). The fault kernel shows the existence of two different nodal lines, but the crossing of only one of them is consistent with the observations.

By comparing the results from the NS and NESW fault kernels with observations, it is possible to hypothesize that propagation started from a point located between 4 and 5 km along the dip direction and at a maximum distance of about 1.8 km along the strike direction, from right to left and for a little more than 1 km.

Fig. 5.15 shows the signals produced by the best constant velocity and diffusive slip propagations. Both models are consistent with observations, so it is not possible to discriminate the actual type of propagation. The constant velocity propagation seems to fit better the propagation along the fault, the mean square deviation is about 0.66

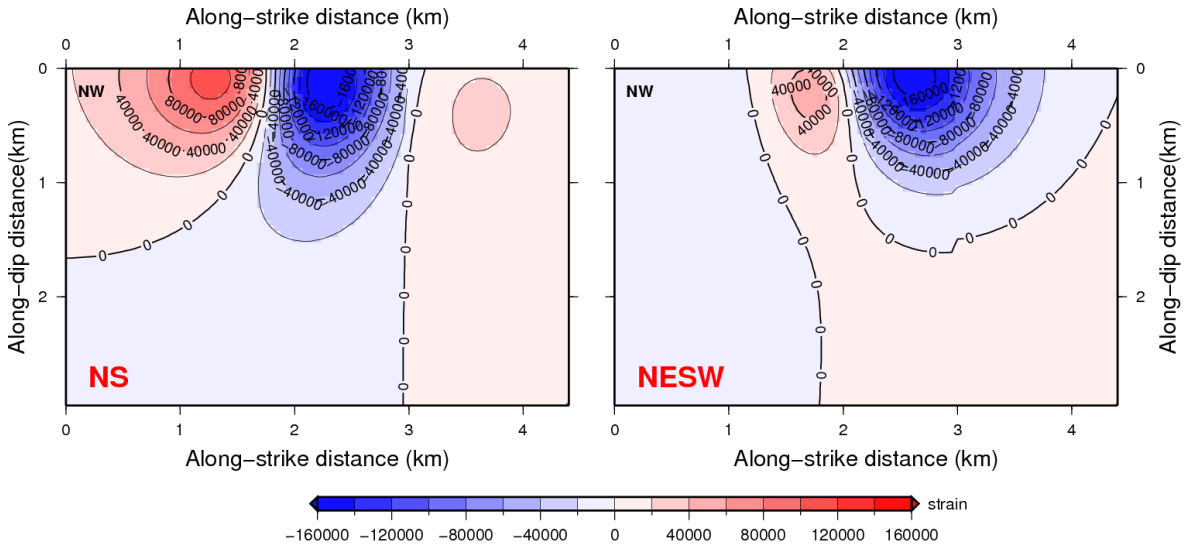

Figure 5.14: Strain ($n\varepsilon$) generated by a small rectangular source ($M = 2.5 \times 10^{16}$Nm, right-lateral strike-slip fault) located in different positions on the fault plane at NS (left plot) and NESW (right plot) surface long-baseline strainmeters.

and it becomes 1.0 when a diffusive slip propagation is supposed. However, there are no elements which allow to prefer one of the two propagations, because both reproduce accurately the recorded signals.

Also in this case the shape of seismic moment released along the path on fault seems unrealistic, exhibiting a peak at the nodal line (see Fig. 5.16). It is important to remember that the time scale for this slow event is much smaller than in the case previously discussed and the geometry of fault is assumed to be the same of San Andreas one. It could be important to deepen the consistence of this hypothesis.

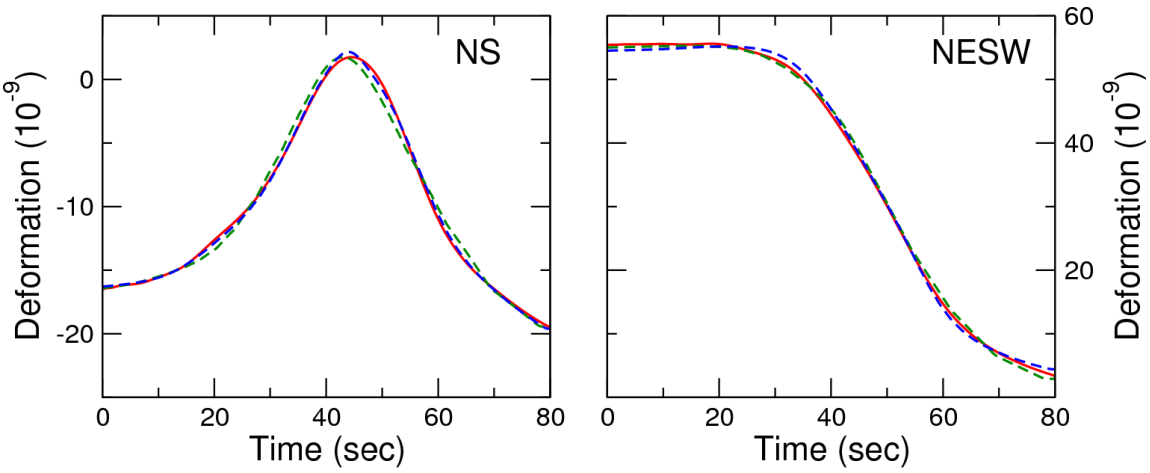

Figure 5.15: Smoothed strain history (red line) recorded by two long-base laser strainmeters (NS and NESW, left and right plots respectively). Blue dashed lines, predicted strain history for the best constant propagation velocity model ($L \sim 1340\,\mathrm{m}$ and $v \sim 17\,\mathrm{m/s}$). Green dashed lines, predicted strain history for the best diffusive model ($L \sim 1360\,\mathrm{m}$ and $c \sim 87\,\mathrm{ms}^{-1/2}$).

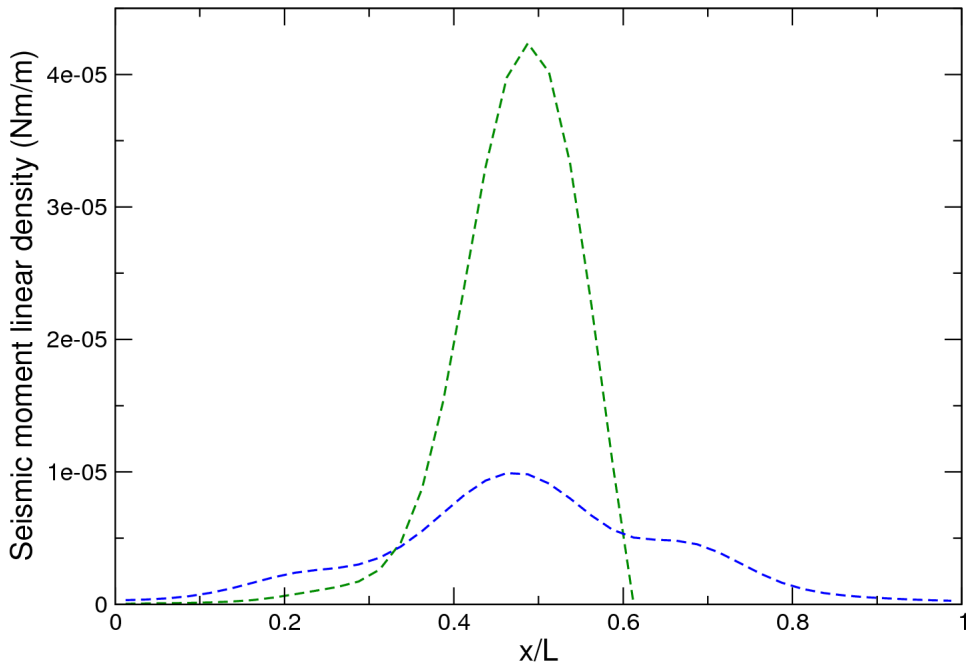

Figure 5.16: Linear density of the seismic moment as a function of the distance along the path for both constant velocity and diffusive slip propagations (blue and green dashed lines, respectively).

5.2.3 The 2003 Tokachi-oki (Japan) slow earthquake

Since 1982 a Sacks-Evertson borehole strainmeter, at a depth of 110 m, is operating at Urakawa Seismological Observatory (KMU) of Hokkaido University in the southern part of the Hidaka Mountains in Japan. This instrument recorded a slow event following a great earthquake occurred off Tokachi (Tokachi-oki) on September 25, 2003 [125]. The strainmeter is located at 105 km from the epicenter of the main shock at azimuth 300 degrees (see Fig. 5.17).

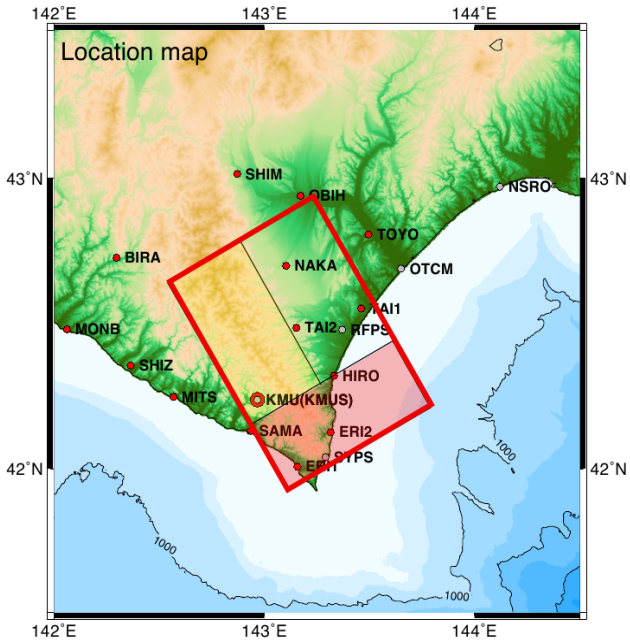

Figure 5.17: Locations of KMU borehole strainmeter and fault source of the slow event (red line). Figure from Ref. [125].

After the main earthquake, the volumetric strain exhibits a marked minimum. It is characterized by a contraction for about 4 days followed by an expansion for 23 days, suggesting the occurence of a slow slip propagation. Fig. 5.18 shows this signal after removing the Earth tides and the effects of air pressure variations and precipitation.

Using a quasistatic calculation to generate synthetic waveforms for the measured quantities, Takanami et al. [125] proposed a 2 stage model of reverse slip propagation down an extension of the main shock rupture plane using a constant velocity propagation model. In the first stage slow slip of 44 cm propagates at 11cm/s on a surface extending 65 km along strike and 32 km downdip from 38 km depth and in the second stage a slow slip of 24 cm propagates at 3 cm/s, on a surface whose dimensions are 32.5 and 66

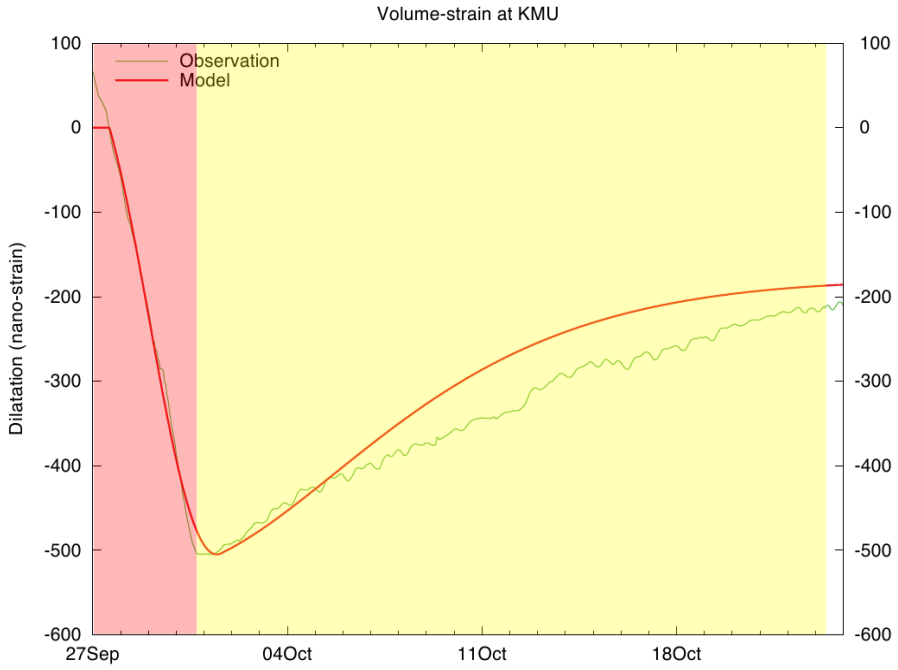

Figure 5.18: Strain history (green line) recorded by the borehole strainmeter KMU. Figure from [125].

km along the strike and dip directions, respectively, from 50.5 km depth. Both faults have strike of 241 degrees and dip of 23 degrees. The predicted signal is shown in Fig. 5.18 (red line).

Signal recorded by KMU borehole strainmeter (green line in Fig. 5.18) has been digitized and both constant velocity and diffusive models have been tested using 1D straight paths on only one thrust fault whose dimensions are about 65 and 98 km along the strike and dip directions (red rectangle in Fig. 5.17) and strike and dip angles are 241 and 23 degrees, respectively. Areal deformation produced by this fault at KMU station is shown in Fig. 5.19.

Fault kernel exhibits the existence of two nodal lines. Furthermore, as the signal is characterized by an initial phase of contraction, it is reasonable to hypothesize that slip propagated from a point located between about 43 and 65 km along the strike direction and 22 and 40 km along the dip one.

Again, both constant velocity and diffusive processes are consistent with observations (Fig. 5.20). Also the mean square deviations are comparable (5.4 and 5.5 for constant velocity and diffusive propagations, respectively). Thus there are no elements which allow to prefer one of the two models.

As for the slow earthquake recorded in the region of Durmid Hill and the F4 fault of Izu-Oshima earthquake, the shape of seismic moment released along the path on fault exhibits a peak at the nodal line (see Fig. 5.21) for both propagation models. One possible source of error could be ascribed to the uncertainty due to existence of a single signal. Moreover, also in this case, it would be important to deepen the source features.

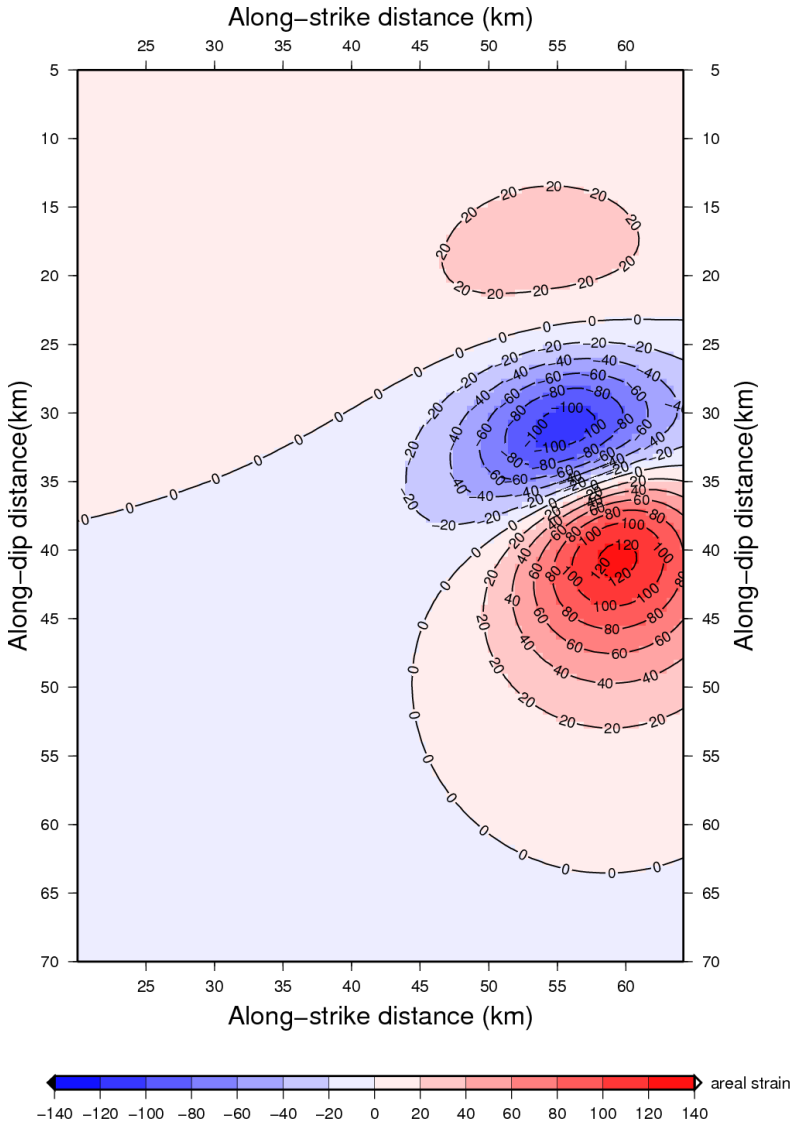

Figure 5.19: Areal strain ($n\varepsilon$) generated by a small rectangular source ($M = 2.5 \times 10^{16}$Nm, thrust faulting) located in different positions on the fault plane at KMU station.

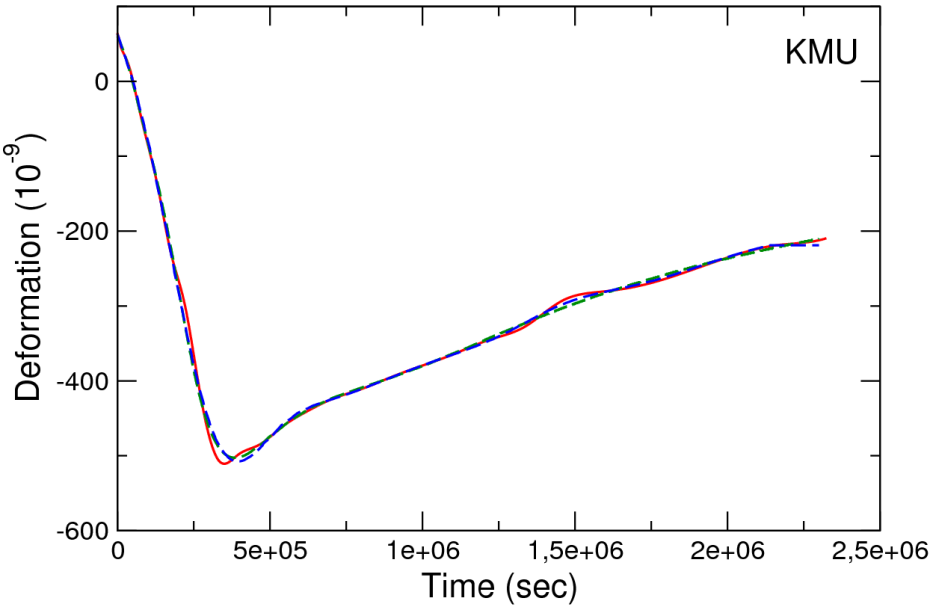

Figure 5.20: Smoothed strain history (red line) recorded at borehole station KMU. Blue dashed lines, predicted strain history for the best constant propagation velocity model ($L \sim 30000\,\mathrm{m}$ and $v \sim 0.014\,\mathrm{m/s}$). Green dashed lines, predicted strain history for the best diffusive model ($L \sim 20000\,\mathrm{m}$ and $c \sim 14\,\mathrm{ms}^{-1/2}$).

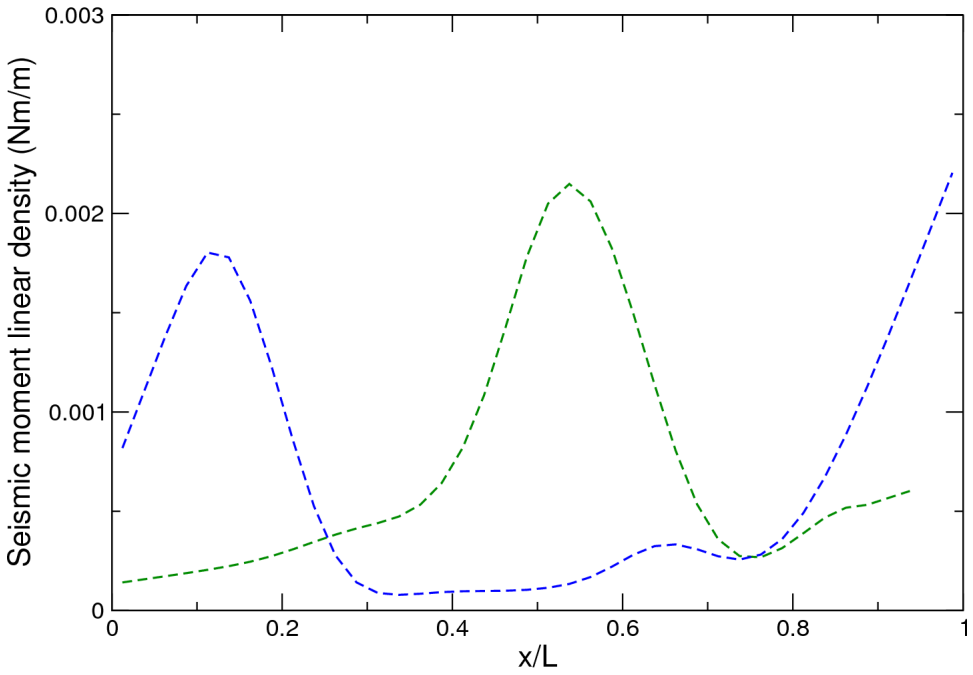

Figure 5.21: Linear density of the seismic moment as a function of the distance along the path for both constant velocity and diffusive slip propagations (blue and green dashed line, respectively).

5.3 Conclusions and open questions

The diffusive character of the rupture propagation, in the past mainly deduced from the observed relationship between seismic moment and characteristic time, was directly observed after the 2009 L'Aquila (Italy) earthquake.

The analysis of signals recorded by two laser interferometers shows peculiar features related to propagation. By using two different propagation mechanisms along 1D straight paths, namely constant propagation velocity and diffusive processes, predicted strain history at both interferometers is fully consistent with diffusive slip propagation, but inconsistent with constant velocity propagation.

Other deformation signals, showing similar characteristics, have been analysed using the two propagation models.

Not all slow earthquakes analysed are consistent with only one of the two models tested. Two of the four slow events (L'Aquila and Izu-Oshima F3 fault) are only consistent with diffusive slip propagation. Constant velocity propagation gives much worst fit to data, being unable to fit the shape of minimum observed on signals recorded by BA interferometer and SHI borehole strainmeter for L'Aquila and Izu-Oshima slow earthquakes, respectively. For both slow events, the seismic moment density decreases about linearly with distance along the path, like the steady-state solution of 1D diffusive processes.

In the other cases (DHL, Tokachi-Oki and Izu-Oshima F4 fault) it is not possible to discriminate the type of propagation; observations are consistent with both diffusive and constant velocity slip propagations. For them, the shape of seismic moment seems somewhat unrealistic, being a bell-shaped distribution, peaked on the nodal line.

These results, as described above, suggest the necessity to deepen the source features, not well constrained in some cases.

Moreover, also the assumption of 1D very thin path might be a source of uncertainty.

Chapter 6

Installation of two laser interferometers at Canfranc (Spain) Underground Laboratory

At present, the Earth Sciences community is focused on developing new interdisciplinary research programs in order to produce high quality data and to allow an advanced study of different, both local and global, geodynamic phenomena. Integrating the knowledge from different sources, it is possible to investigate and to resolve appropriately the structure of the Earth at depth and constrain more the models that define its features, especially in key areas of geodynamic relevance.

The Canfranc Laboratory in Spain is located at depth in one of the most seismically active areas in Western Europe, at the Pyrenean Chain that marks the boundary between the European plate and the Iberian microplate. These features make it particularly suitable for hosting an advanced integrated geodynamic observatory, namely GEODYN.

Two laser interferometers, operating since November 2011, have been installed at Canfranc Underground Laboratory (see Fig. 6.1). These instruments are part of an integrated geodynamic observatory, also equipped with one broad-band seismometer, one accelerometer, and two superficial CGPS stations. This observatory would allow an advanced study of geodynamic phenomena, both local and global, in a spectrum ranging from short period seismic waves to tectonic deformation. Among local phenomena, there are for example measurements of seismic phase velocities, slow earthquakes, strain seasonal changes, tectonic deformation; among global phenomena, seismic core modes, free oscillations of the Earth and Free Core Nutation.

Figure 6.1: Location and directions of the laser interferometers GAL 16 and LAB 780 operating at Canfranc.

6.1 Installation of Canfranc laser interferometers

Two laser strainmeters have been installed in the Tunnel of Somport, along bypass 16 (Galeria 16, azimuth N81.7E) and inside Laboratory 780 (Laboratorio 780, azimuth N-26.6E) respectively [126]. Because of their location, they have been called GAL 16 and LAB 780 (see Fig. 6.2).

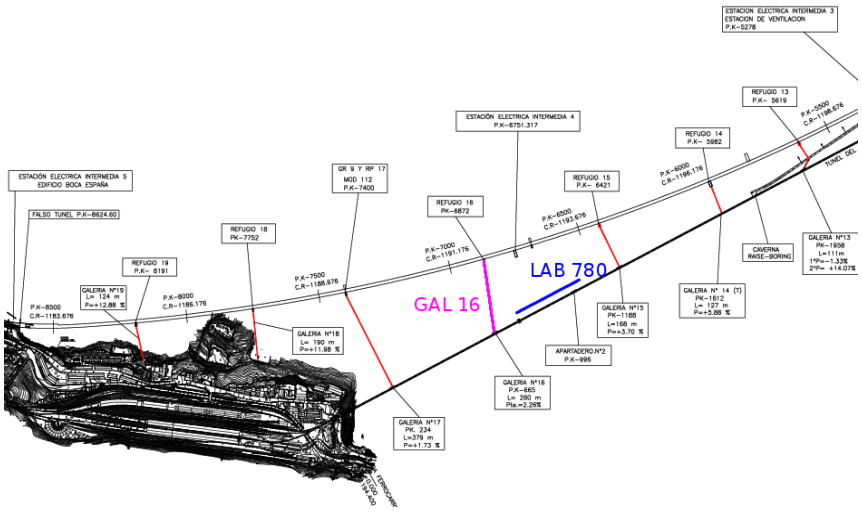

Figure 6.2: Tunnel of Somport and location of the two interferometers GAL 16 and LAB 780 operating at Canfranc.

The instruments have been developed starting from the design of the interferometers

working at Gran Sasso (see Section 3.2) with some improvements. They are based on the classical unequal-arm Michelson set-up and compare the optical length of a longer measurement arm, about 70 meters in length, and a shorter fixed reference arm that is about 12 cm in length.

The installation of these two interferometers started at the end of August 2011. It required the following steps:

- ✓ excavating the tunnel floor down to the rock at the plinth sites (see Fig. 6.3) for isolating the plinths from the floor and anchoring them directly to the rock;

Figure 6.3: Excavation for the main plinth in Bypass 16.

- ✓ making, placing and fixing the plinths (see Fig. 6.4);

Figure 6.4: Positioning of the main plinth in Bypass 16.

- ✓ making and placing the pipe holders for supporting the vacuum line;
- ✓ mounting the vacuum line (pipes, chambers, pumps) hosting some of the optical components and letting the propagation of the laser beam inside evacuated pipes to avoid wavelength changes due to fluctuations of the air density and humidity (see Figs. 6.5 and 6.6);

Figure 6.5: Main plinth (left picture) and vacuum line (right picture) in Bypass 16.

Figure 6.6: End plinth (left picture) and vacuum line (right picture) in Laboratory 780.

- ✓ testing vacuum produced by one vacuum pump for evacuating the pipes and the chambers and maintaining the vacuum level inside them; air pressure inside the pipes and the chambers is measured by one vacuum sensor (see Fig. 6.7);

Figure 6.7: Vacuum pump (left picture) and electro-mechanical high vacuum valve (right picture) inside Bypass 16 and Laboratory 780, respectively.

✓ assembling and aligning the opto-mechanical components (mirrors, lenses, optical isolators, beam splitters, windows, etc.) for manipulating the laser beam and conditioning its propagation (see Fig. 6.8);

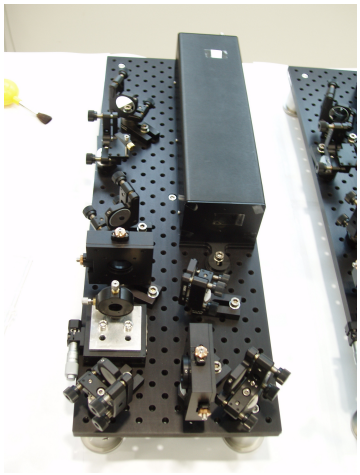

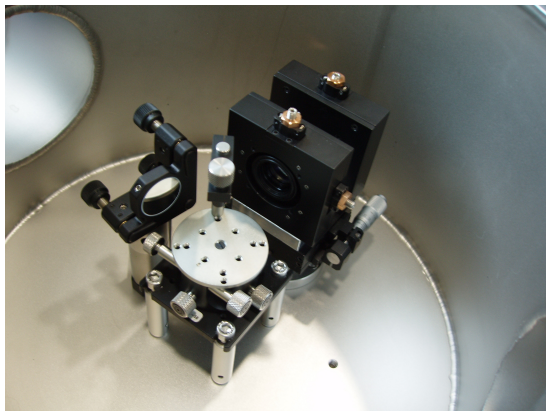

Figure 6.8: Laser head and optics for the laser beam conditioning, placed out of the main chamber of each interferometer (left picture). On the right, part of the optics placed inside the main chamber.

✓ making the electronic circuits (photodetection, environmental sensors, Analog-to-Digital converter) for measuring the intensity of the output laser light at two photodiodes and signals from sensors of air temperature and pressure (see for example the Analog-to-Digital converter in Fig. 6.9);

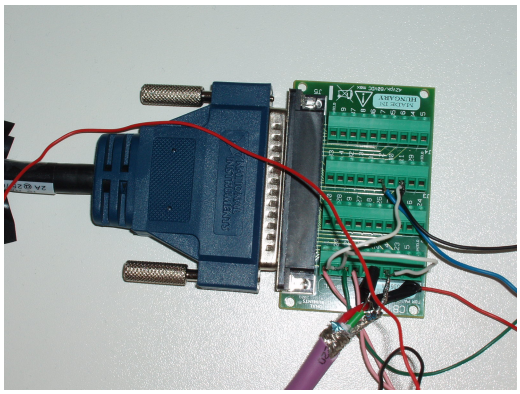

Figure 6.9: Analog-to-Digital converter NI PCI-6221 (37-pin).

✓ setting up the data acquisition and transmission system by means of an internet connection.

In addition, a horizontal hole (about 15 m in length and 20 cm in diameter) has been drilled to connect the two parts of the Laboratory 780.

Each interferometer measures the displacements between two concrete blocks (about $0.2\,\mathrm{m}^3$ and $0.1\,\mathrm{m}^3$) connected directly to the rock by a special cement adhesive and separated from the floor by an about 15 cm wide track (see Fig. 6.10). For each interferometer, a vacuum system encloses the laser beam and it is decoupled from the end monuments and the optical components by bellows. The vacuum system is made of stainless steel. Two custom chambers are at the ends of the DN 100 ISO-K vacuum line, fixed on the terminal plinths. They consist of two custom DN 320 and DN 200 vacuum chambers.

Vacuum is obtained with a pumping station, including a forevacuum pump and a turbomolecular pump. At first the forevacuum pump starts; when a pressure of 10 mbar is reached, the turbomolecular pump can be turned on. All high-vacuum components are manufactured from stainless steel 304L and Viton. Flanges and fittings are conform to the ISO-K and KF standards. The vacuum system is totally reliable from atmosphere to 10^{-5} mbar without baking. The pressure is measured using a Pirani vacuum gauge, from atmosphere to 10^{-4} mbar, range sufficient for the performance of the vacuum monitoring.

Also a continuous monitoring of air temperature and pressure in the bypass and laboratory is carried out by using different sensors. Five temperature sensors are placed at different point along the interferometers. Two of them are placed on the basement of

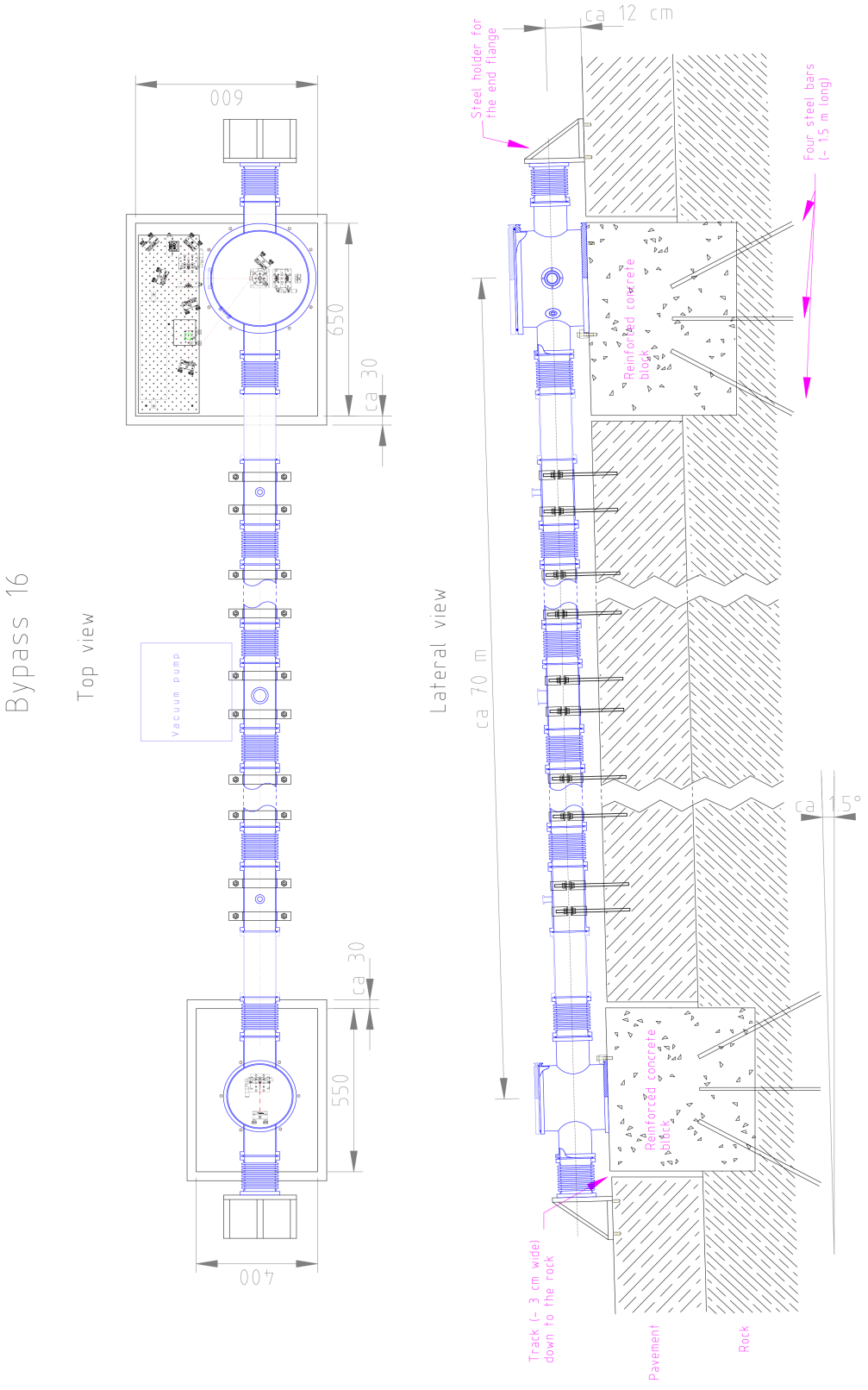

Figure 6.10: Vacuum line set-up in Bypass 16 (all dimensions in millimeters).

the end-plinths; one is located near the optical system on the main plinth; two at middle of the interferometer, on the pipe line and in air fixed to the wall. Also a barometric pressure sensor is placed at middle of the interferometer.

Photodetection, data acquisition and transmission have been designed to reduce the number of in situ operations. It is possible a remote monitoring of the interferometers and controlling of the photodiode-ADC gain and bias.

6.2 Instrumental set-up

The two strainmeters measure distance changes between two end points by means of Michelson-type optical interferometers. The two end points are anchored to the rock; their distance is about 70 meters. Temperature, barometric pressure and vacuum pipe pressure are also monitored at different points along the line of the interferometers.

6.2.1 Interferometer set-up

Two photodiodes measure the intensity of the vertically- and horizontally-polarized components, given by one of the two outputs of each interferometer. In principle the two signals are in quadrature and related to the sine and cosine of a phase change, which is proportional to the baseline extension change. The related Lissajous figure, obtained by plotting the intensity of the vertically-polarized component as a function of horizontally-polarized one, can be inverted for changes in length of the 70-m long baseline and thus for strain.

The interferometers measure the change of distance between two points anchored to the rock and distant about 70 meters, following the classical unequal-arm Michelson set-up, according to what has already been made for the two laser interferometers installed in the Gran Sasso Underground Laboratories [39].

The instruments compare the optical length of a longer measurement arm, about 70 meters in length, and a shorter fixed reference arm that is about 12 cm in length (see Fig. 6.11). Fig. 6.11 also shows a schematic view of optical set-up for the laser beam conditioning, placed on the main plinth and out of the main DN 320 ISO-K chamber.

A collimated light beam, vertically polarized, from HeNe laser is deviated by an alignment mirror and, after passing through an optical isolator which rotates the plane of polarization of 45 degrees and a system of aspherical lenses to collimate it, arrives at

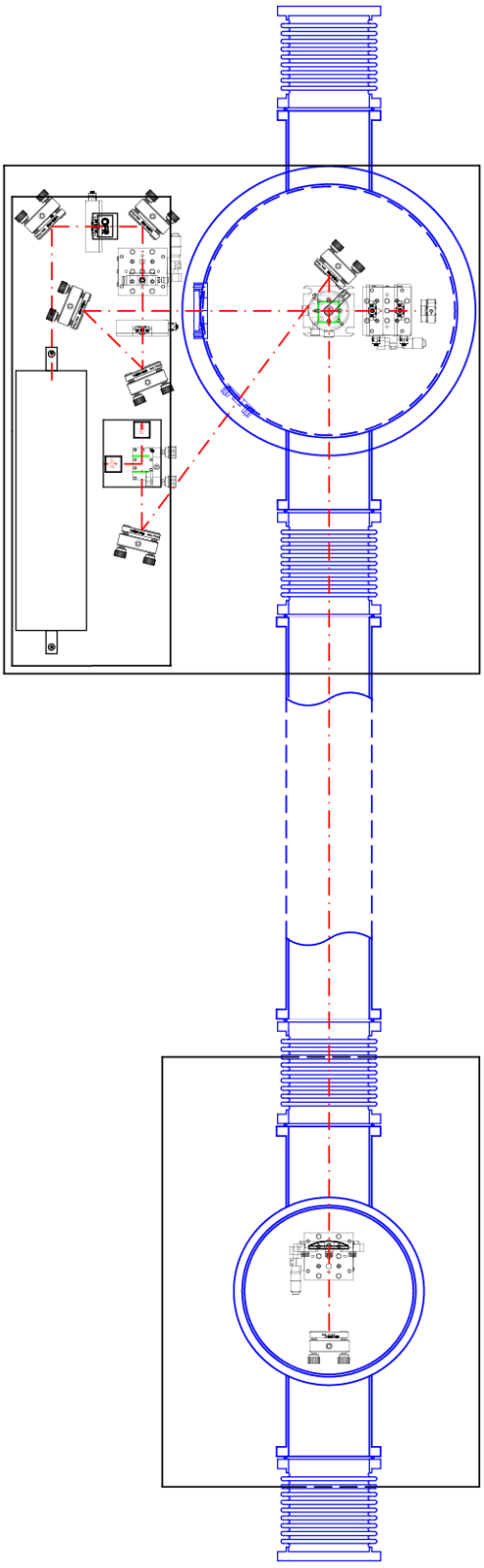

Figure 6.11: Sketch of the opto-mechanical set-up.

a beam splitter located inside the main chamber. Here it is separated equally moving toward two retroreflectors, namely *cat's eye*, located at the ends of the reference and measurement arms respectively (see for example the eye's cat placed in the terminal DN 200 ISO-K chamber, Fig. 6.11). Each cat's eye consists of a system of aspherical lens and mirror which minimizes beam distortion and alignment problems, but overlaps the reflected and incident beams.

The light beam, moving along the reference arm, reaches the cat's eye and is reflected back, passing through a $\lambda/8$ waveplate, necessary to make the exit beam circularly polarized and to produce two output signals in quadrature.

The reflected signals interfere on the beamsplitter; one of the two outputs is in turn split into horizontally- and vertically-polarized components, whose intensities are detected by two photodiodes.

The related Lissajous figure (see Fig. 6.12) can be inverted for changes in length of the 70-meter long measurement arm and thus for strain. A baseline-length change of half a wavelength of the laser light (about 4.52×10^{-9} in strain) is related to a complete round along the ellipse, whose axis lengths and orientations slightly change with time because of mechanical and rock instabilities.

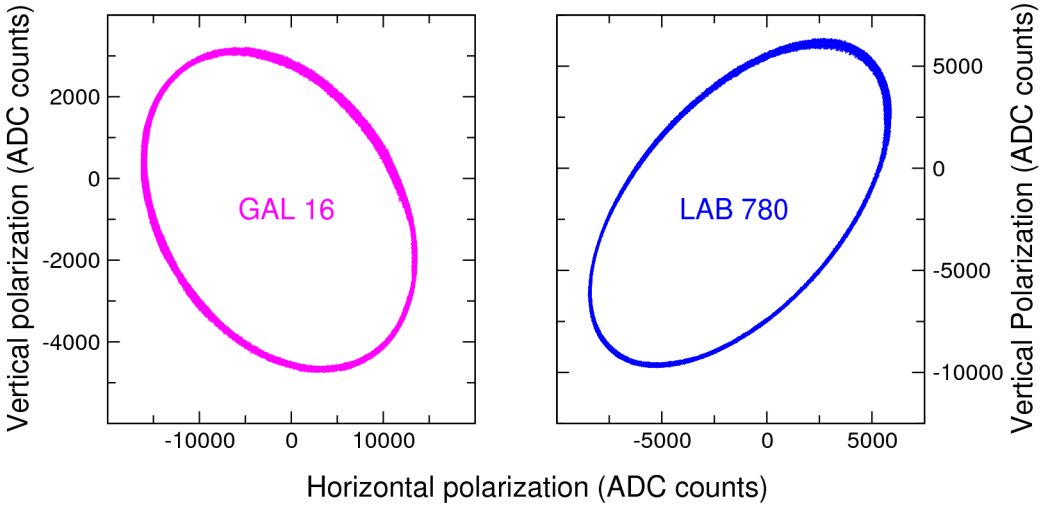

Figure 6.12: Scatter plot of 12 M samples recorded by the two interferometers GAL 16 and LAB 780.

The Lissajous figures of LAB 780 at different times are very stable, suggesting that also the optical alignment of the interferometer is very stable. Because of a degradation in the optical alignment of the GAL 16 interferometer, the Lissajous figures of GAL 16

instead deteriorate in the time. This is probably caused by a floor instability in the bypass, clearly visible in the rock of the walls.

In July 2012, the optical set-up of the reference arm has been slightly changed, placing on the lens translator a round rotatable cylindrical lens mount that contains the $\lambda/8$ waveplate. In this way it is possible to rotate the waveplate easily and to optimize the quality of the Lissajous figure (see Fig. 6.13).

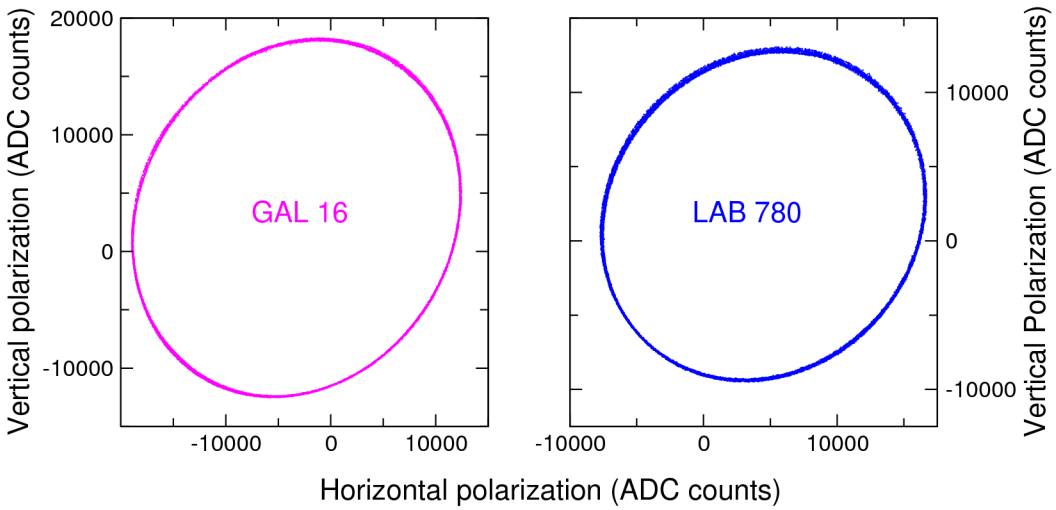

Figure 6.13: Scatter plot of 12 M samples recorded by the two interferometers GAL 16 and LAB 780 with the new optical set-up of the reference arm.

A real time conversion from light intensity to phase, and thus to strain, is not possible. The instabilities of DC level, the interference signal amplitude, and phase lag fluctuations between the photodiode outputs require a non-linear fitting of the Lissajous figure given by few hours of vertically- and horizontally-polarized components.

Photodiode outputs are sampled and stored at 600 samples per second to reduce possible artificial mixing of frequencies due to the non-linear dependence of the light intensity on phase mismatch.

6.2.2 Laser source

As laser source an ML-1 Polarization-Stabilized HeNe Laser by Micro-g LaCoste, Inc. (`http://www.microglacoste.com`) is used (see Fig. 6.14). It provides a linear-polarized, frequency-stabilized or intensity-stabilized, coherent, light source of continuous wave visible (red) laser light with a nominal output power of 1 mW.

This laser is characterized by a Short Term (10 msec) root mean square (RMS) frequency fluctuations smaller than 100 kHz (2×10^{-10}) and long term (days) RMS frequency fluctuations smaller than 800 kHz (2×10^{-9}) for < 1 °C room temperature changes.

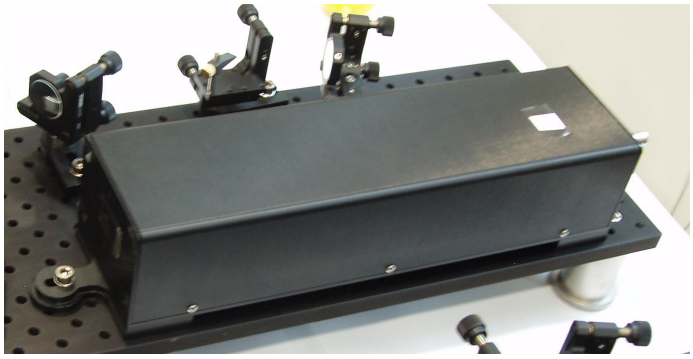

Figure 6.14: ML-1 Polarization-Stabilized HeNe laser.

It consists of a compact laser head and a control unit housing the laser electronics, designed to operate as a stand-alone unit or in conjunction with a remote controller in an integrated system.

The ML-1 housed in the thermally-controlled unit and the laser beam exit at a standard height of 2". The housing can also accommodate an optional fiber optic mount and optical isolator.

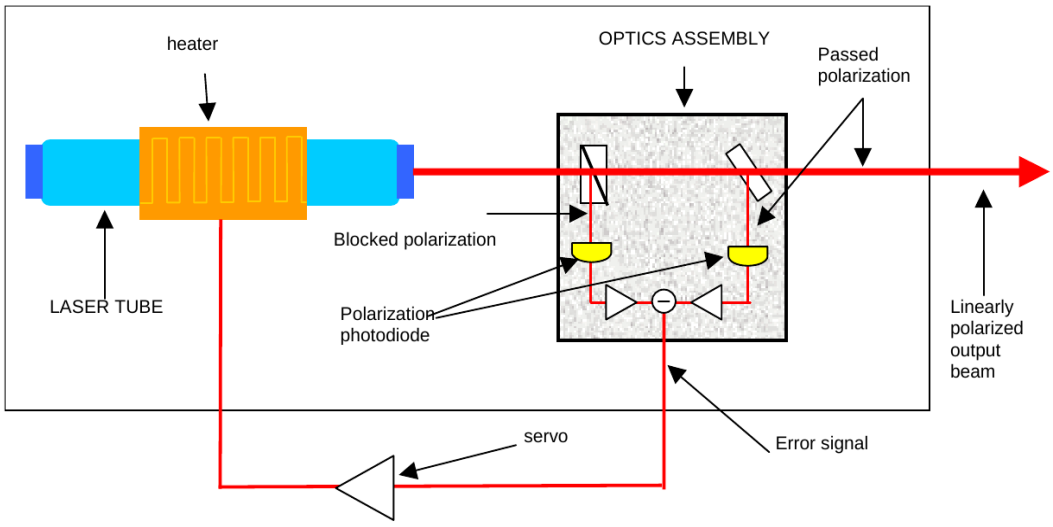

Figure 6.15: Laser Head. Figure from `http://www.microglacoste.com/pdf/ml1-manual.pdf`.

ML-1 frequency stability is obtained by balancing the intensities of two TM00 modes in the laser tube. These modes have orthogonal linear polarizations, and it is possible to detect them separately by independent photodetectors using polarizing optics.

The tube length can be adjusted by changing the temperature through the heater. The variation in length affects the intensities of the blocked and passed polarizations. The difference between the intensities is used to lock the laser cavity with a consequent reduction of the free-running instability of the laser.

There are two possible lock points denoted as red and blue. Their frequencies differ by about 700 MHz and are both quite stabilized. The laser can also be locked to stabilize the output power (intensity) of the laser.

In this case, the frequency-stabilized mode is used.

6.2.3 Photodiodes

To measure the intensity of the vertically- and horizontally-polarized output components of the laser beam, two OPT101 sensors are employed.

The OPT101 is a monolithic photodiode integrated by a transimpedance amplifier, produced by the Texas Instruments (`www.ti.com`). The combination of photodiode and amplifier on a single chip eliminates some common problems, like for example leakage current errors, noise pick-up, and gain peaking due to stray capacitance.

It operates from +2.7 V to +36 V supplies, with a low quiescent current, and for a range of temperature between 0 °C and +70 °C. The output voltage increases linearly with light intensity.

Fig. 6.16 shows the OPT101 basic connections required to operate.

Fig. 6.17 shows the actual pin configurations. In particular Pin 1 and 3 are connected to a positive and negative power supply voltage respectively. The values of capacitors used are $C_1 = 0.1\,\mu\text{F}$ and $C_2 = 100\,\text{pF}$.

Signals produced are sampled and stored at 600 samples per second.

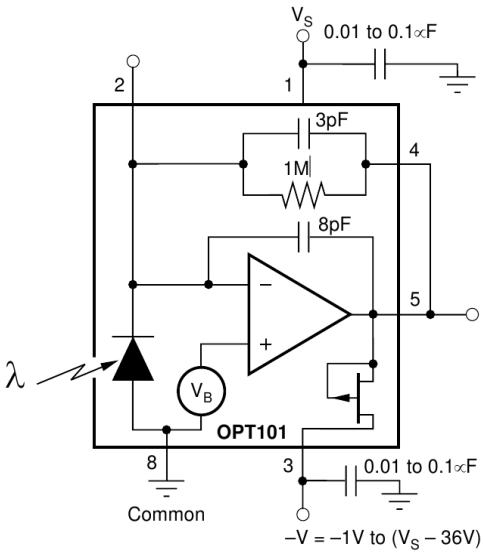

Figure 6.16: Bipolar Power Supply Circuit Connections of the OPT101. Figure from `www.ti.com/lit/ds/symlink/opt101.pdf`.

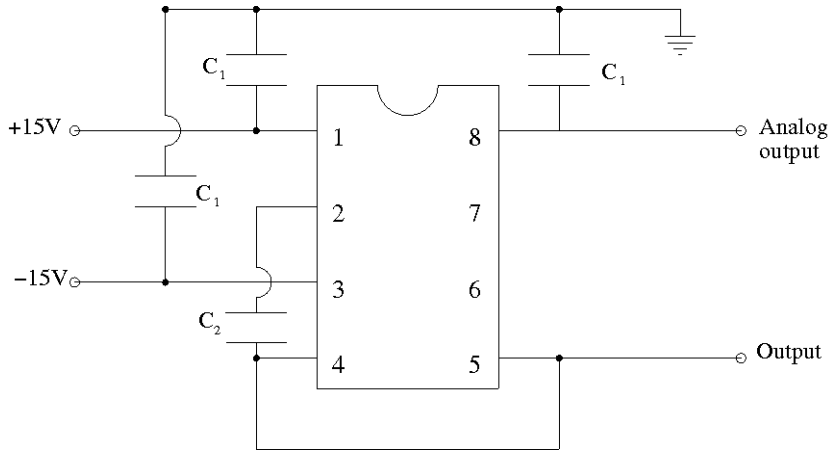

Figure 6.17: OPT101 pin configurations.

6.2.4 Vacuum sensors

To detect the value of pressure inside the vacuum line of the interferometer, an APG100-XLC Active Pirani vacuum gauge is used. This sensor, produced by the Edwards (`http://www.edwardsvacuum.com/`), measures vacuum pressures in a range from 10^{-4} to 10^{3} mbar.

It operates by using electrical supply voltage range from +15 to +30 V, with a minimum value of 13.5 V, and producing a nominal output signal between 0 and 10 V. Its operating temperature range is between 5 °C and 60 °C. Sensor's features include compact size for easy installation, a linear output, a remote calibration, and a replaceable sensor tube.

Figure 6.18: APG100-XLC Active Pirani vacuum gauge.

The APG100-XLC can be mounted in any orientation but manufacturer recommends to mount the gauge tube vertical in order to minimize the build up of process particulates and condensable vapors within the gauge. Changing the orientation, the gauge should be recalibrated at atmospheric pressure.

It operates using RJ45 8-way connector. The pins from 1 to 8 on the electrical connections are: positive supply, supply ground (0 V), pressure measurement, output signal, gauge identification, signal ground, set-point output signal, remote calibration input and the last one pin is not connected.

If the gauge is connected to a voltmeter, the conversion of the voltage (V) in pressure (P) is possible by using one of the following equations

$$P = 10^{(V-6)} \quad \text{mbar} \tag{6.1}$$

$$P = 10^{(V-6.125)} \quad \text{Torr} \tag{6.2}$$

$$P = 10^{(V-4)} \quad \text{Pa} \tag{6.3}$$

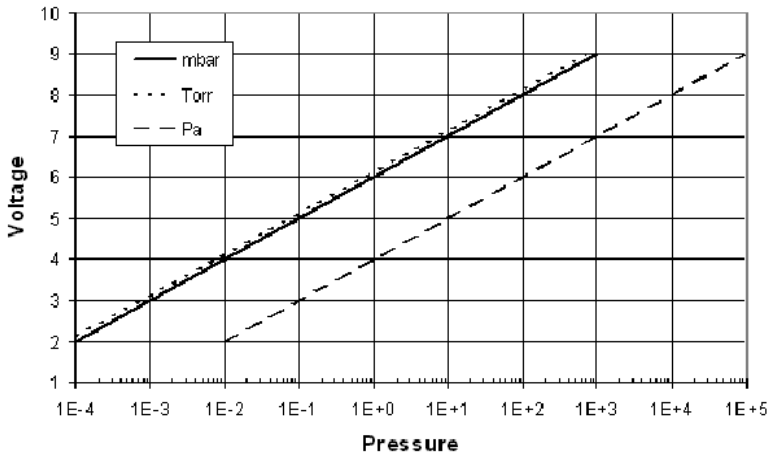

Figure 6.19: Conversion from voltage to pressure for APG100-XLC. Figure from `http://www.edwardsvacuum.com/Viewers/Document.ashx?id=1002&lcid=2057`.

Fig. 6.19 summarizes these conversions. The signal produced is sampled and stored at 20 samples per second.

6.2.5 Temperature sensors

LM35CAZ Precision Centigrade Temperature Sensor is a precision integrated-circuit temperature sensor from the LM35 series, produced by the Texas Instruments (`www.ti.com`), here used for the temperature measurements.

These sensors are suitable for remote applications, characterized by a low output impedance and their output voltage is linearly proportional to the Celsius temperature, with a linear +10.0 mV/°C scale factor.

This sensor does not require any external calibration. Its typical accuracy is ±1/4 °C at room temperature and ±3/4 °C over the full -55 to +150 °C temperature operating range. It can be used with single power supplies, or with plus and minus supplies (as done in this specific case), using a supply voltage from +4 to +30 V. In this specific case a voltage of ±15 V is applied.

Fig. 6.20 shows the application used for the LM35. A 200 Ω load resistor is added to make the sensor relatively immune to wiring capacitance. In this way, in fact, the capacitance forms a bypass from ground to input, not on the output.

Five temperature sensors are placed at different point along the interferometers. Two of them are placed on the basement of the terminal plinths; one is located near the optic

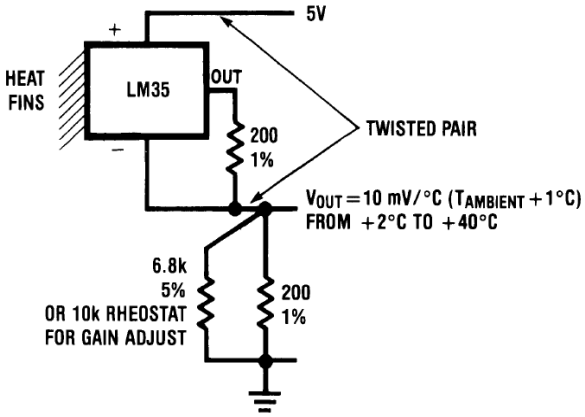

Figure 6.20: Two-Wire Remote Temperature Sensor. Figure from `www.ti.com/lit/ds/symlink/lm35.pdf`.

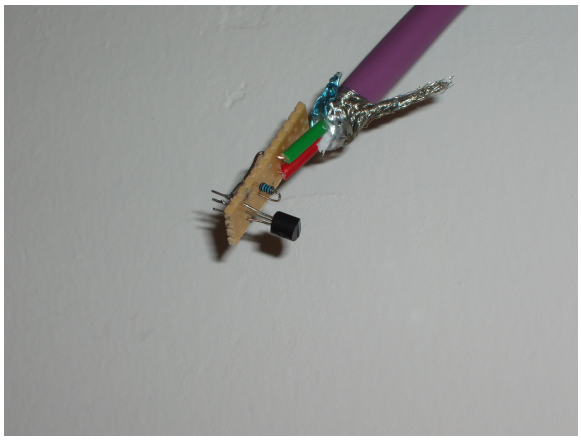

Figure 6.21: LM35 operating mode.

system on the main monument; two at middle of the interferometer, on the pipe line and in the air, fixed to the wall. These signals are sampled and stored at 20 samples per second.

6.2.6 Barometric pressure sensors

MPX2102ASX is a sensor from the MPX2102 series devices, produced by Freescale Semiconductor, Inc. (`http://www.freescale.com/`).

These silicon piezoresistive pressure sensors consist of a single, monolithic silicon diaphragm with the strain gauge and a thin film resistor network integrated on chip. The chip is laser trimmed for precise span and offset calibration and temperature com-

pensation. Fig. 6.22 shows a block diagram of the pressure internal circuit on the chip.

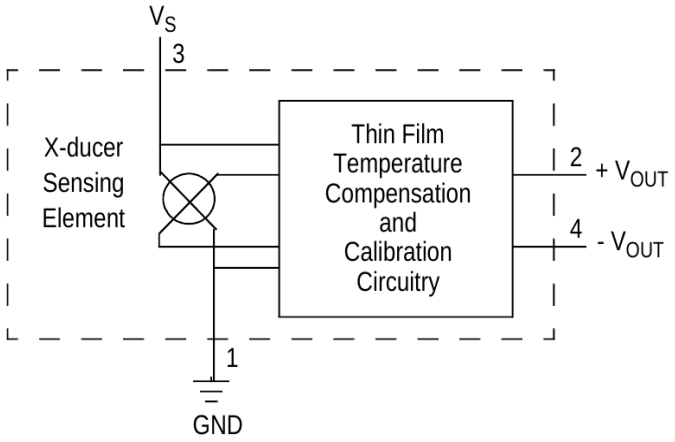

Figure 6.22: Temperature Compensated Pressure Sensor Schematic. Figure from `http://www.freescale.com/files/sensors/doc/data_sheet/MPX2102.pdf`.

This device provides a linear voltage output directly proportional to the applied pressure. It can be used in temperature range between 0 °C and 85 °C, in absolute, differential and gauge configurations. The measuring pressure range is between 20 and 100 kPa, with a sensitivity of 0.4 mV/kPa.

In this specific case, the pressure sensor is placed at middle of each interferometer and the signal produced is sampled and stored at 20 samples per second.

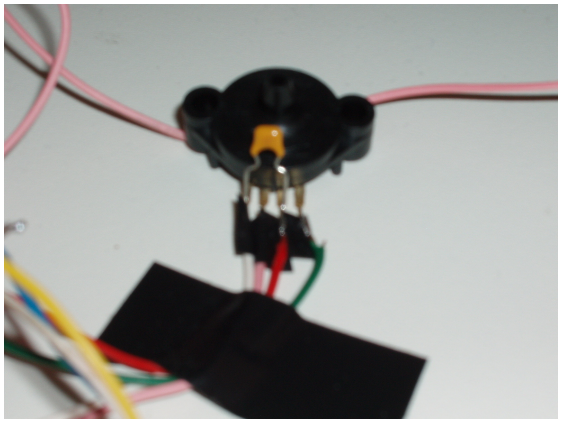

Figure 6.23: MPX2102ASX operating mode.

6.3 First data sequences

Photodiode outputs, temperature, barometric pressure and vacuum pipe pressure are sampled and stored for each interferometer.

A preliminary analysis of the first strain records has been introduced at the 2012 European Geosciences Union (EGU) General Assembly [126].

Plots in Fig. 6.24 show strain recorded by the two interferometers, barometric pressure and one of five temperatures (sensor placed on the basement of the main plinth) after applying a low-pass filter and decimating data at 2 cycles per hour, from December 2011 until September 2012.

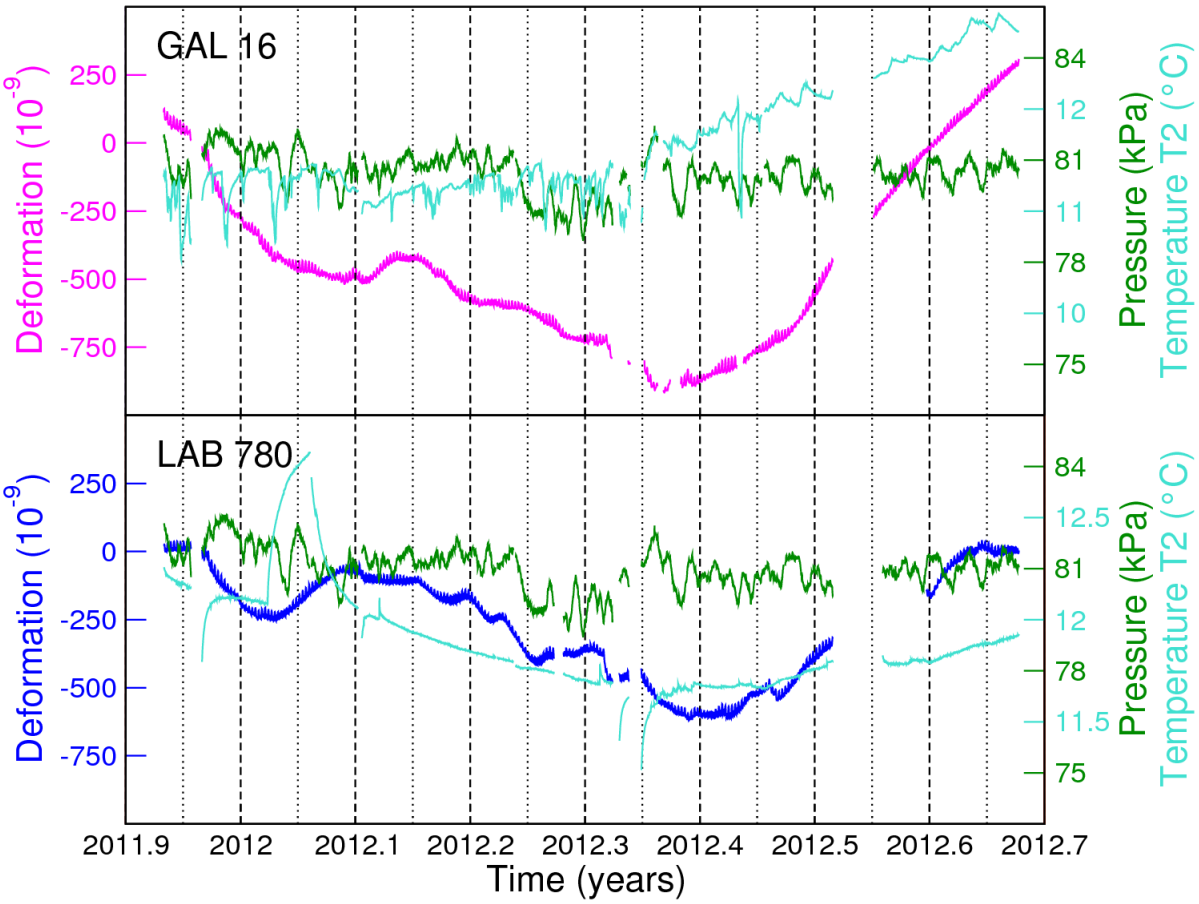

Figure 6.24: Strain, barometric pressure and temperature on the basement of the main plinth for both GAL 16 (upper plot) and LAB 780 (lower plot) interferometers. All data are filtered and decimated at 2 cycles per hour.

Unfortunately, during this period several breaks occurred in the acquisition because of black-outs and UPS malfunctioning. The instruments also suffered technical problems

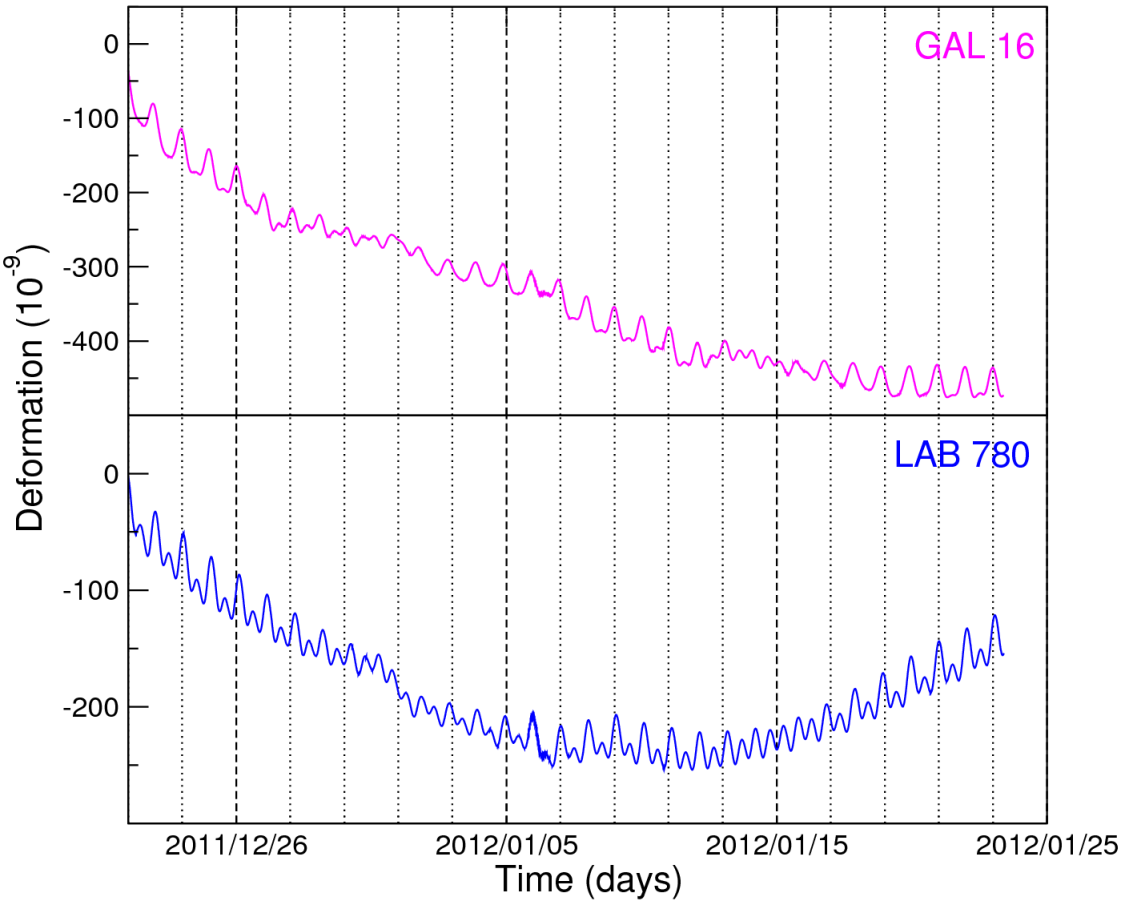

Figure 6.25: Example of strain data low-passed and decimated at 6 cycles per minute by GAL 16 (upper plot) and LAB 780 (lower plot) interferometers.

caused by laser source and pump system malfunction, currently solved but that caused further breaks in the acquisition. After each break the strain level is arbitrarily shifted, trying to connect the trend when and where possible.

Both periodic, as Earth tides and telesisms, and non-periodic signals are generally evident in the strain sequences. The signals are clearly dominated by the diurnal and semidiurnal strain tides, as noticeable in Fig. 6.25 where strain recorded by GAL 16 and LAB 780 interferometers at the end of December 2011 is shown.

Correlations between deformation data and barometric pressure and temperature appear do not to exist, at least on these time scales. The sequences are not sufficiently long to perform attempts for correcting, if necessary, the strain data for environmental effects, for example in the diurnal tidal band.

6.3.1 Pre-analysis

The interferometers are able to record the transit of the seismic waves produced by the earthquakes. For this reason, it is possible to consider the interferometers as long-period seismometers. Depending on the source site, seismic waves are differently attenuated because of the directionality of interferometers, but all phases are recordable and recognizable.

Fig. 6.26 shows an example of strain records in the seismic band, recorded during the transient of teleseismic waves produced by a 5.1 magnitude earthquake occurred off the west coast of Sumatra at a depth of 10 km on January 10, 2012.

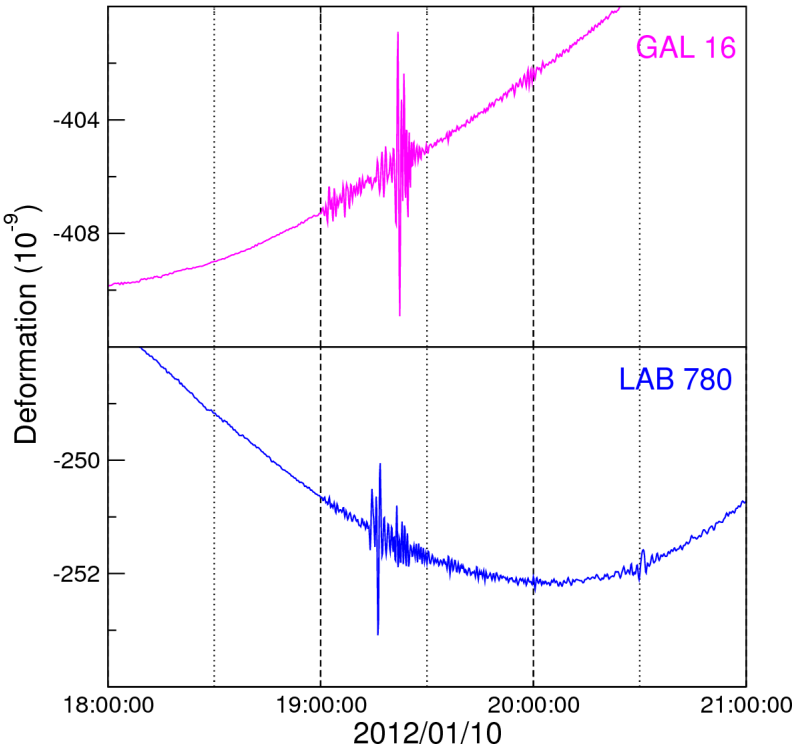

Figure 6.26: Signal, low-passed and decimated at 6 cycles per minute, recorded during the transient of teleseismic waves by both GAL 16 and LAB 780 interferometers.

To understand if it is really possible to use interferometers as seismometers, deformation signals were compared with those recorded by a broad-band seismometer, part of the GEODYN project, installed in Laboratorio 780 on a granite thick slab, coupled to bedrock. Fig. 6.27 shows an example of BB-velocity records, in East-West (HHE), North-South (HHN), and Up-Down directions (HHZ), recorded during the transit of the seismic waves produced by the 2011/12/14 Papua New Guinea earthquake.

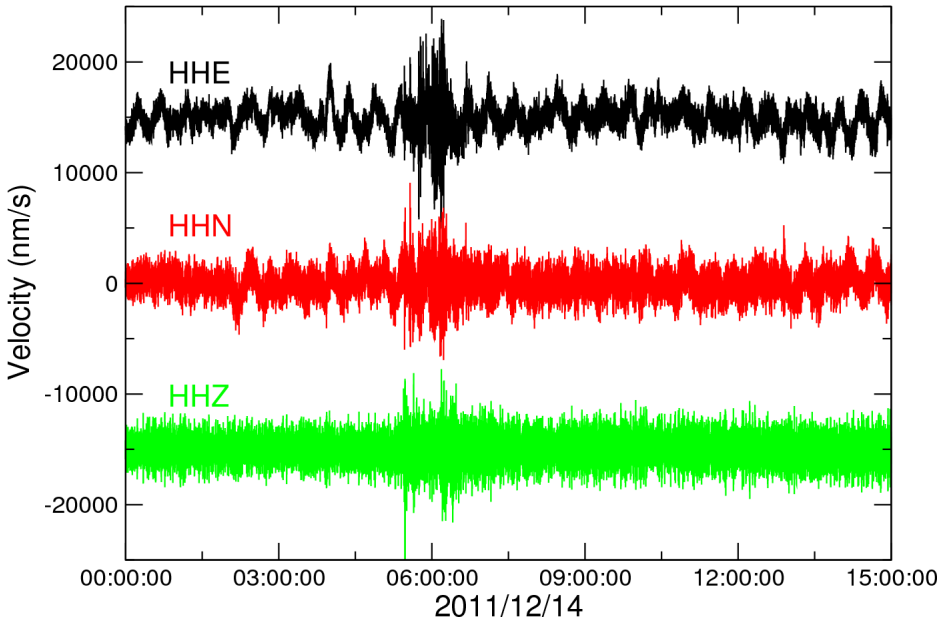

Figure 6.27: East-West, North-South and Up-Down BB-velocity components (black, red and green lines respectively) produced by the 2011/12/14 Papua New Guinea earthquake. Data are sampled at 1 cycle per second.

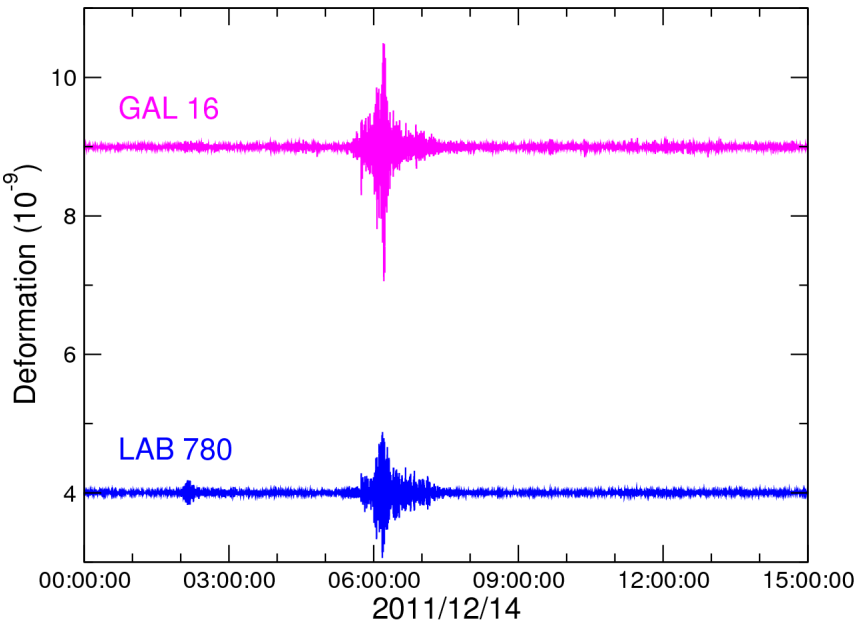

Figure 6.28: Straingrams (magenta and blue lines, GAL 16 and LAB 780 respectively) of Canfranc interferometers produced by the 2011/12/14 Papua New Guinea earthquake. Data are decimated at 1 cycle per second and filtered using a band-pass FIR filter (15 to 150 s).

Fig. 6.28 shows the straingram produced by this earthquake at the Canfranc interferometric station. Signals have been detided, decimated at 1 sample per second and filtered using a band-pass FIR filter (15 to 150 s). This event has been chosen from among those registered simultaneously by both instruments because it produced one of the largest signals on the interferometers.

A comparison between strain and BB-velocity components is shown in Fig. 6.29. Straingrams (magenta and blue lines, GAL 16 and LAB 780 respectively) are compared with seismograms along GAL 16 and LAB 780 directions (indigo and turquoise lines, BB_{GAL} and BB_{LAB} respectively) obtained combining the two horizontal HHE and HHN components of the seismometer. All signals have been decimated at 1 sample per second and filtered using a band-pass FIR filter (15 to 150 s). The agreement between the two different types of signals is evident, confirming the possibility to use the interferometers also as seismometers.

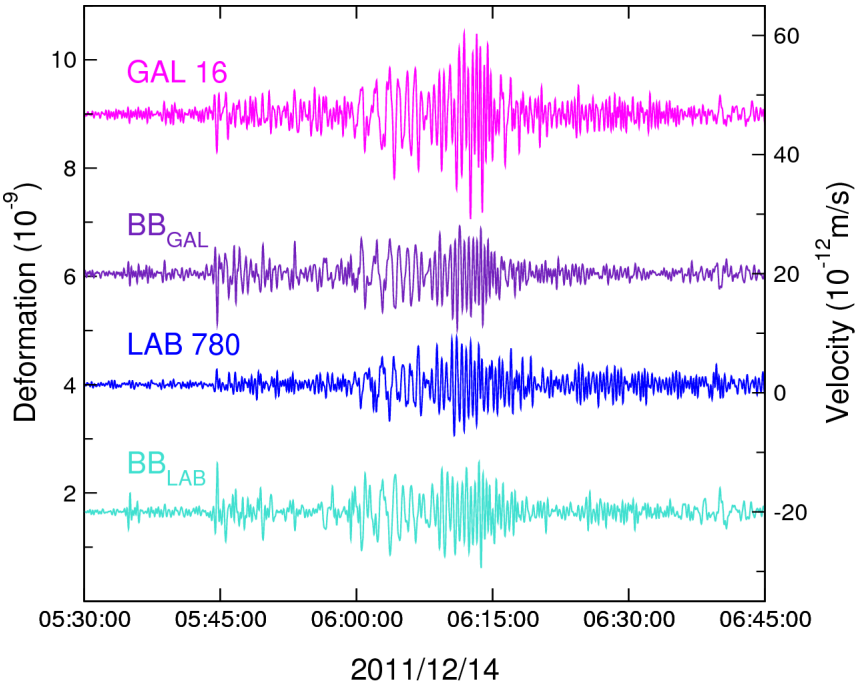

Figure 6.29: Straingrams (magenta and blue lines, GAL 16 and LAB 780 respectively) and seismograms (indigo and turquoise lines, BB_{GAL} and BB_{LAB} respectively) produced by the 2011/12/14 Papua New Guinea earthquake. Data are decimated at 1 cycle per second and filtered using a band-pass FIR filter (15 to 150 s).

Fig. 6.30 shows a comparison between Power Spectral Densities of detided strain data recorded at Canfranc and Gran Sasso stations (about 9- and 46-day-long sequences

respectively) to estimate the S/N level of the Canfranc interferometers and compare it with Gran Sasso one.

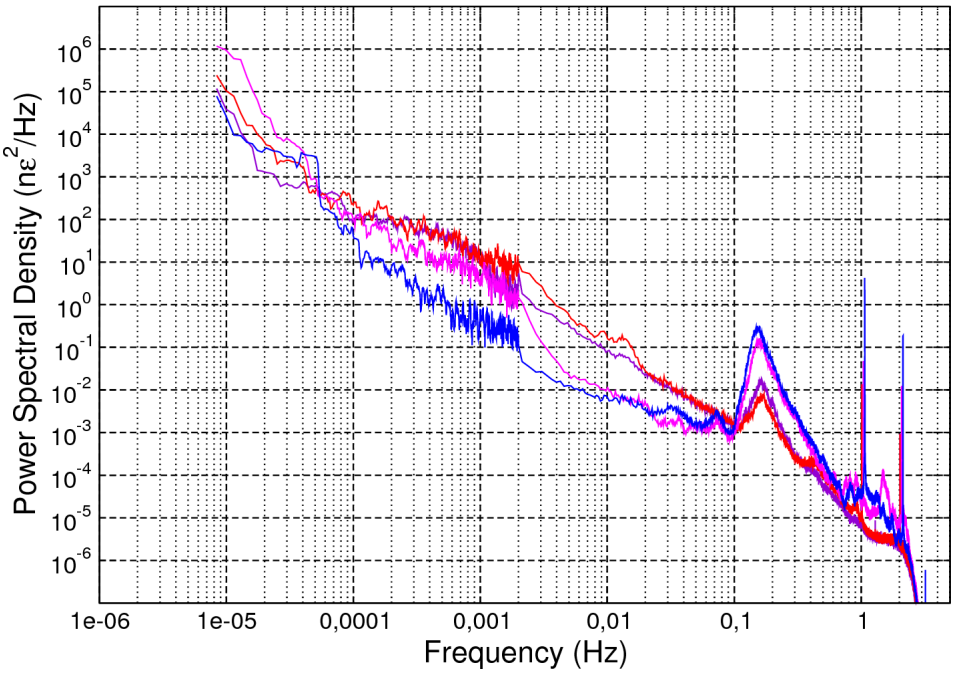

Figure 6.30: Power spectral density of Canfranc (magenta and blue lines, GAL 16 and LAB 780 respectively) and Gran Sasso (violet and red lines, BA and BC respectively) interferometers.

As done in Subsection 3.2.2 for Gran Sasso data, to eliminate the contamination related to Earth tides, these last have been removed from strain sequences by least-squares fitting a sum of sine and cosine functions of variable amplitude at different fixed frequency.

A 7-day-long segment has been extracted from each detided sequence. These segments, characterized by the absence of signals attributable to telesisms, anomalies, periodic or aperiodic phenomena, have been analysed to estimate the spectra.

The higher ($f > 0.002$ Hz) part of the spectrum has been obtained filtering data with a low-pass filter and decimating them at 10 samples per second. To compute the PSD the record has been broken into about 3300-sec-long 50%-overlapped windows, each window has been tapered with a cosine-bell taper, and at the end an average of FFTs on all the windows has been calculated. The lower part of spectrum has been obtained filtering data with a low-pass filter, decimating filtered data at 3 samples per minute, and calculating the FFT on an only one window, again 3300 sec in length, tapering with a cosine-bell taper.

In the frequency range between 10^{-1} and 10^{0} Hz, GAL 16 and LAB 780 spectra are above BA and BC ones, because of a large effect of microseismic activity, but in the frequency range between 10^{-4} and 10^{-3} Hz they are below (more than one order of magnitude in the case of LAB 780).

These first tests evidence a noise level much lower than that of the Gran Sasso instruments, suggesting the capability of producing clear records of low-frequency seismic waves, Earth free oscillations, and possible local aseismic stress release.

6.3.2 Tidal analysis

Reliable use of strain data requires correction for local distortions (see Subsection 3.3.1 for details). These effects can be estimated from tidal records, to which both solid and ocean loading tides contribute. As explained in the previous chapters, the response of the solid Earth to the forcing tidal potential is well acknowledged, while the deformation of the crust induced by the water load due to ocean tides is scarcely known.

Ocean loading effects are estimated using SPOTL [97] (see Appendix D). Mass-loading Green's functions are computed for gbavap, contap and ocenap, representative of an average Earth, a thick continental crust and a thin oceanic crust respectively. Four recent high resolution global ocean models are used, i. e. TPXO7-atlas2011 (`http://volkov.oce.orst.edu/tides/`) developed at Oregon State University [99, 101], FES2004 [108], the most recent version of the Grenoble tide models, HAMTIDE (`http://icdc.zmaw.de/hamtide.html`), developed at Institut für Meereskunde of the Hamburg University, and GOT04, the 2004 version of the Goddard Ocean Tide Model [127].

In all these cases to improve ocean loading predictions, local Mediterranean Sea and Bay of Biscay models are included. Both are characterized by a 1/30 degree resolution grid and include four diurnal (Q_1, O_1, P_1, K_1) and four semidiurnal (N_2, M_2, S_2, K_2) constituents.

Figs. 6.31 and 6.32 show the polygons used to take the local models into account or not. The red points inside the polygons define the grid points at regular intervals on which the Green's function is calculated.

Local models provide more accurate predictions of the tidal components especially near coastal areas, as highlighted by comparing Figs. 6.31 and 6.32 with Fig. 6.33 as regards the amplitude of the K_1 harmonic. For example, the local model of the Mediterranean Sea introduces the Black Sea, which is not included in the global models.

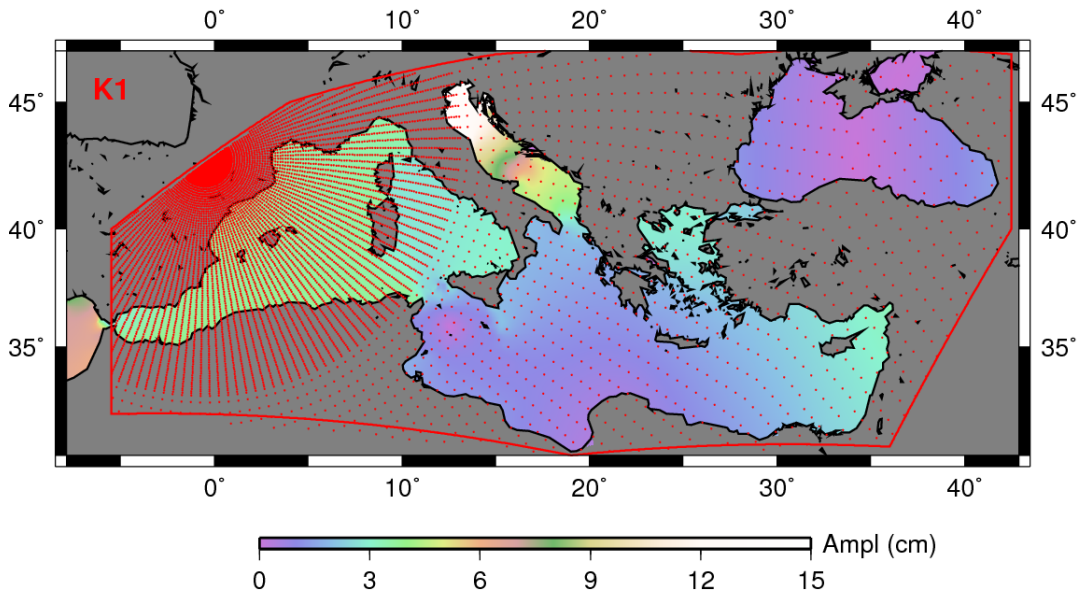

Figure 6.31: Amplitude (cm) of the K_1 tidal component obtained using local Mediterranean Sea model; polygon (red line) and grid points for taking this local model into account or not.

At first, fixing TPXO7-atlas2011 as global ocean model, integrated by the local Mediterranean Sea and Bay of Biscay models, ocean loading tidal strain is estimated using the three gbavap, contap and ocenap Earth models. Fig. 6.34 compares the results (see also Tables 6.1 and 6.2). The discrepancies are much higher for GAL 16 interferometer, up to about 80% in amplitude for the Q_1 tidal component and 310 degrees in phase. By comparing ocean loading tidal strain for LAB 780, the discrepancies are up to about 50% in amplitude and 105 degrees in phase.

In any case, ocean loading tides are much smaller than solid SNRE ones and consequently the expected total tidal strain does not change substantially by more than 4% (21%) in amplitude and 1 (10) degrees in phase for the GAL 16 diurnal (semidiurnal) tidal components and by more than 13% (10%) in amplitude and 2 (12) degrees in phase for the LAB 780 diurnal (semidiurnal) tidal components (see Fig. 6.35 and Tables 6.1 and 6.2) using the three different Earth models.

These results suggest that, even if ocean loading from the three Earth models are very different, its effects on the expected total strain tides are very small and thus predictions are very similar in all cases, especially in the diurnal tidal band.

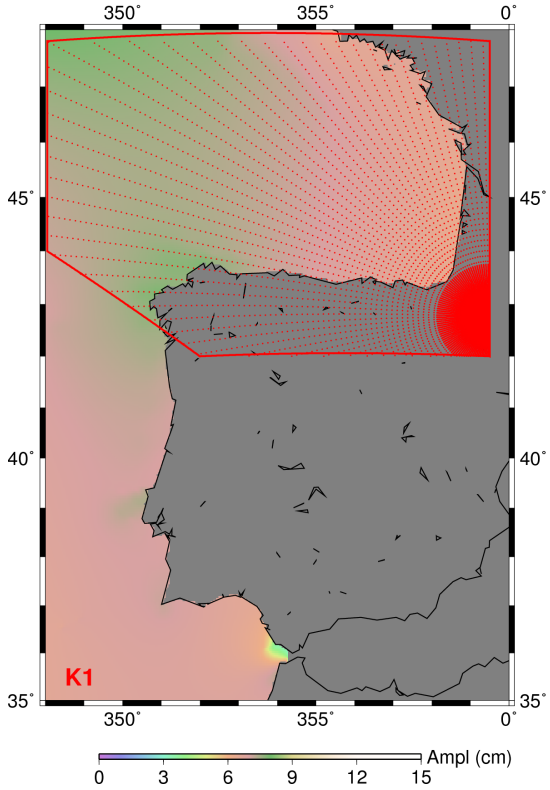

Figure 6.32: Amplitude (cm) of the K_1 tidal component from local Bay of Biscay model; polygon (red line) and grid points for taking this local model into account or not.

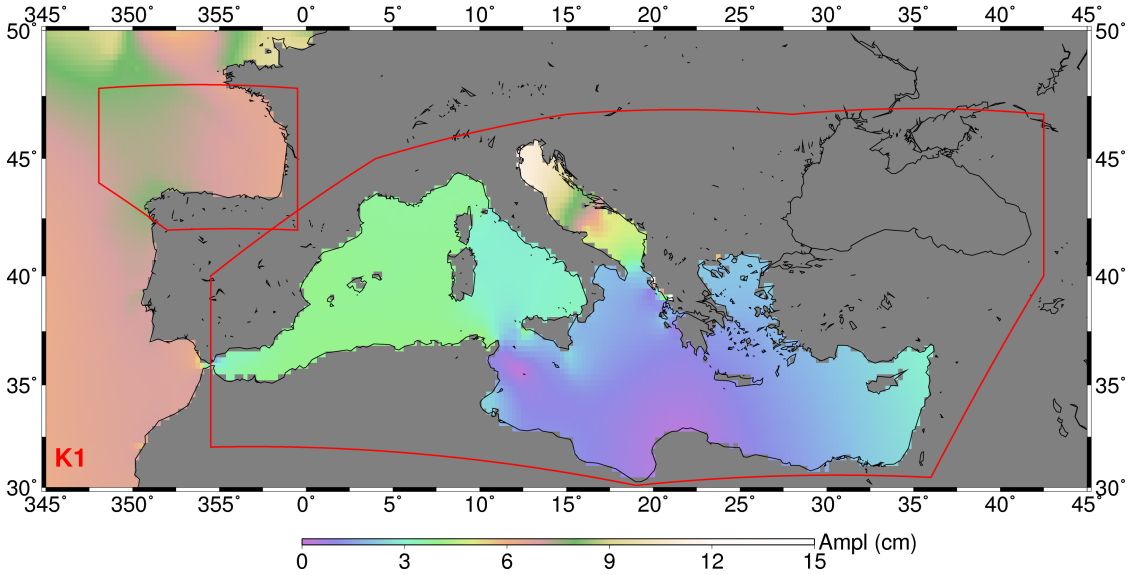

Figure 6.33: Amplitude (cm) of the K_1 tidal component obtained using the TPXO7-atlas2011 global ocean model and polygons (red lines) for taking local Mediterranean Sea and Bay of Biscay models into account or not.

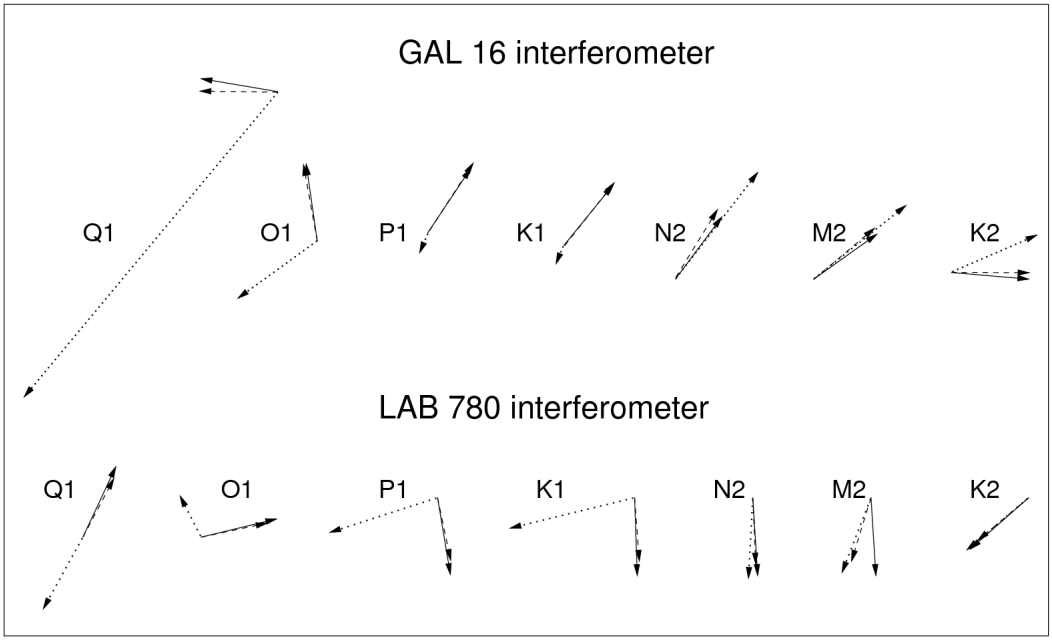

Figure 6.34: Phasor plot of ocean loading tidal strain using gbavap (dotted lines), contap (solid lines), and ocenap (dashed lines) Earth models. Global TPXO7-atlas2011 ocean model, integrated by the local Mediterranean Sea and Bay of Biscay models, IERS 2003 Love numbers. Amplitudes are normalized to the contap amplitudes (see Tables 6.1 and 6.2).

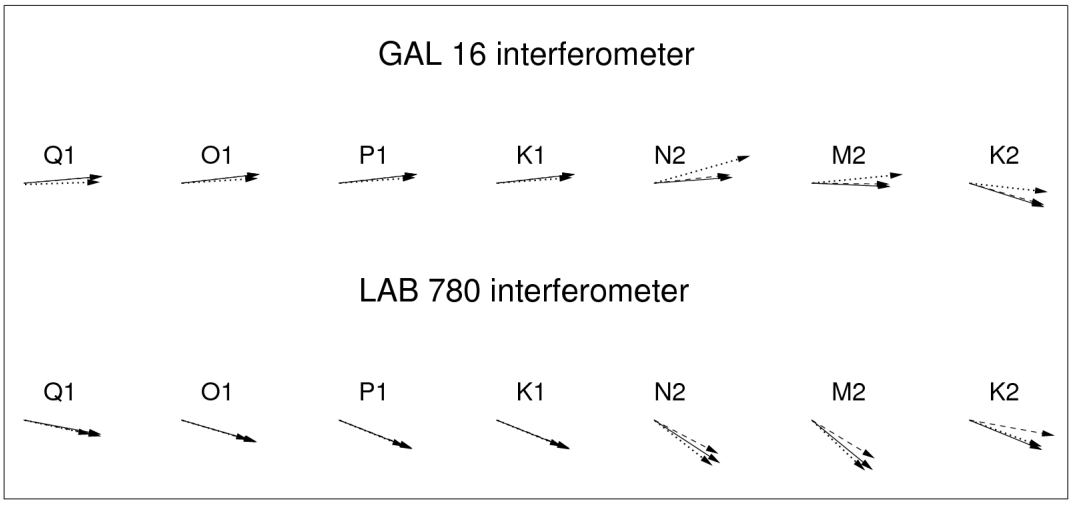

Figure 6.35: Phasor plot of expected total tidal strain using gbavap (dotted lines), contap (solid lines), and ocenap (dashed lines) Earth models. Global TPXO7-atlas2011 ocean model, integrated by the local Mediterranean Sea and Bay of Biscay models, IERS 2003 Love numbers. Amplitudes are normalized to the contap amplitudes (see Tables 6.1 and 6.2).

GAL 16 interferometer

	solid SNRE		ocean loading		expected total	
harmonic	A	ϕ	A	ϕ	A	ϕ
			Gbavap Earth model			
Q_1	1.303	4.768	0.091	-129.819	1.241	1.762
O_1	6.807	4.768	0.260	-144.080	6.586	3.596
P_1	3.168	4.768	0.036	-113.331	3.151	4.194
K_1	9.574	4.768	0.106	-112.144	9.526	4.200
N_2	0.589	-24.000	0.634	52.317	0.962	15.827
M_2	3.075	-24.000	2.777	38.476	5.006	5.467
K_2	0.388	-24.000	0.236	23.352	0.574	-6.413
			Contap Earth model			
Q_1	1.303	4.768	0.018	170.429	1.286	4.969
O_1	6.807	4.768	0.205	98.133	6.798	6.489
P_1	3.168	4.768	0.122	56.303	3.245	6.451
K_1	9.574	4.768	0.391	50.877	9.849	6.406
N_2	0.589	-24.000	0.368	53.232	0.760	4.194
M_2	3.075	-24.000	1.833	35.403	4.307	-2.514
K_2	0.388	-24.000	0.197	-4.888	0.578	-17.581
			Ocenap Earth model			
Q_1	1.303	4.768	0.018	179.217	1.285	4.847
O_1	6.807	4.768	0.204	100.263	6.791	6.478
P_1	3.168	4.768	0.126	57.067	3.246	6.521
K_1	9.574	4.768	0.403	51.727	9.853	6.479
N_2	0.589	-24.000	0.377	58.344	0.740	6.291
M_2	3.075	-24.000	1.873	40.061	4.242	-0.616
K_2	0.388	-24.000	0.197	-0.140	0.573	-16.018

Table 6.1: Amplitudes A ($n\varepsilon$) and phases ϕ (degrees) of solid SNRE, ocean loading and expected total tidal strain for GAL 16 using gbavap, contap and ocenap Earth models, and global TPXO7-atlas2011 integrated by the local Mediterranean Sea and Bay of Biscay models, IERS 2003 Love numbers.

LAB 780 interferometer

	solid SNRE		ocean loading		expected total	
harmonic	A	ϕ	A	ϕ	A	ϕ
			Gbavap Earth model			
Q_1	0.949	-18.655	0.146	119.004	0.847	-12.002
O_1	4.958	-18.655	0.270	117.068	4.768	-16.394
P_1	2.307	-18.655	0.202	-162.131	2.148	-21.859
K_1	6.973	-18.655	0.684	-166.237	6.406	-21.935
N_2	2.057	19.046	2.102	-93.098	2.322	-37.958
M_2	10.742	19.046	10.259	-111.279	8.833	-43.272
K_2	1.354	19.046	0.985	-139.878	0.561	-20.073
			Contap Earth model			
Q_1	0.949	-18.655	0.139	64.895	0.975	-10.520
O_1	4.958	-18.655	0.446	13.528	5.340	-16.107
P_1	2.307	-18.655	0.139	-80.449	2.376	-21.603
K_1	6.973	-18.655	0.417	-88.023	7.130	-21.791
N_2	2.057	19.046	2.025	-86.420	2.472	-33.092
M_2	10.742	19.046	9.928	-106.082	9.552	-39.180
K_2	1.354	19.046	0.998	-138.723	0.573	-22.185
			Ocenap Earth model			
Q_1	0.949	-18.655	0.119	62.102	0.975	-11.766
O_1	4.958	-18.655	0.389	11.942	5.296	-16.515
P_1	2.307	-18.655	0.115	-78.141	2.368	-21.052
K_1	6.973	-18.655	0.341	-85.759	7.112	-21.186
N_2	2.057	19.046	1.731	-87.496	2.280	-27.651
M_2	10.742	19.046	8.516	-107.169	8.935	-31.224
K_2	1.354	19.046	0.862	-139.989	0.630	-10.275

Table 6.2: Amplitudes A ($n\varepsilon$) and phases ϕ (degrees) of solid SNRE, ocean loading and expected total tidal strain for LAB 780 using gbavap, contap and ocenap Earth models, and global TPXO7-atlas2011 integrated by the local Mediterranean Sea and Bay of Biscay models, IERS 2003 Love numbers.

Fig. 6.36 compares ocean loading tidal strain estimated using gbavap as Earth model and four different global ocean models, integrated by the local Mediterranean Sea and Bay of Biscay models (TPXO7-atlas2011, FES2004, HAMTIDE, and GOT04, see upper part in Tables 6.1 and 6.2, and Tables 6.3 and 6.4) at Canfranc station.

Ocean loading differs up to about 50% (4%) in amplitude and 36 (8) degrees in phase for diurnal (semidiurnal) tidal components of GAL 16, and 13% (9%) in amplitude and 11 (5) degrees in phase for diurnal (semidiurnal) tidal components of LAB 780.

Also in this case, since ocean loading tides are much smaller than solid SNRE ones, expected total tidal strain does not change substancially (see Fig. 6.37 and Tables 6.3 and 6.4). The discrepancies are less than 2% in amplitude and 1 degree in phase for both GAL 16 and LAB 780 diurnal tidal components. In the semidiurnal tidal band, the discrepancies are less than 1% in amplitude and 12 degrees for GAL 16, and 2% in amplitude and 3 degrees for LAB 780 interferometer.

Although changing the ocean model, predictions are indistinguishable.

Thus, the ocean loading contribution may differ from case to case even substantially, by using different combinations of ocean and Earth models, but the expected total strain tides (sum of solid spherical non-rotating layered Earth and ocean loading tides) are always very similar to one another.

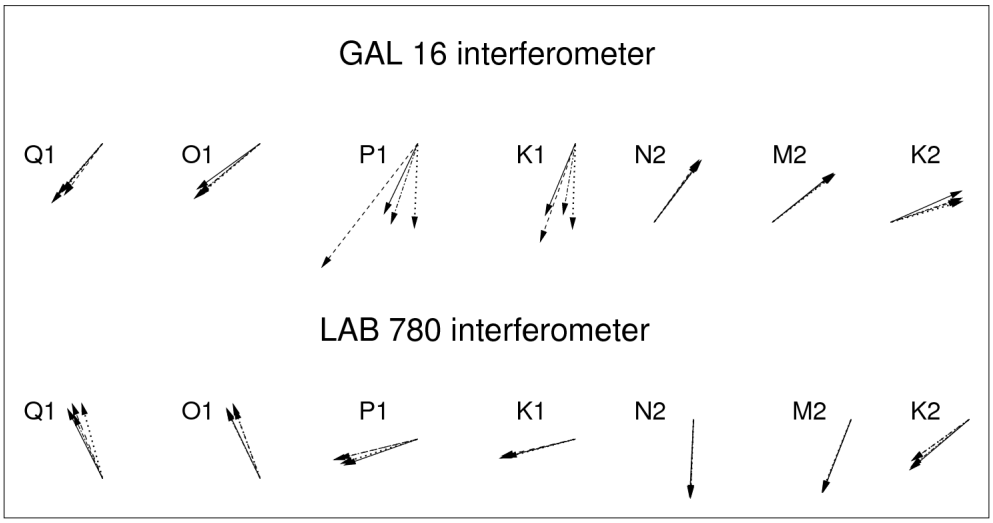

Figure 6.36: Phasor plot of ocean loading tidal strain using gbavap as Earth model and TPXO7-atlas2011 (solid lines), FES2004 (dashed lines), HAMTIDE (dotted lines), and GOT04 (dashed dotted lines) as ocean model, integrated by the local Mediterranean Sea and Bay of Biscay models (see Tables 6.3 and 6.4), IERS 2003 Love numbers. Amplitudes are normalized to the amplitude obtained for TPXO7-atlas2011 (see upper part in Tables 6.1 and 6.2).

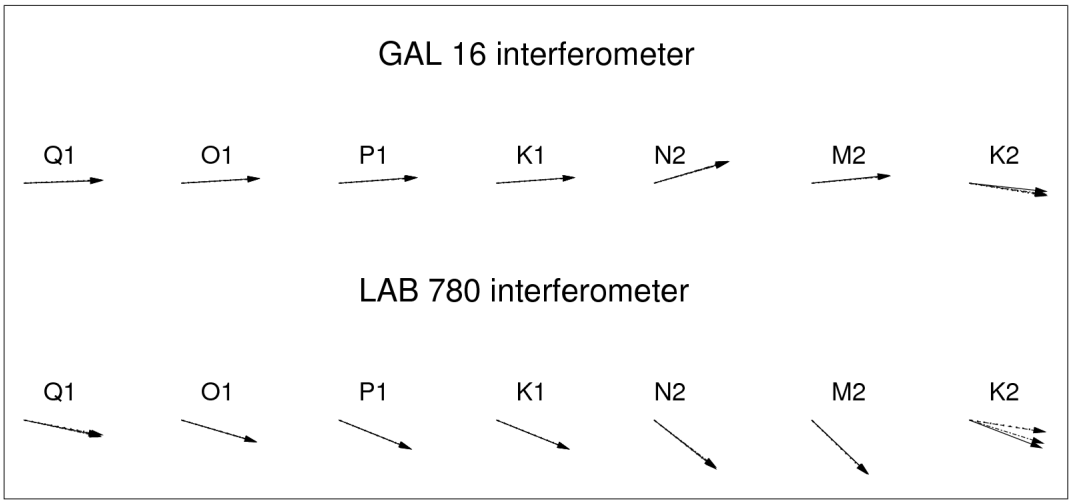

Figure 6.37: Phasor plot of expected total tidal strain using gbavap as Earth model and TPXO7-atlas2011 (solid lines), FES2004 (dashed lines), HAMTIDE (dotted lines), and GOT04 (dash-dotted lines) as ocean model, integrated by the local Mediterranean Sea and Bay of Biscay models (see Tables 6.3 and 6.4), IERS 2003 Love numbers. Amplitudes are normalized to the amplitude obtained for TPXO7-atlas2011 (see upper part in Tables 6.1 and 6.2).

GAL 16 interferometer

	solid SNRE		ocean loading		expected total	
harmonic	A	ϕ	A	ϕ	A	ϕ
FES2004 ocean model						
Q_1	1.303	4.768	0.075	-129.827	1.252	2.311
O_1	6.807	4.768	0.273	-139.526	6.587	3.379
P_1	3.168	4.768	0.038	-92.332	3.163	4.086
K_1	9.574	4.768	0.114	-92.004	9.561	4.090
N_2	0.589	-24.000	0.629	52.918	0.953	15.944
M_2	3.075	-24.000	2.826	37.381	5.076	5.253
K_2	0.388	-24.000	0.231	16.278	0.583	-9.179
HAMTIDE ocean model						
Q_1	1.303	4.768	0.076	-126.608	1.255	2.180
O_1	6.807	4.768	0.290	-140.123	6.572	3.316
P_1	3.168	4.768	0.070	-127.814	3.121	3.826
K_1	9.574	4.768	0.139	-109.644	9.517	4.006
N_2	0.589	-24.000	0.628	54.307	0.944	16.642
M_2	3.075	-24.000	2.790	38.516	5.016	5.572
K_2	0.388	-24.000	0.223	17.924	0.573	-8.947
GOT04 ocean model						
Q_1	1.303	4.768	0.080	-131.407	1.247	2.222
O_1	6.807	4.768	0.269	-140.579	6.587	3.435
P_1	3.168	4.768	0.038	-108.394	3.153	4.129
K_1	9.574	4.768	0.096	-99.695	9.550	4.210
N_2	0.589	-24.000	0.610	53.547	0.935	15.601
M_2	3.075	-24.000	2.781	37.971	5.022	5.257
K_2	0.388	-24.000	0.232	18.800	0.580	-8.215

Table 6.3: Amplitudes A ($n\varepsilon$) and phases ϕ (degrees) of solid SNRE, ocean loading and expected total tidal strain for GAL 16 using contap Earth model and global FES2004, HAMTIDE and GOT04 ocean models, integrated by the local Mediterranean Sea and Bay of Biscay models, IERS 2003 Love numbers.

GAL 16 interferometer

	solid SNRE		ocean loading		expected total	
harmonic	A	ϕ	A	ϕ	A	ϕ
FES2004 ocean model						
Q_1	0.949	-18.655	0.145	105.547	0.876	-10.782
O_1	4.958	-18.655	0.263	110.073	4.797	-16.201
P_1	2.307	-18.655	0.205	-162.350	2.146	-21.891
K_1	6.973	-18.655	0.630	-165.266	6.456	-21.734
N_2	2.057	19.046	2.138	-92.225	2.369	-38.217
M_2	10.742	19.046	10.376	-111.772	8.795	-44.194
K_2	1.354	19.046	0.901	-144.306	0.554	-8.714
HAMTIDE ocean model						
Q_1	0.949	-18.655	0.151	112.168	0.858	-11.019
O_1	4.958	-18.655	0.278	110.045	4.789	-16.056
P_1	2.307	-18.655	0.220	-166.153	2.125	-21.843
K_1	6.973	-18.655	0.659	-166.972	6.421	-21.746
N_2	2.057	19.046	2.124	-92.453	2.354	-38.057
M_2	10.742	19.046	10.312	-111.271	8.854	-43.582
K_2	1.354	19.046	0.907	-144.391	0.550	-8.993
GOT04 ocean model						
Q_1	0.949	-18.655	0.132	114.482	0.864	-12.259
O_1	4.958	-18.655	0.267	116.091	4.774	-16.380
P_1	2.307	-18.655	0.208	-166.270	2.134	-21.652
K_1	6.973	-18.655	0.667	-165.788	6.423	-21.885
N_2	2.057	19.046	2.093	-92.183	2.344	-37.304
M_2	10.742	19.046	10.286	-111.421	8.819	-43.496
K_2	1.354	19.046	0.964	-140.798	0.559	-17.439

Table 6.4: Amplitudes A ($n\varepsilon$) and phases ϕ (degrees) of solid SNRE, ocean loading and expected total tidal strain for LAB 780 using contap Earth model and global FES2004, HAMTIDE and GOT04 ocean models, integrated by the local Mediterranean Sea and Bay of Biscay models, IERS 2003 Love numbers.

After choosing TPXO7-atlas2011 as global ocean model, integrated by the local Mediterranean Sea and Bay of Biscay models, and gbavap as Earth model, predicted and observed tides are compared in both diurnal and semidiurnal tidal bands.

The observations are obtained from the output amplitudes and phases of the VAV03 code (see Appendix A) applied on the pre-whitened strain series (see Table 6.5).

VAV03 results

	GAL 16		LAB 780	
harmonic	A	ϕ	A	ϕ
Q_1	1.452	2.335	0.8734	-15.310
O_1	7.934	7.987	5.168	-20.432
P_1	3.582	8.159	2.252	-33.998
K_1	9.590	11.354	5.667	-35.529
N_2	0.927	5.793	2.775	-40.875
M_2	5.725	12.515	10.025	-51.664
K_2	0.761	10.296	0.375	-57.764

Table 6.5: Amplitudes A ($n\varepsilon$) and phases ϕ (degrees) of observed tidal strain for GAL 16 and LAB 780 interferometers, obtained using VAV03 code and corrected for effects of pre-whitening (see Eq. 4.40).

Figs. 6.38 and 6.39 show diurnal and semidiurnal tidal strain for both GAL 16 and LAB 780 interferometers. In the diurnal tidal band, ocean loading is very small and a good agreement between observed and predicted tides is evident, mainly for GAL 16. This suggests that, if any, local strain distortion effects are small.

Ocean loading is much more consistent in the semidiurnal band; where much larger discrepancies between observed and predicted tides are observable. These discrepancies might be a consequence of inadequate Earth and/or ocean models.

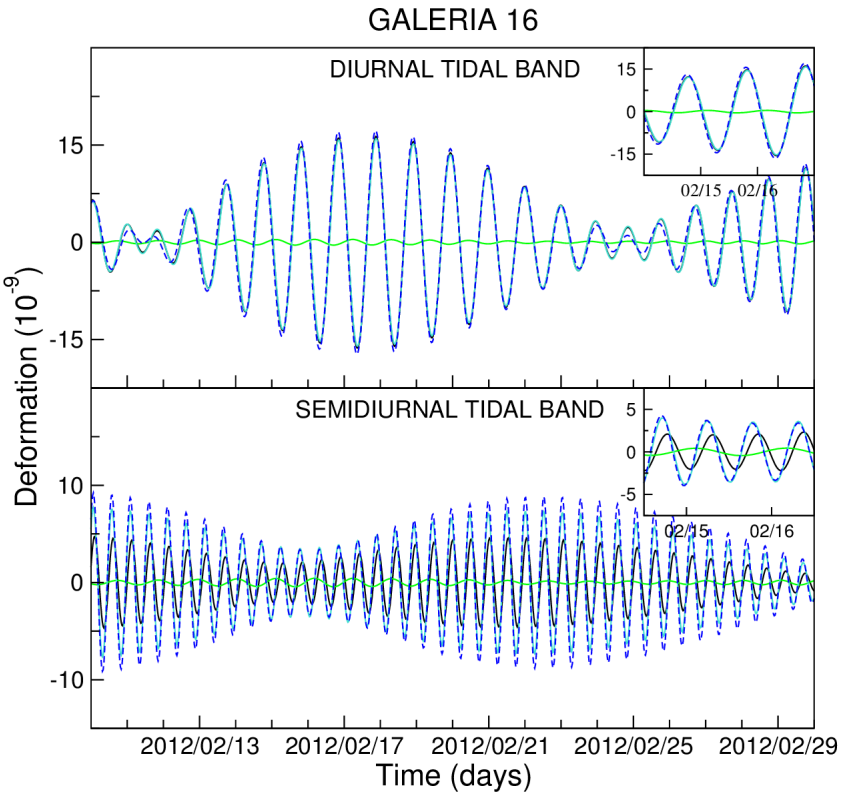

Figure 6.38: Diurnal and semidiurnal tidal strain for GAL 16. Global TPXO7-atlas2011 ocean model, integrated by the local Mediterranean Sea and Bay of Biscay models; Gutenberg-Bullen Earth model; IERS 2003 Love numbers. Solid tides (black lines), ocean loading (green lines), expected total tides (sum of solid tides and ocean loading, turquoise lines) and observed tides (blue dashed lines). Insets represent an enlargement at some days.

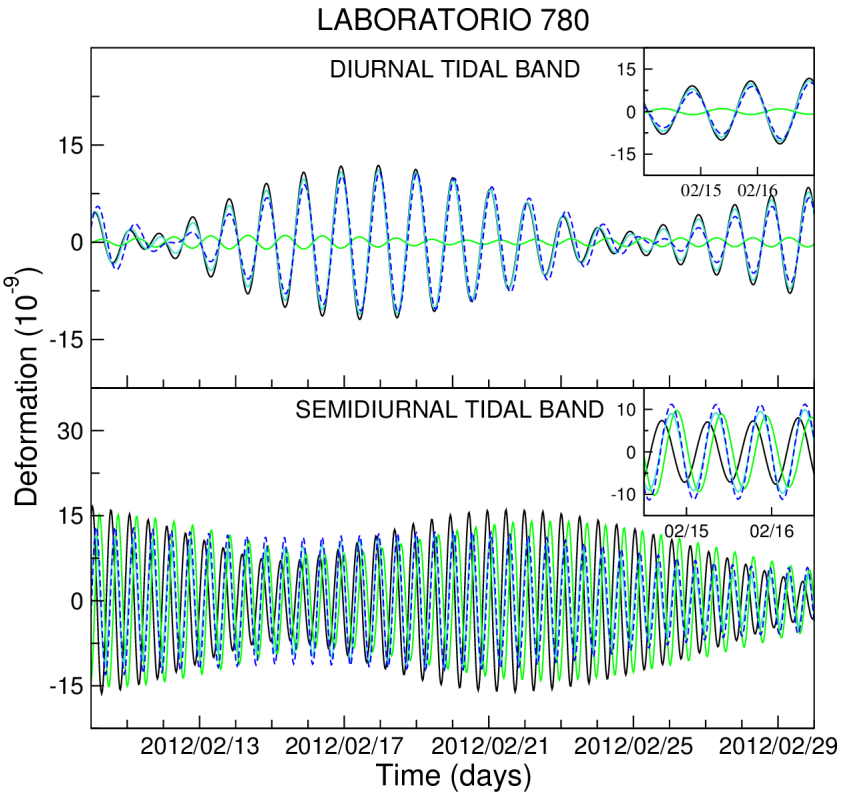

Figure 6.39: Diurnal and semidiurnal tidal strain for LAB 780. Global TPXO7-atlas2011 ocean model, integrated by the local Mediterranean Sea and Bay of Biscay models; Gutenberg-Bullen Earth model; IERS 2003 Love numbers. Solid tides (black lines), ocean loading (green lines), expected total tides (sum of solid tides and ocean loading, turquoise lines) and observed tides (blue dashed lines). Insets represent an enlargement at some days.

6.4 Conclusions

High-sensitivity wide-band strain measurements allow to investigate both local and global geodynamic phenomena in a spectrum ranging from short period seismic waves to tectonic deformation.

Two laser interferometers, called GAL 16 and LAB 780, were installed in the Canfranc (Spain) Underground Laboratory (LSC) at the end of August 2011 and they are working since December 2011. They are part of an advanced integrated geodynamic observatory, called GEODYN, also equipped with one broad-band seismometer, one accelerometer, and two superficial CGPS stations.

The first tests on strain data evidence a low noise level, especially in the frequency band 10^{-4} to 10^{-1} Hz, suggesting the capability of these instruments to produce clear records of low-frequency seismic waves, Earth free oscillations, and possible local aseismic stress release.

The interpretation of strain signals may be complicated by local effects. In the case of large-scale deformations, topography, cavity effects, and heterogeneities make the local field different from the regional one. This is particularly important for global phenomena such as the Earth free oscillations and Earth tides.

Tidal analyses show a good agreement between observed and predicted tides in the diurnal tidal band, mainly for GAL 16. This suggests that, if any, local strain distortion effects are small. Thus the discrepancies in the semidiurnal tidal band might be a consequence of inadequate Earth and/or ocean models.

These results deserve further investigation; in particular it would be interesting to deepen the local distortion effect in the different frequency bands and estimate the ocean loading in more detail, especially in the Bay of Biscay which could be the main source of the discrepancies observed in the semidiurnal tidal band.

Appendix A

Vav03

VAV03 code allows to perform the tidal analysis following the Method of the Least Squares (MLS) [46]. According to this model, each tidal phenomenum can be described through a theoretical tidal signal whose expression $s(t)$ at time t is

$$s(t) = \sum_{\omega=1}^{m} h_\omega \cos(\phi_\omega(t)) = \sum_{\omega=1}^{m} h_\omega \cos(\phi_\omega(0) + \omega t) \tag{A.1}$$

where ω is the frequency (radians per unit of time) of each tidal wave, h_ω and ϕ_ω are the theoretical amplitude and phase of the each tidal component, evaluted at time t and exactly known, and m is the number of total tidal components. Following the development of Tamura of the tide-generating potential [14], $m = 1198$.

The observed tidal signal of a generic sequence can be expressed at time t as

$$S(t) = \sum_{\omega=1}^{m} H_\omega \cos(\Phi_\omega(t)) = \sum_{\omega=1}^{m} H_\omega \cos(\Phi_\omega(0) + \omega t) \tag{A.2}$$

where H_ω and Φ_ω are the observed unknown amplitude and phase, which must to be estimated by the tidal analysis.

These relations can be conveniently re-written by introducing an amplitude factor δ_ω and a phase lag κ_ω, given by

$$\delta_\omega = \frac{H_\omega}{h_\omega} \qquad \kappa_\omega = \Phi_\omega(t) - \phi_\omega(t) \tag{A.3}$$

so that

$$S(t) = \Re\left[\sum_{\omega=1}^{m} x(\omega)\, h_\omega \exp\left(\imath\varphi_\omega(t)\right)\right] \tag{A.4}$$

where

$$x(\omega) = \delta_\omega \exp\left(\imath\kappa_\omega\right) \tag{A.5}$$

In the classical methods of analysis, the tidal parameters were determined directly from measures of H_ω and Φ_ω, but this did not allow the application of MLS since it is impossible taking all the tidal components into account.

Futhermore, often it is impossible to separate tides with frequency very close in the different tidal bands, and considering only a restricted number of harmonics, the equations are not correct, becoming linearly dependent and results are inaccurate.

To overcome this problem, VAV03 applies the method proposed by Venedikov [128, 129] assuming that there is a set of values $x(\omega)$ constant for each tidal group. In this way it is possible to obtain a system of linearly independent equations and estimate δ_ω and κ_ω. At the end, indirectly from these, the amplitudes and phases of observed signals H_ω and Φ_ω are calculated.

VAV03 analyses carefully the data, trying to get better results: data are cleaned from possible anomalies, but by focusing that every anomaly may be a significant geophysical signal.

VAV03 code uses an approximation of the drift by independent polynomials in short time intervals of some hours in length. The polynomial coefficients are treated as unknowns by MLS in the different intervals. This is equivalent to use a filter for each interval, separating the main tidal frequencies, eliminating the drift, and getting at the end a set of filtered numbers. The use of transformed or filtered data allows to obtain frequency dependent residuals and thus frequency dependent estimates of their precision.

In particular VAV03 employs a set of complex filters, amplifying selected basic frequencies corresponding to $\Omega = 1, 2, ..., 6$ cycles per day. The precision is estimated by the residuals of the filtered numbers, getting frequency dependent MSD of unit weight.

It also computes a hypothetical MSD residual under the unrealistic assumption that data are characterized by white noise. Also the Akaike Information Criterion AIC [130] is estimated at every frequency (frequency dependent AIC) and as global value, corresponding to residuals with white noise.

VAV allows to analyse data with gaps, jumps and perturbations of any kind between and within the intervals. To deal the gaps, the observational equations are created only for the existing data, ignoring the missing or perturbed data. This avoids introduction of anomalies and noise trough the interpolations and the reparations of doubtful data. All these features allow to analyse data with an accurate technique, obtaining results quite robust.

Appendix B

Baytap08

Baytap08 code is an improved version of BAYTAP-G program [131, 132], which analyses time series through a Bayesian technique. These series can contain both tidal effects and other kind of signals, including gravity tides, ocean tides, strain and tilt data.

Baytap08 is substantially the same program, modified by Tamura and Agnew, in order to make it easier to use [47].

This program is able to estimate the amplitude and phase of the tidal components, determine the long-period components of data, like trend or drift, and calculate their power spectrum, interpolate missing data and estimate the magnitude of the known offset, search the abnormal data, calculate the Akaike Bayesian Information Criterion (ABIC) to define the goodness of the model fit.

Baytap08 analyses a data series y_i, measured at time $t_i = t_0 + (i-1)\,\Delta$, combination of tidal variations v_i, drift d_i which includes any long-term changes, offsets s_i of unknown amplitude but known times, and auxiliary series x_i.

Tidal variations are expressed as a sum of the different tidal constituents

$$v_i = \sum_{m=1}^{M} \left(A_m C_{mi} + B_m S_{mi}\right) \tag{B.1}$$

where C_{mi} and S_{mi} are the cosine and sine parts of the theoretical tidal components, and A_m and B_m are the tidal constants to be solved for.

There are eight possible arrangements of groups for the tidal analysis, and tidal con-

stants are found for each group.

In principle, if the sum includes all tidal constituents, the inversion for amplitudes and phases would be unstable because of constituents spaced too closely in frequency. For this reason, each C_m and S_m terms are actually the sum of constituents that are grouped together.

The offsets can be expressed as step functions

$$s_i = \sum_{l=1}^{L} h_l H\left(t_i - T_l\right) \tag{B.2}$$

where h_l is the unknown amplitude of the offset evaluted at time T_l and H is the Heaviside step function.

The auxiliary series are other series correlated with the analysed one. It is possible to include three auxiliary series at the same time in the analysis; for each one the model for the correlated part is given by a filter representation

$$c_i = \sum_{k=0}^{K-1} b_k x_{i-k} \tag{B.3}$$

where b_k are the moving average filter weights and are what are solved for.

The model misfit to the data is the residual series r_i

$$r_i = y_i - (v_i + s_i + d_i + c_i) \tag{B.4}$$

Baytap08 solves for all the parameters by minimizing S, which combines the square of the misfit to the model with constraints on the model parameters:

$$\begin{aligned} S &= \sum_{i=1}^{N} \left[y_i - (v_i + s_i + d_i + c_i)\right]^2 + D^2 \sum_{i=1}^{n} \left(d_i - 2d_{i-1} + d_{i-2}\right)^2 \\ &\quad + W^2 \sum_{m=2}^{M} \left(A_m - A_{m-1}\right)^2 + \left(B_m - B_{m-1}\right)^2 \end{aligned} \tag{B.5}$$

where D and W are additional parameters, called hyperparameters, which apply constraints to the model. D is multiplied by the second difference (or optionally third difference) of the drift terms; giving so a smoothness constraint on it. Larger is the value of D, smoother is the series; for D very large, the second difference term would

dominate the sum, and would force d to be a linear drift. It is varied by Baytap08 to find the value that minimizes the ABIC.

The hyperparameter W controls the smoothness of the tidal admittance, in particular how rapidly it can vary with frequency. Usually W is fixed to 1, but sometimes, as when analysing a short data sequence, it is necessary to modify its value for selecting the most suitable model.

Appendix C

LSSA

The Least Squares Spectral Analysis (LSSA) is a technique, based on a least squares fit, for estimating the optimum least-squares spectrum of an unequally or colored time series. This method is similar to Fourier analysis, but suitable for data with non-stationarity constituents, like gaps, datum shifts, linear trend, periodic constituents with known periods, and arbitrary constituents, that may introduce noise and give uncorrected results.

LSSA provides two advantages; first of all systematic noise, including both color and non-stationary signals, can be rigorously represented without producing any shift of the existing spectral peaks, and further time series with unequally spaced data can be analysed.

The vector of data $x(t)$, measured at time t_i, can be represented as a weighted sum of base functions $\phi_i(t)$, so that

$$\underline{x}(t) = \sum_{i=1}^{m} C_i \underline{\phi}_i(t) \tag{C.1}$$

where C_i are unknown weight parameters (components of the covariance matrix). LSSA problem finds the best fitting approximation of the data

$$\underline{\chi} = \sum_{i=1}^{m} C_i' \underline{\phi}_i \tag{C.2}$$

such that the residual vector $\underline{r} = \underline{x} - \underline{\chi}$ is minimized in the least-squares sense. The

estimation of the model parameters can be obtained as

$$\underline{C'} = \left(\underline{\phi}^T \underline{\phi}\right)^{-1} \underline{\phi}^T \underline{x} \tag{C.3}$$

where the matrix $\underline{C'}$ is characterized by a base given by any set of functions that are mutually independent (not necessarily orthogonal) when evaluated at the sample times. At the same time

$$\underline{\chi} = \underline{\phi} \left(\underline{\phi}^T \underline{\phi}\right)^{-1} \underline{\phi}^T \underline{x} \tag{C.4}$$

and the residual vector can be written as

$$\underline{r} = \underline{x} - \underline{\phi} \left(\underline{\phi}^T \underline{\phi}\right)^{-1} \underline{\phi}^T \underline{x} \tag{C.5}$$

In the spectral analysis the base functions used are typically sines and cosines, evenly distributed over the frequency range of interest. Thus

$$\underline{\chi}\left(\omega_j\right) = C'_1 \cos\left(\omega_j t\right) + C'_2 \sin\left(\omega_j t\right) \tag{C.6}$$

If too many frequencies are chosen in a too-narrow frequency range, the functions will not be sufficiently independent, the matrix badly conditioned, and the resulting spectrum will not be meaningful.

The Least Squares Spectrum is defined as the collection of spectral values $s\left(\omega_j\right)$ for all frequencies ω_j for which

$$s\left(\omega_j\right) = \frac{\underline{x}^T \underline{\chi}\left(\omega_j\right)}{\underline{x}^T \underline{x}} \tag{C.7}$$

This means that the LSSA spectrum is described by the percentage variance $s\left(\omega_j\right)$ of the spectral content for a particular cyclic frequency ω_j.

Appendix D

SPOTL

SPOTL is a collection of programs for the computation of loads produced on the solid Earth by ocean tides, combining different tidal and loading models [97]. It also includes programs to convert the loads into harmonic constants for any type of tide (including the ocean tide) and calculate the tide in the time domain from these constants. The package also includes a program for the direct calculation of body tides.

A distinctive feature of this package is the possibility to merge local and global models without difficulty, using polygon files, designed to specify a region or set of regions, which can be included or not for the computational analysis.

In the last version, among these global ocean models NAO99b, GOT04, FES2004, TPXO7.2 and TPXO-atlas2011, CSR4.0, HAMTIDE11A are included.

NAO99b (`http://www.miz.nao.ac.jp/staffs/nao99/index_En.html`) provides major eight constituents (Q_1, O_1, P_1, K_1, N_2, M_2, S_2, K_2) and two long-period constituents (M_f and M_m), by using about 5 years of TOPEX/Poseidon altimeter data into hydrodynamical model. Model region longitude is from 0 to 360 degrees and latitude from -90 to 90 degrees, with a resolution of 0.5 degrees.

GOT04 is the 2004 version of the Goddard Ocean Tide Model [127], that differs from previous version GOT00.2 primarily near the coastlines. It is based on 10 years of Topex/Poseidon altimeter data, plus about 3 years of TOPEX/Poseidon interleaved groundtrack, plus also Earth-observing satellites (ERS-1 and ERS-2) and GEOSAT satellite (GFO) data in shallow and polar seas. It provides eight primary diurnal and semidiurnal tides (Q_1, O_1, P_1, K_1, N_2, M_2, S_2, K_2), on a $1/8^\circ$ resolution full global grid.

FES2004 [108], the most recent version of the Grenoble tide models, is a fully revised version of the global finite-element hydrodynamic tide solutions [109], which uses a refined mesh and assimilates tide gauge and altimetry data from TOPEX/Poseidon and Earth-observing satellites (ERS-2) data. It contains eight primary diurnal and semidiurnal tides (Q_1, O_1, P_1, K_1, N_2, M_2, S_2, K_2), and three long-period constituents (M_4, MS_4, MN_4), on a 1/8° resolution full global grid.

TPXO7-atlas2011 (`http://volkov.oce.orst.edu/tides/`) developed at Oregon State University [101, 99] is an updated version of TPXO7.2; it best-fits, in a least-square sense, the Laplace Tidal Equations and averaged data from TOPEX/Poseidon and Jason, two consecutive satellite missions mapping ocean surface topography (`http://sealevel.jpl.nasa.gov/`). The tides are provided as complex amplitudes of earth-relative sea-surface elevation for eight primary (Q_1, O_1, P_1, K_1, N_2, M_2, S_2, K_2), two long period (M_f, M_m) and three non-linear (M_4, MS_4, MN_4) harmonic constituents, on a 1440×721, 1/4° resolution full global grid. TPXO7-atlas2011 incorporates existing higher resolution local solutions, which are interpolated onto the coarser grid of the global model in coastal areas. It fits coastal tide gauges significantly better than TPXO7.2.

CSR4.0 is an updated version of CSR3.0 [133], computed on the basis of the Orthotide model, developed at Center of Space Research of University of Austin in Texas. It contains about 6.4 years of Topex/Poseidon altimeter data and provides eight primary harmonic constituents (Q_1, O_1, P_1, K_1, N_2, M_2, S_2, K_2) on a 1/4° grid resolution.

HAMTIDE11a solution (`http://icdc.zmaw.de/hamtide.html`), developed at Institut für Meereskunde of the Hamburg University, is obtained by a direct minimization in a least-square sense of cross-calibrated altimeter data from TOPEX/Poseidon, Jason-1, ERS-1, ERS-2, ENVISAT and GFO satellite missions. This model provides Q_1, O_1, P_1, K_1, N_2, M_2, S_2, K_2 and M_4 constituents on a 1/8° resolution full global grid.

SPOTL includes several Green-function's files specified over a given grid of radial distances. The integrated Green's functions are defined as

$$G_i = r_e^2 \int_{\Delta_i}^{\Delta_{i+1}} G(\Delta) \sin \Delta d\Delta \tag{D.1}$$

where Δ is the radial distance from the station and G is the mass-loading Green's function, as defined by Ref. [24]. The radial distance is spaced at equal intervals within four different distance ranges (see Table D.1). Each range, identified by the index j,

range	N_j	δ_j (°)	Δ_L(°)
I	98	0.01	0.025
II	90	0.1	1.05
III	160	0.5	10.25
IV	90	1.0	90.50

Table D.1: Number of intervals N_j, their radial width δ_j and center of first interval Δ_L for the four different distance ranges.

has N_j intervals. The intervals are characterized by their radial width from the station $\delta_j = \Delta_i - \Delta_{i-1}$. Defined $\Delta_L = \Delta_1 + \delta_j/2 = (\Delta_1 + \Delta_2)/2$ and $\Delta_H = \Delta_{N_j+1} - \delta_j/2 = \left(\Delta_{N_j} + \Delta_{N_j+1}\right)/2$ quantities, the total distance coverage is from Δ_1 to Δ_{N_j+1}, with the centers of the intervals running from Δ_L to Δ_H.

Mass-loading Green's functions are computed for the Gutenberg-Bullen Earth model A [24], here referred to as *gbavap*, and two its variants, obtained after replacing top 1000 km by the continental shield crust and mantle structure of Ref. [98] and the oceanic crust and mantle structure of Ref. [98], referred to as *contap* and *ocenap*. Gbavap, contap and ocenap models are representative of an average Earth, a thick continental crust and a thin oceanic crust respectively.

The Green's functions for radial strain ($\varepsilon_{\theta\theta}$) are normalized as

$$G_t(\Delta) = K r_e^2 \Delta^2 G(\Delta) \tag{D.2}$$

where $K = 10^{12}$. The tabulated Green's functions are again re-normalized as

$$G'_t(\Delta) = \frac{r_e^2 G_t(\Delta)}{K r_e^2} \left[\frac{2\sin(\Delta/2)}{\Delta}\right]^2 \tag{D.3}$$

retaining the feature of removing the singularities in G for small Δ. So the Green's function are expressed through the integral

$$\begin{aligned}\int_{\Delta_c-\delta/2}^{\Delta_c+\delta/2} G'_t(x)\frac{\sin(x)}{4\sin^2(x/2)}dx &= \frac{1}{2}G'_t(\Delta_c)\int_{\Delta_c-\delta/2}^{\Delta_c+\delta/2}\cot(x/2)\,dx \\ &= G'_t(\Delta_c)\ln\left[\frac{\sin(\Delta_c/2)\cos(\delta/4)+\cos(\Delta_c/2)\sin(\delta/4)}{\sin(\Delta_c/2)\cos(\delta/4)-\cos(\Delta_c/2)\sin(\delta/4)}\right]\end{aligned}$$

The normalization is done directly in the computations. The Green's functions, defined

in the files used by SPOTL, are unnormalized, as done by Ref. [24], and thus singular at two successive range. For removing these singularities, it is necessary to normalize the values of Green functions for the spherical surface element A at which they are calculated, considering that

$$A = \int_{\Delta-\delta/2}^{\Delta+\delta/2} r_e^2 \sin\theta d\theta \int_0^{2\pi} d\phi = 4\pi r_e^2 \sin\Delta \sin(\delta/2) \tag{D.4}$$

obtaining in this way the form introduced in Eq. D.2.

Figs. D.1 and D.2 show the integrated Green's functions for strain components $\varepsilon_{\theta\theta}$ and $\varepsilon_{\lambda\lambda}$, using the Gutenberg-Bullen average Earth model and its two variants within four different distance ranges. In both cases, the major relative discrepancies between the models are observed for large radial distances.

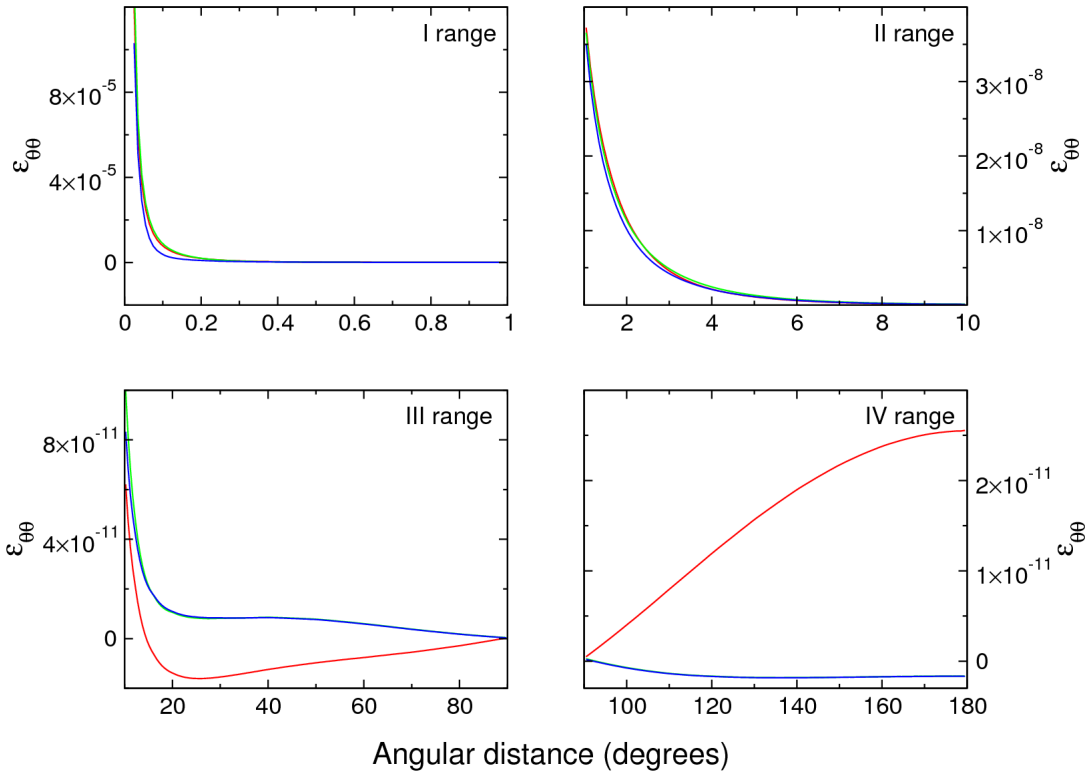

Figure D.1: Integrated Green's functions for $\varepsilon_{\theta\theta}$ using the three different Earth models, within the four different distance ranges, as defined in Table D.1. Red line: gbavap; green line: contap; blue line: ocenap.

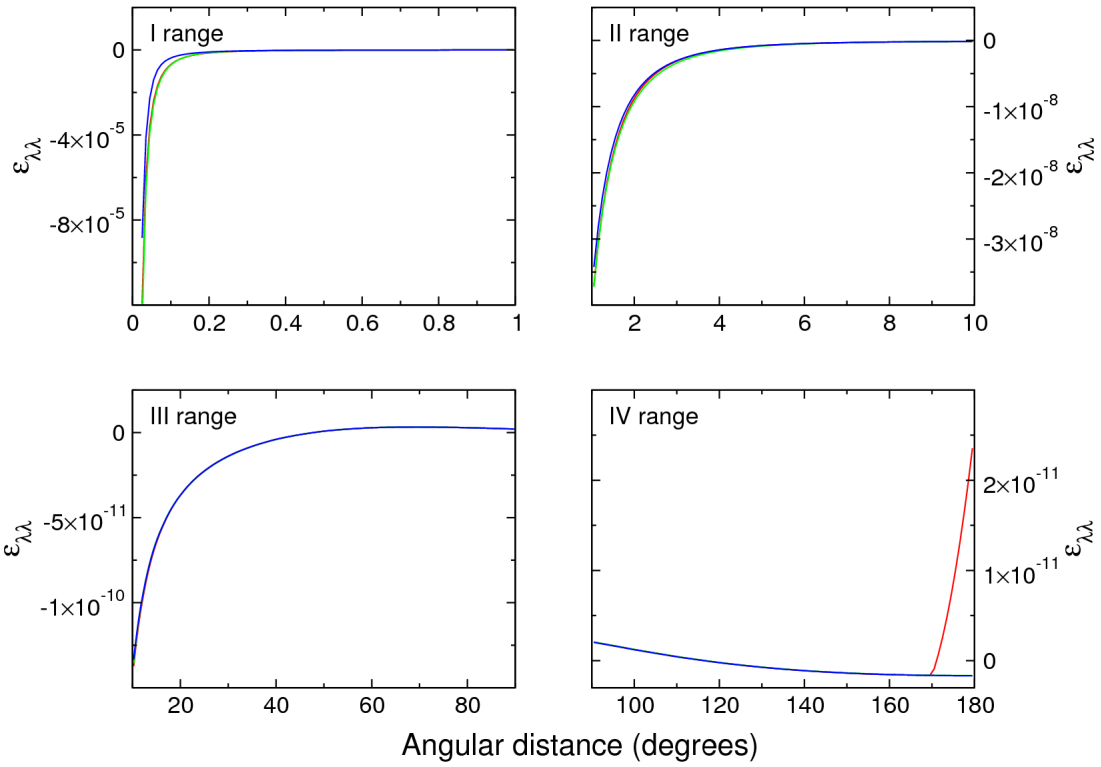

Figure D.2: Integrated Green's functions for $\varepsilon_{\lambda\lambda}$ using three different Earth models, within the four different distance ranges, as defined in Table D.1. Red line: gbavap; green line: contap; blue line: ocenap.

Bibliography

[1] Anderson, E.M., 1905. Dynamics of faulting. *Trans. Edinburgh Geol. Soc.* **8**, 378-402.

[2] Agnew, D.C., 1986. Strainmeters and Tiltmeters. *Reviews of Geophysics* **24(3)**, 579-624.

[3] Benioff, H., 1935. A linear strain seismograph. *Bull. Seism. Soc. Am.* **25**, 283-309.

[4] Benioff, H., 1958. Long waves observed in the Kamchatka earthquake of Nov. 4, 1952. *J. Geophys. Res.* **63**, 589-593.

[5] Benioff, H., 1959. Fused-quartz extensometer for secular, tidal, and seismic strains. *Geol. Soc. Am. Bull.* **70**, 1019-1032.

[6] Sacks, I.S., Suyehiro, S., Evertson, D.W. and Yamagishi, Y., 1971. Sacks-Evertson strainmeter, its installation in Japan and some preliminary results concerning strain steps. *Pap. Meteor. Geophys.* **22**, 195-207.

[7] Gladwin, M.T., 1984. High precision multi-component borehole deformation monitoring. *Rev. Sci. Instrum.* **55**, 2011-2016.

[8] Melchior, P.J., 1983. *The Tides of the Planet Earth, 2nd ed.* Pergamon Press, Oxford.

[9] Agnew, D.C., 2007. Earth Tides, in *Treatise on Geophysics: Geodesy.* Elsevier, New York.

[10] Cartwright, D.E. and Tayler, R.J., 1971. New computations of the tide-generating potential. *Geophys. J. Roy. Astron. Soc.* **23**, 45-74.

[11] Thomson, W., 1881. The tide gauge, tidal harmonic analyser, and tide predicter. *Proceedings of the Institution of Civil Engineers* **65**, 3-24.

[12] Doodson, A.T., 1921. The harmonic development of the tide generating potential. P*roc. Roy. Soc. Series A - Containing Papers of a Mathematical and Physical Character* **100**, 305-329.

[13] Cartwright, D.E. and Edden, A.C., 1973. Corrected tables of tidal harmonics. *Geophys. J. Roy. Astron. Soc.* **33**, 253-264.

[14] Tamura, Y., 1987. A harmonic development of the tide-generating potential. *Bull. Inf. Mareés Terrestres* **99**, 6813-6855.

[15] Xi, Q., 1989. A new complete development the tide-generating potential for the epoch J2000.0. *Bull. Inf. Mareés Terrestres* **99**, 6766-6812.

[16] Roosbeek, F., 1996. RATGP95: An harmonic development of the tide generating potential. *Geophys. J. Int.* **126**, 197-204.

[17] Jeffreys, H., 1976. *The Earth: Its Origin, History and Physical Constitution.* Cambridge University Press, Cambridge.

[18] Love, A., 1911. *Some problems of geodynamics.* Dover Publications, New York.

[19] Love, A., 1944. *The Mathematical Theory of Elasticity*, 4th ed. Dover Publications, New York.

[20] Wahr, J.M., 1981. Body tides on an rotating, elliptical, elastic and oceanless Earth. *Geophys. J. Roy. Astron. Soc.* **64**, 677-703.

[21] Wang, R., 1994. Effect of rotation and ellipticity on Earth tides. *Geophys. J. Int.* **117**, 562-565.

[22] Mathews, P.M., Herring, T.A. and Buffett, B.A., 2002. Modeling of nutation-precession: New nutation series for nonrigid Earth, and insights into the Earth's interior. *Geophys. Res. Lett.* **107(B4)**, 2068.

[23] Mathews, P.M., Buffett, B.A. and Shapiro, I.I., 1995. Love numbers for a rotating spheroidal Earth: New definitions and numerical values. *Geophys. Res. Lett.* **22**, 579-582.

[24] Farrell, W.E., 1972. Deformation of the Earth by Surface Loads. *Rev. Geophys. Space Phys.* **10**, 761-797.

[25] Munk, W.H. and MacDonald, G.J.F., 1960. *The Rotation of the Earth.* Cambridge University Press, Cambridge.

[26] Longman, I.M., 1962. A Green's function for determining the deformation of the Earth under surface mass loads: 1. Theory. *J. Geophys. Res.* **67**, 845-850.

[27] Longman, I.M., 1963. A Green's function for determining the deformation of the Earth under surface mass loads: 2. Computation and numerical results. *J. Geophys. Res.* **68**, 485-496.

[28] Pagiatakis, S.D., 1990. The response of a realistic Earth to ocean tide loading. *Geophys. J. Int.* **103**, 541-560.

[29] Levine, J. and Hall, J.L., 1972. Design and operation of a methane absorption stabilized laser strainmeter. *J. Geophys. Res.* **77**, 2595-2609.

[30] Goulty, N.R., King, G.C.P. and Wallard, A.J., 1974. Iodine stabilized laser strainmeter. *Geophys. J. R. Astron. Soc.* **39**, 269-282.

[31] Buklerskii, A.V., Kart, A.M., Klyachko, B.S., Kravchuk, V.K., Milyukov, V.K., Melezhnikov, I.V., Myasnikov, A.V., Nesterov, V.V. and Rudenko, V.N., 1995. Baksan laser interferometer. *Meas. Tech.* **38**, 1073-1081.

[32] Takemoto, S., Araya, A., Akamatsu, J., Morii, W., Momose, H., Ohashi, M., Higashi, T., Fukuda, Y., Miyoki, S., Uchiyama, T., Tatsumi, D., Hanada, H., Naito, I., Telada, S., Ichikawa, N., Onoue, K. and Wada, Y., 2004. A 100 m laser strainmeter system installed in a 1 km deep tunnel at Kamioka, Gifu, Japan. *J. Geodyn.* **38**, 477-488.

[33] Javan, A., Bennet Jr., W.R. and Herriot, D.R., 1961. Population inversion and continuous optical maser oscillation in a gas discharge containing a helium neon mixture. *Phys. Rev. Lett.* **6**, 106-110.

[34] Park, J., Amoruso, A., Crescentini, L. and Boschi, E., 2008. Long-period toroidal earth free oscillations from the great Sumatra-Andaman earthquake observed by paired laser extensometers in Gran Sasso, Italy. *Geophys. J. Int.* **173**, 887-905.

[35] Crescentini, L., Amoruso, A. and Scarpa, R., 1999. Constraints on slow earthquake dynamics from a Swarm in Central Italy. *Science* **286**, 2132-2134.

[36] Amoruso, A. and Crescentini, L., 2009. The geodetic laser interferometers at Gran Sasso, Italy: recent modifications and correction for local effects. *J. Geodyn.* **48**, 120-125.

[37] Amoruso, A. and Crescentini, L., 2009. Slow diffusive fault slip propagation following the 6 April 2009 L'Aquila earthquake: Italy. *Geophys. Res. Lett.* **36**, L24306.

[38] Crescentini, L. and Renzella, G., 1991. A wide band high-sensitivity laser strainmeter. *Rev. Sci. Instrum.* **62**, 1206-1209.

[39] Crescentini, L., Amoruso, A., Fiocco, G. and Visconti, G., 1997. Installation of a high-sensitivity laser strainmeter in a tunnel in central Italy. *Rev. Sci. Instrum.* **68**, 3206-3210.

[40] Berger, J. and Levine, J., 1974. The spectrum of Earth strain from 10^{-8} to 10^{2} Hz. *J. Geophys. Res.* **79**, 1210-1214.

[41] Beavan, R.J. and Goulty, N.R., 1977. Earth-strain observations made with the Cambridge laser strainmeter. *Geophys. J. Int.* **48**, 293-305.

[42] Harrison, J.C., 1976. Cavity and topographic effects in tilt and strain measurements. *J. Geophys. Res.* **81**, 319-328.

[43] Hart, R.H.G., Gladwin, M.T., Gwyther, R.L., Agnew, D.C. and Wyatt, F.K., 1996. Tidal calibration of borehole strainmeters: removing the effects of small-scale inhomogeneity, *J. Geophys. Res.* **101**, 25553-25571.

[44] Amoruso, A., Crescentini, L. and Scarpa, R., 2000. Removing tidal and atmospheric effects from Earth deformation measurements. *Geophys. J. Int.* **140**, 493-499.

[45] Amoruso, A., Botta, V. and Crescentini, L., 2012. Free Core Resonance parameters from strain data: sensitivity analysis and results from the Gran Sasso (Italy) extensometers. *Geophys. J. Int.* **189**, 923-936.

[46] Venedikov, A.P., Arnoso, J. and Vieira, R., 2003. VAV: a program for tidal data processing. *Computers and Geosciences* **29**, 487-502.

[47] Tamura, Y. and Agnew, D.C., 2008. *Baytap08 Users Manual*. SIO Technical Report, Scripps Institution of Oceanography. Available at: `:http://repositories.cdlib.org/sio/techreport/82/`.

[48] Vanicek, P., 1971. Further development and properties of the spectral analysis by least-squares. *Astrophys. Space Sci.* **12**, 10-33.

[49] Amoruso, A. and Crescentini, L., 2008. Free Core Resonance parameters from strain data: results from the Gran Sasso (Italy) extensometers. *Earth Tide Symposium 2008 "New Challenges in Earth's Dynamics"*. Jena, September 1-5, 2008.

[50] Amoruso, A., Botta, V., Crescentini, L., Milyukov, V.K. and Myasnikov, A.V. - manuscript in preparation

[51] Wilhelm, H., Zürn, W. and Wenzel, H.G., 1997. *Tidal Phenomena*. Springer Verlag, Berlin.

[52] Sasao, T., Okubo, S. and Saito, M., 1980. A simple theory on the dynamical effects of a stratified fluid core upon nutational motion of the Earth, in *Nutation and the Earth's Rotation*. Proc. IAU Symp., **78**, 165–183, eds. Fedrov, E.P., Smith, M.L., Bender, P.L., Kluwer, Dordrecht.

[53] Buffett, B., Mathews, P.M., Herring, T.A. and Shapiro, I.I., 1991. Forced nutations of the Earth: influence of inner core dynamics: 4. Elastic deformation. *J. Geophys. Res.*, **96(B5)**, 8258-8274.

[54] Hinderer, J., Boy, J.P., Gegout, P., Defraigne, P., Roosbeek, F. and Dehant, V ., 2000. Are the free core nutation parameters variable in time? *Phys. Earth planet. Inter.* **117**, 37-49.

[55] Toomre, A., 1974. On the nearly diurnal wobble of the Earth. *Geophys. J. Roy. Astron. Soc.* **38**, 335-348.

[56] Zürn, W., 1997. The Nearly-Diurnal Free Wobble-Resonance, in *Tidal Phenomena*. Springer Verlag, Berlin.

[57] Lambeck, K., 1980. *The Earth's Variable Rotation: Geophysical Causes and Consequences*. Cambridge University Press, Cambridge.

[58] Hinderer, J., Legros, H. and Amalvict M., 1982. A search for Chandler and nearly diurnal free wobbles using Liouville equations. *Geophys. J. Roy. Astron. Soc.* **71**, 303-332.

[59] Rochester, M.G. and Smylie, D.E., 1974. On changes in the trace of the Earth's inertia tensor. *J. Geophys. Res.* **79**, 4948.

[60] Lambeck, K. 1988. *Geophysical Geodesy: The Slow Deformations of the Earth.* Oxford Science Publications, Oxford.

[61] Hough, S.S., 1895. The oscillations of a rotating ellipsoidal shell containing fluid. *Phil. Trans. R. Soc. London* **186**, 469-506.

[62] Jeffreys, H. and Vicente, R.O., 1957. The theory of nutation and the variation of latitude. *Mon. Not. R. Astron. Soc.* **117**, 142-161.

[63] Wu, X. and Wahr, J.M., 1997. Effects of non-hydrostatic core-mantle boundary topography and core dynamics on Earth rotation *Geophys. J. Int.* **128**, 18-42.

[64] Wahr, J.M. and Sasao, T., 1981. A diurnal resonance in the ocean tide and in the Earth's load response due to the resonant free 'core nutation'. *Geophys. J. Roy. Astr. Soc.* **64**, 747-765.

[65] Dehant V., 1987. Tidal parameters for an inelastic Earth. *Phys. Earth Planet Int.* **49**, 97-116.

[66] Dehant, V., Defraigne, P. and Wahr, J.M., 1999. Tides for a convective Earth. *J. Geophys. Res.* **104**, 1035-1058.

[67] Mathews P.M., 2001. Love numbers and gravimetric factor for diurnal tides. *J. Geod. Soc. Japan* **47**, 231-236.

[68] Sasao, T., and Wahr, J.M., 1981. An excitation mechanism for the free core nutation. *Geophys. J. Roy. Astr. Soc.* **64**, 729-746.

[69] Dehant, V., and Defraigne, P., 1997. New transfer functions for nutations of a non-rigid Earth. *J. Geophys. Res.* **102**, 659-688.

[70] Schastok, J., 1997. A new nutation series for a more realistic model Earth. *Geophys. J. Int.* **130**, 137-150.

[71] Cummins, P. and Wahr, J., 1993. A study of the Earth's core nutation using gravity data. *J. Geophys. Res.* **98**, 2091-2104.

[72] Defraigne, P., Dehant, V. and Hinderer, J., 1994. Stacking gravity tide measurements and nutation observations in order to determine the complex eigenfrequency of the nearly diurnal free wobble. *J. Geophys. Res.* **99(B5)**, 9203-9213.

[73] Polzer, G., 1997. Analysis of earth tide observations for the determination of core resonance parameters. *PhD thesis*, Karlsruhe University, Karlsruhe.

[74] Ducarme, B., Sun, H.P. and Xu, J.Q., 2007. Determination of the free core nutation period from tidal gravity observations of the GGP superconducting gravimeter network. *J. Geod.* **81**, 179-187.

[75] Ducarme, B., Rosat, S., Vandercoilden, L., Xu, J.Q. and Sun, H.P., 2009. European tidal gravity observations: comparison with Earth Tides models and estimation of the Free Core Nutation (FCN) parameters, in *Observing Our Changing Earth*, International Association of Geodesy Symposia, Vol. 133, pp. 523-532, ed. Sideris, M.G., Springer Verlag, Berlin.

[76] Neuberg, J., Hinderer, J. and Zürn, W., 1987. Stacking gravity tide observations in Central Europe for the retrieval of the complex eigenfrequency of the nearly diurnal free wobble. *Geophys. J. Roy. Astron. Soc.* **91**, 853-868.

[77] Sato, T., Tamura, Y., Higashi, T., Takemoto, I., Nakagawa, I., Morimoto, N., Fukuda, Y., Segawa, J. and Seama, N., 1994. Resonance parameters of nearly diurnal free core nutation measured with three superconducting gravimeters in Japan. *J. Geomagn. Geoelectr.* **46**, 571-586.

[78] Florsch, N., Chambat, F., Hinderer, J. and Legros, H., 1994. A simple method to retrieve the complex eigenfrequency of the Earth's nearly diurnal free wobble: application to the Strasbourg superconducting gravimeter data. *Geophys. J. Int.* **116**, 53-63.

[79] Merriam, J.B., 1994. The nearly diurnal free wobble resonance in gravity measured at Cantley, Quebec. *Geophys. J. Int.* **119**, 369-380.

[80] Hinderer, J., Crossley, D. and Xu, H., 1995. The accuracy of tidal gravimetric factors and nearly diurnal free wobble resonance parameters in superconducting gravimetry. *Proceedings of the 12th International Symposium Earth Tides, Beijing, China,* 289-295.

[81] Florsch, N. and Hinderer, J., 2000. Bayesian estimation of the free core nutation parameters from the analysis of precise tidal gravity data. *Phys. Earth Planet Int.* **117**, 21-35.

[82] Sato, T., Tamura, Y., Matsumoto, K., Imanishi, Y. and McQueen, H., 2004. Parameters of the fluid core resonance inferred from superconducting gravimeter data. *J. Geodyn.* **38**, 375-389.

[83] Rosat, S. and Lambert, S.B., 2009. Free core nutation resonance parameters from VLBI and superconducting gravimeter data. *Astron. Astrophys.* **503**, 287-291.

[84] Rosat, S., Florsch, N., Hinderer, J. and Llubes, M., 2009. Estimation of the free core nutation parameters from SG data: sensitivity study and comparative analysis using linearized least-squares and Bayesian methods, *J. Geodyn.* **48**, 331-339.

[85] Herring, T., Gwinn, C. and Shapiro, I., 1986. Geodesy by radiointerferometry: studies of the forced nutations of the Earth. 1. Data analysis. *J. Geophys. Res.* **91**, 4745-4755.

[86] Roosbeek, F., Defraigne, P., Feissel, M. and Dehant, V., 1999. The free core nutation period stays between 431 and 434 sidereal days. *Geophys. Res. Lett.* **26(1)**, 131-134.

[87] Vondràk, J. and Ron, C., 2006. Resonant period of free core nutation - its observed changes and excitations. *Acta Geodyn. Geomater.* **3(143)**, 53-60.

[88] Lambert, S.B. and Dehant, V., 2007. The Earth's core parameters as seen by the VLBI. *Astron. Astrophys.* **469**, 777-781.

[89] Koot, L., Rivoldini, A., de Viron, O. and Dehant, V., 2008. Estimation of Earth interior parameters from a Bayesian inversion of very long baseline interferometry nutation time series. *J. Geophys. Res.* **113**, B08414.

[90] Sato, T., 1989. Fluid core resonance measured by quartz tube extensometers at Esashi Earth tides station. *Proceedings of the 11th International Symposium Earth Tides, Helsinki*, Schweitzerbart, Stuttgart, 573-582.

[91] Li, H., Takemoto, S., Yamamoto, T. and Otsuka, S., 1995. The fluid-core dynamic effect observed with a laser strainmeter. *J. Geod. Soc. Japan*, **41**, 99-109.

[92] Mukai, A., Takemoto, S. and Yamamoto, T., 2004. Fluid core resonance revealed from a laser extensometer at the Rokko-Takao station, Kobe, Japan. *Geophys. J. Int.* **156**, 22-28.

[93] Ping, J., Tsubokawa, T., Tamura, Y., Heki, K., Matsumoto, K. and Sato, T., 2006. Observing long-term FCR variation using Esashi extensometers. *J. Geodyn.* **41**, 155-163.

[94] McCarthy, D.D. and Petit, G., 2004. IERS Conventions (2003), IERS Technical Note 32, Verlag des Bundesamts für Kartographie und Geodäsie, Frankfurt am Main, 127 pp.

[95] Press, W.H., Teukolsky, S.A., Vetterling, W.T. and Flannery, B.P., 1992. *Numerical Recipes in C: The Art of Scientific Computing*. Cambridge University Press, Cambridge.

[96] Goulty, N.R., 1976. Strainmeters and tiltmeters in Geophysics. *Tectonophysics* **34**, 245-256.

[97] Agnew, D.C., 1996. SPOTL: Some Programs for Ocean-Tide Loading. *SIO Ref. Ser. 96-8*, p. 34. Scripps Institution of Oceanography, La Jolla, CA.

[98] Harkrider, D., 1970. Surface waves in multilayered elastic media (2): higher mode spectra and spectral ratios from point sources in plane-layered earth models. *Bull. Seismo. Soc. Amer.* **60**, 1937-1987.

[99] Egbert, G.D. and Erofeeva, S.Y., 2002. Efficient inverse modeling of barotropic ocean tides. *J. Atmos. Oceanic Technol.* **19**, 183-204.

[100] Ray, R.D., 1999. A global ocean tide model from TOPEX/POSEIDON altimetry: GOT99. 2. NASA Technical Memorandum 209478.

[101] Eanes, R.J., 1994. Diurnal and semidiurnal tides from TOPEX/POSEIDON altimetry, EOS. *Trans. Am. Geophys. Un.* **75**, 108.

[102] Matsumoto, K., Takanezawa, T. and Ooe, M., 2000. Ocean tide models developed by assimilating TOPEX/POSEIDON altimeter data into hydro-dynamic model, a global model and regional model around Japan. *J. Oceanogr.* **56**, 567-581.

[103] Ingber, L., 1993. Simulated Annealing: Practice Versus Theory. *J. of Mathematical and Computer Modeling* **18**, 29-57.

[104] Sambridge, M., 1999a. Geophysical inversion with a neighbourhood algorithm: I. Searching a parameter space. *Geophys. J. Int.* **138**, 479-494.

[105] Sambridge, M., 1999b. Geophysical inversion with a neighbourhood algorithm II. Appraising the ensemble. *Geophys. J. Int.* **138**, 727-746.

[106] Milyukov, V.K. and Myasnikov, A.V., 2005. Metrological characteristics of the Baksan laser interferometer. *Izmerit. Tekhnika* **12**, 26-30.

[107] Milyukov, V.K., Klyachko, B.S., Myasnikov, A.V., Striganov, P.S. and Yanin, A.F., 2005. A laser interferometer-deformograph for monitoring the crust movement. *Instruments and Experimental Techniques* **48**, 780-795.

[108] Lyard, F., Lefevre, F., Letellier, T. and Francis, O., 2006. Modelling the global ocean tides: modern insights from FES2004. *Ocean Dynam.* **56**, 394-415.

[109] Le Provost, C., Genco, M.L., Lyard, F., Vincent, P. and Canceil, P., 1994. Spectroscopy of the world ocean tides from a finite element hydrodynamic model. *J. Geophys. Res.* **99**, 777-797.

[110] Milyukov, V.K., Kopaev, A.V., Lagutkina, A.V., Mironov, A.P. and Myasnikov, A.V., 2007. Observations of crustal tide strains in the Elbrus area. I*zvestiya, Physics of the Solid Earth* **43**, 922-930.

[111] Molodensky, S.M., 1983. Determination of Tidal Strain Perturbations for a Plain Topography. *Izv. AN SSSR, Ser. Fiz. Zemli* **7**, 80-96.

[112] Kanamori, H., 1977. Seismic and aseismic slip along subduction zones and their tectonic implications, in *Island Arcs, Deep Sea Trenches and Back-Arc Basins,*

Maurice Ewing Ser. **3**, 163-174, eds Talwani, M. and Pitman, W., III AGU, Washington, D.C.

[113] Sacks, I.S., Suyehiro, S., Linde, A.T. and Snoke, J.A., 1978. Slow earthquakes and stress redistribution. *Nature* **275**, 599-602.

[114] Linde, A.T., Suyehiro, K., Miura, S., Sacks, I.S. and Takagi, A., 1988. Episodic aseismic earthquake precursors. *Nature* **334**, 513-515.

[115] Linde, A.T., Gladwin, M.T., Johnston, M.J.S., Gwyther, R.L. and Bilham, R.G., 1996. A slow earthquake sequence on the San Andreas Fault. *Nature* **383**, 65-68.

[116] Kawasaki, I., Asai, Y., Tamura, Y., Sagiya, Y., Mikami, N., Okada, Y., Sakata, M. and Kasahara, M., 1995. The 1992 Sanriku-Oki, Japan, Ultra-slow earthquake. *J. Phys. Earth* **43**, 105-116.

[117] Schwartz, S.Y. and Rokosky, J.M., 2007. Slow slip events and seismic tremor at circum-Pacific subduction zones. *Rev. Geophys.* **45**, RG3004.

[118] Ide, S., Beroza, G.C., Shelly, D.R. and Uchide, T., 2007. A scaling law for slow earthquakes. *Nature* **447**, 76-79.

[119] Amoruso, A., Crescentini, L., Morelli, A. and Scarpa, R., 2002. Slow rupture of an aseismic fault in a seismogenic region of central Italy. *Geophys. Res. Lett.* **29(24)**, 2219.

[120] Walters, R.J., Elliott, J.R., D'Agostino, N., England, P.C., Hunstad, I., Jackson, J.A., Parsons, B., Phillips, R.J. and Roberts, G., 2009. The 2009 L'Aquila earthquake (central Italy): A source mechanism and implications for seismic hazard. *Geophys. Res. Lett.* **36**, L17312.

[121] Amoruso, A. and Crescentini, L., 2009. Details of a slow earthquake following the 2009/04/06 L'Aquila earthquake, as observed by paired laser extensometers in Gran Sasso, Italy. *Eos Trans. AGU*, **90(52)**, Fall Meet. Suppl., Abstract U12A-08.

[122] Crescentini, L., Amoruso, A. and Botta, V., 2012. Slow diffusive fault slip propagation: direct evidences from high-sensitivity strain measurements. *Geophysical Research Abstracts*, **14**, EGU2012-3661, EGU General Assembly 2012.

[123] Sacks, I.S., Linde, A.T., Snoke, J.A. and Suyehiro, S., 1981. A slow earthquake sequence following the Izu-Oshima earthquake of 1978, in *Earthquake Prediction: An International Review, Maurice Ewing Ser.* **4**, pp. 617-628, eds Simpson, D.W. and Richards, P.G., AGU, Washington, D.C.

[124] Agnew, D.C., and Wyatt, F.K., 2003. *Long-Base Laser Strainmeters: a review.* SIO Technical Report 2, Scripps Institution of Oceanography.

[125] Takanami, T., Sacks, S., Linde, A., Peng, H. and Kitagawa, G., 2011. Slow Slip Following the 2003 Tokachi-oki M8 Earthquake off Hokkaido. *Geophysical Research Abstracts* **13**, EGU2011-2316, 2011. EGU General Assembly 2011.

[126] Crescentini, L., Botta, V., Amoruso, A. and Bettini, A., 2012. Installation of two high-sensitivity laser strainmeters in a new underground geodynamical observatory (GEODYN) at Canfranc (Spain). *Geophysical Research Abstracts*, **14**, EGU2012-3663, EGU General Assembly 2012.

[127] Ray, R.D., 1999. A global ocean tide model from TOPEX/POSEIDON altimetry: GOT99.2. NASA Technical Memorandum 209478.

[128] Venedikov, A.P., 1961. Application à l'analyse harmonique des observations des marées terrestres de la Méthode des moindres carrées. *Comptes Rendues Académie Bulgare des Sciences* **14(7)**, 671-674.

[129] Venedikov, A.P., 1966. Une méthode d'analyse des marées terrestres à partir d'enregistrements de longueurs arbitraires. *Observatoire Royal de Belgique, Série Géophysique* **71**, 463-485.

[130] Sakamoto, Y., Ishiguro, M. and Kitagawa, G., 1986. *Akaike information criterion statistics.* D. Reidel Publishing Company, Tokyo.

[131] Ishiguro, M. and Tamura Y., 1985. BAYTAP-G in TIMSAC-84. *Computer Science Monographs*, **22**, Institute of Statistical Mathematics, Tokyo, Japan.

[132] Ishiguro, M., Akaike, H., Ooe, M. and Nakai, S., 1981. A Bayesian approach to the analysis of earth tides. *Proceedings of the 9th International Symposium Earth Tides*, 283-292, E. Schweizerbart'sche Verlag, Stuttgart, Germany.

[133] Eanes, R.J., 1994. Diurnal and semidiurnal tides from TOPEX/POSEIDON altimetry. *EOS, Trans. Am. Geophys. Un.* **75**, 108.